

The Pennsylvania State University
The Graduate School
Department of Electrical Engineering

**IMPLEMENTATION OF PARALLELIZED
FINITE DIFFERENCE TIME DOMAIN (FDTD)
ALGORITHM AND ITS APPLICATION TO
THE MODELING OF METAMATERIALS**

A Dissertation in
Electrical Engineering
By
Lai-Ching Ma

© 2008 Lai-Ching Ma

Submitted in Partial Fulfillment
of the Requirements
for the Degree of
Doctor of Philosophy

May 2008

The dissertation of Lai-Ching Ma was reviewed and approved* by the following:

Raj Mittra
Professor of Electrical Engineering
Thesis Advisor
Chair of Committee

Kultegin Aydin
Professor of Electrical Engineering

James K. Breakall
Professor of Electrical Engineering

Michael T. Lanagan
Associate Professor of Engineering Science and Mechanics

W. Kenneth Jenkins
Professor of Electrical Engineering
Head of the Department of Electrical Engineering

*Signatures are on file in the Graduate School

ABSTRACT

Finite Difference Time Domain (FDTD) method is a widely used full-wave numerical technique for solving electromagnetic problems in a wide range of applications. It has significant advantages over other numerical techniques, namely that it is easy to understand, simple to implement, and is well suited for solving general type of problems involving complex structures and arbitrarily inhomogeneous materials that require wideband solutions. In recent years, the development in parallel computation has led to a parallelized version of the FDTD solver, which has become one of the most desirable tools for treating extremely large and complex problems in a time-efficient manner.

In this dissertation we focus our attention primarily on two aspects, namely the implementation of a parallelized 3-D FDTD algorithm and its application to the modeling of metamaterials. First, we begin by proposing an efficient, parallel implementation of the Periodic Boundary Condition (PBC) in FDTD, which is based on the split-field method. The parallel scheme is based on a one-cell overlapping approach that is employed in the conventional FDTD method, which is extended in this work to include the PBC to model problems with periodic geometries. Next, a new, stable implementation of the Convolutional Perfectly Matched Layer (CPML) is implemented in the PBC/FDTD algorithm to truncate the computational domain with open boundaries.

Second, we propose a scheme to excite a desired incident field distribution in the computational domain to solve scattering problems that involve infinite structures. This scheme is based on modifying the conventional Total-Field/Scattered-Field (TF/SF) technique, which, in

its original form, applies only to finite structures. The performance of the proposed scheme is studied by launching two different incident field distributions, namely a Gaussian beam and a plane wave.

Third, we carry out an extensive study of the electromagnetic (EM) response of a Double-Negative (DNG) slab, comprising of a combination of split-rings and wires, by using the parallel FDTD technique. Initially, we perform a preliminary analysis of the scattering characteristics of an infinite DNG slab, by using the proposed PBC/FDTD technique, to retrieve the effective material parameters via the modified inversion approach, which is described in this work. Some problem areas that may be encountered when using effective material parameters in real-world applications are identified, and the importance of carrying out rigorous simulations, which model the original structure, comprising of inclusions in a background medium accurately, is recognized. Finally, the EM response of a finite, artificial-DNG slab, illuminated either by a Gaussian beam or a small dipole is studied by using the parallel FDTD solver.

TABLE OF CONTENTS

LIST OF FIGURES	ix
LIST OF TABLES.....	xxii
ACKNOWLEDGEMENTS.....	xxiii
Chapter 1 INTRODUCTION	1
1.1 Motivation and Background.....	1
1.2 Research Objectives	7
1.3 Chapter Outline	9
Chapter 2 PARALLEL FDTD TECHNIQUE.....	11
2.1 Introduction	11
2.1.1 A Brief Review of the FDTD Algorithm.....	11
2.2 Parallel FDTD Technique	13
2.2.1 MPI Library	15
2.2.2 Parallel Field Exchanging Algorithm	15
2.2.3 Parallel Implementation of Other Tasks	18
2.2.4 Design of Parallel Settings.....	18
2.3 Efficiency Analysis of the Parallel FDTD Solver	20
2.3.1 Performance Analysis on Large Computer Cluster (LOFAR BlueGene/L).....	20
2.3.2 Performance Analysis on Small Computer Cluster	24
2.4 Examples of Practical Problem Solved	26
2.4.1 Vivaldi Antenna Array.....	26
2.4.2 Electronic Packaging Problem.....	29
2.4.3 Metamaterial Structures	31
2.5 Conclusions	33

Chapter 3	EFFICIENT PARALLEL IMPLEMENTATION OF PERIODIC BOUNDARY CONDITION IN THE FDTD INCORPORATING THE CONVOLUTIONAL PML	34
3.1	Introduction	34
3.2	Review of the Existing PBC/FDTD Methods	37
3.2.1	Existing PBC/FDTD Methods	37
3.2.2	Formulation of Field Transformation	39
3.2.3	Formulation of Split-Field Method	40
3.2.4	Updating Procedure Based on the Split-Field Method	41
3.2.5	Enforcement of the PBC	44
3.3	Parallel Implementation of the PBC/FDTD Method	46
3.3.1	Communication Between Two Neighboring Subdomains	46
3.3.2	Communication Between Two Subdomains on Two Opposite Side of Periodic Boundaries	49
3.3.3	Numerical Test of Parallel Efficiency	50
3.4	Implementation of CPML into PBC/FDTD Method	52
3.4.1	Formulation of the CPML	52
3.4.2	CPML Formulation Within the PBC/FDTD Following the Conventional Way	55
3.4.3	Suggested Cause for the Instability	58
3.4.4	Modified CPML Implementation	59
3.5	Calculation of Transmission and Reflection Coefficients Using the PBC/FDTD Solver	63
3.5.1	One-Step Approach—Extraction of Magnitude of T and R Coefficients	64
3.5.2	Two-Step Approach—Extraction of Both Magnitude and Phase of T and R Coefficients	65
3.6	Numerical Examples	67
3.6.1	Singly-Periodic Lossy Screen	67
3.6.2	Metamaterial Slab That Exhibits Double-Negative Behavior	70
3.6.3	Double-Screen FSS Used in Reflector Antenna System	74
3.6.4	Study of Terahertz Transmission for Periodic Arrays of Dielectric and Conducting Spheres	80
3.7	Conclusions	85

Chapter 4 IMPLEMENTATION OF TRANSPARENT SOURCE IN THE SCATTERING PROBLEM INVOLVING LARGE INFINITE STRUCTURES.....	86
4.1 Introduction	86
4.2 Implementation of the Proposed Excitation Scheme	90
4.3 The Performance of the Proposed Excitation Scheme for Launching a Gaussian Beam.....	93
4.3.1 Effect of the Size of the Computational Domain.....	94
4.3.2 Effect of the Electrical Length of the Spot Size	98
4.4 Numerical Examples for Gaussian Beam Illumination.....	101
4.4.1 Study of the Extraordinary Transmission (ET) in Stacks of Doubly-Periodic Subwavelength Hole Arrays	101
4.4.2 Double-Negative (DNG) Array	104
4.5 The Performance of the Proposed Excitation Scheme in Launching a Uniform Plane Wave.....	104
4.5.1 Effect of Extending the TF/SF Interface into the PML Region.....	105
4.5.2 Effect of the Size of the TF/SF Interface in the Direction Normal to the Plane of Incidence	107
4.5.3 Effect of the Incident Direction, Polarization, and Frequency of the Excited Wave	108
4.5.4 Accuracy Improvement by Applying Window to the Incident Field Used on the TF/SF Interface Within the PML Region.....	120
4.6 Guidelines for Using the Proposed Excitation Scheme in Plane Wave Excitation.....	127
4.7 Numerical Example for Plane Wave Illumination	130
4.8 Conclusions	133
Chapter 5 INVESTIGATION OF DOUBLE-NEGATIVE METAMATERIAL SLABS BY USING THE FDTD TECHNIQUE	135
5.1 Introduction	135
5.2 EM Response of the Infinite, Doubly-Periodic DNG Slab with Plane Wave Illumination	142
5.2.1 Model Description of the Array Comprising of Split-Ring Resonators and Wires.....	142
5.2.2 Scattering Parameters Measurements Obtained from the PBC/FDTD Code	143

5.2.3	Phase Data Inside the DNG Slab	149
5.3	Retrieval of Effective Material Constitutive Parameters Using the Inversion Approach	152
5.3.1	Basic Assumption of Effective Material Constitutive Parameters	153
5.3.2	Review of the Inversion Approach	154
5.3.3	Retrieval of the Effective Material Parameters from the Numerical S-Parameters Obtained from FDTD Simulations of Metamaterials	160
5.3.4	Summary of the Difficulties Encountered Using the Inversion Approach for Effective Medium Characterization	187
5.3.5	Re-examination of the Concept of the Effective Material Parameters	189
5.4	EM Response of a Finite Artificial-DNG Slab with Localized Beam Illumination	194
5.4.1	FDTD Model.....	196
5.4.2	Total Transmission and Reflection Power Under Gaussian Beam Illumination	197
5.4.3	EM Response of the Artificial-DNG Slab at Normal Incidence with Ey Polarization.....	201
5.4.4	EM Response of the Artificial-DNG Slab at Oblique TM_z Incidence Coming from $(\theta=150^\circ, \phi=90^\circ)$ with Hx Polarization.....	209
5.4.5	EM Response of the Artificial-DNG Slab at Oblique TE_z Incidence Coming from $(\theta=150^\circ, \phi=0^\circ)$ with Ey polarization.....	216
5.5	EM Response of a Finite Artificial-DNG Slab Excited by Small Dipole	220
5.6	Conclusions	226
Chapter 5 CONCLUSIONS AND FUTURE WORK		228
BIBLIOGRAPHY.....		232

LIST OF FIGURES

Figure 2.1:	The three-dimensional spatial grid (Yee's cell) used in the FDTD algorithm.....	11
Figure 2.2:	Diagram illustrating three kinds of parallel processing configurations.....	14
Figure 2.3:	Configuration of field exchange between two neighboring processors.....	16
Figure 2.4:	The updating procedure in a single cycle of the parallel FDTD algorithm. The steps for parallel field exchange are highlighted in red box.....	17
Figure 2.5:	Antenna element (Left) and the 100x100 patch antenna array (Right).	21
Figure 2.6:	The geometry of a single antenna element.	21
Figure 2.7:	The far-field pattern of the 100x100 patch antenna array in the (a) x-z plane and (b) y-z plane.....	22
Figure 2.8:	Simulation time of the patch antenna array using different number of processors on the LOFAR BlueGene/L.....	23
Figure 2.9:	Scalability of the parallel FDTD code on the LOFAR BlueGene/L.....	23
Figure 2.10:	Efficiency of the parallel FDTD code on the LOFAR BlueGene/L.	24
Figure 2.11:	Efficiency and scalability of the parallel FDTD as a function of the number of processors on a recently-built computer cluster.	25
Figure 2.12:	Photo of the Westerbork Synthesis Radio Telescope.	27
Figure 2.13:	The geometry of the Vivaldi antenna array (Left) and its single element (Right).....	27
Figure 2.14:	The E-plane far-field pattern of the Vivaldi array antenna where only the center element is excited and all the others are terminated with 50 Ω impedances. (a) 4.7 GHz, and (b) 5.3 GHz.....	28
Figure 2.15:	Input impedance and the scattering parameter at the central active element. (a) and (b) Real and imaginary part of input impedance; (c) and (d) Magnitude and phase of S11.....	29
Figure 2.16:	The stack-up of the chip package.....	30
Figure 2.17:	(a) The circuit structure (b) and one layer of printed circuit board.	31

Figure 2.18: The scattering parameters of the chip package.....	31
Figure 3.1: Geometry of freestanding frequency selective surfaces consisting of (a) conducting patches; and (b) apertures.....	35
Figure 3.2: (a) A typical example of a PBG structure and (b) its transmission characteristics.....	36
Figure 3.3: Classification of the PBC/FDTD techniques: Direct Field methods and Field-Transformation methods.....	38
Figure 3.4: A passive periodic structure under the excitation of a plane wave. The periodic boundaries for the unit cell at (x_0, y_0) is highlighted in red.	39
Figure 3.5: The three-dimensional spatial grid used in the split-field PBC/FDTD algorithm.....	42
Figure 3.6: The updating procedure in a single cycle of the serial split-field PBC/FDTD algorithm.....	43
Figure 3.7: Schematic showing the computational domain extended beyond the periodic boundaries. During each cycle, after the fields inside the periodic boundary have been computed, the tangential magnetic fields in the extended region can be “copied” from the field values of their periodic “image”, as illustrated by the red arrow.....	45
Figure 3.8: Configuration of field exchange between two neighboring processors.....	47
Figure 3.9: The updating procedure in a single cycle of the parallel split-field PBC-FDTD algorithm. The steps for parallel field exchange are highlighted in red boxes.	48
Figure 3.10: Configuration of field exchange between two processors at the two opposite periodic boundaries.	50
Figure 3.11: The parallel efficiency versus the number of processors when using the PBC/FDTD code (Blue) and the standard FDTD code (red) without the PBC.	52
Figure 3.12: Diagram of the boundary condition, excitation and measurement settings used in testing the CPML implemented in the PBC/FDTD algorithm.	57
Figure 3.13: (a) The transient waveform and (b) the spectrum of the incident signal used in testing the CPML implemented in the PBC/FDTD algorithm.	57

- Figure 3.14:** Transient waveform E_x measured at a point inside the total-field region for (a) the first 300 cycles, and (b) the first 4000 cycles, respectively, using CPML (Blue) and UPML (Red). The CPML is implemented in the same way as done in the standard FDTD method.....58
- Figure 3.15:** Transient waveform E_x measured at a point inside the total-field region using the UPML(Blue), the Mur (Green), and our proposed CPML (Red): (a) the first 800 cycles, (b) between cycles 100 and 200, and (c) the transient waveform from the 5000th to 100000th cycles, using the proposed CPML algorithm.42
- Figure 3.16:** Schematic setting of the TS/SF interface and the measurement planes employed in computing the T/R coefficients using the first approach.65
- Figure 3.17:** Schematic settings of the TS/SF interface and the measurement planes employed in computing the T/R coefficients using the second approach. Two simulations are required: (a) one with the periodic structure, and (b) one with the structure removed.....66
- Figure 3.18:** Geometry of a free-standing, two-dimensional screen, comprising of infinitely long, parallel, and equally-spaced conducting bars.....67
- Figure 3.19:** Time-domain far-field (Blue: Real, Red: Imaginary) for the first three transmitting Floquet modes (a-c) of the lossy screen shown in Fig. 3.18.69
- Figure 3.20:** Magnitude of transmission coefficient for the first three Floquet modes of the lossy screen shown in Fig. 3.18. Our results are displayed in colors and the results from [21] are displayed in black.....70
- Figure 3.21:** The unit structure comprising of a split-ring and a wire.....71
- Figure 3.22:** Unit cells for the 1- and 6-layer slab. Note that the array is doubly-periodic along the x- and y-directions.....72
- Figure 3.23:** Magnitude of transmission (Blue) and reflection (Red) coefficients of the EBG array: (a) 1-layer, and (b) 6-layer.....73
- Figure 3.24:** Configuration of the dual-feed offset Cassegrain system, with FSS used as sub-reflector.74
- Figure 3.25:** Geometry of the FSS unit cell used in the sub-reflector shown in Fig. 3.24...75
- Figure 3.26:** Illustration of the FDTD mesh used: (a) the x-y plane, and (b) the x-z plane (only mesh in z-direction is shown).76
- Figure 3.27:** Transient waveform E_x at three different locations: (a) above the TF/SF interface; (b) inside the FSS composite; and (c) below the FSS.....78

Figure 3.28: A closer look at the last 10,000 cycle of the time-domain signals in Fig. 3.27.....	79
Figure 3.29: Transient far-field in the (a) transmission and (b) reflection direction.....	79
Figure 3.30: Comparison of the magnitudes of the T and R coefficients obtained by the FDTD and a periodic MoM solver.....	80
Figure 3.31: An array of spheres under the illumination of a Gaussian beam. The periodicity for the spheres is (a) 2 mm, (b) 3 mm, (c) 4 mm, respectively. The Gaussian beam has a beam-width of 25 mm (shown by blue circle) in all cases.	81
Figure 3.32: Magnitude of transmission coefficient obtained from FDTD calculation (yellow) and experiment for the Si ₃ N ₄ spheres with periodicities of (a) 2mm, (b) 3mm, and (c) 4 mm, from 50 to 200 GHz.....	82
Figure 3.33: Magnitude of transmission coefficient obtained from FDTD calculation (yellow) and experiment (red) for the brass spheres with periodicities of (a) 2mm, (b) 3mm, and (c) 4 mm, from 50 to 200 GHz.	83
Figure 3.34: The electric field distribution over the transverse cross-section of Si ₃ N ₄ sphere (periodicity = 2 mm) at each resonant frequency, ranging from (a) 60 – 90 GHz, and (b) 90 – 120 GHz.	84
Figure 4.1: Total-field/scattered field zoning of the FDTD space lattice in the conventional TF/SF approach. Note that the PML region is not drawn in the figure.	86
Figure 4.2: Total-field/scattered field zoning of the FDTD space lattice in the modified TF/SF approach, which is extended to stratified media to solve the problem of scattering from a buried-object. Note that the PML region is not drawn in the figure.....	87
Figure 4.3: Total-field/scattered field zoning of the FDTD space lattice in the generalized-TF/SF approach, where the TF/SF interface is allowed to be partially embedded with the PML region.	89
Figure 4.4: Total-field/scattered field zoning of the FDTD space lattice in our proposed TF/SF approach, where the scatterer is allowed to be extended into the PML region without truncating the TF/SF interface.	91
Figure 4.5: Two possible total-field/scattered field zoning of the FDTD space lattice in the proposed TF/SF approach for a finite scatterer. The TF/SF setting in (a) is preferable to that in (b) since the incidence wave propagates along a direction closer to that of the normal of the TF/SF interface in (a).....	92

- Figure 4.6:** The $|E_x|$ distribution for the measured field on the TF/SF interface (Left) and the incident field (Right) at 10 GHz, when a normally incident Gaussian beam of spot size (w) is excited inside a computational domain of three different sizes (L): (i) $L = 2w$; (ii) $L = 3w$; and (iii) $L = 4w$96
- Figure 4.7:** Comparisons of the measured $|E_x|$ on the TF/SF interface for three different domain sizes and the incident $|E_x|$ at 10 GHz on the line of observation along the x- (Left) and y- (Right) directions, respectively. The Gaussian beam settings are as follows: (a) and (b) Normal incidence; (c) and (d) Oblique 30° TE_z incidence from $\phi=270^\circ$; and (e) and (f) Oblique 30° TM_z incidence from $\phi=180^\circ$97
- Figure 4.8:** The $|E_x|$ distribution for the measured field on the TF/SF interface at (a) 1.67 GHz, (b) 3.33 GHz, (c) 5.0 GHz, and (d) 10 GHz, when a normally incident Gaussian beam of spot size ($w = 90$ mm) is excited. The frequency-independent incident field distribution is also shown in (e).99
- Figure 4.9:** Comparisons of the measured $|E_x|$ on the TF/SF interface at four different frequencies and the incident $|E_x|$ on the line of observation along the x- (Left) and y- (Right) directions, respectively. The Gaussian beam settings are as follows: (a) and (b) Normal incidence; (c) and (d) Oblique 30° TE_z incidence from $\phi=270^\circ$; and (e) and (f) Oblique 30° TM_z incidence from $\phi=180^\circ$100
- Figure 4.10:** (a) Photograph of the copper plate perforated with subwavelength hole arrays (Source: Fig. 1 (a) of Ref. [70]). (b) 3-D view, and (c) side view of the whole structure in FDTD model.102
- Figure 4.11:** Experimental quasi-optical bench set-up. The propagating path of the Gaussian beam is highlighted in blue. (Source: Fig. 3 of Ref. [70]).103
- Figure 4.12:** Comparison of the transmission coefficient between the FDTD result and the experiment data in Ref. [70]. The co-pol. FDTD result is shown in red and the cross-pol. level is below -80 dB (not shown). The experimental results from ref. [70] for the co-pol. and cross-pol. are shown in cyan solid and dashed line, respectively, for the same setting.103
- Figure 4.13:** Snapshots of E_x on the XZ plane for an Ex-polarized plane wave incident from $\theta=180^\circ$, computed by using the proposed TF/SF formulation (a) extending into the PML; and (b) truncated at the inner PML boundary.106
- Figure 4.14:** Maximum error of E and H fields measured on the TF/SF interface for a normally incident plane wave as computed by using the proposed TF/SF formulation for different domain sizes and FDTD discretizations.109

- Figure 4.15:** Normalized magnitude of the measured (a) E_x and (b) H_y at 10 GHz, in the TF region up to 1λ away from the TF/SF interface. A normally incident Ex-polarized plane wave is excited by using the proposed TF/SF formulation at $Z=0$. The relative error of both E_x and H_y ranges from -0.39% to 0.12% within this region.....110
- Figure 4.16:** Snapshots of E_x on the XZ plane for an E_θ -polarized plane wave incident from $(\theta=170^\circ, \phi=180^\circ)$, excited by using the proposed TF/SF formulation, at (a) $t = 0.11$ ns and (b) $t = 0.24$ ns.....112
- Figure 4.17:** Snapshots of E_x on the XZ plane for an E_θ -polarized plane wave incident from $(\theta=150^\circ, \phi=180^\circ)$, excited by using the proposed TF/SF formulation, at (a) $t = 0.21$ ns and (b) $t = 0.32$ ns.....113
- Figure 4.18:** Normalized magnitude of E and H fields measured on the TF/SF interface along the x-direction, for (a) an E_ϕ -polarized and (b) an E_θ -polarized plane wave incident from $(\theta=150^\circ, \phi=180^\circ)$, computed by using the proposed TF/SF formulation.114
- Figure 4.19:** Normalized magnitude of H_y (at 10 and 15 GHz) on the TF/SF interface along the x-direction expressed in terms of wavelength. An E_θ -polarized plane wave coming from $(\theta=150^\circ, \phi=180^\circ)$ is excited by using the proposed TF/SF formulation in a domain of size 1000 mm.115
- Figure 4.20:** Normalized magnitude of E_x (Blue) and H_y (Red) at 10 GHz, along the x-direction, measured on the TF/SF interface. The excited E_θ -polarized plane wave is incident from $\phi=180^\circ$ and (a) $\theta=170^\circ$; and (b) $\theta=150^\circ$. Region between the two black dashed lines has a relative error of less than 4%.....117
- Figure 4.21:** Normalized magnitude of E_x (Blue) and H_y (Red) at 10 GHz, along the x-direction, measured at one wavelength above the TF/SF interface. The excited E_θ -polarized plane wave is incident from $\phi=180^\circ$ and (a) $\theta=170^\circ$; and (b) $\theta=150^\circ$. Region between the two black dashed lines has a relative error of less than 4%.118
- Figure 4.22:** Comparison of the phase of H_y at 10 GHz along the x-direction, between the measured and the incident fields, located at one wavelength above the TF/SF interface. The excited E_θ -polarized plane wave is incident from $\phi=180^\circ$ and (a) $\theta=170^\circ$; and (b) $\theta=150^\circ$119
- Figure 4.23:** Normalized magnitude of the measured E_x (Left) and H_y (Right) at 10 GHz, in the TF region up to 1λ away from the TF/SF interface (at $Z = 0$). The excited E_θ -polarized plane wave is incident from $\phi=180^\circ$ and (a) and (b) $\theta=170^\circ$; and (c) and (d) $\theta=150^\circ$120

Figure 4.24: Incident field amplitude (Red) applied on the TF/SF interface along the x-direction, with field tapering inside the PML region on the positive x-end. The amplitude falls to $1/e^2$ at the outermost PML layer.....122

Figure 4.25: Snapshot of E_x at $t = 0.32$ ns, on the XZ plane for an E_θ -polarized plane wave incident from $(\theta=150^\circ, \phi =180^\circ)$, The plane wave is excited by using the proposed TF/SF formulation and an addition of Gaussian window on the incident field amplitude as shown in Fig. 4.23.122

Figure 4.26: Comparison of the normalized magnitude of E_x (Left) and H_y (Right) at 10 GHz excited with (Red) and without (Blue) applying a Gaussian tapering window on the “incident field” in the PML region on the positive x-end. The excited E_θ -polarized plane wave is incident from $\phi =180^\circ$ and $\theta=150^\circ$. The fields are measured on the TF/SF interface (a-b); and at one wavelength above the TF/SF interface (c-d), respectively.124

Figure 4.27: Normalized magnitude of the measured E_x (Left) and H_y (Right) at 10 GHz, in the TF region up to 1λ away from the TF/SF interface (at $Z = 0$). A Gaussian tapering window is applied to the “incident field” in the PML region on the positive x end. The excited E_θ -polarized plane wave is incident from $\phi =180^\circ$ and $\theta=150^\circ$125

Figure 4.28: Comparison of the incident field inside the PML region (Blue) which is computed by using the calibration process in [64], and the incident field that we actually apply (Red) on the TF/SF interface.125

Figure 4.29: Comparison of the normalized magnitude of E_x (Left) and H_y (Right) at 10 GHz excited with (Red) and without (Blue) using the calibrated incident field (shown in Fig. 4.28) inside the PML region. The excited E_θ -polarized plane wave is incident from $\phi =180^\circ$ and $\theta=150^\circ$. The fields are measured on the TF/SF interface (a-b), and at one wavelength above the TF/SF interface (c-d), respectively..126

Figure 4.30: Normalized magnitude of the measured (a) E_x and (b) H_y at 10 GHz, in the TF region up to 1λ away from the TF/SF interface (at $Z = 0$). The incident field inside the PML region is calibrated and applied on the TF/SF interface. The excited E_θ -polarized plane wave is incident from $\phi =180^\circ$ and $\theta=150^\circ$127

Figure 4.31: The typical field distribution in the plane of incidence, when a plane wave of moderate incident angle is excited by using our proposed scheme. (a) The interested region is completely embedded inside the uniform field region, and (b) The interested region is partly embedded inside the non-uniform field region. An extension of computational domain is necessary to obtain accurate results.....129

Figure 4.32: Geometry of the scattering problem of a buried object.	131
Figure 4.33: The scattered field in the presence of the ground and the dielectric cube (b) The scattered field contributed by the dielectric cube only.	132
Figure 4.34: The far-zone scattered electric field from a dielectric cube for our FDTD result (Red) and those obtained in [71] (Black solid and dashed lines).....	133
Figure 5.1: ϵ - μ space.	136
Figure 5.2: Left-handed and right-handed medium.....	137
Figure 5.3: Refraction at the interface between air and DNG material.....	138
Figure 5.4: Superlensing effect by a DNG slab.....	138
Figure 5.5: (a) First prototype of DNG structure made of split-ring resonator (SSR) and wires; (b) Measured transmission magnitude... ..	139
Figure 5.6: (a) Diagram of experimental set up; (b) Measured power at different direction.	139
Figure 5.7: Magnitude of the transmission coefficient for the 1-layer (Blue) and 6- layer (Red) slabs with different types of inclusions: (a) split-ring and wires; (b) wires alone; and (c) split-ring alone.	145
Figure 5.8: Phase of the transmission coefficient for the 1-layer (Blue) and 6-layer (Red) slabs with different types of inclusions: (a) split-ring and wires; (b) wires alone; and (c) split-ring alone.....	146
Figure 5.9: Magnitude of the reflection coefficient for the 1-layer (Blue) and 6-layer (Red) slabs with different types of inclusions: (a) split-ring and wires; (b) wires alone; and (c) split-ring alone.....	147
Figure 5.10: Phase of the reflection coefficient for the 1-layer (Blue) and 6-layer (Red) slabs with different types of inclusions: (a) split-ring and wires; (b) wires alone; and (c) split-ring alone.	148
Figure 5.11: Magnitude and Phase measured inside the 6-layer DNG slab, along two different lines in the propagation direction at (a) 15.2 GHz; and (b) 19.6 GHz. The circles represent the boundaries between the adjacent layers.	150
Figure 5.12: (a) The slope of the phase against propagation distance computed using the phase data obtained from FDTD simulations. (b) The real part of refractive index extracted from the slope in (a). The slope and the refractive index are only computed within the two 3-dB passbands (in grey) of the 6-layer slab	151

- Figure 5.13:** Wave reflection and transmission at normal incidence by a planar interface.....161
- Figure 5.14:** Comparison of the extracted impedance Z (LEFT: real part, RIGHT: imaginary part) for slabs of 1-, 2-, and 3-layers with inports and outputs placed at different locations: (a) and (b) 1 FDTD cell; (c) and (d) 2 FDTD cells; and (e) and (f) 3 FDTD cells beyond the outermost edge of the metallic inclusions on each side of the slab.....162
- Figure 5.15:** The wave impedance retrieved from the 1-layer slab.....163
- Figure 5.16:** The solutions for n'' derived from the two roots in (7.4) for the 1-layer slab.....164
- Figure 5.17:** The solutions for (a) n' , (b) ϵ'' , and (c) μ'' , computed by using the positive root in (7.4) with a branch index of $m = 0, -1, \text{ and } +1$, respectively.....165
- Figure 5.18:** The solutions for (a) n' , (b) ϵ'' , and (c) μ'' , computed by using the negative root in (7.4) with a branch index of $m = 0, -1, \text{ and } +1$, respectively... ..166
- Figure 5.19:** (a) The value of $|nk_0d|$ for all remaining solutions obtained from the inversion approach; Comparison of the (b) real and (c) imaginary parts of n for all remaining solutions obtained from the inversion approach (lines) and from the SPSL approximation (circles), in the frequency band (iii) through (v) as shown in Fig. 5.16 (b).....168
- Figure 5.20:** The SPSL solutions over the entire observation frequency band: effective (a) n ; (b) ϵ ; and (c) μ . Note that the SPSL condition is not satisfied over the entire band.....169
- Figure 5.21:** The extracted material parameters for the 1-layer case: (a) n ; (b) ϵ ; and (c) μ . Grey area represents the non-physical region where no solutions can be found to satisfy both ϵ'' and $\mu'' \leq 0$. The black circles in (a) represent the refractive index computed by using the phase data computed in Sec. 5.2.3.....171
- Figure 5.22:** The wave impedance retrieved for the 1-layer slab comprising of different types of inclusions: (a) SSRs and wires; (b) wires alone; and (c) SSRs alone. Grey area represents the non-physical region where no solutions can be found to satisfy both ϵ'' and $\mu'' \leq 0$173
- Figure 5.23:** Refractive index retrieved for the 1-layer slab, comprising of different types of inclusions: (a) SSRs and wires; (b) wires alone; and (c) SSRs alone. Grey area represents the non-physical region where no solutions can be found to satisfy both ϵ'' and $\mu'' \leq 0$174

- Figure 5.24:** Effective electric permittivity retrieved for the 1-layer slab, comprising of different types of inclusions: (a) SSRs and wires; (b) wires alone; and (c) SSRs alone. Grey area represents the non-physical region where no solutions can be found to satisfy both ϵ'' and $\mu'' \leq 0$175
- Figure 5.25:** Effective magnetic permeability retrieved for the 1-layer slab comprising of different types of inclusions: (a) SSRs and wires; (b) wires alone; and (c) SSRs alone. Grey area represents the non-physical region where no solutions can be found to satisfy both ϵ'' and $\mu'' \leq 0$176
- Figure 5.26:** The set of all possible solutions of n' for the DNG slabs with multi-layer inclusion: (a) 2-layer; (b) 3-layer; and (c) 6-layer.178
- Figure 5.27:** The set of all possible solutions of n'' for the DNG slabs with multi-layer inclusion: (a) 2-layer; (b) 3-layer; and (c) 6-layer.179
- Figure 5.28:** Comparison of the wave impedance extracted for the DNG slab, starting from one and up to four layers: (a) real; and (b) imaginary part.180
- Figure 5.29:** Comparison of the refractive index extracted for the DNG slab, starting from one and up to four layers: (a) real; and (b) imaginary part.181
- Figure 5.30:** Comparison of the effective electric permittivity extracted for the DNG slab, starting from one and up to four layers: (a) real; and (b) imaginary part.183
- Figure 5.31:** Comparison of the effective magnetic permeability extracted for the DNG slab, starting from one and up to four layers: (a) real; and (b) imaginary part.184
- Figure 5.32:** The values of $|nk_0d|$ (blue) and $|n'k_0d|$ (red), where n is computed by using the inversion approach; and the comparison of the S-parameters obtained by using FDTD (lines) and those recovered by using the SPSL solutions (dots) in the region where (b) $|nk_0d| < 0.2$; and (c) $|n'k_0d| < 0.2$185
- Figure 5.33:** Comparison of the magnitude of the S-parameters, recovered from the retrieved n and Z of the 1-layer slab (solid) and obtained from the direct FDTD simulations (circle dash) for 1-layer up to 6-layer slabs in (a) through (f).186
- Figure 5.34:** Comparison of the magnitude of the S-parameters, recovered from the retrieved n and Z of the 3-layer slab (solid) and obtained from the direct FDTD simulations (circle dash) for 1-layer up to 6-layer slabs in (a) through (f).192

- Figure 5.35:** Ray picture illustrating the propagation of a uniform plane wave through a homogeneous DNG slab in free space.....194
- Figure 5.36:** Geometry of a six-layer artificial DNG slab and three incident settings.....195
- Figure 5.37:** Comparison of the magnitude of transmission and coefficient coefficients for the infinite array under plane wave illumination (solid lines) and finite array under Gaussian beam illumination (dots) at normal incidence for E_y polarization.198
- Figure 5.38:** Comparison of the magnitude of transmission and coefficient coefficients for the infinite array under plane wave illumination (solid lines) and the finite array under Gaussian beam illumination (dots) at oblique incidence (30° off-normal), for (a) TM_z polarization and (b) TE_z polarization.200
- Figure 5.39:** The magnitude (Left) and phase (Right) of E_y at 15.3 GHz on the YZ plane (E-plane), for three different configurations at normal incidence: (a) and (b) With DNG slab; (c) and (d) for the DNG slab replaced by a dielectric slab of $\epsilon_r = 4$ of the same size; and (e) only for free space. The DNG or dielectric slab occupies the region between $z = -23.75$ and 0 mm, the excitation plane is on $z = 0$ mm, and the region above 0 mm is free space.....202
- Figure 5.40:** The magnitude (Left) and phase (Right) of E_y at 15.3 GHz on the XZ plane (H-plane), for three different configurations at normal incidence: (a) and (b) With DNG slab; (c) and (d) for the DNG slab replaced by a dielectric slab of $\epsilon_r = 4$ of the same size; and (e) only for free space. The DNG or dielectric slab occupies the region between $z = -23.75$ and 0 mm, the excitation plane is on $z = 0$ mm, and the region above 0 mm is free space.....203
- Figure 5.41:** Magnitude of E_y at 15.3 GHz on the XY plane at 2 mm (Left) and 19 mm (Right) from the top surface of the slab, for three different configurations at normal incidence: (a) and (b) With DNG slab; (c) and (d) for the DNG slab replaced by a dielectric slab of $\epsilon_r = 4$ of the same size; and (e) only for free space.205
- Figure 5.42:** Phase of E_y at 15.3 GHz along the beam axis from $z = -24$ to 27.75 mm, with the DNG slab occupying the region between $z = -23.75$ and 0 mm. The red dashed line indicates the value of phase at the source. Notice that the measured phase restores to its value at the source at $z = 23.5$ mm, indicated by the vertical black dashed lines, which is the expected image location when the refractive index of the slab is equal to -1207

- Figure 5.43:** (a) Magnitude of E_y at the beam axis and (b) the 3-dB beam width on the E- and H-planes along the longitudinal direction at 15.3 GHz, inside the transmission region of the DNG slab. The corresponding magnitude and beam width with all structures removed are also plotted in dotted lines. The vertical dash line at $z = 23.5$ mm indicates the expected image location when the refractive index of the slab is equal to -1208
- Figure 5.44:** The magnitude (Left) and phase (Right) of E_y at 15.3 GHz on the YZ plane (E-plane), for three different configurations at oblique TMz incidence (30° off-normal): (a) and (b) With DNG slab; (c) and (d) for the DNG slab replaced by a dielectric slab of $\epsilon_r = 4$ of the same size; and (e) only for free space. The DNG or dielectric slab occupies the region between $z = -23.75$ and 0 mm, the excitation plane is on $z = 0$ mm, and the region above 0 mm is free space.....211
- Figure 5.45:** Magnitude of E_y at 15.3 GHz on the XY plane at 19 mm above the slab at oblique TMz incidence (30° off-normal) for three different configurations: (a) With DNG slab; (b) for the DNG slab replaced by a dielectric slab of $\epsilon_r = 4$ of the same size; and (c) only for free space.212
- Figure 5.46:** The normalized magnitude of S_z at 15.3 GHz on the YZ plane (E-plane) between $z = -24$ mm and 0 mm at oblique TMz incidence (30° off-normal) for two different configurations: (a) dielectric slab; (b) DNG slab. (c) is the figure extracted from (b) over the free space region above the DNG slab.....213
- Figure 5.47:** The transmitted beam maxima locations versus the longitudinal direction (Blue) at 15.4 GHz for TMz incidence of DNG slab. These data are separated into two groups according to the distances from the slab, and utilized to track the exit location of the beam at the slab surface at $z = 0$ mm. See the red and black lines for the trace path using the fields near to ($5 - 10$ mm) and far away from ($15-21$ mm) the slab.....214
- Figure 5.48:** The exit location of the beam at the top surface of the slab on $z = 0$ at TMz incidence, for three different configurations: (i) the beam that dominate in the region near to (Blue circles) and far away (Blue crosses) from the DNG slab ;(ii) With dielectric slab (Green circles); and (iii) only for free space. (Red circles). The incident beam enters the slab at $x = 42.75$ mm (black line)...215

- Figure 5.49:** The magnitude (Left) and phase (Right) of E_y at 15.3 GHz on the XZ plane (H-plane) at oblique TE_z incidence (30° off-normal) for three different configurations: (a) and (b) With DNG slab; (c) and (d) for the DNG slab replaced by a dielectric slab of $\epsilon_r = 4$ of the same size; and (e) only for free space. The DNG or dielectric slab occupies the region between $z = -23.75$ and 0 mm, the excitation plane is on $z = 0$ mm, and the region above 0 mm is free space.....218
- Figure 5.50:** The exit location of the beam at the top surface of the slab on $z = 0$ for three different configurations: (i) the beam that dominates in the region near to (Blue circles) and far away (Blue crosses) from the DNG slab; (ii) With dielectric slab (Green circles); and (iii) only for free space. (Red circles). The incident beam enters the slab at $x = 42.75$ mm (black line).... 219
- Figure 5.51:** The exit location of the beam at the top surface of the slab on $z = 0$ at TE_z incidence, for three different configurations: (i) With DNG slab (Blue); (ii) With dielectric slab (Green); and (iii) only for free space. (Red). The incident beam enters the slab at $y = 42.5$ mm (black line)..220
- Figure 5.52:** The magnitude (Left) and phase (Right) of E_y at 15.3 GHz on the YZ plane (E-plane), for two different configurations with dipole excitation at $z = -32.35$ mm: (a) and (b) With DNG slab; (c) and (d) only for free space. The DNG slab occupies the region between $z = -23.75$ and 0 mm, and the region above 0 mm is free space.....222
- Figure 5.53:** The magnitude (Left) and phase (Right) of E_y at 15.3 GHz on the XZ plane (H-plane), for two different configurations with dipole excitation at $z = -32.35$ mm: (a) and (b) With DNG slab; (c) and (d) only for free space. The DNG slab occupies the region between $z = -23.75$ and 0 mm, and the region above 0 mm is free space.....223
- Figure 5.54:** Magnitude of E_y on the XY plane at 12.25 mm above the DNG slab at frequencies of (a) 14.8 GHz, (b) 15.4 GHz, and (c) 16.0 GHz with dipole excitation at 11.5 mm below the bottom surface of the slab...224
- Figure 5.55:** (a) Magnitude of E_y at the centre axis and (b) the 3-dB beam width on the E- and H-planes along the longitudinal direction at 15.3 GHz, inside the transmission region of the DNG slab excited by small dipole. The corresponding magnitude and beam width with all structures removed are also plotted in dotted lines. The vertical dash line at $z = 12.25$ mm indicates the expected image location when the refractive index of the slab is equal to -1225

LIST OF TABLES

Table 2-1:	Problem size vs. simulation on a small cluster	25
Table 3-1:	Total number of sets of update equations in a three-dimensional case.....	44
Table 3-2:	Comparison of the total simulation times using different number of CPUs, for the parallel PBC/FDTD code and the general FDTD code.....	51
Table 4-1:	Maximum relative deviation of the E and H fields along the y-direction for E_ϕ -polarized plane waves.....	107

ACKNOWLEDGEMENTS

I would like to express my deepest gratitude to my advisor, Professor Raj Mittra, for his guidance, instruction, and support throughout my thesis project. I would also like to thank the members of my doctoral committee, Professor Kultegin Aydin, Professor James K. Breakall, and Professor Michael T. Lanagan, for patiently reviewing my thesis and administering the Comprehensive and Final Oral Examinations.

I would like to thank all my colleagues in the FDTD research group of the Electromagnetic Communication Laboratory (ECL) at Penn State, Dr. Wenhua Yu for his insightful discussion on the FDTD technique, Mr. Yongjun Liu and Mr. Xiaoling (Bob) Yang for their technical support in computer and software development. My special thanks go to my colleagues in the same lab, Dr. Kai Du, Dr. Nader Farahat and Dr. Tao Su, for their valuable and insightful discussions on various EM concepts and research techniques.

Last but not least, I am dedicating this thesis to my husband, Neng-Tien, for his love and support throughout my graduate studies. Without his encouragement over the years, the completion of this thesis would not have been possible.

Chapter 1

INTRODUCTION

1.1 Motivation and Background

Computational electromagnetics (CEM) tools are widely used for electromagnetic modeling, simulation, and analysis of the electromagnetic responses of complex systems subjected to various electromagnetic stimuli. They also help us gain an understanding of the underlying physics that governs the system response, and to design or modify these systems for improved performance. With the availability of affordable and powerful computers during the past few decades, CEM tools have gained powerful roles in both scientific research and engineering applications. Before the advent of the computers, the solution of electromagnetic problem often relied on simplifying the geometry of the problem in order to apply a closed-form solution. However, these assumptions were often too crude to yield accurate results for most practical problems. The full-wave CEM tools deal with Maxwell's equations directly without making any prior assumptions; hence they are numerically rigorous. The application ranges from military defense, such as radar and radome design, to commercial applications in the areas of communication, computing (design of miniature electronic components) and biomedicine research.

Many CEM methods have been developed over the years. The most widely used full-wave techniques are: Method of Moments (MoM) [1]; Finite Element Method (FEM) [2]; and, Finite Difference Time Domain (FDTD) Method [3]. Each of these methods has its own advantages and disadvantages. For example, the MoM is well-known to be most efficient for

analyzing large structures involving only metallic conductors or homogeneous dielectrics, although it can also be used to analyze printed structures on infinite, planar stratified media, backed by a ground plane. Unlike the FEM and FDTD, the MoM does not require a special treatment for an open-region problem. However, the solution of inhomogeneous dielectric or complex geometry presents great challenges because a volume formulation must be used to handle these problems, and this makes them computationally very expensive. In addition, the conventional MoM requires the solution of a dense matrix, which is very difficult when the number of unknowns (N) is large. Using a direct solver, the requirement on c.p.u. time and memory is on the order of $o(N^3)$ and $o(N^2)$, respectively. With the typical discretization of 10 cells per wavelength, the problem size that can be accommodated on a PC with 2 GB memory is limited to objects with relatively small dimensions.

In contrast to the MoM, FEM is better suited for dealing with general electromagnetic radiation and scattering problems involving complex structures and inhomogeneous materials. In addition, the use of unstructured mesh allows an accurate modeling of complex structures. FEM requires the solution of a sparse matrix, which can also present difficulties when the number of unknowns becomes very large. Both MoM and FEM are primarily frequency-domain methods; and they require that the simulations be carried out one frequency at a time. Moreover, the incorporation of material nonlinearities into frequency-domain methods is quite difficult.

The FDTD method, which was introduced in a seminal work by Yee in 1966 [3], is now one of the most widely used CEM tools because it is simple to understand, easy to implement and, in common with the FEM, is also general-purpose in nature. Furthermore, it is a fully explicit algorithm, and hence, requires no matrix equations. And yet, it can conveniently handle problems involving complex structures with arbitrarily inhomogeneities. Furthermore, several

efficient schemes have been implemented in the FDTD algorithm to deal with frequency-dependent [4-5] and nonlinear materials [6]. Another advantage of the FDTD is its capability to perform broadband analysis in a single simulation. This can be readily done by simulating the device to be modeled with a broadband excitation pulse, and subsequently applying a Fourier transform to the time-domain data in order to extract the solution at the desired frequencies.

Over the past 40 years, extensive research has been done to advance the FDTD technique and to overcome its shortcomings. One of the major limitations of the original FDTD algorithm was encountered when modeling open-region problems, because it was not easy to implement the radiation boundary condition in the FDTD algorithm. To circumvent this problem, different schemes for truncating the outer boundary of the computation domain, known as absorbing boundary conditions (ABCs), have been proposed to handle the propagation of outgoing waves in open space with little reflection. Currently, the Uniaxial Perfectly Matched Layer (UPML) [7] and the Convolutional Perfectly Matched Layer (CPML) [8], that are the successors of the original PML [9] proposed in the 1990's, are the most widely used ABC algorithms. Typically, these ABCs have reflection coefficients of less than -60 dB from the outer-boundary over a wide band, for waves incident on the boundary at different angles.

Another drawback of the original FDTD algorithm is that it employed a Cartesian mesh to discretize the computational domain. Thus, when the geometry under consideration is either curved, or has slanted surfaces, the staircasing introduced in the FDTD method may render the results inaccurate, because the original geometry is distorted in the process. Some simpler approaches to circumventing this problem include the contour-path subcell models [10] and the conformal modeling technique [11], which account for the material inhomogeneity within a single FDTD cell. Other approaches [12-14] hybridize the FDTD method with other geometry-

conforming algorithms, such as the Finite Element (FE) and Finite Volume (FV) techniques. The unstructured mesh required by these techniques is introduced only in the regions that require a conformal mesh for accurate modeling, while the structured FDTD mesh is still employed in all other areas to preserve the computational efficiency of the FDTD algorithm.

Additionally, an FDTD modeling of multi-scale structures may place heavy burden on the computational resources, even though a non-uniform meshing scheme [15] can help reduce the total number of the FDTD cells. From Courant's stability condition [16], the maximum allowed time-step size is determined by the smallest FDTD cell-size of the computational domain. Consequently, the FDTD simulation may have to run a very large number of cycles before it can reach the steady state. Thin wire/slot model [17-18] for this specific geometry, as well as subgridding techniques [19-20] for general type geometries have been proposed to alleviate this problem. In these approaches, the global FDTD mesh does not need to be refined significantly in order to accurately model the fine structure; therefore, the time-step size does not become extremely small.

For all the computational methods discussed above, the maximum problem size that can be handled is severely limited by the available computational resources, namely computer memory and c.p.u. time. For direct MoM or FEM solvers that deal with dense or sparse matrices, respectively, the c.p.u. time and memory requirement grow much faster than linearly with the increase in the total number of unknowns. On the other hand, for the FDTD solver, the c.p.u. time and memory requirement grow as $N^{4/3}$ and N , respectively, i.e., almost linearly, as we increase the total number of FDTD cells (N) [21]. Therefore, among all the three methods, the FDTD appears to have the best potential insofar as solving large-scale problems is concerned. Additionally, the recent advances in parallel computing and high-speed communication between

processors have made a profound impact on the landscape of CEM, particularly to the FDTD method, because it can solve very large problems on parallel platforms, owing to its excellent scaling characteristics that is not shared by its other two competitors.

Parallel computing operates on the principle that large problem can be divided into smaller ones, whose solutions can be carried out concurrently using multiple processors. It is well known that the FDTD algorithm is embarrassingly parallel in nature, since the field at a particular node depends only on the fields in its immediate neighborhood. Consequently, in the parallel FDTD scheme, the computational domain is divided into a number of smaller subdomains that are then mapped onto independent processors on the parallel platform. Each processor now only deals with the field computation in a much smaller subdomain, relieving the burdens on both computer memory as well as time, encountered when attempting to solve the original problem on a single processor. The parallel FDTD algorithm has been implemented in different ways and tested on different computer platforms, and high parallel efficiency has been demonstrated in many cases [22-25]. This opens the opportunity to rigorously simulate the response of many extremely large and complex electromagnetic systems, which cannot be handled by other full-wave computational algorithms, at least in a time-efficient manner.

One of the classical examples of such a problem is the modeling of large antenna arrays. Before the advent of parallel FDTD technique, the simulation of the entire array structure was very difficult, if not impossible. Consequently, to get around this limitation, a smaller array of manageable size was first modeled, by exciting the center element and terminating all others. The far-field pattern, which is known as the active element pattern, was then computed and subsequently multiplied by the array factor to evaluate the pattern of the entire array. However, such a calculation neither considers the mutual coupling effect between distant elements of the

array, nor does it account for the edge effects. Consequently, the results suffer from inaccuracies in the far-field pattern at wide angles off main beam direction.

The emergence of new technologies, such as those based on the use of metamaterials, have also created a new class of extremely large-scale electromagnetic problems, even though their physical dimensions are not all that large in comparison to the wavelength. For example, with an ever-increasing demand for high-performance computers, the clock frequencies, interconnect densities, as well as the complexities of the modern microprocessors have been steadily increasing. Traditional circuit theories, which rely on the assumption of low frequency operation and negligible mutual coupling effects between components, may no longer be valid, and the designs based on these low frequency approximations may severely affect the performance of the device. It is therefore necessary to employ an efficient and accurate full-wave electromagnetic solver to design these advanced microprocessors [26].

The study of metamaterials, particular double-negative (DNG) metamaterials, is another recently emerging field in science and engineering disciplines. Following the first realization of DNG metamaterials in 2000 [27], such materials have gained widespread attention because of their interesting properties, as well as potential applications. The simulation of the EM response of such metamaterial structure with the modeling of real inclusions is always a challenging task. Usually, most of these structures consist of inclusions with fine features and subwavelength periodicities. Consequently, the number of degree of freedoms (DoFs) can be very large, and this places a heavy burden on computational resources when we attempt to characterize them.

The parallel FDTD solver is extremely well-suited for solving the large-scale problems mentioned above in a time-efficient manner. In addition, since the simulation time can be

significantly shortened by parallel processing, the parallel FDTD solver can also be used as an optimization tool for electromagnetic design problems.

1.2 Research Objectives

The parallel FDTD technique, mentioned in the last section, has become considerably mature after long years of development. In 2005, the author joined the research team of the Electromagnetic Communication Laboratory (EMC Lab) of the Electrical Engineering Department at Penn State University and was assigned to develop a new 3-D parallel FDTD package named General Electromagnetic Simulator (GEMS) [28]. In the past, a serial 3-D FDTD solver named Conformal FDTD (CFDTD) solver [29-30] was developed by the EMC Lab, and the author was assigned to help parallelize the above. The result was PFDTD [29], the parallel version of the code, which has been used to solve large problems involving antennas and arrays, some with several thousand elements, that are often located on complex platforms.

The research objective of this dissertation is to further embellish the present FDTD algorithm by developing new schemes that would enable it to solve a wide variety of practical problems. Towards this end, three issues will be addressed in this thesis to fill the gaps in the existing FDTD algorithms.

First of these, which has never been addressed before, is the implementation of the periodic boundary condition (PBC) for analyzing infinite, single- or doubly-periodic structures in a parallel code. By incorporating the PBC, it is possible to reduce the original problem to that of a single unit cell, considerably simplifying the simulation process. However, the simulation time may still be extensive because of the multiple reflections that might occur, especially when the periodic structure is comprised of multiple screens, and the waves can bounce back and forth

between them. To address this problem, we have developed an efficient, parallel implementation of the PBC/FDTD algorithm that can significantly reduce the lengthy simulation time.

Second, most of the existing PBC/FDTD algorithms based on a split-field formulation [31] employ the well developed UPML [7] to truncate the outer boundary of the computational domain. Recently, the CPML [8] has been proposed for truncating the FDTD mesh when solving general electromagnetic problems that are aperiodic in nature. The CPML, which has the advantages of being simpler to implement than the UPML, is essentially independent of the material that it terminates, and it significantly attenuates the evanescent modes. Therefore, the CPML is a very desirable candidate for implementation in the present periodic problem, and this implementation has been carried out in this work.

Third, the conventional total-field/scattered-field (TF/SF) technique [32], which is typically used to excite a plane wave in the scattering problem, fails when the scattering structure is infinite in extent. In addition, the conventional TF/SF technique has been applied only to launch a uniform plane wave. However, it has never been used in the past to excite other forms of incident field distribution. For example, the Gaussian beam is also a commonly-used source when the scattering effect on a localized region of the structure is desired in a rough-surface-scattering problem. To handle such excitations, we have developed a new excitation scheme to launch the desired incident field distribution in scattering problems, where the scatterer can either be finite or infinite.

The second research objective of this effort is to investigate the electromagnetic response of a class of double-negative metamaterial structures, where the inclusions inside such structures are accurately modeled by using the parallel FDTD technique. Effective medium theory is a very popular approach for characterizing metamaterials [33], because it is straightforward to use.

However, the use of these effective medium parameters often oversimplifies the EM properties of metamaterials, so much so that these parameters may fail to accurately predict the true performance of the antenna/metamaterials composites designed for real-world applications. Therefore, it is important to carry out a rigorous simulation of the original physical structure for accurately analyzing the performance of the composite system. However, the task of numerically simulating these structures can be formidable because they often contain inclusions that have subwavelength periodicities as well as features. The parallel FDTD solver is a very useful tool for analyzing these structures because of its capability to accurately model inhomogeneous materials with complex configurations, which require the solution of extremely large-scale problems in a time-efficient manner.

1.3 Chapter Outline

The remaining chapters of this thesis are organized as follows:

Chapter 2 presents the parallel FDTD algorithm, followed by a discussion on some design rules of the parallel setting, which offers the best performance of the FDTD solver. The efficiency of the parallel FDTD solver on different computer clusters is studied in this chapter. Finally, several representative examples of large-scale electromagnetic problems are presented.

Chapter 3 describes the procedure for an efficient, parallel implementation of the split-field based PBC/FDTD algorithm. An instability issue encountered in the incorporation of CPML into the PBC/FDTD algorithm is identified, and a new, stable and efficient CPML scheme is proposed for implementation in the PBC/FDTD algorithm to mitigate this problem.

Chapter 4 deals with an excitation scheme, based on modifying the conventional TF/SF approach, to launch the desired incident field distribution in scattering problems involving

infinite structures. The performance of the proposed scheme is studied, when used to launch two different incident field distributions, namely a Gaussian beam and a uniform plane wave.

Chapter 5 presents an extensive FDTD study of the electromagnetic response of a DNG slab comprising of a combination of split-rings and wires. Three scattering cases are investigated: an infinite slab excited by a plane wave, a finite slab excited by Gaussian beams and, a small dipole. The first case is investigated by using the technique proposed in Chapter 3, while the second and third are modeled via the parallel FDTD code in conjunction with the technique proposed in Chapter 4. The use of effective medium approach is also presented and discussed.

Finally, Chapter 6 presents a summary and conclusions of this research, and suggests some avenues for further development of the research presented in this thesis.

Chapter 2

PARALLEL FDTD TECHNIQUE

2.1 Introduction

The Finite Difference Time Domain (FDTD) algorithm, as first proposed by Yee in 1966 [3], is a simple and elegant way to discretize and solve the differential form of Maxwell's equations. Over the years, researchers have put forward considerable effort in embellishing this full-wave numerical technique. The interested reader is referred to the existing literature [21,34-36] for details of these algorithms and the histories of their developments.

In this chapter, we begin by reviewing some fundamental concepts of the FDTD method, which facilitate the understanding of the parallel-FDTD technique. Next, we will go into some details of this technique, including the process of data communication, followed by a discussion on some design rules for the parallel setting, which provides the best parallel performance of the FDTD solver. Next, we will evaluate the parallel performance of the existing parallel FDTD code on two computer clusters with different number of nodes. Finally, we will present examples of three large and complex EM problems that have been solved to demonstrate the power of the parallel FDTD algorithm when solving extremely large and complex problems in a time-efficient manner.

2.1 A Brief Review of the FDTD Algorithm

In the FDTD method, the two Maxwell's curl equations are first expressed in the differential form, and the spatial and temporal derivatives are then approximated using central-

differences. This results in two staggered three-dimensional grids for the E- and H-fields, respectively. These fields are not only spatially offset by half cell-size, but are also temporally displaced from each other by half time-step. Figure 2.1 illustrates the position of each of the six E- and H-field components in a single FDTD cell, which is also known as Yee's cell.

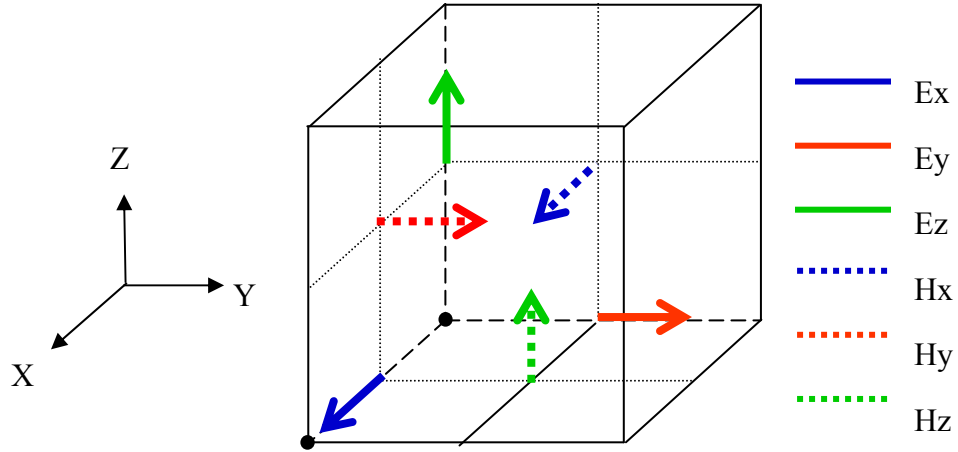


Fig. 2.1: The three-dimensional spatial grid (Yee's cell) used in the FDTD algorithm.

For simplicity, we only consider the lossless case here, though the lossy case presents no particular difficulties. The update equations for the x-component of the E- and H-fields, at the n^{th} time-step, are given below:

$$\begin{aligned}
 E_x^{n+1}(i+0.5, j, k) &= E_x^n(i+0.5, j, k) \\
 &+ \frac{\Delta t}{\epsilon \Delta y} [H_z^{n+0.5}(i+0.5, j+0.5, k) - H_z^{n+0.5}(i+0.5, j, k)] \\
 &- \frac{\Delta t}{\epsilon \Delta z} [H_y^{n+0.5}(i+0.5, j, k+0.5) - H_y^{n+0.5}(i+0.5, j, k-0.5)]
 \end{aligned} \tag{2.1}$$

$$\begin{aligned}
 H_x^{n+0.5}(i, j+0.5, k+0.5) &= H_x^{n-0.5}(i, j+0.5, k+0.5) \\
 &- \frac{\Delta t}{\mu \Delta y} [E_z^n(i, j+1, k+0.5) - E_z^n(i, j, k+0.5)] \\
 &+ \frac{\Delta t}{\mu \Delta z} [E_y^n(i, j+0.5, k+1) - E_y^n(i, j+0.5, k)]
 \end{aligned} \tag{2.2}$$

where i, j, k denote the x -, y -, and z -coordinates of the field point in the primary FDTD grid, viz., the E-grid, respectively; Δt is the Courant time-step; Δy and Δz are the cell-sizes along the y - and z -directions, respectively; and, ϵ and μ are the electric permittivity and magnetic permeability, respectively, at the location of the field point. Note that each of the E (or H) field values is updated from their corresponding values at the previous time-step, by using the H (or E) field values at the four surrounding field points.

2.2 Parallel FDTD Technique

The FDTD algorithm is well known to be inherently parallel in nature, because it utilizes the fact that the field at a particular node depends only on the fields in its immediate neighborhood. Consequently, the domain decomposition technique lends itself easily to parallel implementation of the FDTD method [22,23,37]. In this approach, the computational domain is first subdivided into a number of subdomains (see Fig. 2.2). It is natural to choose the boundaries of the subdomains such that they coincide with the grid lines of the electric field. Each subdomain is then mapped onto independent processor of the computer cluster. Therefore, each processor deals with only the task of field computation of a much smaller subdomain, relieving the burdens on both the computer memory and the c.p.u. time, in comparison to that experienced when attempting to solve the original problem using a single processor.

However, the spatial decomposition obviously introduces artificial boundaries at the interfaces of the subdomains. At the common surfaces between two adjacent subdomains, it becomes necessary to exchange field information in order to carry out the updating of the fields at the nodes located adjacent to the interface.

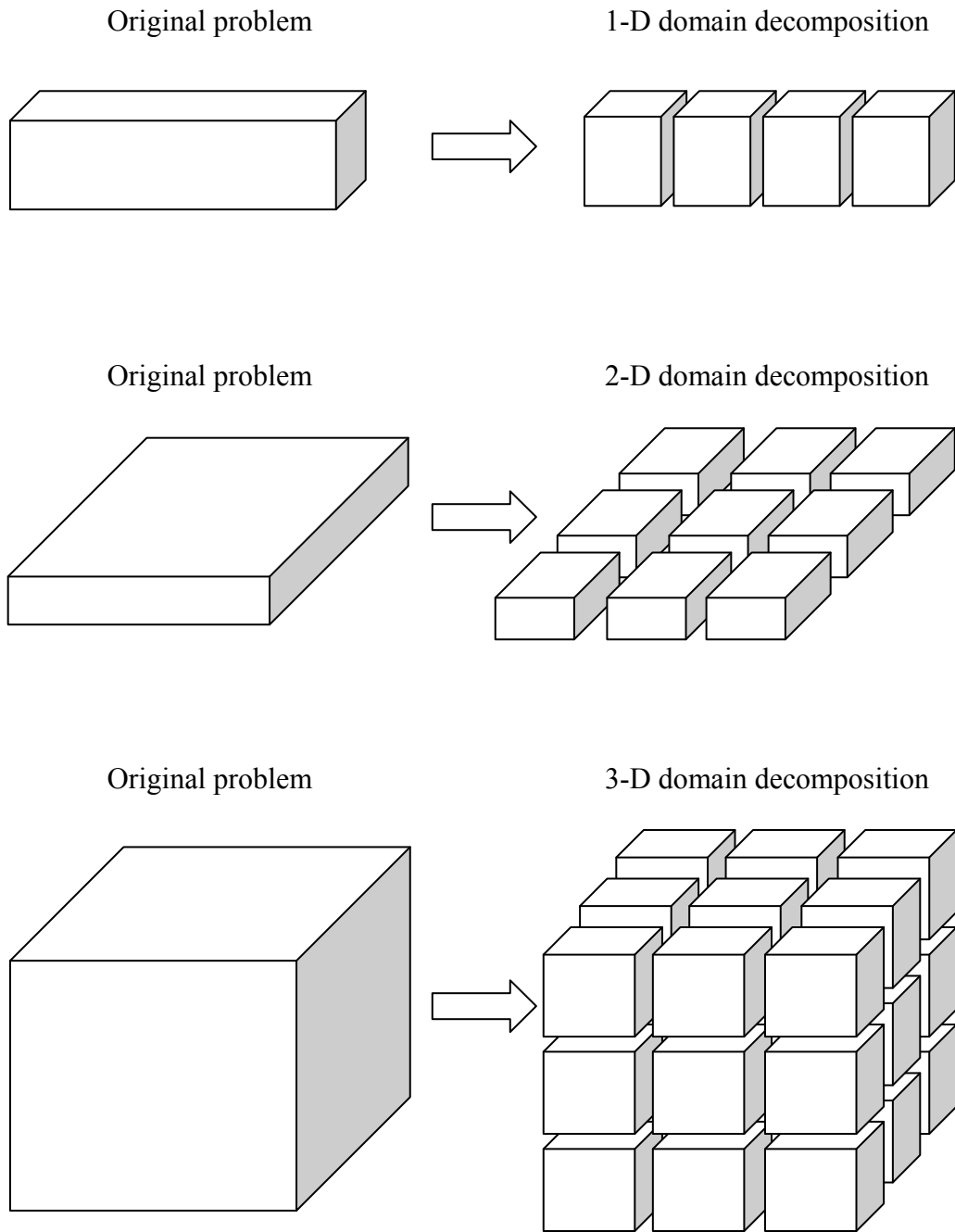


Fig. 2.2: Diagram illustrating three kinds of parallel processing configurations.

2.2.1 MPI Library

The data communication process alluded to above can be readily implemented by using the Message Passing Interface (MPI) library [24,29,38]. The MPI, developed by the MPI forum in the 1980's and early 1990's, is a standard specification [39-41] of a set of library calls for passing messages between computers interconnected via a data communication network. It is an application-programming interface, which is portable across different platforms. Implementation of the MPI standard exists for all major computer architectures, including supercomputers, all versions of UNIX-based machine, as well as Windows NT and later versions. The MPI standard defines interfaces for two most common programming languages, C and FORTRAN (as well as C++ and FORTRAN 90). That is, each MPI function can be called either from a C or FORTRAN program.

2.2.2 Parallel Field Exchanging Algorithm

Several schemes [24,29] have been proposed to exchange information on the tangential electric and/or magnetic fields at points located at the interfaces between adjacent subdomains. In the following, we will describe the scheme that is employed for the parallel FDTD solver that we have developed.

In this scheme, a one-cell overlap region is introduced at the interface between adjacent subdomains. For the sake of simplicity, we assume that the computational domain is partitioned only along one direction, say, the x-direction, as shown in Fig. 2.3. Only the tangential magnetic fields, viz., H_y and H_z , in the overlapped cells are exchanged at each time-step. Consequently, the fields located at the common interface, viz., E_y , E_z and H_x , can be computed by using the conventional FDTD update equations for each processor, since all the necessary information

pertaining to the field values in the neighborhood of the interface is available. Figure 2.4 depicts the flowchart for the updating procedure in a single cycle of the parallel FDTD algorithm, with the step of field exchange highlighted in red.

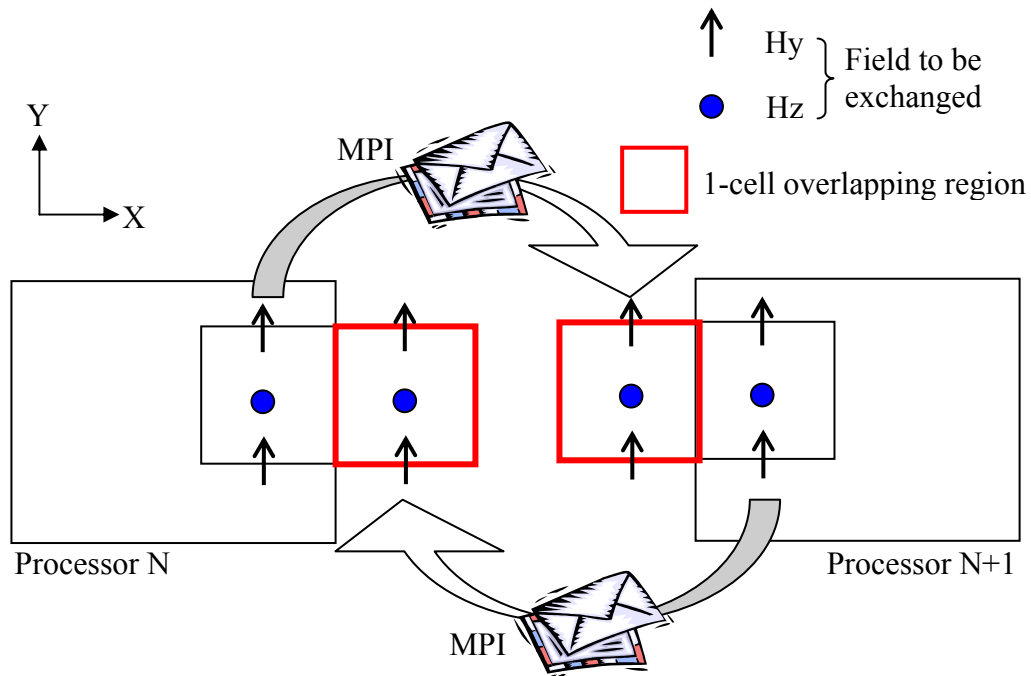


Fig. 2.3: Configuration of field exchange between two neighboring processors.

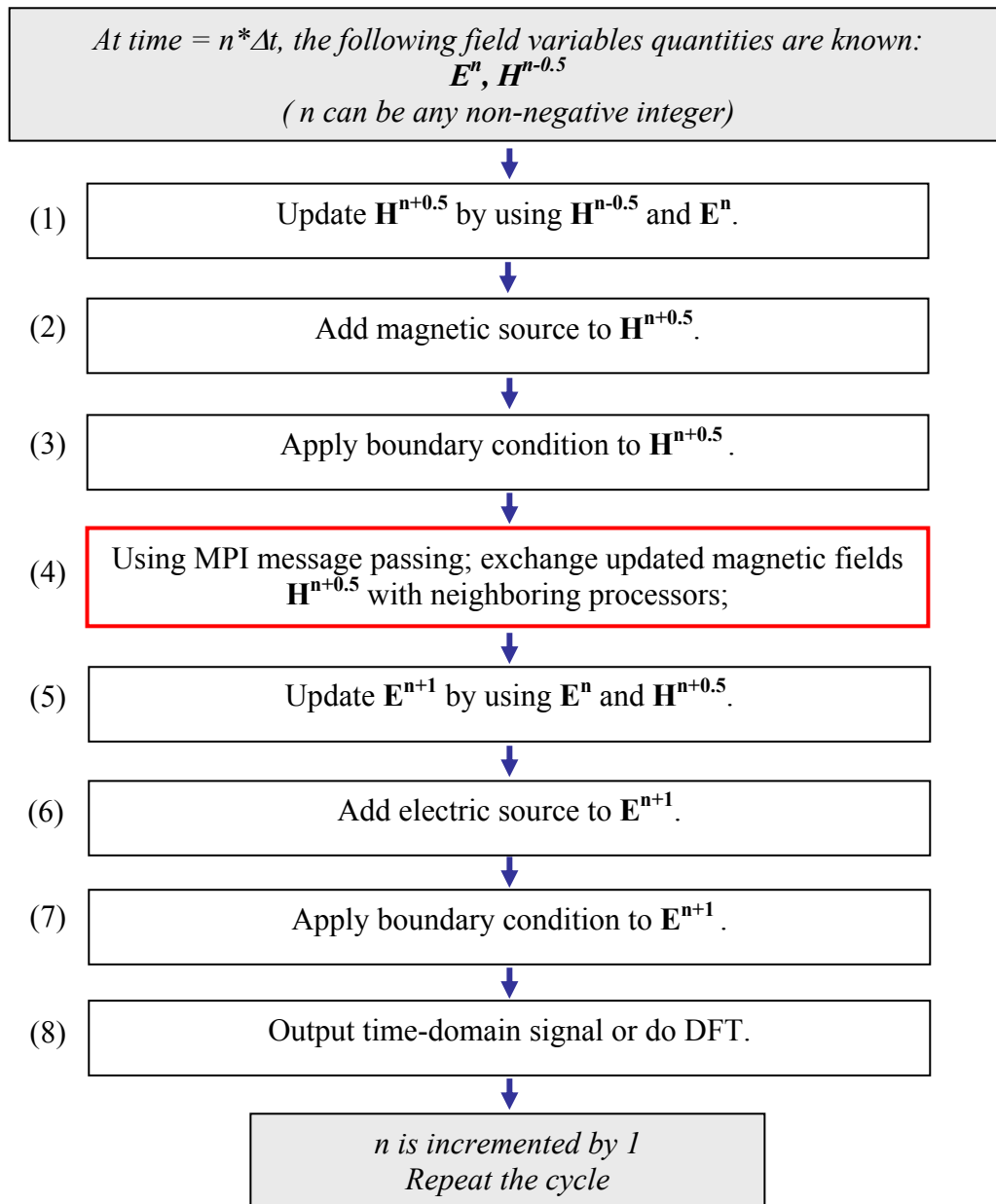


Fig. 2.4: The updating procedure in a single cycle of the parallel FDTD algorithm. The steps for parallel field exchange are highlighted in red box.

2.2.3 Parallel Implementation of Other Tasks

In the FDTD simulation, other tasks besides the field computation can also be performed. For example, we may carry out the voltage and current measurement, compute the DFT of the time-domain field in a region of interest (to be used to calculate Huygens' current or field distribution at the desired frequency), and to implement post-processing steps such as far-field calculation. These tasks need to be incorporated into the parallel program in a way such that the efficiency of the code is not affected [24,38]. A general rule is that each processor should execute all the tasks localized in its subdomain. One processor is assigned to collect the results from all processors, and, to output the results to appropriate files, if necessary.

In addition, the generation of the material distribution for the Yee's grid could place heavy burden on computational resources since the problem size that can be handled is dramatically increased compared to that of a serial FDTD solver. Consequently, a parallel implementation of the generation of material distribution is necessary to support the parallel FDTD algorithm when solving large and complex problems. The interested reader is referred to [25,42] for details of this implementation.

2.2.4 Design of Parallel Settings

The parallel setting of an FDTD project includes the following parameters: the total number of subdomains; the number of subdomains along each direction; and, the dimension of each subdomain in terms of the FDTD cells.

Usually, the value of the first parameter is fixed because the maximum number of processors available is limited. With a fixed total number of subdomains, the computational domain can be divided in many ways. However, it has been demonstrated that different settings

of spatial decomposition can result in different computational times for the same problem [24,38].

We will discuss below some rules to be followed in order to shorten the computation time.

The most important consideration is load-balancing, i.e., the distribution of operations to be performed across the processors. In each parallel-FDTD iteration, each processor needs to wait before starting the iteration pertaining to the next time-step, until data communication for all other processors has been completed. Therefore, if one processor has to perform more operations than all the other processors, the latter will have an idle period at each time-step. This, in turn, would result in a degradation of the performance of the parallel FDTD code.

An accurate estimation of load is by no means an easy task, because it depends on a number of factors. Some factors are crucial, such as the number of FDTD cells in the x-, y- and z-directions within the perfectly matched layer (PML). On the other hand, some are much less important, such as localized source and output, and the implementation of boundary conditions excluding the PML, because the operations involved in these steps are much less intensive. One simple way to assign a subdomain to each processor is explained below.

Again, for the sake of simplicity, we consider only the case of 1-D parallel processing here, say, along the x-direction. First, if there are n_{cell} cells and n_p processors in the x-direction, and PML is not employed, each processor will handle n_{cell}/n_p cells. Next, if an n_{pml} -layer PML is employed on both sides, the total number of FDTD cells would be $(n_{\text{cell}} + 2n_{\text{pml}})$. Therefore, each processor would be handling $(n_{\text{cell}} + 2n_{\text{pml}})/n_p$ cells, except for the processor which includes the PML, and, hence we would need to deal with $(n_{\text{cell}} + 2n_{\text{pml}})/n_p - n_{\text{pml}}$ cells.

The second consideration pertains to the overhead introduced by data communication between adjacent processors. This overhead depends on the network speed, and the total number of field values that need to be exchanged. While the first factor is limited by the computational

resources available, one can design the parallel setting in a way such that it minimizes the area of subdomain interface in terms of cell number. For example, when the computation domain has an elongated shape along one direction, a 1-D parallel configuration along this direction is the most desirable parallel setting.

2.3 Efficiency Analysis of the Parallel FDTD Solver [25]

In this dissertation, the FDTD results have been obtained by using a 3-D parallel electromagnetic simulation software package, called GEMS (General Electromagnetic Simulator) [28], which is based on the parallel conformal FDTD method [29]. This solver has been tested on many computer platforms, and it has achieved a high level of parallel efficiency on small-to-large clusters, comprising of up to 6000 processors. A typical plot of the scaling characteristic of GEMS on two different clusters will be presented in the next section.

2.3.1 Performance Analysis on Large Computer Cluster (LOFAR BlueGene/L [43])

The first test problem we consider is a 100×100 patch antenna array (see Fig. 2.5), whose individual element is shown in Fig. 2.6. A non-uniform mesh is employed to model this geometry, since the radius of a coaxial probe feed is typically very small compared to the wavelength. The computational domain consists of $1534\Delta \times 1837\Delta \times 74\Delta$ (Degrees of Freedom (DoFs) about $1.3E9$), which requires about 60 gigabytes of memory for the FDTD simulation. A 6-layer PML is used to truncate all the six walls of the computational domain. The coaxial cables are truncated by the PML layer in order to mimic an infinitely long cable.

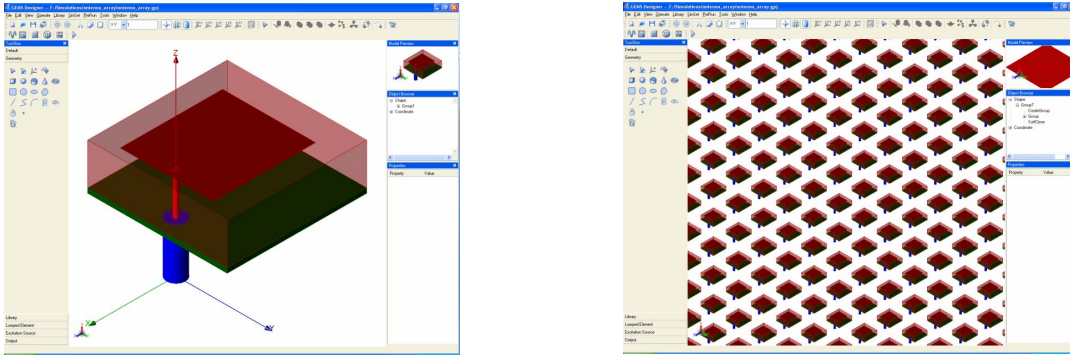


Fig. 2.5: Antenna element (Left) and the 100x100 patch antenna array (Right).

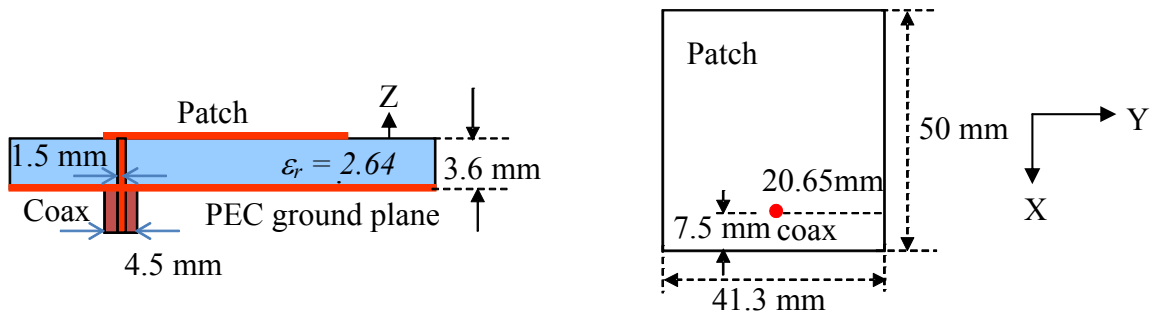
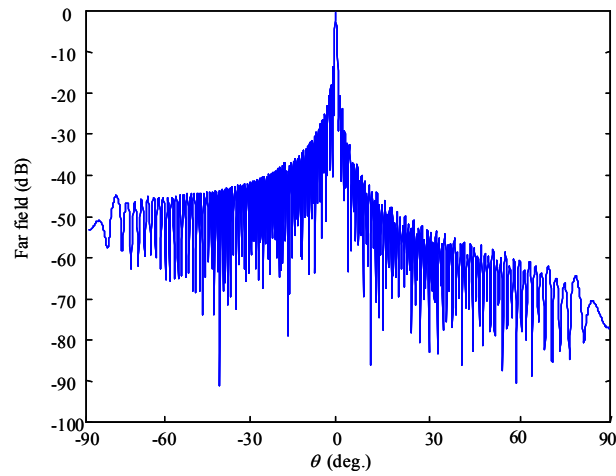


Fig. 2.6: The geometry of a single antenna element.

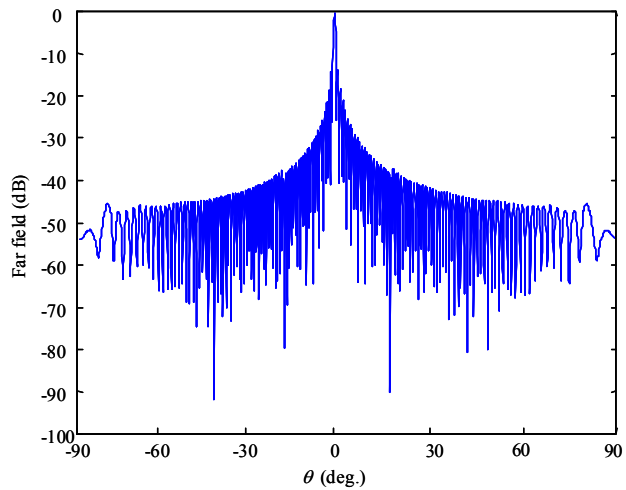
First, we use a cluster built with 52 regular AMD 2300 processors to run the above array problem for 30,000 time-steps, which takes approximately 24 hours. The far field patterns of the 100×100 patch antenna array are plotted in Figs. 2.7 (a)-(b). The asymmetric pattern in Fig. 2.7 (a) is caused by the unbalanced location of the excitation source.

Next, we use the LOFAR BlueGene/L (6000 nodes) to re-simulate the same problem on varying number of processors, ranging from 288 up to 4000. Figure 2.8 illustrates the simulation time as a function of the number of processors used. The processor layouts are chosen to be 288 ($12 \times 12 \times 2$), 450 ($15 \times 15 \times 2$), 800 ($20 \times 20 \times 2$), 1080 ($18 \times 28 \times 2$), 1408 ($22 \times 32 \times 2$), 1872 ($26 \times 36 \times 2$), 2128 ($28 \times 38 \times 2$), 2992 ($34 \times 44 \times 2$), 3312 ($36 \times 46 \times 2$) 3648 ($38 \times 48 \times 2$) and 4000 ($40 \times 50 \times 2$). As

can be seen from Fig. 2.8, running the problem on 4000 processors requires only 715 seconds, or approximately 12 minutes to complete the same task.



(a)



(b)

Fig. 2.7: The far-field pattern of the 100x100 patch antenna array in the (a) x-z plane and (b) y-z plane.

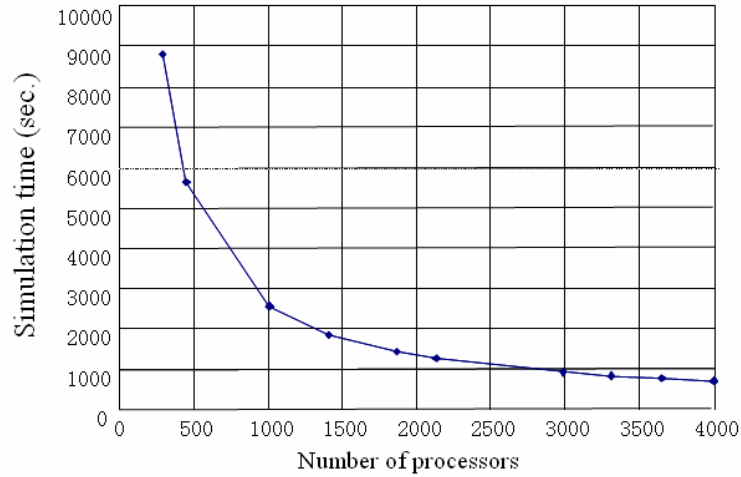


Fig. 2.8: Simulation time of the patch antenna array using different number of processors on the LOFAR BlueGene/L.

We now turn to the efficiency analysis of the parallel FDTD code performed on the LOFAR BlueGene/L supercomputer. The scalability and efficiency of the parallel FDTD code on the LOFAR BlueGene/L are plotted in Figs. 2.9 and 2.10, respectively. It should be noted that the efficiency is as high as 90 percent for the case of balanced load, and this is excellent.

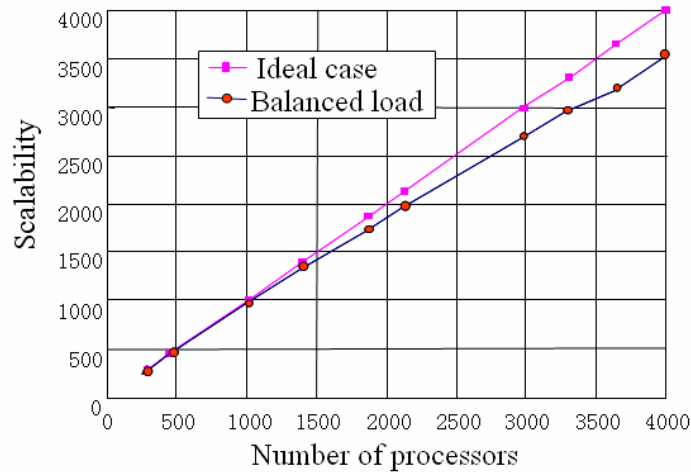


Fig. 2.9: Scalability of the parallel FDTD code on the LOFAR BlueGene/L.

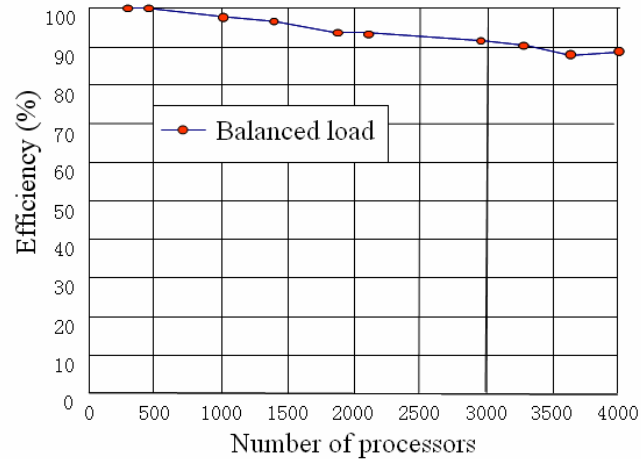


Fig. 2.10: Efficiency of the parallel FDTD code on the LOFAR BlueGene/L.

2.3.2 Performance Analysis on Small Computer Cluster

In this section, we present the test results for the performance of the FDTD solver on a recently-built Beowulf clusters (16-nodes) comprising of high performance servers, which achieves a relatively high parallelization efficiency by utilizing high performance optical networks for communication [28]. The specific processor is Intel the Xeon 2.33 GHz, with a 4 MB L2 cache and an 8 GB physical memory, with the two processors mounted on one motherboard. Four computational cores are placed in one box, and a double-port Myrinet card with the corresponding switch are chosen to connect the compute nodes.

Next, we use a simple example to investigate the performance of this typical cluster as we increase the number of compute cores. The computational domain is discretized into $600 \times 600 \times 600$ uniform cells and the PEC boundary condition is used to truncate the FDTD mesh. The results for the efficiency and scalability are plotted in Fig. 2.11.

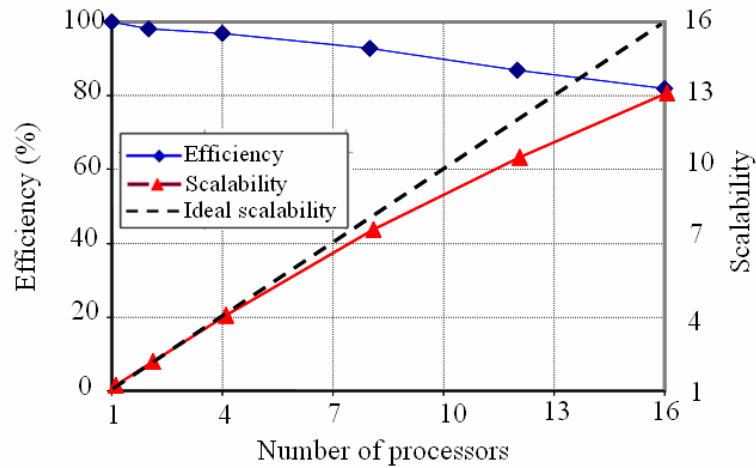


Fig. 2.11: Efficiency and scalability of the parallel FDTD as a function of the number of processors on a recently-built computer cluster.

The performance of a small cluster with 4 nodes (8 dual-core processors and a total of 32 GB memory) is used to simulate several problems of different sizes, and the simulation time for 1,000 time-steps are summarized in Table 2-1.

Table 2-1: Problem size vs. simulation on a small cluster

Problem size (unit: cell)	Simulation time (1,000 time steps)
100x100x100 (1 million)	13 sec.
200x200x200 (8 million)	59 sec.
300x300x300 (27 million)	2 min. 54 sec.
400x400x400 (64 million)	6 min. 25 sec.
500x500x500 (125 million)	13 min. 10 sec.
600x600x600 (216 million)	20 min. 30sec.
700x700x700 (343 million)	32 min. 40 sec.
800x800x800 (512 million)	48 min. 30 sec.
900x900x900 (729 million)	65 min. 30 sec.
970x970x970 (913 million)	87 min. 10 sec.

2.4 Examples of Practical Problem Solved

Many extremely large and complex problems, requiring large DoFs, can now be rigorously solved in a time-efficient manner on a computer cluster by using GEMS, the high performance 3-D parallel FDTD solver. Below are some of the problems that we have tackled.

2.4.1 Vivaldi Antenna Array [44]

In this example, we have employed the parallel FDTD code to simulate a $9 \times 8 \times 2$ array dual-polarized Vivaldi element array using the LOFAR BlueGene/L supercomputer in Sec. 2.3.1. This wideband Vivaldi antenna array has been used as a Focal Plane Array (FPA), and successfully tested on the Westerbork Synthesis Radio Telescope [45] (see Fig. 2.12).

Figure 2.13 shows the geometries of a single Vivaldi antenna element as well as the Vivaldi array antenna that have been simulated. Each array element utilizes two Vivaldi elements that are deposited on the opposite sides of a dielectric substrate, whose dielectric constant is 2.2 and conductivity equals 0.011 S/m. The array antenna is comprised of two 8×9 grids of Vivaldi elements, assembled in a cross-type configuration as shown in the figure. The element dimensions is $2.7 \text{ cm} \times 0.32 \text{ cm} \times 9.842 \text{ cm}$ and that of the array are $25.25 \text{ cm} \times 25.25 \text{ cm} \times 9.842 \text{ cm}$. Coaxial cables with 50Ω characteristic impedance are connected from underneath the array, where the voltage and current of each Vivaldi element are measured at a distance of 8 cm below the junction, and used later for the computation of the input impedances and S-parameters. The fed lines are terminated with PML to simulate infinitely long coaxial cables. The frequency range of interest is from 1.0 GHz to 8.0 GHz.

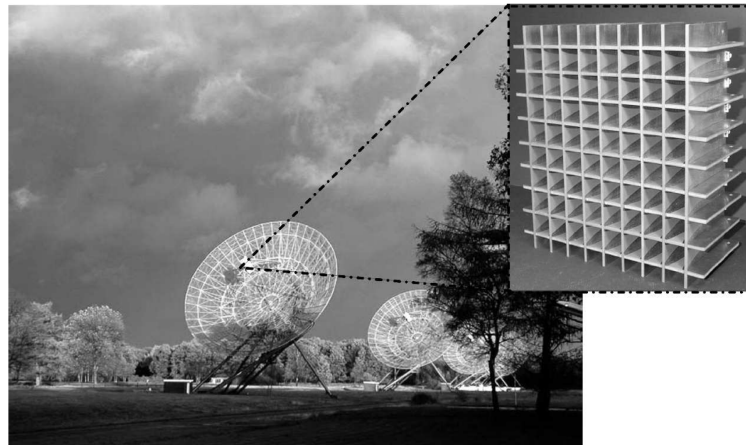


Fig. 2.12: Photo of the Westerbork Synthesis Radio Telescope.

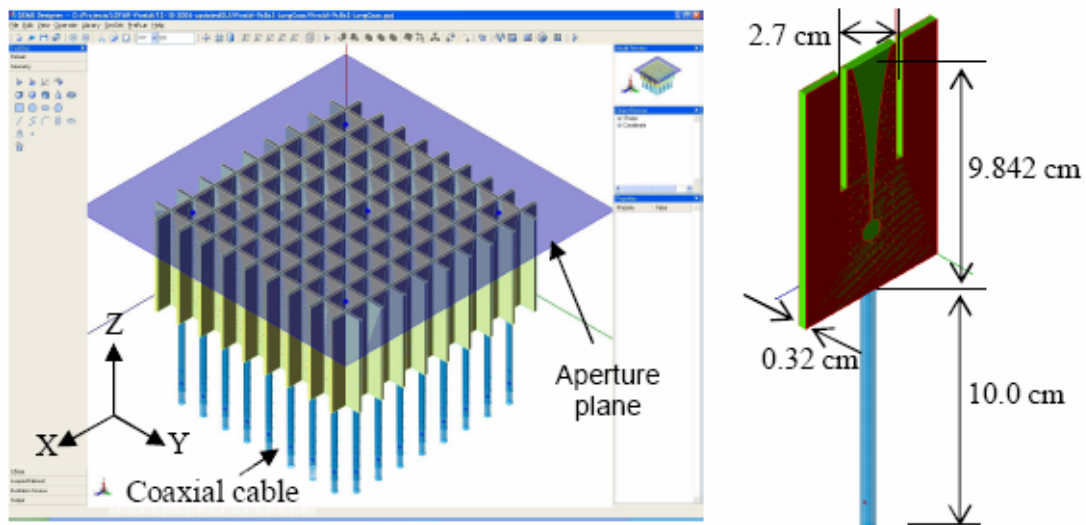


Fig. 2.13: The geometry of the Vivaldi antenna array (Left) and its single element (Right).

The computational domain contains $1330\Delta \times 1330\Delta \times 718\Delta$ (DoFs $\sim 7.6E9$) cells. It required a total of 103 hours, using 505 processors on the LOFAR BlueGene/L, to complete the FDTD simulation of 50000 time-steps, including the computation of the far-field pattern at the

desired frequency points. It should be noted that the simulation time can be scaled down almost linearly by increasing the number of processors.

Figures 2.14–15 shows the comparison of the far-field pattern, input impedance, and scattering parameter between the measured data and the FDTD results. As can be seen from all of the above figures, the agreement between these two results is good.

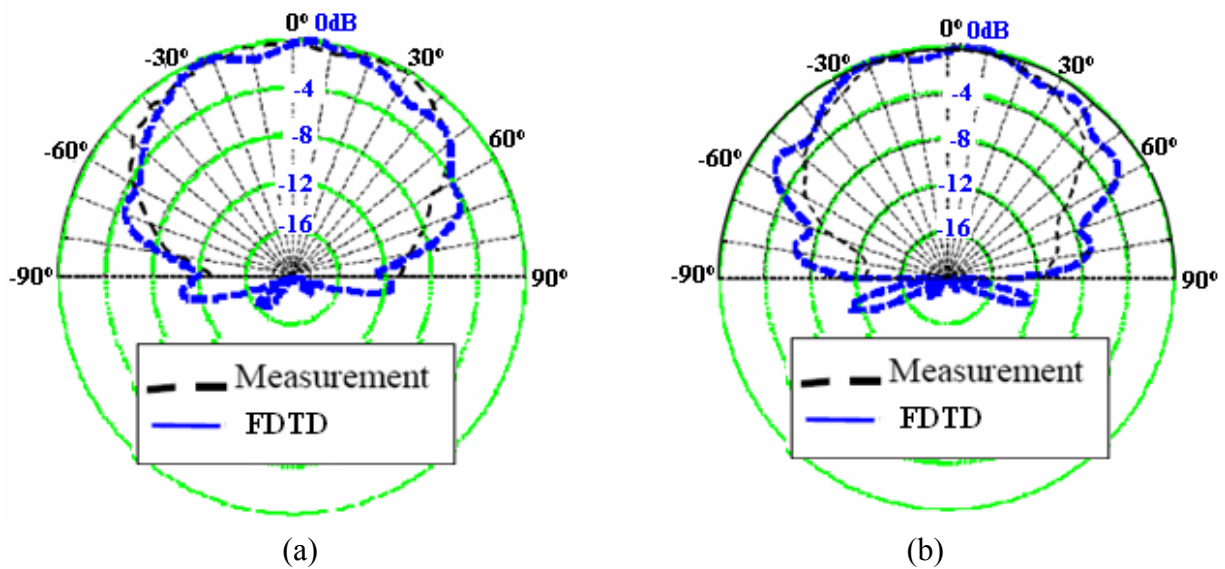


Fig. 2.14: The E-plane far-field pattern of the Vivaldi array antenna where only the center element is excited and all the others are terminated with 50Ω impedances. (a) 4.7 GHz, and (b) 5.3 GHz.

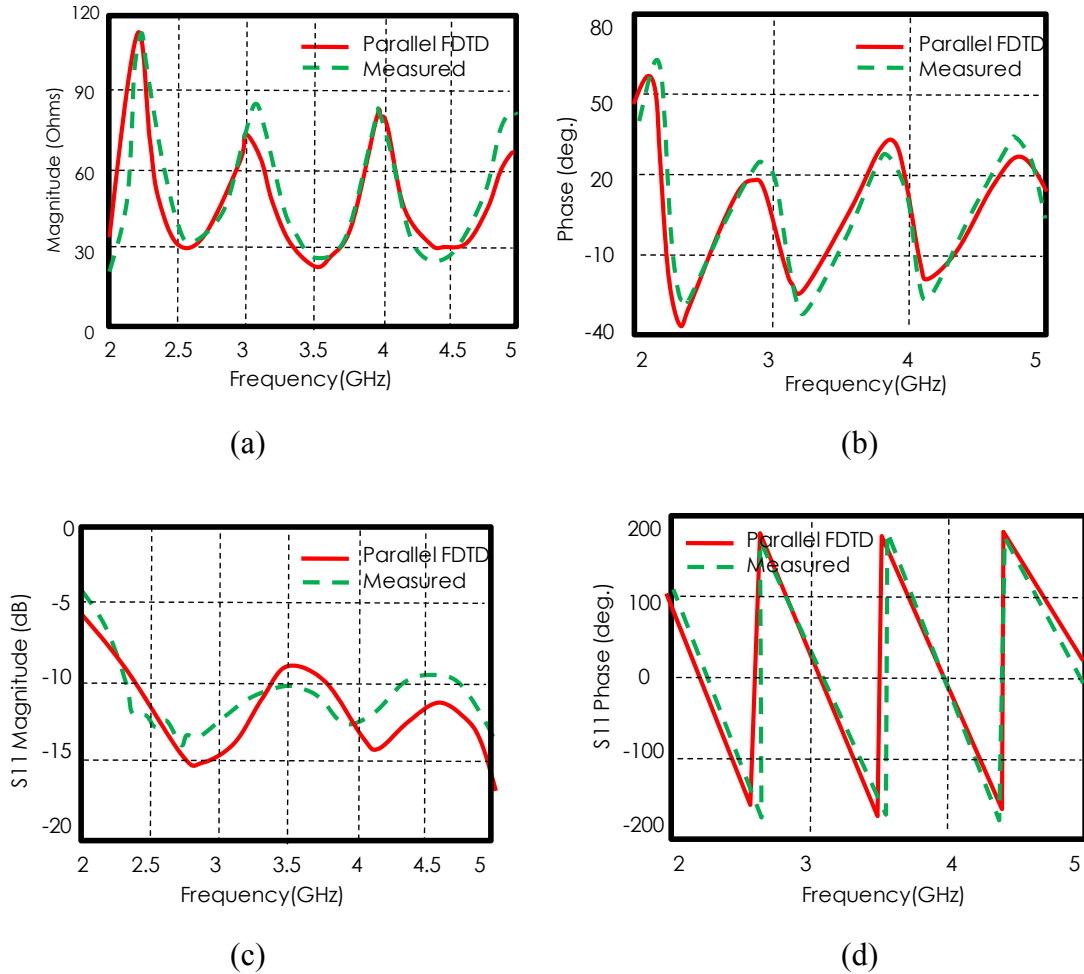


Fig. 2.15: Input impedance and the scattering parameter at the central active element. (a) and (b) Real and imaginary part of input impedance; (c) and (d) Magnitude and phase of S11.

2.4.2 Electronic Packaging Problem [46]

The second example involves the simulation of the electromagnetic characteristics of complex and multilayered package, which includes numerous structures with subwavelength feature. The number of DoFs associated with this problem is so large that it is virtually impossible to solve the problem at hand without using the parallel FDTD technique.

The chip in this investigation is an 8-layer printed circuit board, separated by dielectric layers, ground and power layers. The stack-up geometry of the laminate package structure is shown in Fig. 2.16. The circuit structure and one layer of the printed circuit board are also shown in Fig. 2.17 to demonstrate the complexity of the geometry. The computational domain has a dimension of $11700 \mu\text{m} \times 21250 \mu\text{m} \times 1012 \mu\text{m}$, and a total of $1670\Delta \times 1755\Delta \times 121\Delta$ (DoFs about $2.1\text{E}9$) cells. A 10-layer PML is used to truncate all the four side walls of the computational domain, and a PEC boundary condition is used to truncate the top and bottom walls. Again, we use 4,000 CPUs of the IBM BlueGene/L supercomputer (see Sec. 2.3.1) to simulate this problem, and the simulation for 80,000 time-steps requires 6 hours and 5 minutes. We have also used a cluster with specifications similar to the one used in Sec. 2.3.2, with 48 nodes (96 CPUs) to simulate the same problem but with the computational domain discretized into $1160\Delta \times 1913\Delta \times 194\Delta$ (DoFs about $2.6\text{E}9$) uniform cells. It required 11 hours 3 minutes for 80,000 time-steps when using 91 processors. The simulated scattering parameters are plotted in Fig. 2.18.

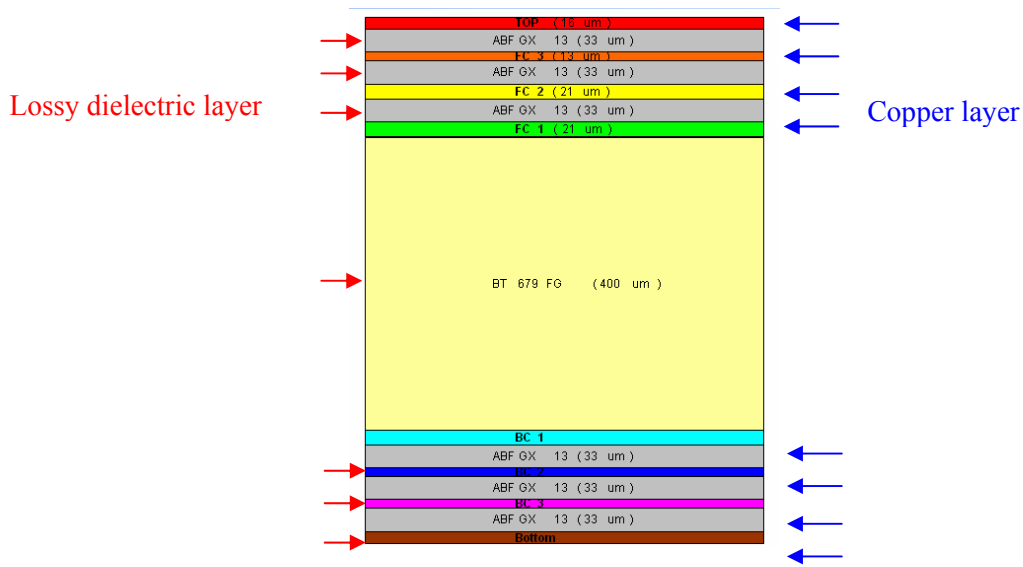


Fig. 2.16: The stack-up of the chip package.

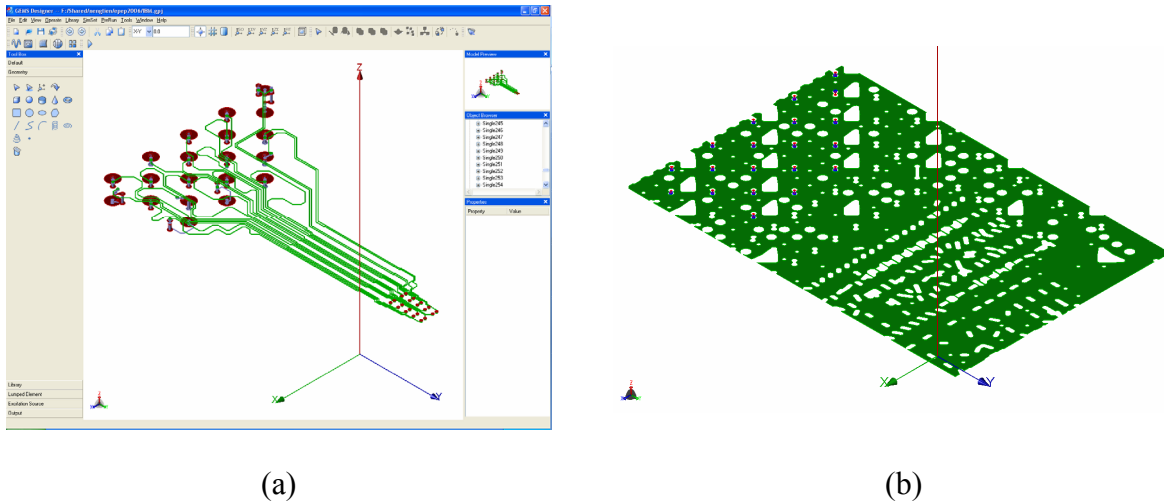


Fig. 2.17: (a) The circuit structure (b) and one layer of printed circuit board.

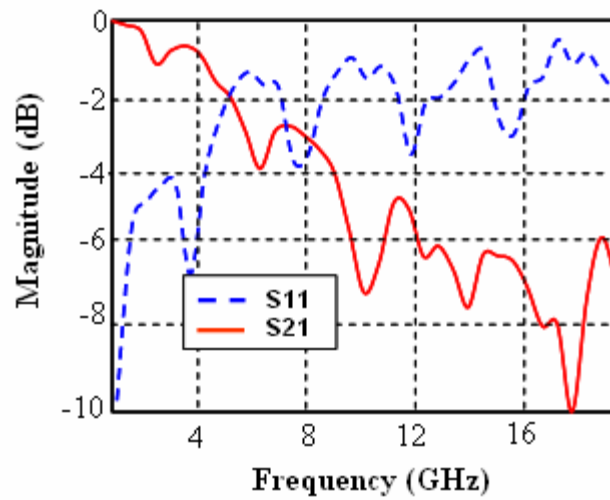


Fig. 2.18: The scattering parameters of the chip package.

2.4.3 Metamaterial Structures

Metamaterials are man-made composite structures that are tailored to exhibit certain unusual properties not readily found in nature. In particular, double-negative (DNG) metamaterials, whose electric permittivity and magnetic permeability both have negative real

parts, have attracted much attention recently because of their interesting properties, as well as potential applications. Although the concept of DNG has stemmed from Vesalago's pioneering work [47] in 1968, research on DNG metamaterials has not attracted widespread attention until the first experimental realization of DNG metamaterials in 2000 [48].

The simulation of the EM response of a metamaterial slab, containing inclusions that impart its unique characteristics, is a challenging task indeed. This is because most of these configurations typically contain inclusions with subwavelength periodicities, and the inclusions themselves have fine features. Consequently, the simulation of such structures places a heavy burden on the computational resources. This often prompts one to resort to solving a simplified problem, in which the original structure is replaced by a homogeneous block of an equivalent medium of the same size, which is characterized by an effective electric permittivity and magnetic permeability at the desired frequency. However, as will be shown in Chapter 5, the solution of such simplified problem may not predict the true response of the desired structure, e.g., a practical antenna-metamaterials composite. Therefore, it is both important and necessary, in real-world applications, to perform a rigorous simulation of the practical system, where the inclusions inside the metamaterial structures are also modeled accurately, in order to evaluate, in a reliable manner, the performance of a system that contains such materials.

In Chapter 5, we will simulate the scattering response of a metamaterial slab comprising of a total of $38 \times 17 \times 6 = 3876$ pairs of split-ring resonator and wire (see Fig. 5.36). The slab has the dimensions of $85.5 \text{ mm} \times 85 \text{ mm} \times 23.75 \text{ mm}$, corresponding to $4.3 \lambda \times 4.3 \lambda \times 1.2 \lambda$ at the center frequency of interest (15 GHz). Two types of excitation will be considered, namely a Gaussian beam and a small dipole excitation. The computational domain contains a total of $684 \Delta \times 680 \Delta \times 582 \Delta$ (DoFs $\sim 1.6\text{E}9$) with a uniform discretization of 0.125 mm. At 15 GHz, the

cell-size is only $\lambda/160$, and this is necessary to accurately model the fine features of the inclusions. The simulations have been run for a total of 21000 time-steps, until the field reaches its steady state. The above simulation requires approximately 17 hours, when using 15 CPUs in the cluster described in Sec. 2.3.2, while it takes about 14 hours when we use 504 CPUs on the LOFAR Bluegene/L. The interested reader is referred to Chapter 5 for the results.

2.5 Conclusions

In this chapter, we have presented the parallel FDTD algorithm, which is based on the domain decomposition approach, and which implements the data communication between processors by using the MPI library. A one-cell overlapping region is introduced at the interface between subdomains. In this scheme, only the tangential H-fields in the overlapping cell need to participate in field exchange between processors. Some design rules of the parallel settings for optimizing the parallel performance of the FDTD solver have also been discussed.

For the 3-D parallel FDTD solver (named GEMS), the author participated in whose development, we have evaluated its parallel performance on different computer clusters, and found that its parallel efficiency is excellent for small or large clusters. On large computer cluster up to 6000 processors, the parallel efficiency for the balanced load case was still found to be as high as 90 percent.

Finally, three practical examples have been presented to demonstrate the power of the 3-D parallel FDTD code in solving extremely electrically large and complex problems in a time-efficient manner.

Chapter 3

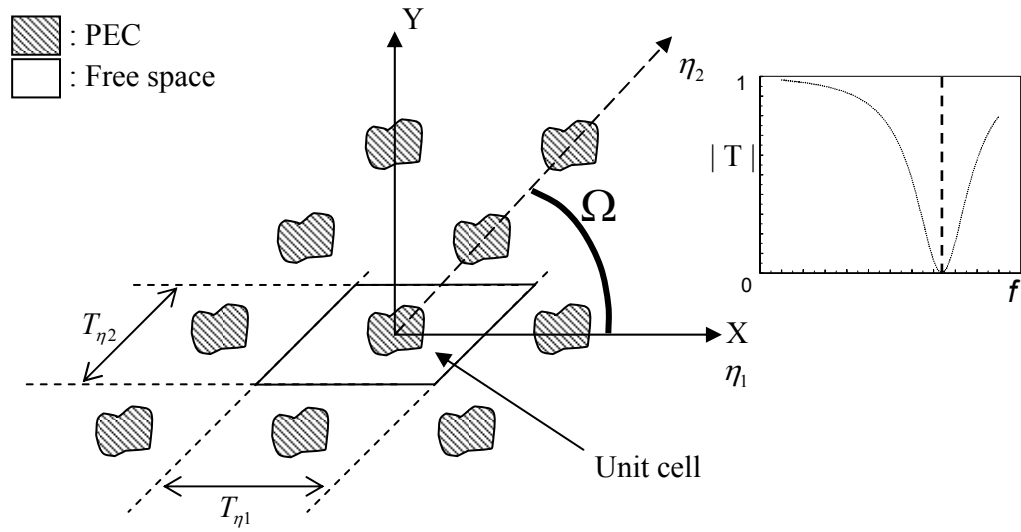
EFFICIENT PARALLEL IMPLEMENTATION OF PERIODIC BOUNDARY CONDITION IN THE FDTD INCORPORATING THE CONVOLUTIONAL PML

3.1 Introduction

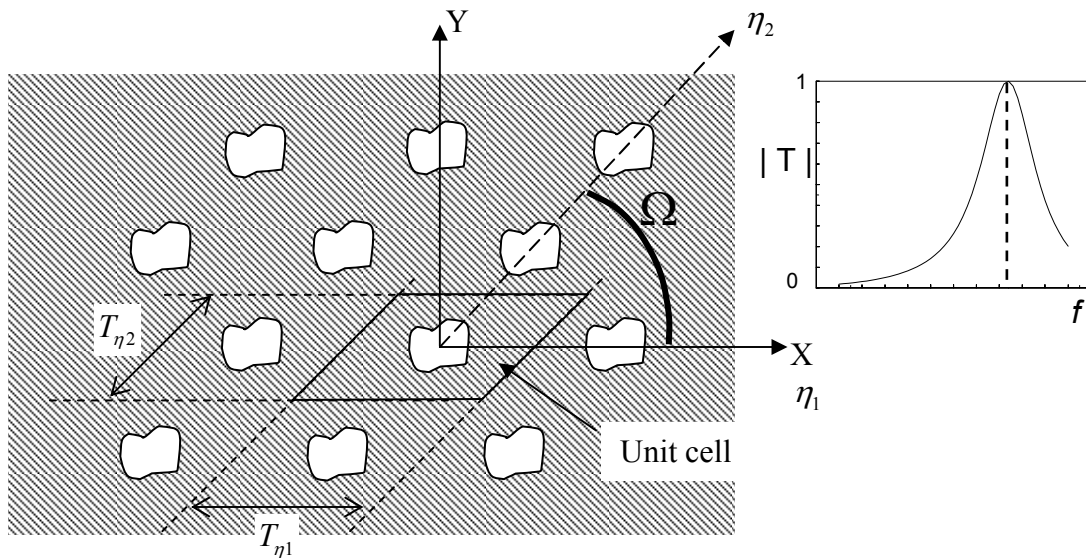
Two-dimensional periodic structures, that exhibit spatial filtering characteristics, find a variety of applications in communication as well as defense. For example, the so-called Frequency Selective Surface (FSS) [49,50], which is a periodic array of either conducting patches or perforated aperture elements (see Fig. 3.1), can be used on the screen door of a microwave oven to reflect microwave energy at 2.45 GHz while allowing visible light to pass through. It can also be used as a radome to control the energy that reaches an antenna, and/or to reduce its radar cross section. Other types of periodic structures that have received considerable attention are photonic bandgaps (PBGs), shown in Fig. 3.2, and electromagnetic metamaterials (MTMs). The PBGs, characterized by passbands and stopbands for electromagnetic waves, operate in a frequency range where its periodicity is typically on the order of a wavelength. On the other hand, metamaterials that are often tailored to have certain effective material parameters when homogenized, have periodicities that are small fractions of a wavelength.

Several FDTD techniques [31,51-54] have been proposed for analyzing infinite, singly- or doubly-periodic structures. By incorporating the periodic boundary condition (PBC) which takes advantage of the periodicity inherent in the geometry as well as the excitation, it is possible to reduce the original problem to that of a single unit cell, considerably simplifying the simulation process. However, the simulation time may still be extensive because of the multiple

reflections that might occur, especially when the periodic structure is comprised of multiple screens, and the waves can bounce back and forth between them.



(a)



(b)

Fig. 3.1: Geometry of freestanding frequency selective surfaces consisting of (a) conducting patches; and (b) apertures.

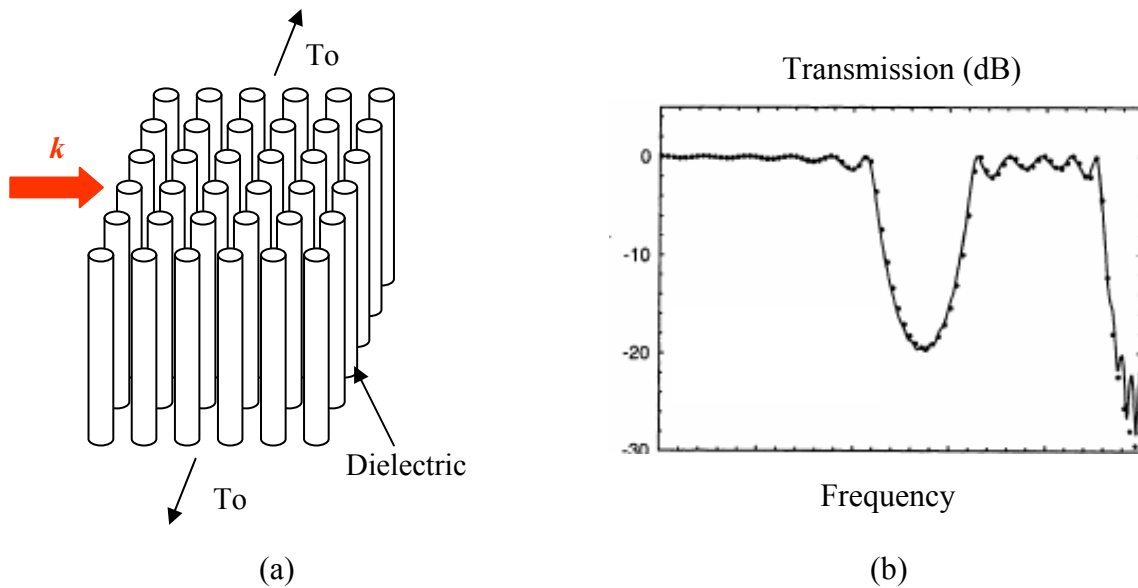


Fig. 3.2: (a) A typical example of a PBG structure and (b) its transmission characteristics.

A good absorbing boundary condition that terminates the boundaries of an open problem is essential to ensure both accuracy and stability of the FDTD solution in the presence of multiple reflections in a periodic structure. Recently, the convolutional PML (CPML) [8] has been introduced for truncating the FDTD mesh when solving general electromagnetic problems that are aperiodic in nature. The CPML, which was preceded by the uniaxial PML (UPML) [7], has the advantages of being simpler to implement than the UPML; is essentially independent of the material that it terminates; and, significantly attenuates the evanescent modes. Therefore, the CPML is a very desirable candidate for implementation in the present periodic problem. However, the incorporation of the CPML into the PBC/FDTD algorithm needs to be carried out with considerable care, since the updating procedure in the PBC version of the algorithm differs significantly from that of the conventional FDTD algorithm for aperiodic structures.

In this chapter, we begin by presenting an efficient, parallel implementation of the periodic boundary condition in FDTD, based on the split-field method [31], which can

significantly reduce the total simulation time when multiple processors are used. The parallel efficiency of this implementation will be evaluated numerically and compared to that of the conventional FDTD code. In the next section, we describe an instability problem, which, to the best of our knowledge, has not been identified in any prior publications. The problem arises when the CPML is implemented in the PBC/FDTD method in the same manner as has been successfully done in the conventional FDTD method. Following upon this, we suggest a possible cause for this instability, and then go on to propose a stable, and yet simple implementation of CPML in the PBC/FDTD algorithm. Finally, we present numerical examples to demonstrate the accuracy of the code and illustrate its application to a number of representative problems.

3.2 Review of the Existing PBC/FDTD Methods

Before presenting our work in the following sections, we will first briefly review several existing FDTD techniques for analyzing infinite periodic structures, and follow this up by formulating the split-field method, into which the parallel implementation and the CPML are to be incorporated.

3.2.1 Existing PBC/FDTD Methods

Taflove and Hagness [21] have divided the PBC/FDTD techniques into two categories, namely the field transformation and direct methods, as illustrated in Fig. 3.3. As the name implies, the former employ a field transformation [51]—discussed in the next section—to eliminate the time delay in the transverse plane for the oblique incidence case, and subsequently discretize the resulting equations in the FDTD format. The remaining PBC/FDTD techniques are simply referred to as the direct methods. In general, the field transformation methods are

preferable to the direct methods as the latter suffer from several limitations. For example, the Sine-Cosine Method [52] can only deal with a single frequency at a time, while the Angle-Update Method presented in [21] is limited to a maximum steering angle of approximately 35° . Additionally, its implementation suffers from the drawback that it must carry out the angle-dependent process of bookkeeping of the fields derived at previous time-steps.

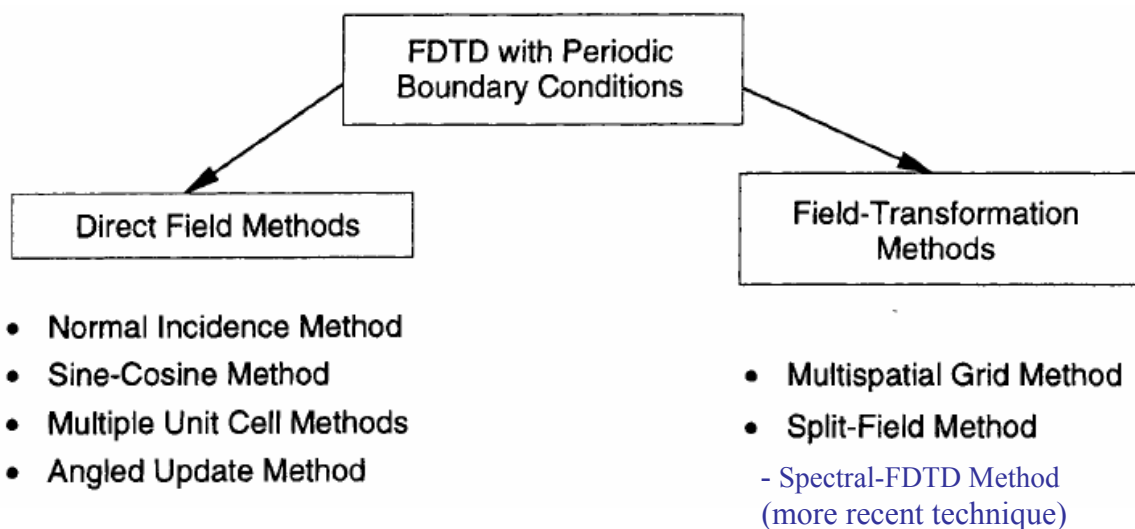


Fig. 3.3: Classification of the PBC/FDTD techniques: Direct Field methods and Field-Transformation methods (from Ref. [28]).

Among all the field transformation techniques, we have chosen to work with the split-field method for several reasons. First, as opposed to the multiple-grid method [53], the split-field method utilizes the conventional Yee's grid, rather than dual-grid which is more complex. Second, it has a more relaxed stability requirement than that of the multiple grid approach. On the other hand, the spectral-FDTD method [54] does show a significant advantage, in terms of stability, over the split-field method when the incident angle of the illumination is close to grazing. However, the spectral approach is much less efficient when we desire the frequency

response for a fixed incident angle, because the spectral-FDTD method computes the response of an incident field for only a fixed wavenumber, as opposed to a fixed incident angle, each time the simulation is run.

3.2.2 Formulation of Field Transformation

For the sake of simplicity, we limit our discussion in this chapter solely to passive infinitely periodic structure, with periodicities D_x and D_y in the x - and y -directions, respectively. We assume a uniform plane wave illumination with the propagation vector of $\vec{k} = (k_x, k_y, k_z)$, as shown in Fig. 3.4.

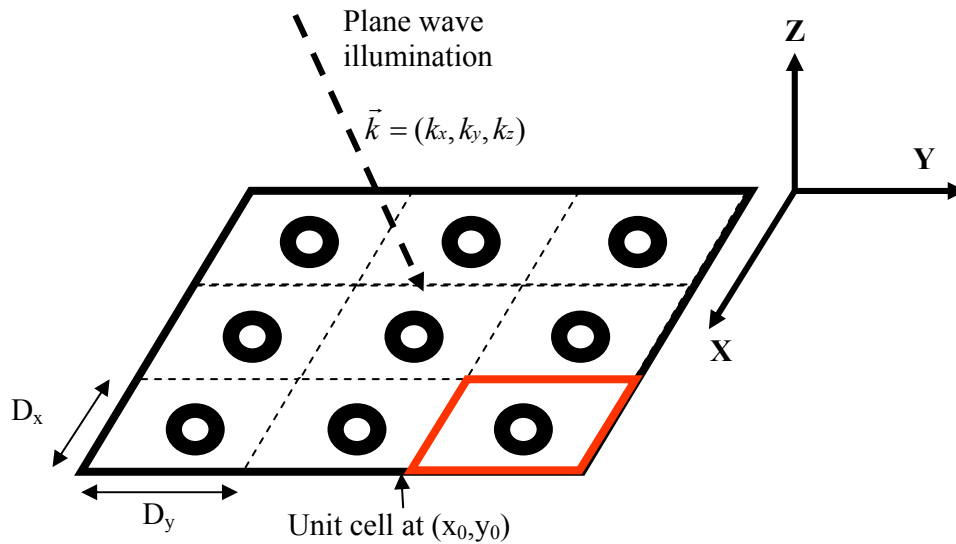


Fig. 3.4: A passive periodic structure under the excitation of a plane wave. The periodic boundaries for the unit cell at (x_0, y_0) is highlighted in red.

For the oblique incidence case, the field quantities in the periodic structure must obey the lateral phase shift conditions across the x - y plane, as dictated by the wave numbers k_x and k_y of

the incident field. The boundary conditions of the unit cell highlighted in red can be described by (3.1a-b) below for the E-field (similarly for the H-fields):

$$E(x_0 + D_x, y, z) = E(x_0, y, z) \exp(-jk_x D_x) \quad (3.1a)$$

$$E(x, y_0 + D_y, z) = E(x, y_0, z) \exp(-jk_y D_y) \quad (3.1b)$$

To suppress the phase factor, we introduce a set of auxiliary variables P and Q, known as the transformed fields as follows:

$$P = E \exp(jk_x x + jk_y y) \quad (3.2)$$

$$Q = H \exp(jk_x x + jk_y y) \quad (3.3)$$

Substituting (3.2) into (3.1a-b), we obtain the following boundary conditions for the transformed field P:

$$P(x_0 + D_x, y, z) = P(x_0, y, z) \quad (3.4a)$$

$$P(x, y_0 + D_y, z) = P(x, y_0, z) \quad (3.4b)$$

and similarly for Q. In summary, substituting (3.2) and (3.3) into Maxwell's curl equations maps the solution space, specifically the variables P and Q, that enables us to enforce the periodic boundary conditions by requiring that the tangential components of the transformed fields be identical on the opposing boundary walls of a single unit cell.

3.2.3 Formulation of Split-Field Method

In the last section, we have provided an explanation as to how the phase variation across the x-y plane for the oblique incidence case can be removed by introducing the transformed fields P and Q, that are related to the direct fields E and H, respectively. However, the transformed set of Maxwell equations for the transformed fields contain additional terms that

were not there originally, and this leads to some difficulties when the modified equations are discretized.

The split-field method provides an efficient and simple way to discretize the transformed field equations by splitting the fields into two parts. A new set of split variables denoted by the subscript “a”, are defined as follows:

$$P_x = P_{xa} - \frac{\bar{k}_y}{\varepsilon_{xr}} \eta_0 Q_z \quad Q_x = Q_{xa} + \frac{\bar{k}_y}{\mu_{xr} \eta_0} P_z \quad (3.5a)$$

$$P_y = P_{ya} + \frac{\bar{k}_x}{\varepsilon_{yr}} \eta_0 Q_z \quad Q_y = Q_{ya} - \frac{\bar{k}_x}{\mu_{yxr} \eta_0} P_z \quad (3.5b)$$

$$P_z = P_{za} + \frac{\bar{k}_y}{\varepsilon_{zr}} \eta_0 Q_x - \frac{\bar{k}_x}{\varepsilon_{zr}} \eta_0 Q_y \quad Q_z = Q_{za} - \frac{\bar{k}_y}{\mu_{zr} \eta_0} P_x + \frac{\bar{k}_x}{\mu_{zr} \eta_0} P_y \quad (3.5c)$$

where η_0 is the impedance of the free space, \bar{k}_x , \bar{k}_y and \bar{k}_z are the projections of the wave vector of the incident plane wave along x, y, and z, respectively.

The details of the discretization process will not be discussed here since they are not relevant to the present discussion. The reader interested in further details is referred to the existing literature [21,31]. Nevertheless, to facilitate the discussion of the parallel implementation based on the split-field methods in Sec. 3.3, we will provide a qualitative view of the updating procedure in the following section.

3.2.4 Updating Procedure Based on the Split-Field Method

Figure 3.5 shows the spatial grid used in the split-field approach; this is identical to the Yee’s cell. This implies that the transformed field (P_i / Q_i) as well as the “a” split fields (P_{ia} / Q_{ia})

are positioned at the same location of the direct field (E_i / H_i), where the subscript denotes the x-, y-, or z-component.

Despite the use of identical spatial grid, the updating procedure in the split-field method is far more complex than the one in the conventional FDTD algorithm. Figure 3.6 depicts the flowchart for the updating procedure in a single cycle, which can be divided into two steps. Steps (1) through (4) update the split fields with the subscript “a”, viz., P_a and Q_a , followed by the steps (5) through (8) that update the transformed fields, namely P and Q. Notice that when multiple tasks are involved in a single step, they can be performed in an arbitrary order.

It should be pointed out that the time is advanced by only a half time-step Δt in each cycle, implying that a dual time grid is employed. For normal incidence, Δt is equal to the Courant’s time-step; however, Δt must be reduced to obtain stable results, as the incident angle is increased.

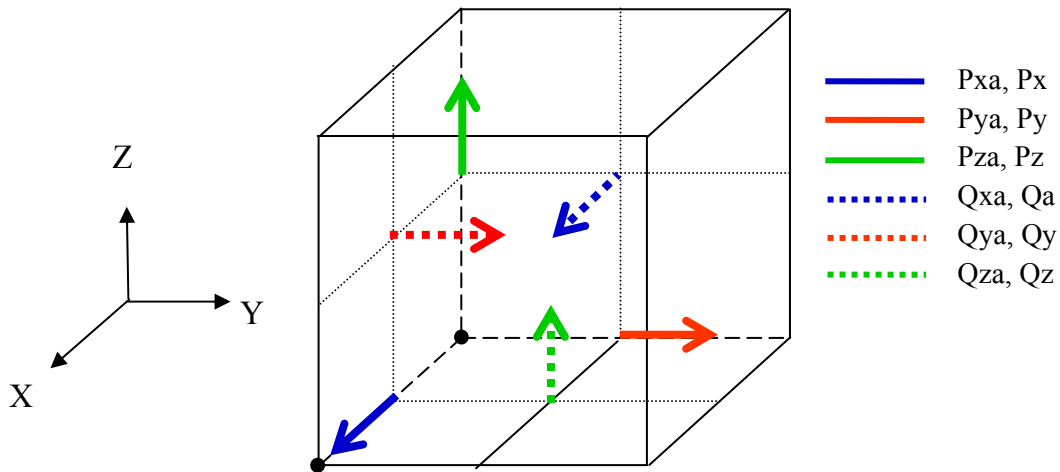


Fig. 3.5: The three-dimensional spatial grid used in the split-field PBC/FDTD algorithm.

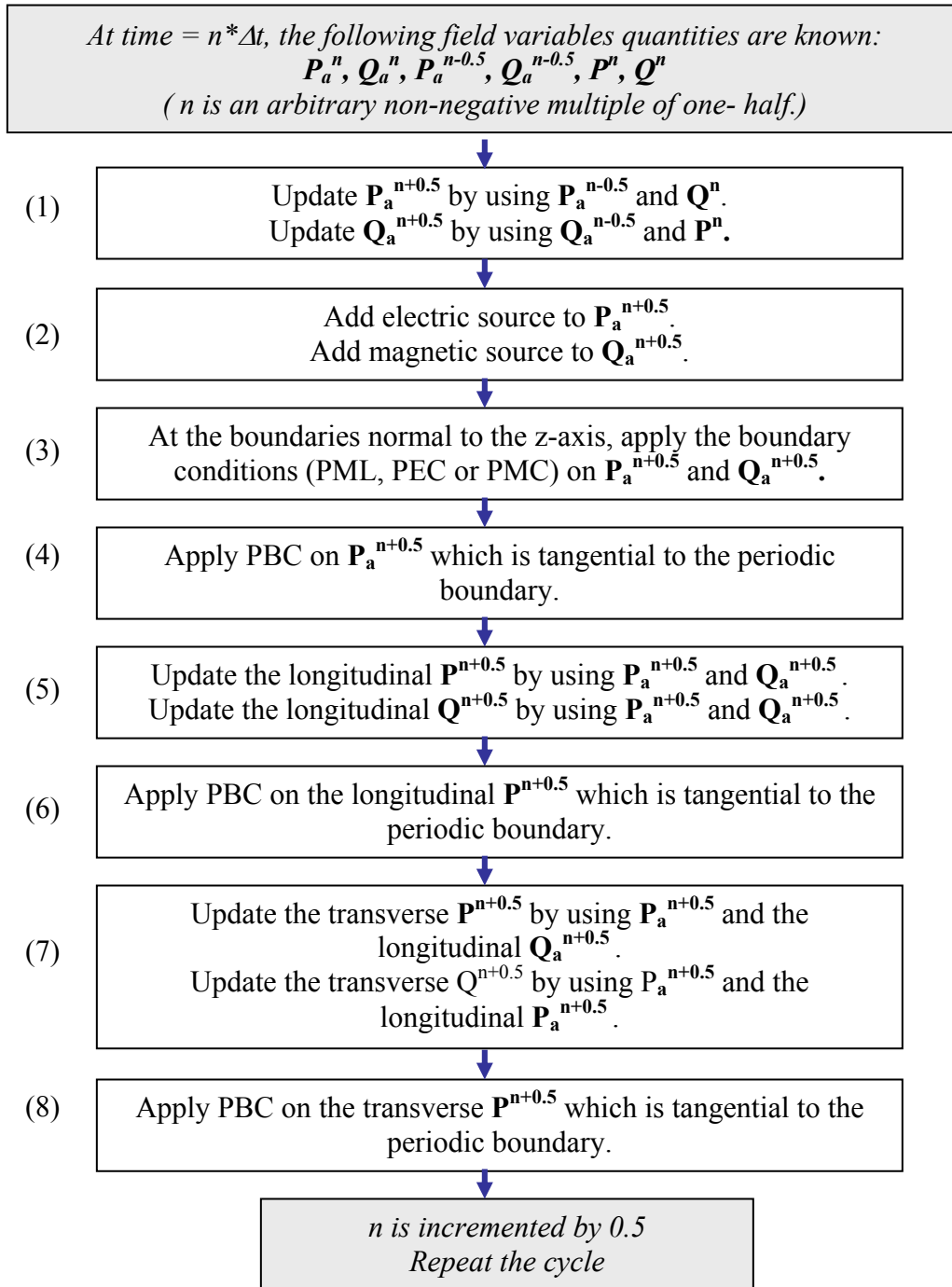


Fig. 3.6: The updating procedure in a single cycle of the serial split-field PBC/FDTD algorithm.

3.2.5 Enforcement of the PBC

As discussed in 3.2.2, in the field transformation technique, the periodic boundary condition constrains the enforcement of the tangential fields at like positions on the opposite walls of the unit cell to be identical. Consequently, in the split-field method, a natural way is to apply the PBC on the tangential P and P_a at the unit cell boundaries directly, and ignore their magnetic counterparts, i.e., tangential Q and Q_a , because they are offset from the unit cell boundaries by at least one half-cell in the Yee's grid. However, it has been found that the implementation of this approach is both complex and inefficient. For the tangential P and P_a on the periodic boundary, some of the neighboring Q and Q_a lie outside the simulation area, and hence, their values need to be "borrowed" from the fields at the opposite sides of the unit cell at like positions. This implies that, depending on their locations, P and P_a need to be updated by using different sets of equations. Table 3-1 counts the total number of sets of update equations required in a three-dimensional case. To make matters even worse, a multiple set of PML update equations need to be enforced at different locations.

Table 3-1: Total number of sets of update equations in a three-dimensional case.

Field Component	P_x	P_y	P_z	P_{xa}	P_{ya}	P_{za}
No. of sets	3	3	9	3	3	9

In one of the earliest work on the PBC/FDTD methods [52], an alternative approach has been proposed for the PBC implementation, which bypasses the difficulties encountered in using the direct approach. The computational domain is first extended one cell outward at the periodic boundaries, as shown in Fig. 3.7. After the magnetic fields (Q or Q_a) inside the unit cell have

been updated from the FDTD algorithm, the tangential magnetic fields at the extended cells, which are always located one half-cell from the periodic boundary, can be “copied” from the field values of their periodic “image”, which are located one half-cell inwards from the opposite periodic boundary at like positions, via the use of PBC equations. In this way, all the P and P_a fields, regardless of whether they are on the periodic boundary or not, can be updated in the same way. Also, the tangential P and P_a on the periodic boundary automatically comply with the PBC equations. This alternative approach not only simplifies the updating process, but also facilitates the parallel implementation, which will be discussed in the following section.

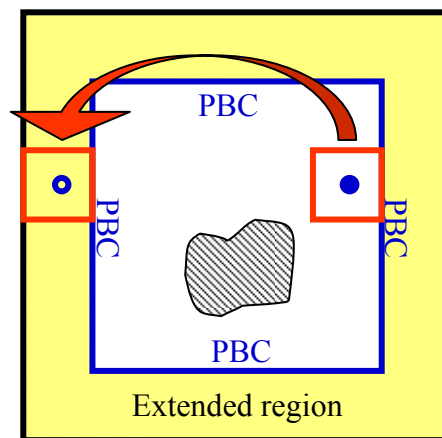


Fig. 3.7: Schematic showing the computational domain extended beyond the periodic boundaries. During each cycle, after the fields inside the periodic boundary have been computed, the tangential magnetic fields in the extended region can be “copied” from the field values of their periodic “image”, as illustrated by the red arrow.

3.3 Parallel Implementation of the PBC/FDTD Method

In this section, we present a parallel implementation of the PBC/FDTD method based on the domain decomposition approach, as discussed earlier in Chapter 2, utilizing a one-cell overlap region to exchange information between neighboring subdomains.

3.3.1 Communication Between Two Neighboring Subdomains

If we utilize Yee's spatial grid in the split-field PBC/FDTD, we can employ the same parallel updating scheme as we use in the conventional FDTD to the present PBC case as well. To do this, we extend the subdomain outwards by one cell at the interface that is shared with another subdomain, and then exchange the magnetic fields in the overlapping cells in each cycle. However, we point out that the PBC/FDTD updating procedure is different from that in the conventional FDTD in the following two ways: (i) two sets of magnetic fields (Q and Q_a) are updated, rather than a single set (H) that is updated in each conventional FDTD cycle; (ii) the order for updating different components of the magnetic fields is important. Figure 3.8 illustrates the parallel implementation of the domain decomposition method, and the field exchange in the overlapping cells for the PBC/FDTD, while Fig. 3.9 depicts the flowchart for the updating procedure in a single cycle of the parallel exchange process—shown in the red boxes in the figure. Note that the total number of steps in each cycle remains the same as that shown in Fig. 3.6 for a serial code. This is because the PBC implementation using the approach discussed in Sec. 3.2.4 enables us to follow both a simple and efficient way to combine with the parallel exchanging step between neighboring subdomains. This will be discussed further in the following section.

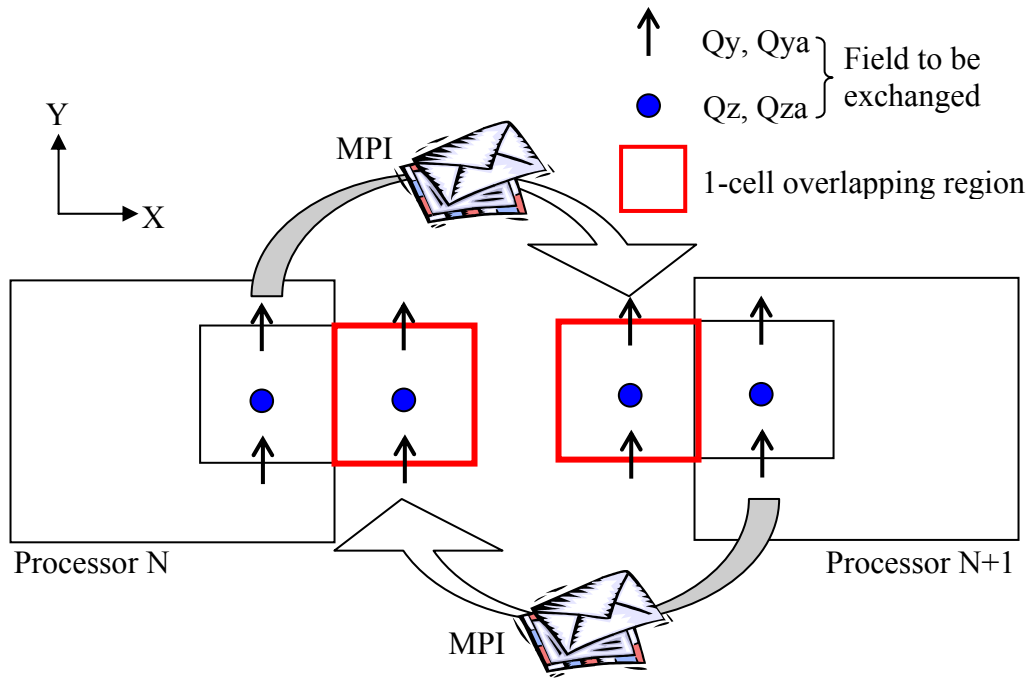


Fig. 3.8: Configuration of field exchange between two neighboring processors.

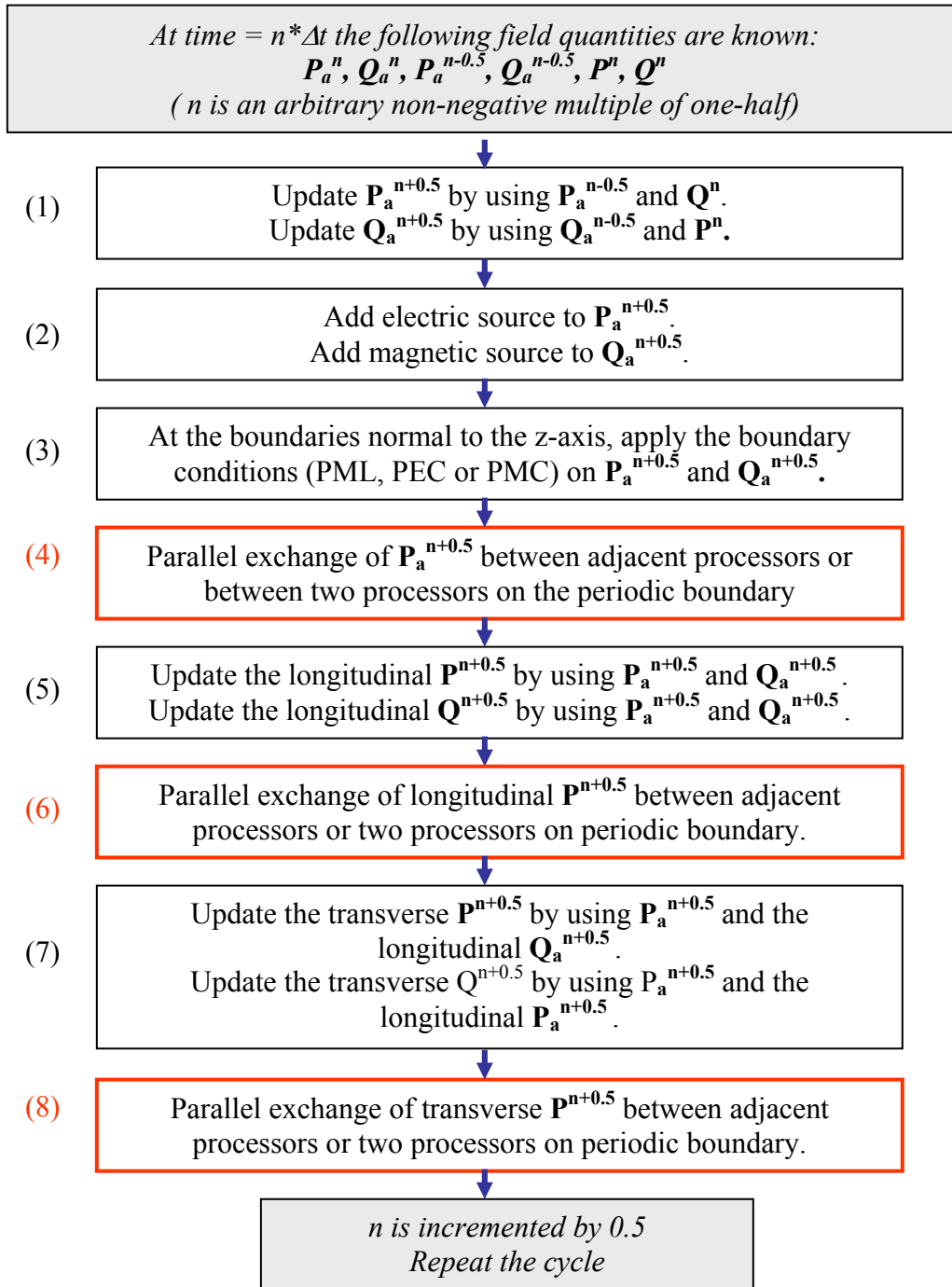


Fig. 3.9: The updating procedure in a single cycle of the parallel split-field PBC-FDTD algorithm. The steps for parallel field exchange are highlighted in red boxes.

3.3.2 Communication Between Two Subdomains on Two Opposite Side of Periodic Boundaries

When the domain decomposition is carried out either along the x- or the y-directions, or along both, the opposite periodic walls are located within separate subdomains. This, in turn, implies that there would be a need for field exchange between these subdomains in order to enforce the PBC.

As outlined in Sec. 3.2.4, the above exchange, carried out during the enforcement of the PBC, is very similar to that between two neighboring subdomains in the domain decomposition method. First, the boundary is extended outwards by one cell; and, second, the tangential magnetic fields in the extended cell region are computed by copying the fields at the “image” locations, either in neighboring subdomains for the domain decomposition method, or on opposite walls of the periodic boundary. Note that, for the latter case, the field exchange can be carried out within a single processor or between two processors, depending upon the way the domain is divided. Nevertheless, we use the same parallel exchanging scheme even when the field is communicated within the same processor for the sake of coding simplification. In view of the similarities mentioned above, a parallel field exchanging scheme similar to that described in Sec. 3.3.1 can be applied here to exchange the tangential magnetic fields near the periodic boundaries on opposite sides, as illustrated in Fig. 3.10. The number of field exchanges as well as the structure are identical for both types of parallel exchanges; hence, they are easily combined into a single step, as shown in Fig. 3.8.

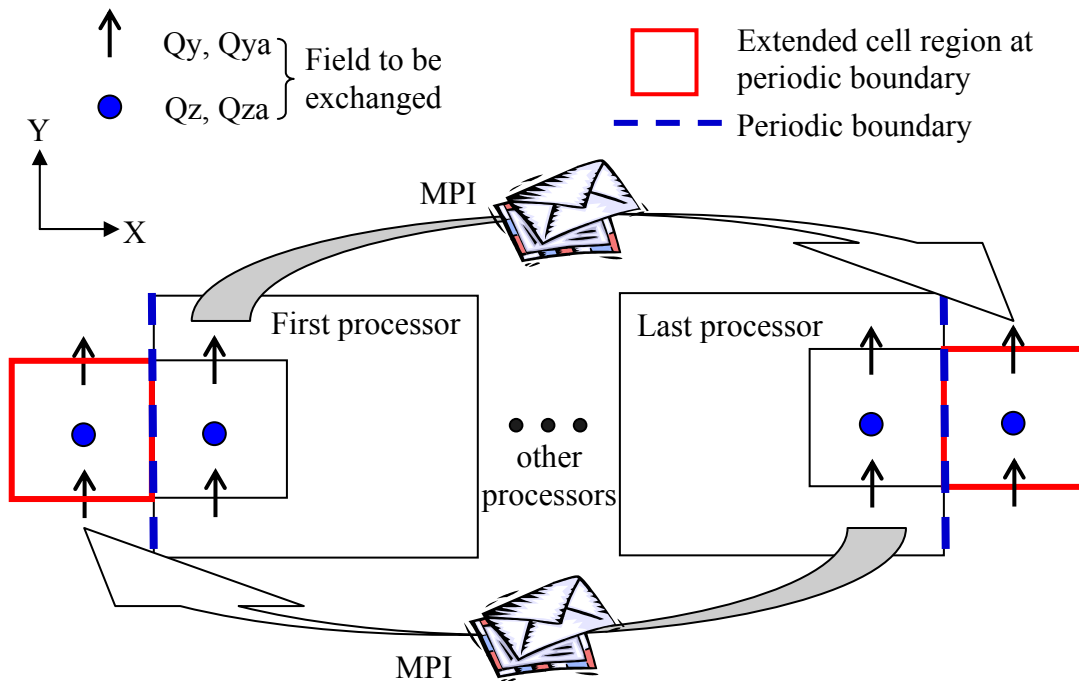


Fig. 3.10: Configuration of field exchange between two processors at the two opposite periodic boundaries.

3.3.3 Numerical Test of Parallel Efficiency

In this section, we analyze the efficiency of the parallel PBC/FDTD code by using a simple example, which has $300 \times 300 \times 300$ FDTD cells. The region is only free space, and is excited by a plane wave incident at an oblique angle of 10° . The domain decomposition is applied along the x-direction and different number of processors is used for different runs. In each run, 1000 FDTD cycles are performed and the simulation time is recorded. For comparison, we also perform identical tests using the parallel-FDTD code, run on the same computer platforms.

All tests have been performed on a computer platform named GEMS box [28], which integrates 4 nodes (8×2.33 Woodcrest Intel processors, 16 cores, and 32 GB memory) for parallel processing and one Myrinet fiber network system for data communications between processors and other components. Due to the limitation on the maximum number of available cores, we have performed the tests on only 1 to 15 processors.

Table 3-2 shows the simulation time for all the cases studied. Notice that, for this test case, the simulation time for the PBC/FDTD code is slightly greater than twice that for the conventional FDTD code, because the updating process for the former involves considerably larger number of arithmetic operations. The parallel efficiency for each case is computed by using (2.3.1) and is plotted in Fig. 3.11. The parallel efficiency of the PBC/FDTD code is only slightly lower than that of the reference case, even though twice the number of the magnetic fields, viz., Q and Q_a , are involved in the field exchanging step in each cycle for the PBC/FDTD code. It should also be noted that this test example is only a medium-size problem, and that the parallel efficiency is expected to improve as the problem size is increased.

Table 3-2: Comparison of the total simulation times using different number of CPUs, for the parallel PBC/FDTD code and the general FDTD code.

Number of CPUs used	1	2	3	5	10	15
Simulation time for the PBC/FDTD code	4898 s	2462 s	1656 s	1005 s	566 s	432 s
Simulation time for the FDTD code	2065 s	4038 s	702 s	425 s	232 s	178 s

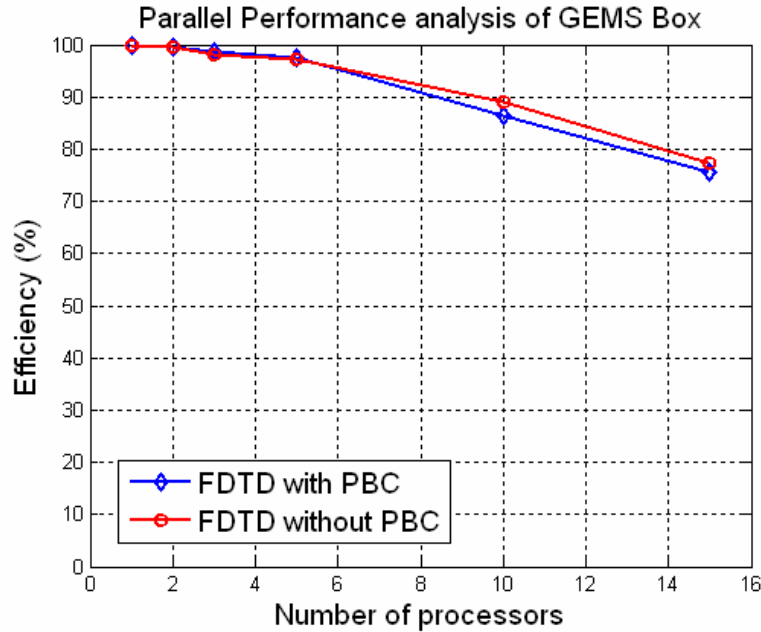


Fig. 3.11: The parallel efficiency versus the number of processors when using the PBC/FDTD code (Blue) and the standard FDTD code (red) without the PBC.

3.4 Implementation of CPML into PBC/FDTD Method

In this section, we first begin with a brief review of the CPML formulation. Next, we identify an instability issue encountered in the CPML implementation into the PBC/FDTD algorithm, even though it is carried out by following the same approach that has been successfully implemented in the conventional FDTD method. Following that, we suggest a possible cause for this, and go on to propose a stable, yet simple implementation of the CPML in the PBC/FDTD algorithm.

3.4.1 Formulation of the CPML

Roden and Gedney [8] first proposed an efficient implementation of the complex frequency-shifted PML [55] (CFS-PML) in the FDTD method based on a stretched-coordinate

formulation [56] incorporated into a recursive convolution algorithm [4], which is known as the CPML. For simplicity, we consider the lossless case without loss of generality. Note that σ_i are the coefficients used in the coordinate stretching process, and they are not to be confused with the conductivity of the host medium (zero for lossless case) in the following discussion.

Transforming the Maxwell's equations in the stretched-coordinate space, the x-projection of the Ampere's law for the lossless case can be expressed as:

$$j\omega\epsilon_x E_x = \frac{1}{S_y} \frac{\partial}{\partial y} H_z - \frac{1}{S_z} \frac{\partial}{\partial z} H_y \quad (3.9)$$

where

$$S_i = \kappa_i + \frac{\sigma_i}{\alpha_i + j\omega\epsilon_o} \quad (3.10)$$

are the metrics of the stretched-coordinates, where $\kappa_i \geq 1$. The metrics are known as the complex-frequency shifted (CFS) coordinates. Also the parameters σ_i , $\alpha_i \geq 0$ are introduced in the PML region to absorb the outgoing waves. (Note that $\kappa_i = 1$, and $\sigma_i = \alpha_i = 0$ outside the PML regions.) The introduction of a non-zero α_i can improve the PML performance at low frequencies, by enhancing the absorption of the evanescent waves. An extra term appears when we substitute the impulse response of S_i^{-1} into (3.9) and discretize the update equations. This term can be computed efficiently by using the recursive convolution method. The details of this derivation are omitted here, and the interested reader can refer to [8,21] for details.

Consider the FDTD updating in the PML regions that terminates either the positive or the negative z-boundary. For this case, only S_z is stretched, i.e., $S_x = S_y = 1$, and the update equation, corresponding to (3.9), has the following form:

$$\begin{aligned}
E_{x_{i+\frac{1}{2},j,k}}^{n+1} &= E_{x_{i+\frac{1}{2},j,k}}^n + \frac{C_e}{\Delta y} (H_{z_{i+\frac{1}{2},j+\frac{1}{2},k}}^{n+\frac{1}{2}} - H_{z_{i+\frac{1}{2},j-\frac{1}{2},k}}^{n+\frac{1}{2}}) \\
&- \frac{C_e}{\kappa_z \Delta z} (H_{y_{i+\frac{1}{2},j,k+\frac{1}{2}}}^{n+\frac{1}{2}} - H_{y_{i+\frac{1}{2},j,k-\frac{1}{2}}}^{n+\frac{1}{2}}) - \psi_{xz}^{n+1}
\end{aligned} \tag{3.11}$$

The extra term ψ_{xz} in (3.11) is updated by using

$$\psi_{xz}^{n+1} = b_z \psi_{xz}^n + a_z \frac{C_e}{\Delta z} (H_{y_{i+\frac{1}{2},j,k+\frac{1}{2}}}^{n+\frac{1}{2}} - H_{y_{i+\frac{1}{2},j,k-\frac{1}{2}}}^{n+\frac{1}{2}}) \tag{3.12}$$

and the other variables are defined as :

$$C_e = \frac{\Delta t}{\varepsilon_x} \tag{3.13}$$

$$a_z = \exp \left[- \left(\frac{\sigma_z}{\kappa_z} + \alpha_z \right) \left(\frac{\Delta t}{\varepsilon_0} \right) \right] \tag{3.14}$$

$$b_z = \frac{\sigma_z}{(\sigma_z \kappa_z + \kappa_z^2 \alpha_z)} \left\{ \exp \left[- \left(\frac{\sigma_z}{\kappa_z} + \alpha_z \right) \left(\frac{\Delta t}{\varepsilon_0} \right) \right] - 1.0 \right\} \tag{3.15}$$

The extra term ψ_{xz} , originates a convolution operator (explained in [8,21]), which is discretized by applying the midpoint rule¹. The resulting sum can be computed efficiently by using the recursive convolution method expressed in (3.12). It should be pointed out that that we purposely use a different time index, $n+1$, for the extra term, instead of $(n+1/2)$ that is used in most of the papers discussing the CPML. This is done to preserve the same form commonly used in the midpoint rule, though both implementations are actually equivalent to each other.

¹ The midpoint rule states that the midpoint m_k of each of the intervals as the point at which to evaluate the function for the Riemann sum. Namely, for the Riemann integral $\int_a^b f(t) dt$ with n equal intervals,

$$\int_a^b f(t) dt = \frac{b-a}{n} (f(m_1) + f(m_2) + \dots + f(m_n)) + o\left(\frac{1}{n^2}\right) \text{ where } m_i \text{ is the midpoint of the } i\text{-th interval.}$$

In summary, the field updating inside the CPML region is carried out differently from that outside the CPML region in two ways. First, a factor of $1/\kappa_i$ is introduced in the spatial differentiation term—the third term on the r.h.s. of (3.11)—that corresponds to the direction along which the PML-type ABC is applied. Second, the extra term is updated by using the recursive convolution method as expressed in (3.12).

3.4.2 CPML Formulation Within the PBC/FDTD Following the Conventional Way

To the best of the author's knowledge, to-date only one publication [57] has discussed the CPML formulation within the context of split-field PBC/FDTD method and has obtained stable results for the test example investigated. In this paper, the update equations, analogous to (3.11) and (3.12), are derived in the same way as in the conventional FDTD method, as explained below.

For the split-field PBC/FDTD method, the CPML implementation only affects the updating of P_a and Q_a , because the terms with spatial derivatives only appear in these equations. Consider the field updates in the CPML region which terminates either the positive or the negative z -boundaries. The update equation for P_{ax} is similar to (3.9), used to update E_x in the conventional FDTD method, and is given below for the lossless case:

$$j\omega\varepsilon_x P_{xa} = \frac{\partial}{\partial y} Q_z - \frac{1}{S_z} \frac{\partial}{\partial z} Q_y \quad (3.16)$$

Transformation of (3.16) into the time-domain, followed by its discretization, leads us to the update equation for P_{xa} :

$$\begin{aligned}
P_{xa_{i+\frac{1}{2},j,k}}^{n+1} &= P_{xa_{i+\frac{1}{2},j,k}}^n + \frac{C_e}{\Delta y} (Q_{z_{i+\frac{1}{2},j+\frac{1}{2},k}}^{n+\frac{1}{2}} - Q_{z_{i+\frac{1}{2},j-\frac{1}{2},k}}^{n+\frac{1}{2}}) \\
&- \frac{C_e}{\kappa_z \Delta z} (Q_{y_{i+\frac{1}{2},j,k+\frac{1}{2}}}^{n+\frac{1}{2}} - Q_{y_{i+\frac{1}{2},j,k-\frac{1}{2}}}^{n+\frac{1}{2}}) - \psi_{xz_{i+\frac{1}{2},j,k}}^{n+1}
\end{aligned} \tag{3.17}$$

where C_e remains the same as stated in (3.13), but the extra term ψ_{xz} is updated differently than before, since the time is now advanced by only half a time-step in each cycle. Thus, we rewrite (3.12) as:

$$\psi_{xz_{i+\frac{1}{2},j,k}}^{n+1} = b_z \psi_{xz_{i+\frac{1}{2},j,k}}^{n+\frac{1}{2}} + a_z \frac{C_e}{\Delta z} (Q_{y_{i+\frac{1}{2},j,k+\frac{1}{2}}}^{n+\frac{1}{2}} - Q_{y_{i+\frac{1}{2},j,k-\frac{1}{2}}}^{n+\frac{1}{2}}) \tag{3.18}$$

where a_z and b_z are also defined differently in the following way:

$$a_z = \exp \left[- \left(\frac{\sigma_z}{\kappa_z} + \alpha_z \right) \left(\frac{\Delta t}{2\epsilon_0} \right) \right] \tag{3.19}$$

$$b_z = \frac{\sigma_z}{(\sigma_z \kappa_z + \kappa_z^2 \alpha_z)} \left\{ \exp \left[- \left(\frac{\sigma_z}{\kappa_z} + \alpha_z \right) \left(\frac{\Delta t}{2\epsilon_0} \right) \right] - 1.0 \right\} \tag{3.20}$$

The expressions given in (3.17) through (3.20) have been incorporated into a code that combines the CPML with the PBC/FDTD method, and tested by using a simple example, as shown schematically in Fig. 3.12. The computational domain consists of 30 x 30 x 30 cells, the medium is free space, and is excited by an Ex-polarized plane wave propagating toward the negative z-direction. Figures 3.13(a) and (b) show the temporal response and the spectrum of the incident source, which is a modulated Gaussian pulse with both the modulation and 3-dB frequencies at 10 GHz. Its strength is 1 V/m. The FDTD cell-size used is 1 mm in all directions, which is equal to $\lambda/30$ at 10 GHz. The side boundaries at XMIN, XMAX, YMIN, and YMAX are terminated by using the PBC, while the boundaries on the ZMIN and ZMAX sides are truncated by the CPML to simulate an open region problem. The simulation process is repeated

by using a code that combines the UPML with the identical PBC/FDTD code. For comparison, the same set of parameters, viz., σ_z , κ_z , $\alpha_z (= 0)$, are employed in the stretched coordinate system for both types of PML, and the number of layers (six) used is identical.

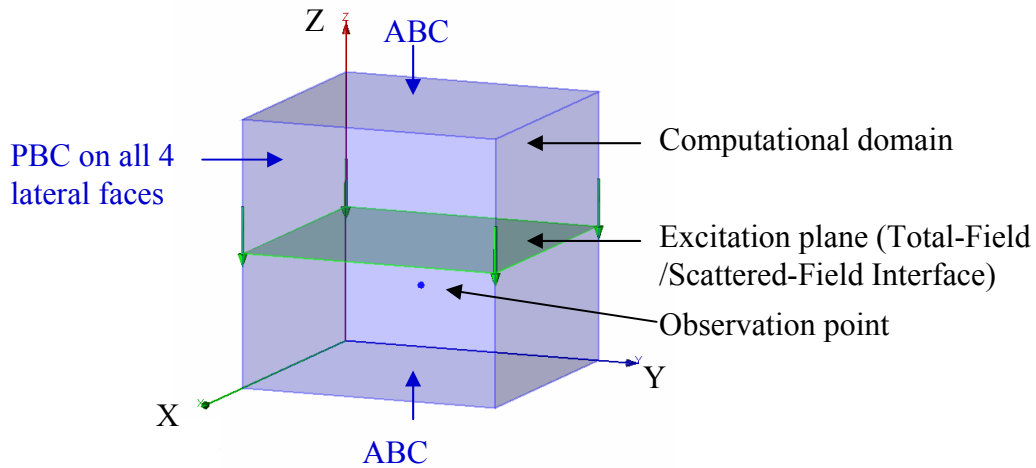


Fig. 3.12: Diagram of the boundary condition, excitation and measurement settings used in testing the CPML implemented in the PBC/FDTD algorithm.

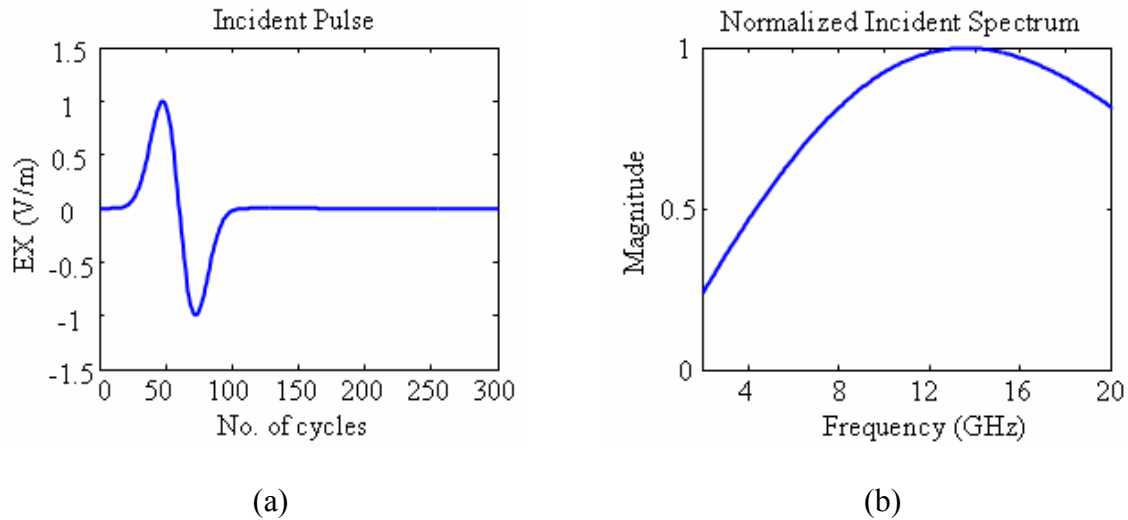


Fig. 3.13: (a) The transient waveform and (b) the spectrum of the incident signal used in testing the CPML implemented in the PBC/FDTD algorithm.

Figures 3.14 (a) and (b) plot the time-domain E_x measured at a point located in the total-field region for the first 300 and 4000 cycles, respectively, for both types of PML. When we compare the results to the incident pulse shown in Fig. 3.13 (a), we find that the time-domain signals in Fig. 3.14 (a) are very similar to the incident pulse for both cases, which implies that both PMLs are well capable of absorbing the outgoing waves during the early FDTD cycle times. However, as may be clearly seen from Fig. 3.14 (b), the instability begins to appear at around 2700 cycles with the CPML implemented in the conventional manner, while the fields remain stable throughout the entire simulation with the UPML implementation.

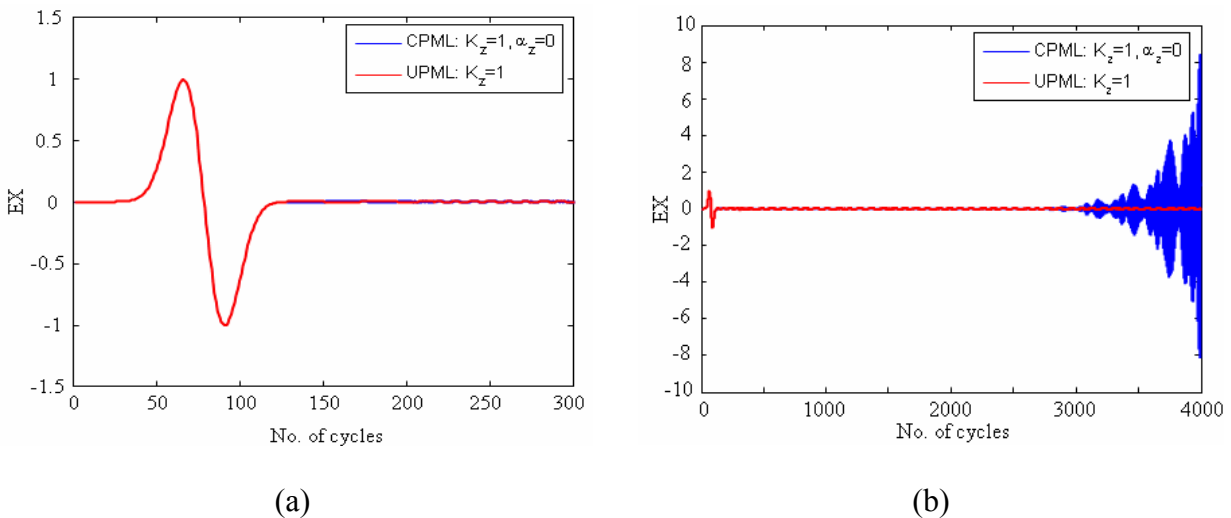


Fig. 3.14: Transient waveform E_x measured at a point inside the total-field region for (a) the first 300 cycles, and (b) the first 4000 cycles, respectively, using CPML (Blue) and UPML (Red). The CPML is implemented in the same way as done in the standard FDTD method.

3.4.3 Suggested Cause for the Instability

In order to explain the instability, we take a closer look into the extra term ψ_{xz} in the CPML formulation of the conventional FDTD method. As discussed in Sec. 3.4.1, this term is derived from a convolution operator when we use the CFS-stretched coordinates. During the

discretization process, the midpoint rule is applied, and the sum is computed by using the recursive convolution method. The time indices in (3.12) preserves the form that is similar to the one used in the midpoint rule for the evaluation of a Riemann integral $\int_0^{n\Delta t} f(t)dt$ divided into n equal time intervals Δt . The midpoint rule also suggests that (3.12) follows a centre-differencing scheme and preserves a second order accuracy of $O(\Delta t^2)$.

On the other hand, if we update the ψ_{xz} in the split-field PBC/FDTD method based on its value at the previous cycle, which is $\Delta t/2$ earlier in time, the update equation of (3.12) is transformed into (3.18). It should be pointed out that the time indices in (3.18) no longer preserve the same form as used in the midpoint rule. In fact, (3.18) implies the use of a forward-differencing scheme, which has been demonstrated to be unstable in many situations.

3.4.4 Modified CPML Implementation

It is not straightforward to implement the CPML into the split-field PBC/FDTD method that utilizes either the midpoint rule, or the centre-differencing scheme. When we update the ψ_{xz} by using its value at the previous cycle, we should use the corrected form of (3.18) which reads:

$$\psi_{xz}^{n+1}{}_{i+\frac{1}{2},j,k} = b_z \psi_{xz}^{n+\frac{1}{2}}{}_{i+\frac{1}{2},j,k} + a_z \frac{C_e}{\Delta z} (Q_y^{n+\frac{1}{4}}{}_{i+\frac{1}{2},j,k+\frac{1}{2}} - Q_y^{n+\frac{1}{4}}{}_{i+\frac{1}{2},j,k-\frac{1}{2}}) \quad (3.21)$$

where C_e , a_z and b_z remains the same as in (3.13), (3.19) and (3.20), respectively. However, this updating process cannot be applied by using (3.21), since the field values at $(n+1/4)\Delta t$ are unknown.

To circumvent this problem, we propose an alternative approach to updating the extra term, while we still apply the midpoint rule. To this end, we introduce two auxiliary variables $\psi_{xz,odd}$ and $\psi_{xz,even}$ that replace the single variable ψ_{xz} , previously used at the same locations; however, they are now updated alternately during the odd and even number of FDTD cycles, respectively, as explained below.

During the odd cycle, where n is any odd multiple of a half-integer, we use $\psi_{xz,odd}$, and (3.17) and (3.18) become:

$$P_{xa_{i+\frac{1}{2},j,k}}^{n+1} = P_{xa_{i+\frac{1}{2},j,k}}^n + \frac{C_e}{\Delta y} (Q_{z_{i+\frac{1}{2},j+\frac{1}{2},k}}^{n+\frac{1}{2}} - Q_{z_{i+\frac{1}{2},j-\frac{1}{2},k}}^{n+\frac{1}{2}}) - \frac{C_e}{\kappa_z \Delta z} (Q_{y_{i+\frac{1}{2},j,k+\frac{1}{2}}}^{n+\frac{1}{2}} - Q_{y_{i+\frac{1}{2},j,k-\frac{1}{2}}}^{n+\frac{1}{2}}) - \psi_{xz,odd_{i+\frac{1}{2},j,k}}^{n+1} \quad (3.22)$$

$$\psi_{xz,odd_{i+\frac{1}{2},j,k}}^{n+1} = b_z \psi_{xz,odd_{i+\frac{1}{2},j,k}}^n + a_z \frac{C_e}{\Delta z} (Q_{y_{i+\frac{1}{2},j,k+\frac{1}{2}}}^{n+\frac{1}{2}} - Q_{y_{i+\frac{1}{2},j,k-\frac{1}{2}}}^{n+\frac{1}{2}}) \quad (3.23)$$

During the even cycle, where n is any even multiple of a half-integer, $\psi_{xz,even}$ is utilized instead.

(3.17) and (3.18) become:

$$P_{xa_{i+\frac{1}{2},j,k}}^{n+1} = P_{xa_{i+\frac{1}{2},j,k}}^n + \frac{C_e}{\Delta y} (Q_{z_{i+\frac{1}{2},j+\frac{1}{2},k}}^{n+\frac{1}{2}} - Q_{z_{i+\frac{1}{2},j-\frac{1}{2},k}}^{n+\frac{1}{2}}) - \frac{C_e}{\kappa_z \Delta z} (Q_{y_{i+\frac{1}{2},j,k+\frac{1}{2}}}^{n+\frac{1}{2}} - Q_{y_{i+\frac{1}{2},j,k-\frac{1}{2}}}^{n+\frac{1}{2}}) - \psi_{xz,even_{i+\frac{1}{2},j,k}}^{n+1} \quad (3.24)$$

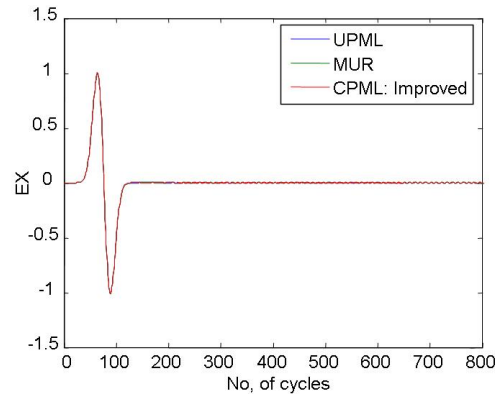
$$\psi_{xz,even_{i+\frac{1}{2},j,k}}^{n+1} = b_z \psi_{xz,even_{i+\frac{1}{2},j,k}}^n + a_z \frac{C_e}{\Delta z} (Q_{y_{i+\frac{1}{2},j,k+\frac{1}{2}}}^{n+\frac{1}{2}} - Q_{y_{i+\frac{1}{2},j,k-\frac{1}{2}}}^{n+\frac{1}{2}}) \quad (3.25)$$

where C_e , a_z and b_z remain the same as given in (3.13), (3.14) and (3.15), respectively.

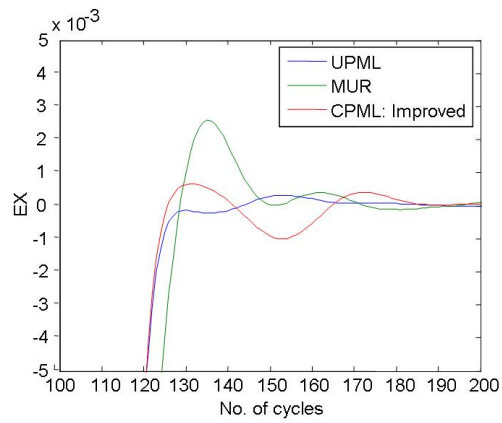
By utilizing two auxiliary variables, and updating them at alternate cycles, the time difference between each variable during the current and previous updating turns is automatically

forced to be Δt . Therefore, no additional space is required to store the values at previous times, and the implementation of (3.23) and (3.25) becomes straightforward. Most importantly, the present updating equations (3.23) and (3.25) obey the midpoint rule.

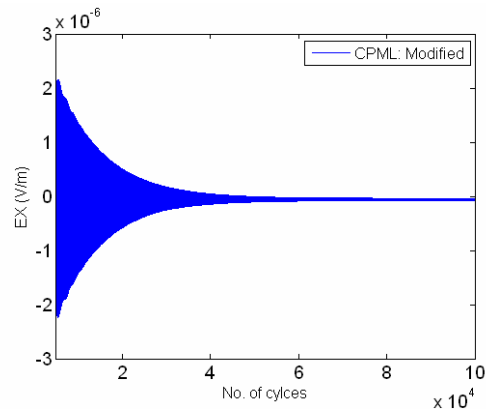
The test example in Sec. 3.2.3 is repeated with the modified CPML implementation in the PBC/FDTD method. Figures 3.15 (a)-(b) plot the time-domain signals E_x for the cases employing three different types of ABCs, namely the modified CPML, the UPML and the Mur's first order boundary condition, for different time intervals. As shown in Fig. 3.15 (a), the fields are almost identical to each other for all three cases during the first 800 cycles. If we take a closer look at around the 130th cycle, when the field tends to reach a steady state (see Fig. 3.15(b)), we find that Mur's first order condition exhibits the worst performance among the three ABCs, while those of the modified CPML and the UPML are comparable to each other. To further test the stability of the modified CPML implementation, the test example for the modified CPML case is run for 10^5 cycles. Figure 3.15 (c) plots the time domain signal from 5000th to 100000th cycles, which converges monotonically, and decreases to a very low level of less than 10^{-8} at the end of the simulation. We conclude, therefore, that the proposed modified CPML implementation is stable.



(a)



(b)



(c)

Fig. 3.15: Transient waveform E_x measured at a point inside the total-field region using the UPML (Blue), the Mur (Green), and our proposed CPML (Red): (a) the first 800 cycles, (b) between cycles 100 and 200, and (c) the transient waveform from the 5000th to 100000th cycles, using the proposed CPML algorithm.

3.5 Calculation of Transmission and Reflection Coefficients Using the PBC/FDTD Solver

Transmission (T) and reflection (R) characteristics of EBG or metamaterial slabs, that are periodic structures, are often of interest. Before presenting the numerical examples of these periodic structures that are being investigated in the following section, we will first outline the formulation of the time-domain near-to-far transformation based on the transformed field, and then illustrate the two ways of using the far-field data to calculate the T and R coefficients.

If we invoke Floquet's theorem for periodic structures, we only need to consider the fields in a unit cell to calculate the far field of a periodic structure. Furthermore, in addition to the fields in the specular directions, higher-order harmonics, also called grating lobes, may contribute to the radiated fields, if they are in the visible range. For a doubly-periodic structure with periodicities D_x and D_y , each Floquet mode can be identified by its mode indices (m_x, m_y) , where m_x and m_y can be any arbitrary integers. The first Floquet mode, with mode indices $(0, 0)$, corresponds to that predicted by Snell's law, while the higher-order Floquet modes, usually much weaker than the first one, typically radiate in other directions. Conventionally, the T and R characteristics refer only to the dominant $(0,0)$ Floquet mode, and higher-order modes do not play a direct role when defining these characteristics. The time-domain far field for the Floquet mode (m_x, m_y) can be computed at time t by using the transformed field on an aperture as shown below:

$$E_{far-field, m_x, m_y}(t) = \frac{1}{A_{unit\ cell}} \sum_{unit\ cell} P(x, y, t) * \exp[j * 2\pi * (\frac{m_x x}{D_x} + \frac{m_y y}{D_y})] * \Delta_x \Delta_y \quad (3.26)$$

where $P(x,y,t)$ is the transformed E-field located at (x,y) on the aperture, Δ_x and Δ_y are the cell-sizes in the x- and y-directions, respectively, and $A_{unit\ cell}$ is the cross-sectional area of the unit

cell. Note that for $m_x = m_y = 0$, the above expression is simply a summation of the area-weighted transformed field over the entire aperture.

Two approaches will be suggested below for the calculation of T and R coefficients by using the far-field data. While the first method can only extract the magnitude and not the phase of these coefficients in a single simulation, the second method can do both by using a two-step process. In both methods, a total-field/scattered-field (TF/SF) formulation is utilized to launch a plane wave illuminating the periodic structure.

3.5.1 One-Step Approach—Extraction of Magnitude of T and R Coefficients

In this approach, the far field is computed by employing (3.26) on two aperture planes as shown in Fig. 3.16—one below the periodic structure (Plane-1) and the other above the TF/SF interface (Plane-2). The former captures the transmitted field and thus can be used for calculating the transmission coefficient. The latter, located in the scattered field region, captures the reflected field and is used to compute the reflection coefficient.

The far field of incident wave in the propagating direction is required for the purpose of normalization, and is derived from:

$$E_{far-field,inc}(t) = \frac{1}{A_{unitcell}} \sum_{unitcell} P_{inc}(x, y, t) * \Delta_x \Delta_y = \frac{1}{A_{unitcell}} \sum_{unitcell} P_{inc}(t) * \Delta_x \Delta_y = P_{inc}(t) \quad (3.27)$$

where $P_{inc}(t)$ is the incidence pulse and is known. The magnitude of T and R coefficients can be computed by the using the FFT as follows:

$$|T| = \left| \frac{FFT[E_{far-field,Plane1}(t)]}{FFT[P_{inc}(t)]} \right| \quad (3.28a)$$

$$|R| = \left| \frac{FFT[E_{far-field,Plane2}(t)]}{FFT[P_{inc}(t)]} \right| \quad (3.28b)$$

where $E_{far-field,Plane1}(t)$ and $E_{far-field,Plane2}(t)$ are the time-domain far fields computed by using the fields on the planes 1 and 2, respectively.

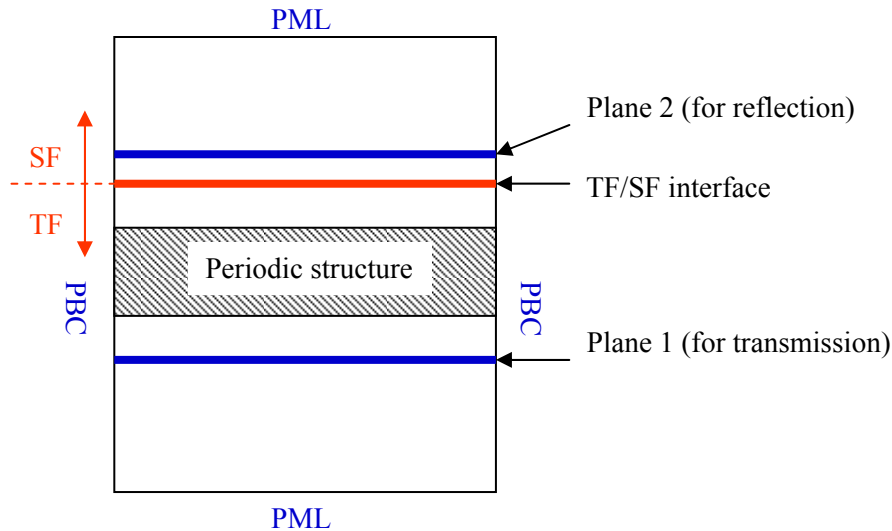


Fig. 3.16: Schematic setting of the TS/SF interface and the measurement planes employed in computing the T/R coefficients using the first approach.

3.5.2 Two-Step Approach—Extraction of Both Magnitude and Phase of T and R Coefficients

When both the magnitude and the phase of T and R coefficients are desired, it is necessary to compute the far fields of the distributions on both planes 1 and 2, as depicted in Fig. 3.17 (a). However, since the plane for the reflection coefficient computation (Plane-2) is located in the total-field region, we must remove the contribution of the incident field to the field distribution on the aperture, in order to isolate the reflected field.

To compute the contribution from the incident field, a second FDTD simulation is run with identical FDTD settings, viz., mesh, time-step size Δt , and source, but with the periodic structure removed (see Fig. 3.17 (b)). The far field on Plane-2 is computed by evaluating the far

field in the time-domain, contributed by the incident field only, on the lit side of the periodic surface. Note that, in this case, the steady state is reached with a much smaller number of FDTD time-steps because there are no multiple reflections. The magnitudes of the T and R coefficients can again be computed by using the FFT as shown below:

$$T = FFT[E_{far-field,Plane1}(t)] / FFT[E_{far-field,Plane1,inc}(t)] \quad (3.29a)$$

$$R = FFT[E_{far-field,Plane2}(t) - E_{far-field,Plane1,inc}(t)] / FFT[E_{far-field,Plane1,inc}(t)] \quad (3.29b)$$

where $E_{far-field,Plane1}(t)$ and $E_{far-field,Plane2}(t)$ are the time-domain far fields computed by using the fields on plane-1 and -2, respectively, first in the presence of the periodic structure, and then with the above structure removed.

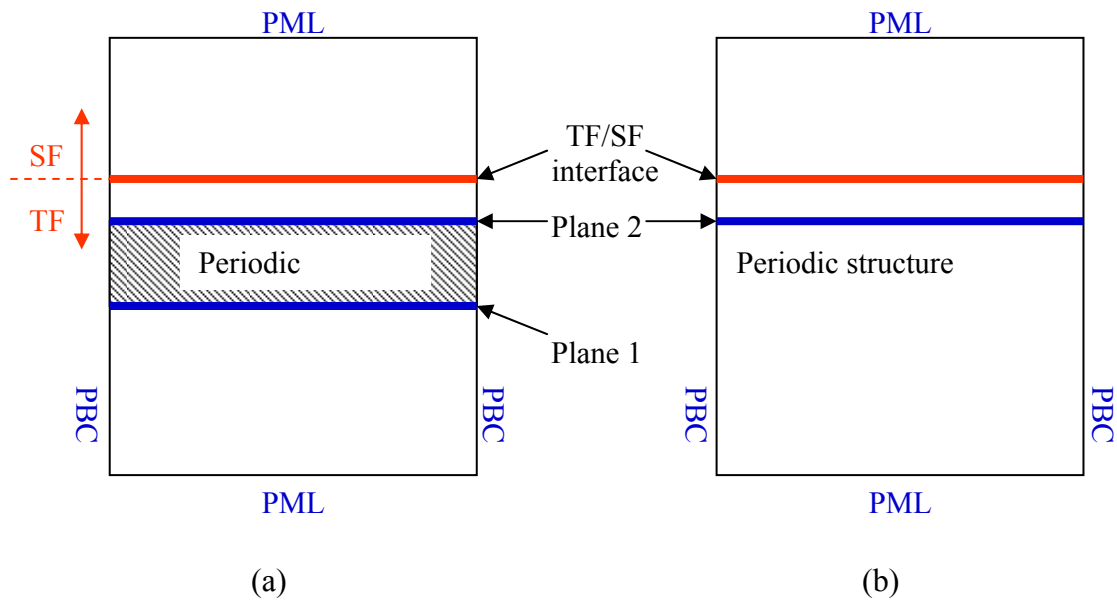


Fig. 3.17: Schematic settings of the TS/SF interface and the measurement planes employed in computing the T/R coefficients using the second approach. Two simulations are required: (a) one with the periodic structure, and (b) one with the structure removed.

3.6 Numerical Examples

In this section, we present four examples involving infinite, singly- or doubly-periodic structures, analyzed by using the parallel PBC/FDTD code with CPML implementation, as described above. They are: (1) singly-periodic lossy screen; (2) EBG array that exhibits double-negative characteristics; (3) double-screen FSS employed in reflector antenna systems for frequency re-use; and, (4) arrays of dielectric and conducting spheres that find applications at terahertz.

3.6.1 Singly-Periodic Lossy Screen

The first example is a free-standing, two-dimensional screen, comprising of infinitely long, parallel, and equally-spaced conducting bars, as depicted in Fig. 3.18. The bars are aligned along the y -direction, normal to the plane of incidence; thus, both the geometry and the fields are uniform along the y -direction. By keeping only a single FDTD cell along the y -direction, we can dramatically reduce the computational resources required for the present problem to nearly those required for a 2-D problem, without the need to modify the existing FDTD code designed to solve 3-D problems.

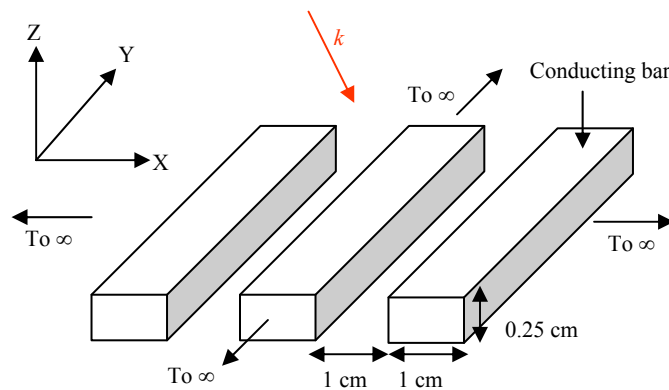
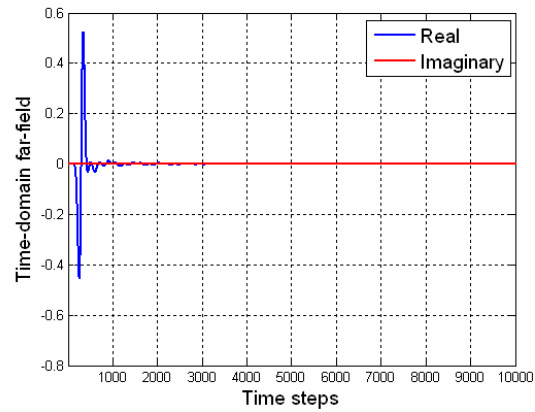


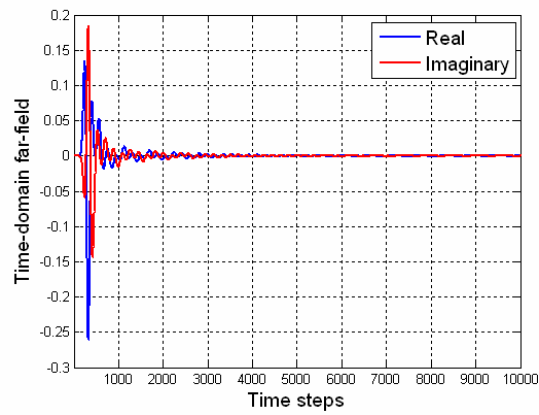
Fig. 3.18: Geometry of a free-standing, two-dimensional screen, comprising of infinitely long, parallel, and equally-spaced conducting bars.

The details of the geometry and FDTD settings are as follows. Each bar has a width of 1 cm and thickness of 0.25 cm, and the spacing between them is 1 cm. Its conductivity is chosen to be $6.3492 \Omega^{-1}\text{m}^{-1}$ such that its sheet resistance is equal to $63 \Omega/\text{square}$. An Ey-polarized plane wave is excited at five cells above the top surface of screen by using the TF/SF formulation, to illuminate the screen at angle of 30° from the positive z-direction. Since we are interested in the frequency range of 0.05 to 30 GHz, we excite the geometry with a modulated Gaussian signal whose modulation and 3-dB frequencies are both 15 GHz. A uniform FDTD mesh of cell-size 0.03125 cm, which is equal to $\lambda_0/32$ (λ_0 is the free space wavelength) at the highest frequency of interest, is employed throughout to discretize the computational domain in all three directions. The computational domain has a dimension of $64\Delta \times 1\Delta \times 58\Delta$, and is terminated by the PBC in the x- and y-directions and the PMLs in the z-direction. For good absorption of the outgoing waves, the two PML-regions are kept 25 FDTD cells away from either side of the screen surface. Since only the magnitude of transmission coefficient is desired, the planes for measuring T and R are set in the same manner as that described in Sec. 3.5.1.

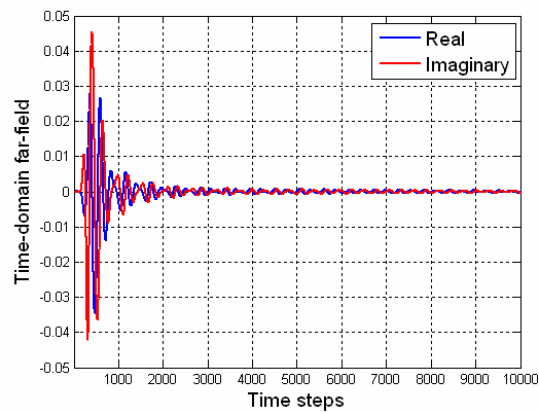
The FDTD simulation has been carried out on a Pentium IV computer, equipped with a 2.0 GHz CPU and 2 GB physical memory, for 10,000 cycles. The total CPU time consumed, including both field updating process and far-field calculation, is approximately one minute. Figures 3.19 (a)–(c) show the time-domain far field for the first few transmitting Floquet modes, which have reached the steady state before the simulation ends. The magnitude of the transmission coefficient is then computed by using (3.28a), and plotted in Fig. 3.20 together with that derived from the MoM/mode-matching method [21]. As we see from the above figure, the agreement between the two results is excellent.



(a)



(b)



(c)

Fig. 3.19: Time-domain far-field (Blue: Real, Red: Imaginary) for the first three transmitting Floquet modes (a-c) of the lossy screen shown in Fig. 3.18.

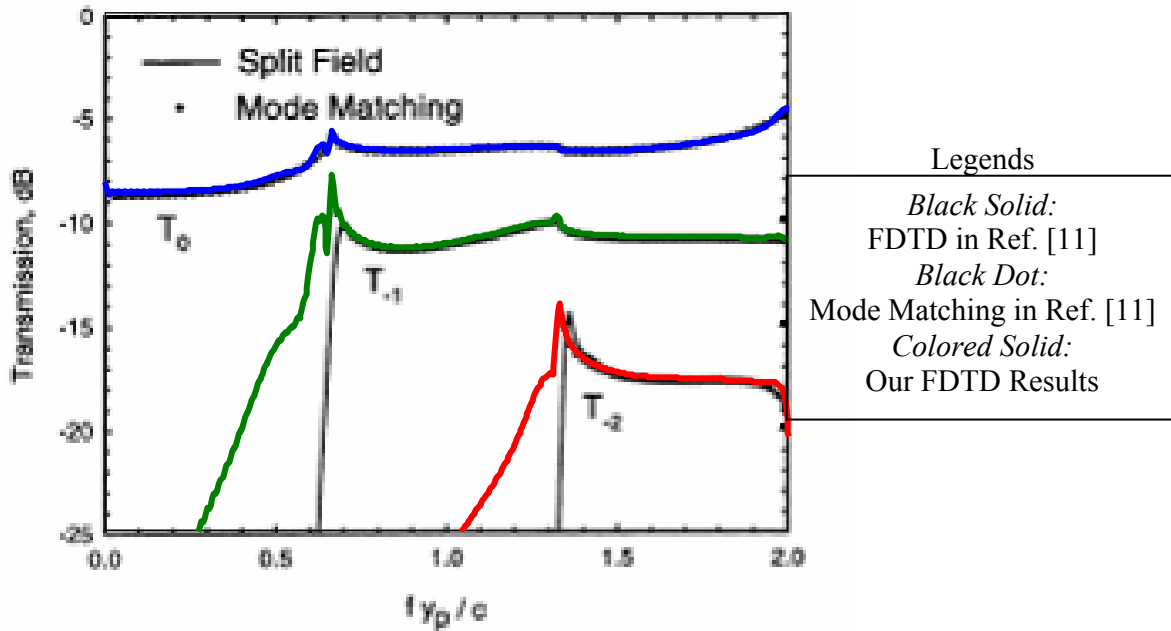


Fig. 3.20: Magnitude of transmission coefficient for the first three Floquet modes of the lossy screen shown in Fig. 3.18. Our results are displayed in colors and the results from [21] are displayed in black.

3.6.2 Metamaterial Slab that Exhibits Double-Negative Behavior

Double-negative (DNG) metamaterials are artificially engineered to have both negative effective permittivity and permeability at certain frequencies. In 2001, Smith et al. [48] utilized Pendry's ideas [58-59] to design a device that experimentally demonstrated the realization of the first DNG metamaterial composed of split-ring resonators (SSRs) and thin wires. Since then, because of the various interesting phenomena and potential applications suggested, research on DNG metamaterials has become a popular topic of interest to many research groups around the world.

The DNG structure in this investigation is an infinite, doubly-periodic array comprising of a combination of SSRs and thin wires, which may be either a single- or multi-layer

configuration, embedded in a dielectric slab. In this study, the dielectric is simply free space. The SRR and the wire are both made of perfect conductors, and their geometries are shown in Fig. 3.21. The SRR is a square ring, 3 mm on the side and 0.25 mm in width, with a 0.5 mm wide gap in the center of its side arm. The thin wire, located 0.25 mm away from the SRR, has a width of 0.5 mm, and the wires on the same row of the array are connected together to form a long, infinite wire. The array has a periodicity of 2.25 mm and 5 mm along the x- and y-directions, respectively. For the multi-layer case, the inclusions in two adjacent layers are separated by 4 mm from each other. In this investigation, the arrays of up to six-layer are studied. The PBC/FDTD code is utilized to obtain the T and R characteristics at normal incidence, from which the effective constitutive parameters can be extracted using an inversion approach [33]. In this chapter, we will only discuss the FDTD simulation to obtain the T and R characteristics, and defer the process for deriving the effective constitutive parameters until Chapter 5, where we present a comprehensive study of this DNG structure array.

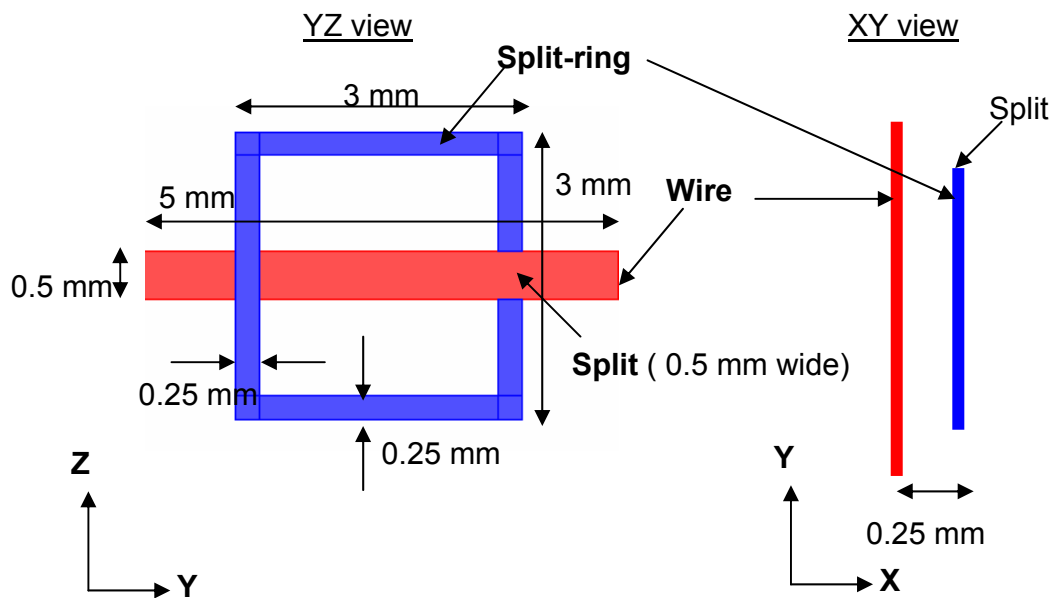


Fig. 3.21: The unit structure comprising of a split-ring and a wire.

It is important to recognize that we need both the magnitude and phase of the T and R coefficients to extract the effective constitutive parameters, and this leads us to use the two-step approach outlined in Sec. 3.5.2. We also point out that there is no well-defined reference plane for either T or R in this structure, because the inclusions are not planar. We have chosen to define these reference planes, somewhat arbitrarily, by using a separation distance of 4 mm for multi-layer case, so that planes are defined to be located 2 mm away from the centre of the outermost layer on each side of the slab.

Figures 3.22 (a) and (b) show the unit cells for the single- and six-layer case, respectively. Because we are dealing with a fine structure, we need to use a small cell-size of $\Delta = 0.125$ mm, which corresponds to $\lambda/120$ at the highest frequency of interest (20 GHz), and we adopt a uniform mesh throughout the computational domain. For the single- and six-layer case cell distributions are as follows: $18 \Delta \times 40 \Delta \times 84 \Delta$ and $18 \Delta \times 40 \Delta \times 225 \Delta$, respectively. A normal incident, Ey-polarized plane wave is to excite the array.

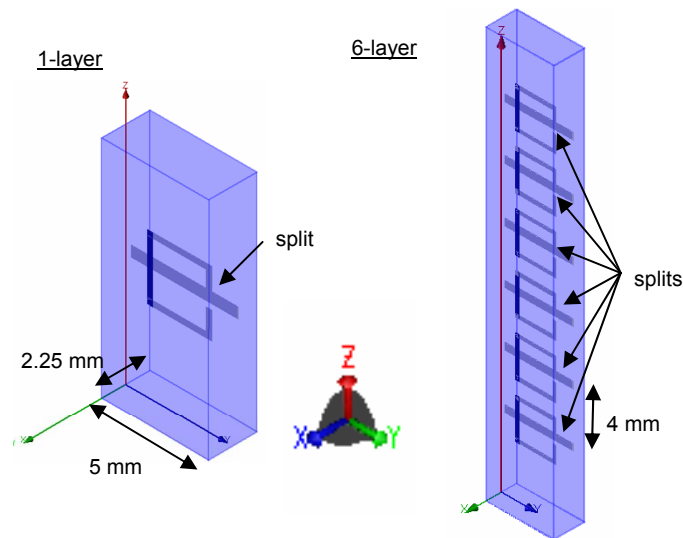
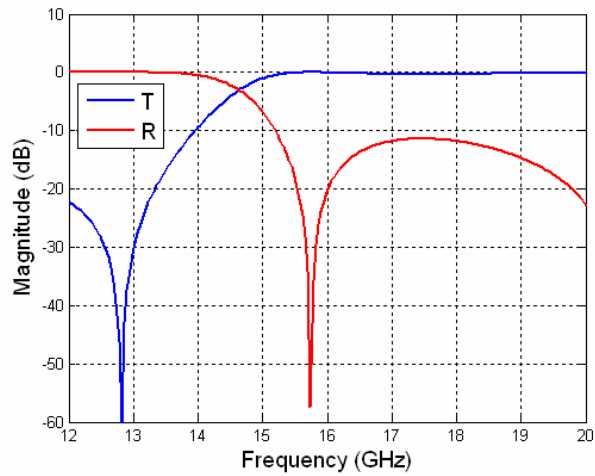
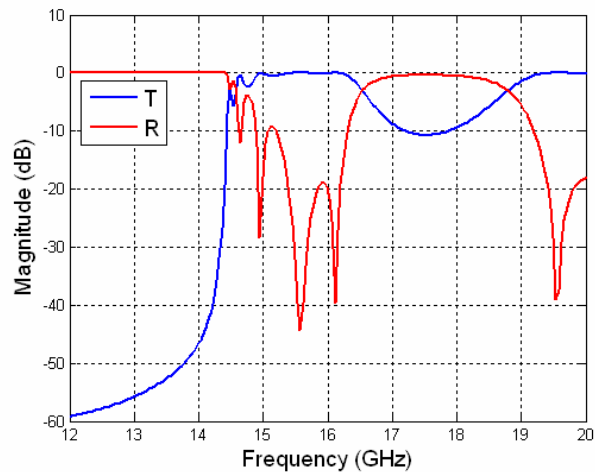


Fig. 3.22: Unit cells for the 1- and 6-layer slab. Note that the array is doubly-periodic along the x- and y-directions.

The simulation has been run for 100,000 cycles for the single- and six-layer cases. The magnitude of the T and R coefficients for both cases are plotted in Figs. 3.23 (a)-(b), respectively. In Chapter 5, we will revisit and validate these results by comparing them with those computed by using the conventional FDTD method for the same periodic array, but with a finite size.



(a)



(b)

Fig. 3.23: Magnitude of transmission (Blue) and reflection (Red) coefficients of the EBG array: (a) 1-layer, and (b) 6-layer.

3.6.3 Double-Screen FSS Used in Reflector Antenna System

The FSS can be used as a subreflector in a dual-band reflector antenna system, where it acts as filter that is transparent at one frequency band and opaque at the other. In this application, two feed horns operating at different frequencies are optimized independently, and then placed at the real and virtual foci of the subreflector, respectively. We can achieve a dual-frequency operation using a single main reflector, and thus reduce the cost of the antenna system significantly.

Figure 3.24 shows the configuration of the dual-feed offset Cassegrain system of our interest, in which the FSS is designed to have total transmission at 19 GHz and total reflection at 45 GHz. The infinite FSS is simulated by using two different numerical techniques, the PBC/FDTD solver and an MoM solver. The latter employs the FFT technique to accelerate the simulation process, though it is limited to planar-type FSS structures only.

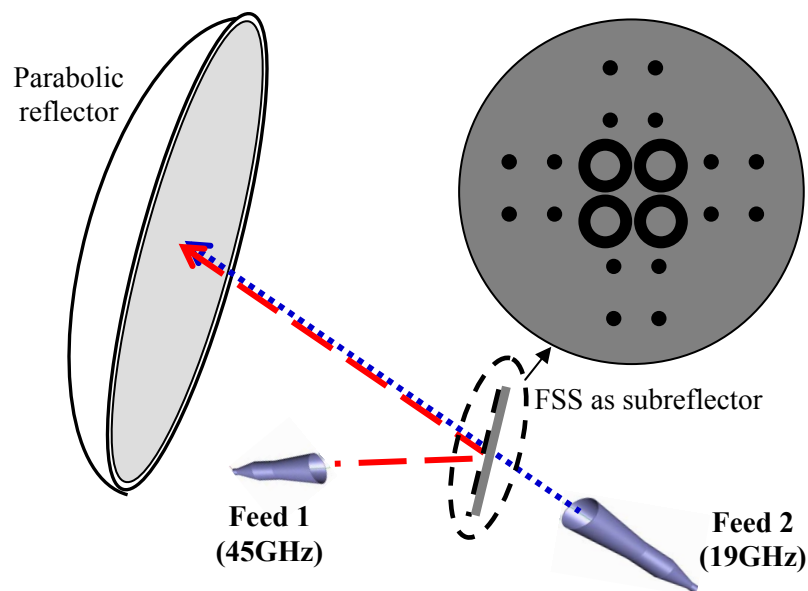


Fig. 3.24: Configuration of the dual-feed offset Cassegrain system, with FSS used as sub-reflector.

Figure 3.25 shows the geometry of the FSS unit cell designed for the frequency re-use operation. Its dimensions are $0.25 \text{ cm} \times 0.25 \text{ cm} \times 0.3174 \text{ cm}$. Each unit cell structure consists of two identical ring-type thin metallic screens which are 0.2946 cm apart and embedded within seven dielectric layers with dielectric constants ranging from 1.06 to 3.03. In general, the ring-type FSS behaves as a band-stop filter. In this design, the ring has a mean circumference of 0.004 m , and is sandwiched between two dielectric layers with average dielectric constant of 2.95. The first resonance is estimated to occur at 44 GHz , at which the mean circumference is equal to one effective wavelength. A double-screen design is used to further enhance its T and R characteristic at 19 and 45 GHz .

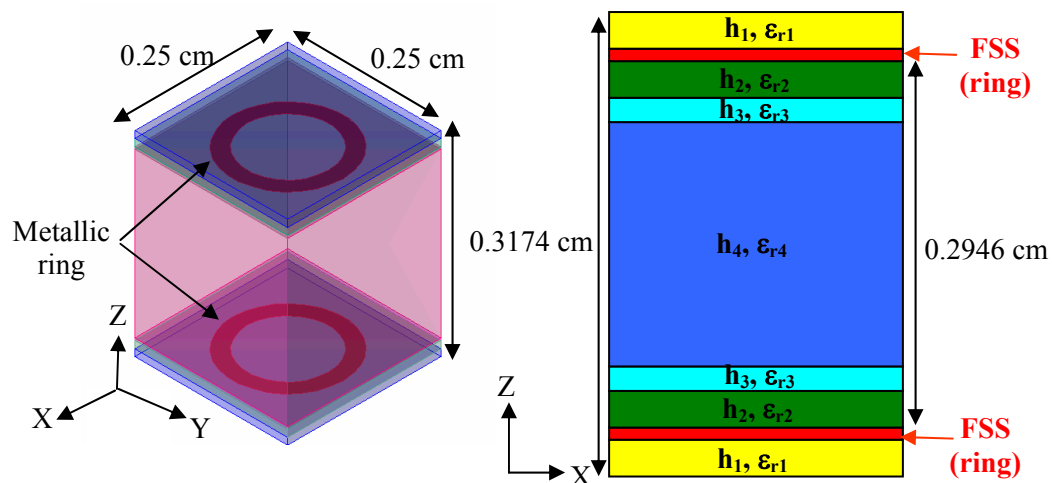


Fig. 3.25: Geometry of the FSS unit cell used in the sub-reflector shown in Fig. 3.24.

The mesh distribution adopted is shown in Figs. 3.26 (a)–(b). On the x - y plane, a 64×64 uniform mesh is utilized to accurately model the curvature of the rings. Along the z -direction, a nonuniform mesh is adopted such that the cell-size is finer near the interface between the two

dielectric layers. In order to obtain an accurate result, we limit the ratio of the cell-sizes between adjacent cells to less than 1.08. The smallest cell-size is determined by the thickness of the thinnest dielectric layer: Two cells are accommodated within the thinnest dielectric layer; hence, the smallest cell-size Δ_z is 0.0019 cm. Under these constraints, the largest cell is found to be 0.011185 cm, which corresponds to $\lambda/52$ at the highest frequency of interest.

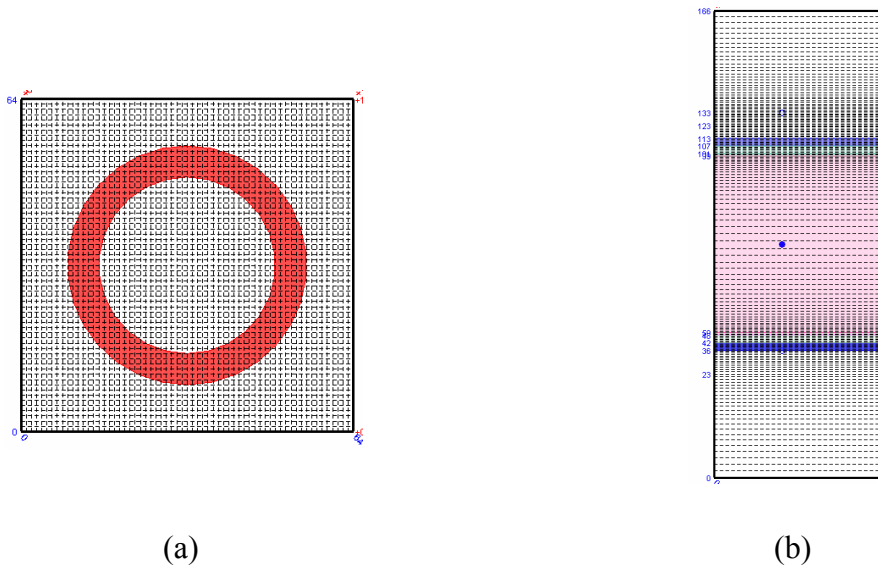


Fig. 3.26: Illustration of the FDTD mesh used: (a) the x-y plane, and (b) the x-z plane (only mesh in z-direction is shown).

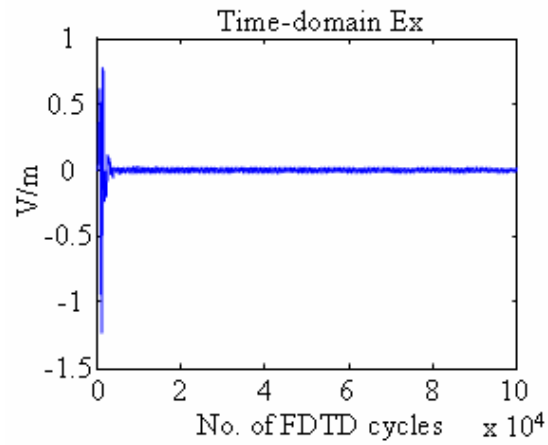
An Ex-polarized plane wave is excited to illuminate the structure at normal incidence from the positive z-direction. The excitation used is a modulated Gaussian pulse with both the modulation and 3-dB frequencies pegged at 25 GHz. The planes for T and R measurements are chosen in the same manner as that described in Sec. 3.5.1 since only the magnitude of T and R is desired. For multi-screen FSS, it usually takes a long time for the fields to die out; therefore, the total number of FDTD cycles run is set to be 100,000. In order to significantly reduce the

simulation time, a total number of 15 CPUs are involved in parallel processing, and the computational domain is divided into three and five sub-regions in the x- and z- directions, respectively. Note that the memory requirements for this problem size can be satisfied even though we use a single processor, equipped with a 2 GB memory.

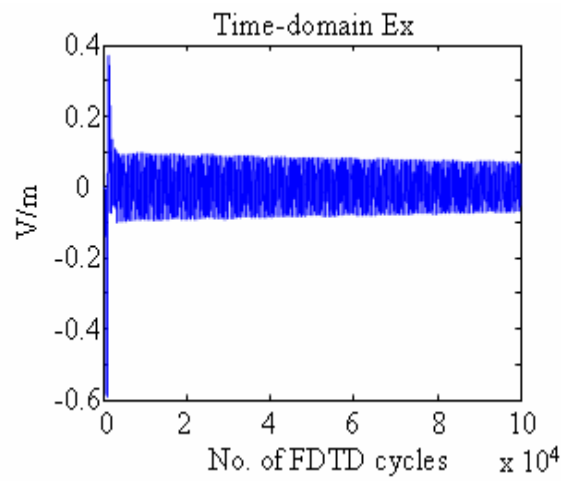
The FDTD simulation has been run on a computer platform named GEMS box, and the simulation takes 25 minutes to complete. The project is also simulated via the use of an MoM solver. The same discretization of 64×64 is adopted in the x-y plane, and the solution is computed for frequencies ranging from 1 to 50 GHz, with a step size of 1 GHz. The serial MoM code has been run on a Pentium IV computer equipped with a 2.0 GHz CPU and 2 GB physical memory, and the simulation takes 53 minutes to complete.

Figures 3.27 (a)-(c) show the time-domain signature of E_x at three different locations, viz., above the TF/SF interface; inside the FSS composite; and below the FSS. At all these positions, the fields are found to decay very slowly once we go past the first few thousand cycles. Figure 3.28 shows a closer look of these time signals for the last 10,000 cycle. As may be seen, the slowly decaying field oscillates essentially monochromatically at 52 GHz, which is the first resonance of the FSS composite.

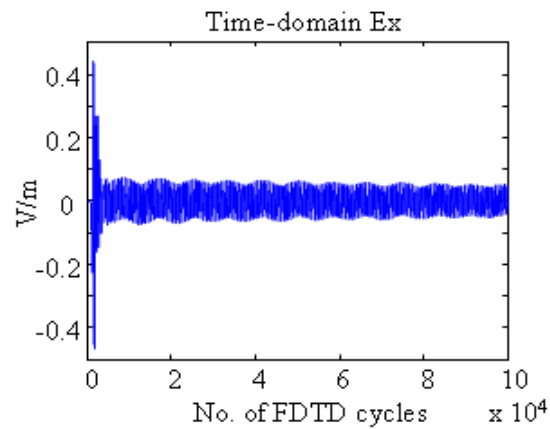
Figures 3.29 (a)-(b) plot the FDTD time-domain far fields in the transmission and reflection directions, respectively. We note that, in contrast to the near-field, the far field has already reached its steady state. Figure 3.30 plots the magnitude of the T and R coefficients from 1 to 50 GHz computed from the FDTD and FSS solvers. Excellent agreement can be observed over a wide frequency range covering up to 50 GHz. The simulation confirms that this FSS meets the design goal that nearly full transmission (FDTD: - 0.005 dB, MoM: -0.003 dB) and reflection (FDTD: - 0.03 dB, MoM: -0.05 dB) are obtained at 19 and 45 GHz, respectively.



(a)



(b)



(c)

Fig. 3.27: Transient waveform E_x at three different locations: (a) above the TF/SF interface; (b) inside the FSS composite; and (c) below the FSS.

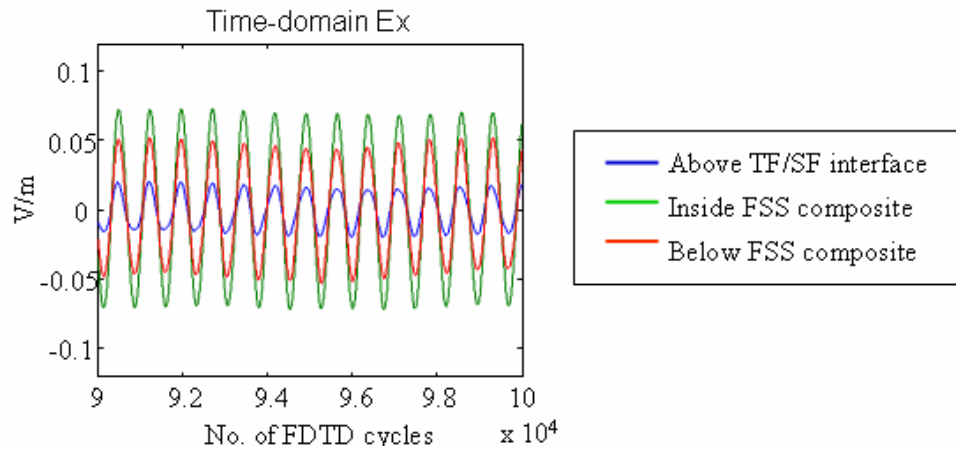
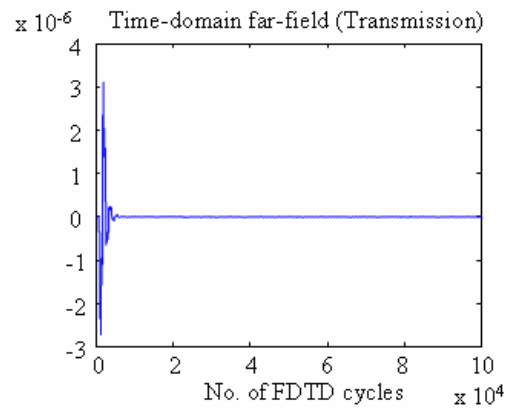
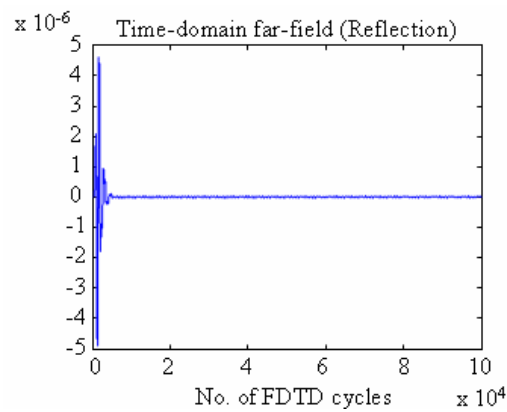


Fig. 3.28: A closer look at the last 10,000 cycle of the time-domain signals in Fig. 3.27.



(a)



(b)

Fig. 3.29: Transient far-field in the (a) transmission and (b) reflection direction.

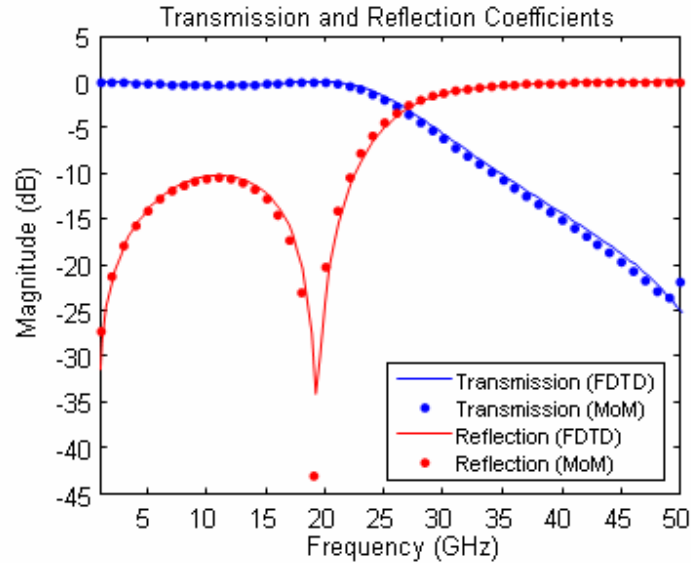


Fig. 3.30: Comparison of the magnitudes of the T and R coefficients obtained by the FDTD and a periodic MoM solver.

3.6.4 Study of Terahertz Transmission for Periodic Arrays of Dielectric and Conducting Spheres

The last example is concerned with a study of scattering characteristics for periodic arrays with terahertz applications [60] by using our PBC/FDTD code. Both FDTD simulations and experiments were conducted by the research group at Materials Research Institute of the Penn State University [61].

The goal of this work is to study the terahertz transmission through periodic arrays of dielectric and conducting spheres partially embedded in PTFE substrate ($\epsilon_r \sim 2$). Each sphere has a diameter of 2 mm, and is made up of either silicon nitrate Si_3N_4 ($\epsilon_r \sim 8.9$) or brass. The spheres are arranged in a square grid with periodicity varying from 2 mm to 4 mm. In the experiment, a large periodic array of spheres were illuminated by a Gaussian light beam with

spot-size of 25 mm as shown in Fig. 3.31, and the S-parameters were measured by utilizing Terahertz Time-Domain Spectroscopy.

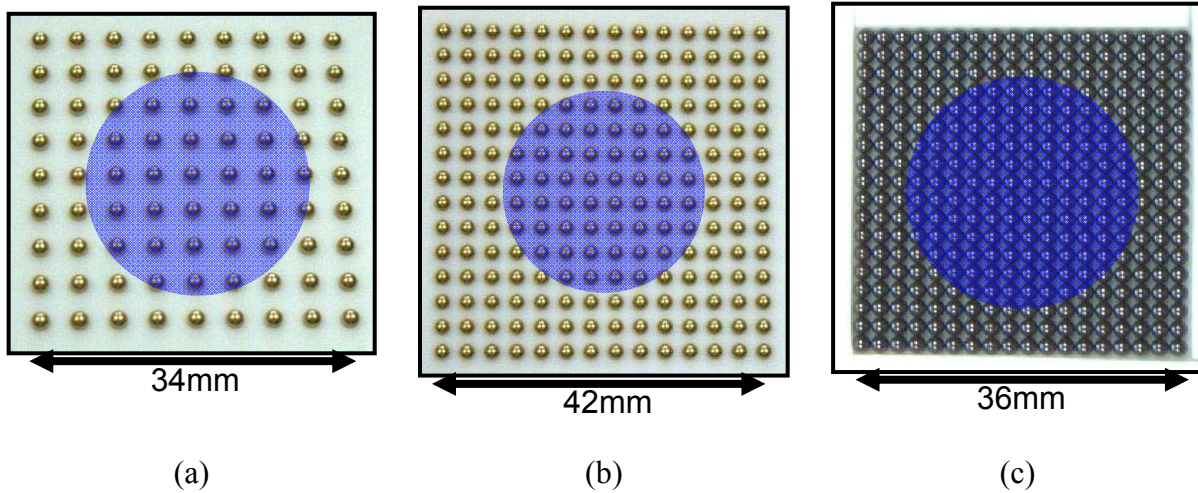


Fig. 3.31: An array of spheres under the illumination of a Gaussian beam. The periodicity for the spheres is (a) 2 mm, (b) 3 mm, (c) 4 mm, respectively. The Gaussian beam has a beam-width of 25 mm (shown by blue circle) in all cases.

Figures 3.32 and 3.33 show the transmission coefficient magnitude from 50 to 200 GHz, obtained from FDTD calculation and experiment, for Si_3N_4 and brass spheres, respectively. As can be seen from the figures, the agreement between these two methods is better for Si_3N_4 spheres than that for Brass, and the agreement gets better as the separation distance between spheres becomes larger. The electric field distribution over the transverse cross-section of Si_3N_4 sphere can also be computed by the FDTD at each resonant frequency, as shown in Fig. 3.34.

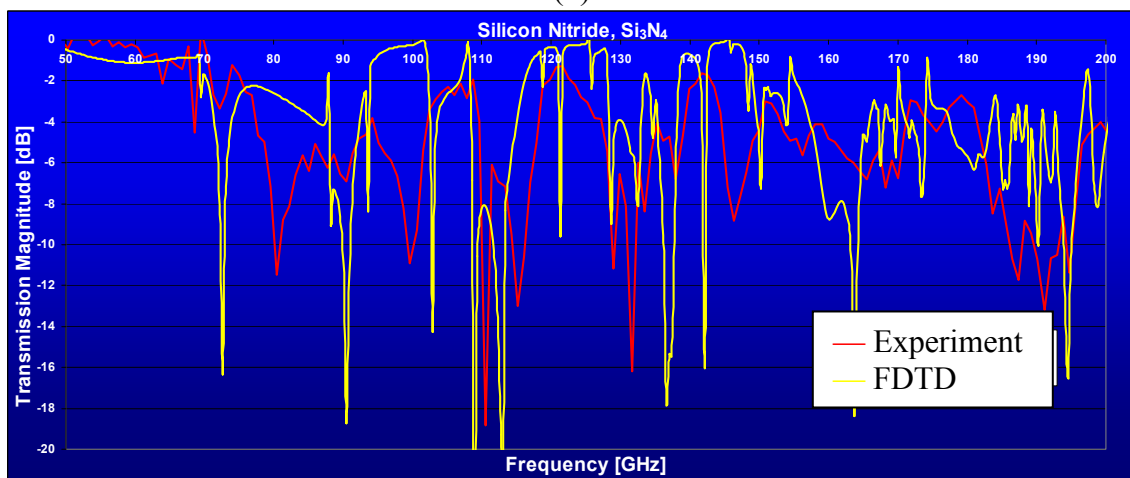
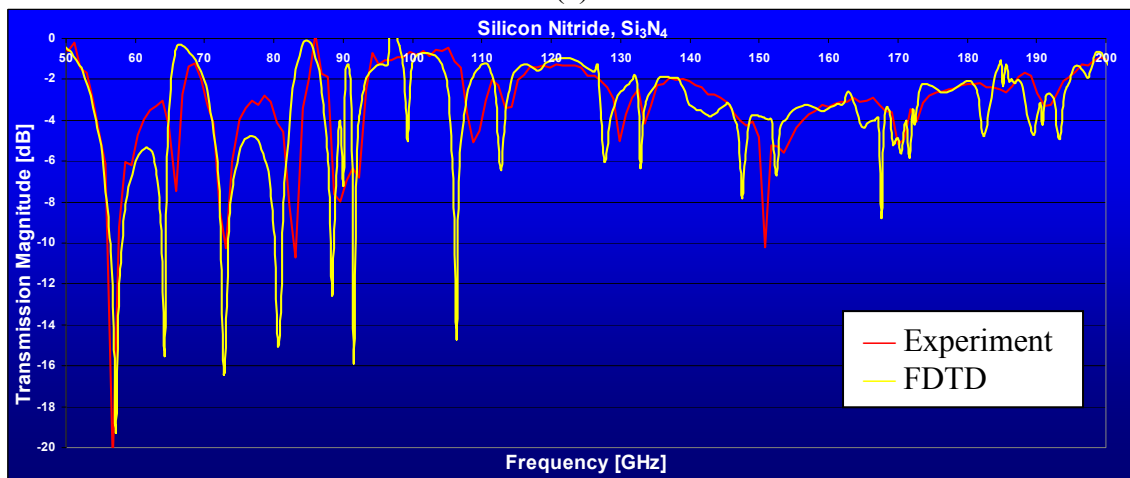
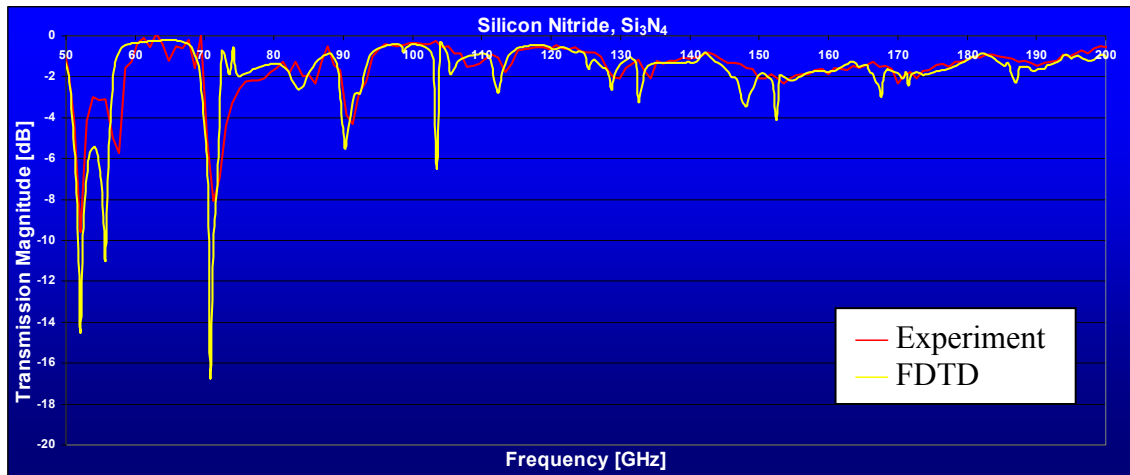
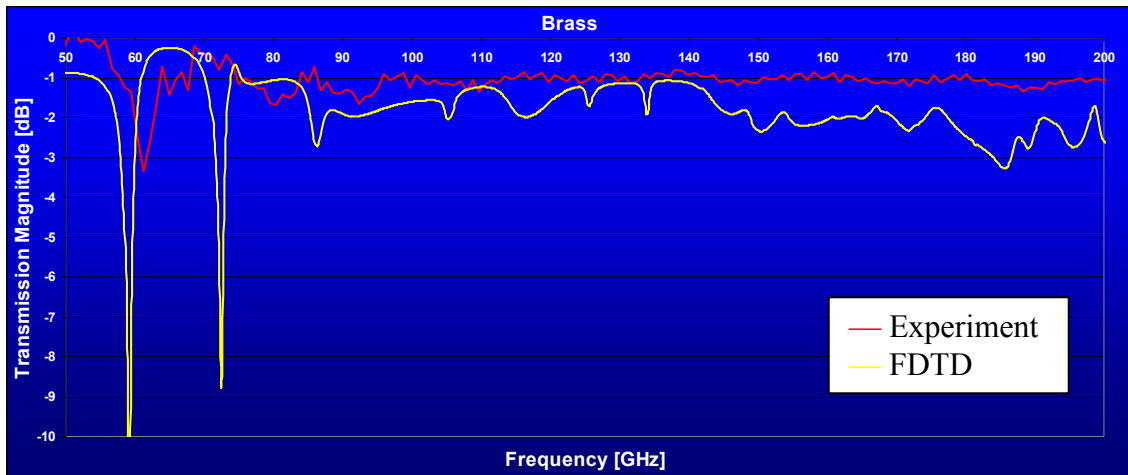
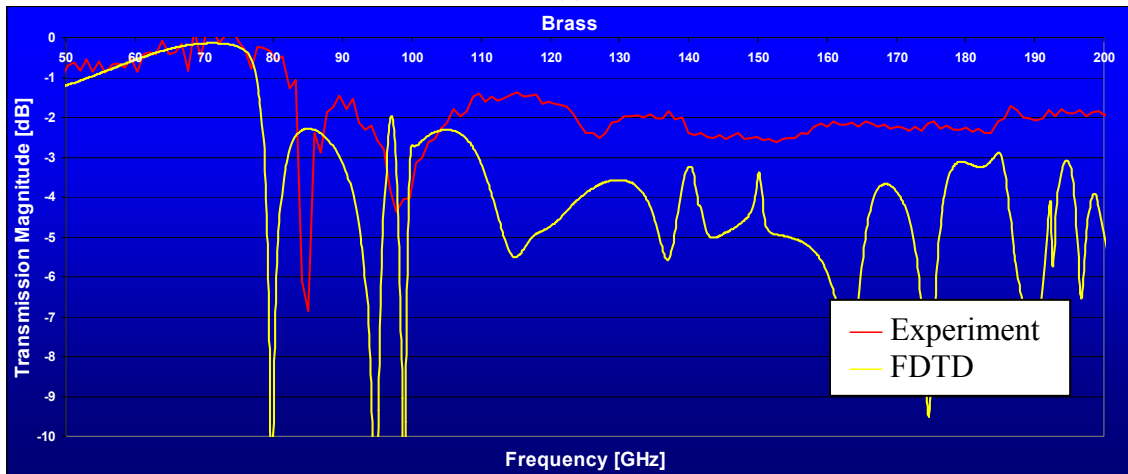


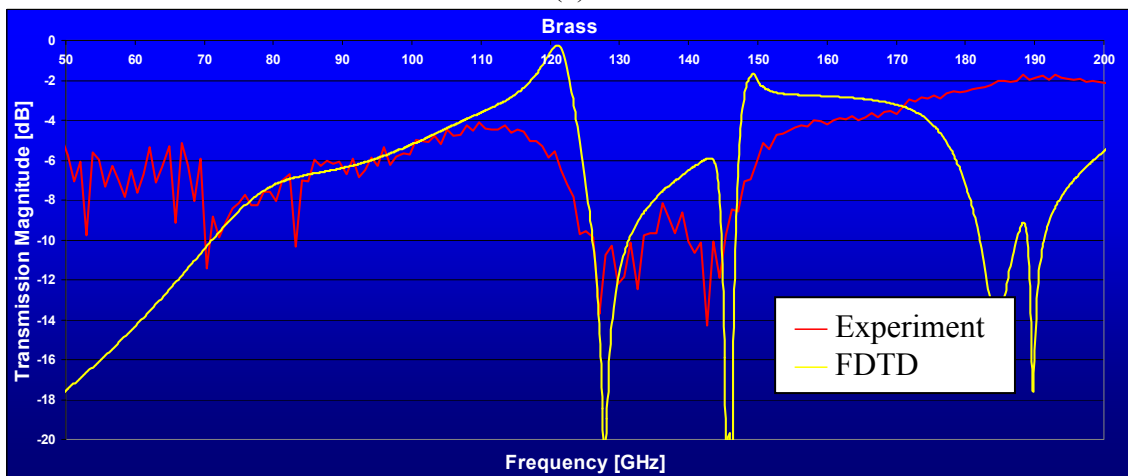
Fig. 3.32: Magnitude of transmission coefficient obtained from FDTD calculation (yellow) and experiment for the Si_3N_4 spheres with periodicities of (a) 2mm, (b) 3mm, and (c) 4 mm, from 50 to 200 GHz.



(a)

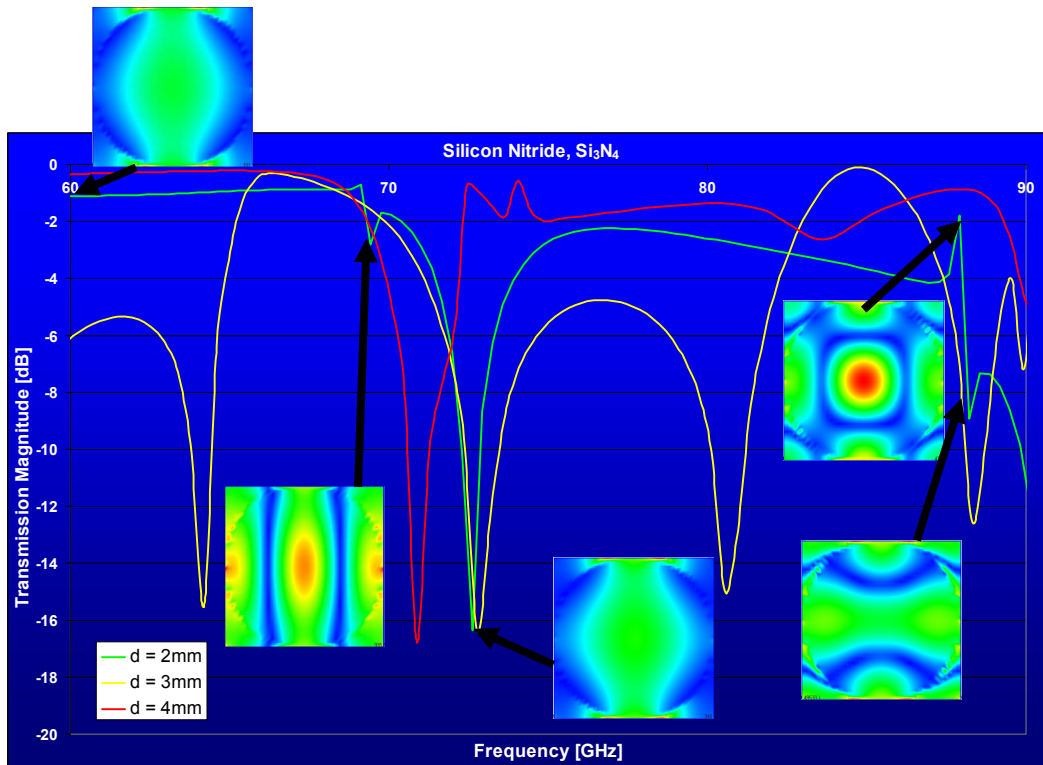


(b)

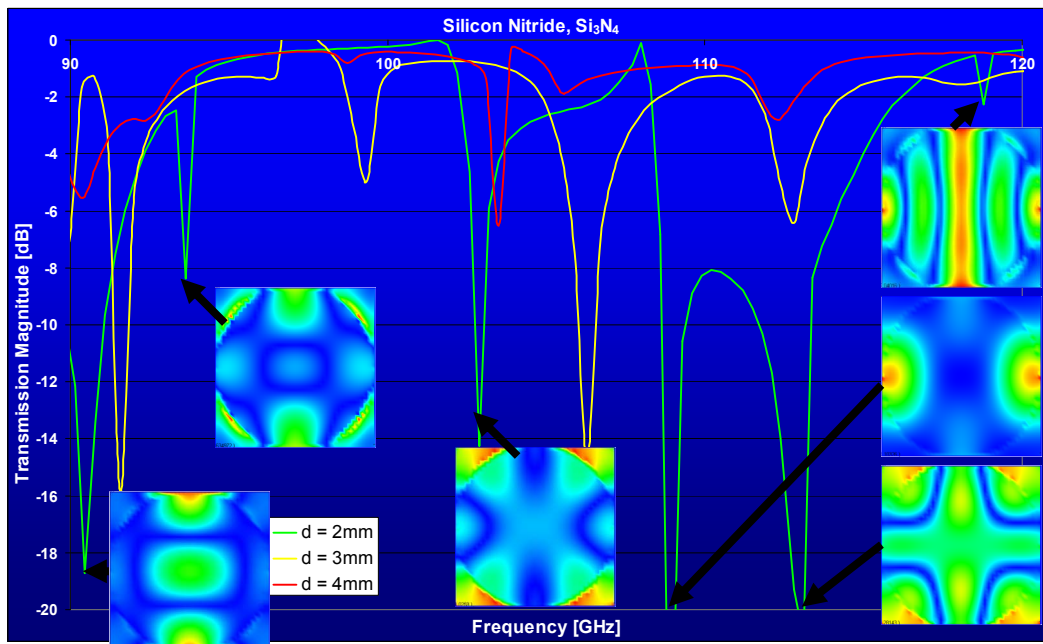


(c)

Fig. 3.33: Magnitude of transmission coefficient obtained from FDTD calculation (yellow) and experiment (red) for the brass spheres with periodicities of (a) 2mm, (b) 3mm, and (c) 4 mm, from 50 to 200 GHz.



(a)



(b)

Fig. 3.34: The electric field distribution over the transverse cross-section of Si_3N_4 sphere (periodicity = 2 mm) at each resonant frequency, ranging from (a) 60 – 90 GHz, and (b) 90 – 120 GHz.

3.7 Conclusions

In this chapter, we have proposed the parallel implementation of the split-field based PBC/FDTD solver, which can significantly reduce the total simulation time when multiple processors are used. The parallel technique utilizes the domain decomposition approach as discussed in Chapter 2. By extending one FDTD cell outwards at the periodic boundaries, the process of applying the PBC and that of the parallel field-exchange can be combined into a single step. It has been demonstrated that the efficiency of the parallel PBC/FDTD code is nearly as high as that of the parallel 3-D FDTD code.

In addition, we have identified an instability issue that occurs when we combine the most recently developed CPML with the split-field PBC/FDTD method in the same way as what has been successfully done for the standard FDTD method. The origin of this instability was traced to the employment of the forward-differencing scheme in the update equations. A stable, still simple implementation of CPML on the PBC-FDTD algorithm has been proposed to correct the situation. In this implementation, two auxiliary variables (instead of one) are utilized and updated in alternate cycles, and the update equations now process a center-differencing format.

The present PBC-FDTD solver works only for a non-dispersive medium, and can be generalized to work for dispersive medium for wider applications.

Chapter 4

IMPLEMENTATION OF TRANSPARENT SOURCE IN THE SCATTERING PROBLEM INVOLVING LARGE INFINITE STRUCTURES

4.1 Introduction

Introducing a plane wave source in the FDTD scattering problem involving infinite structures is always challenging. The conventional total-field/scattered-field (TF/SF) technique [21,32,62], which is typically used to launch a plane wave in the scattering problem, divides the computational domain into two regions, namely the total-field (TF) and the scattered-field (SF) regions, as shown in Fig. 4.1. The incident field is computed prior to the main FDTD simulation, and then inserted into the FDTD grid on the TF/SF boundary, which is located in free space. In this formulation, the scatterer has to be confined within the TF/SF boundary. Consequently, this technique is not suitable for a problem involving a scatterer of infinite extent, since the scatterer is usually terminated inside the PML to model it.

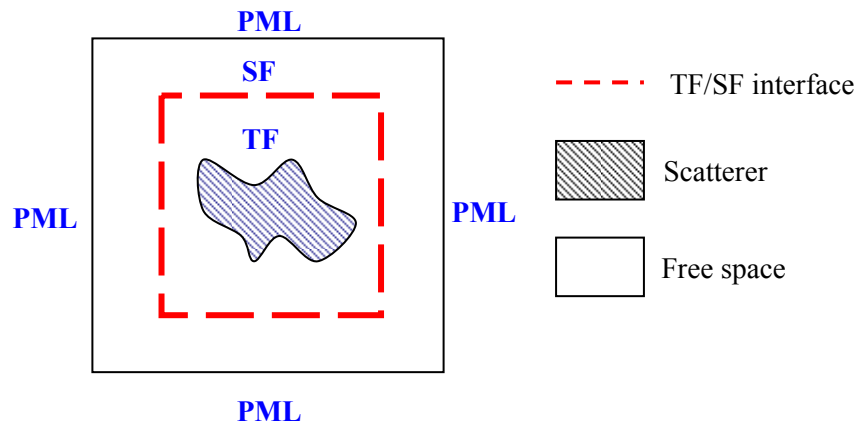


Fig. 4.1: Total-field/scattered field zoning of the FDTD space lattice in the conventional TF/SF approach. Note that the PML region is not drawn in the figure.

Several attempts have been made to overcome the limitation alluded to above. For instance, the concept of TF/SF has been extended from free-space to stratified media [63], to study the problem of scattering by a buried object, as shown in Fig. 4.2. The “incident field” employed in the TF/SF formulation is redefined to be the total field in the presence of the stratified media under a plane wave illumination, and is computed by using an analytical expression. However, this approach only works in special cases, where a closed-form solution of the “incident field” can be derived in the presence of the background medium.

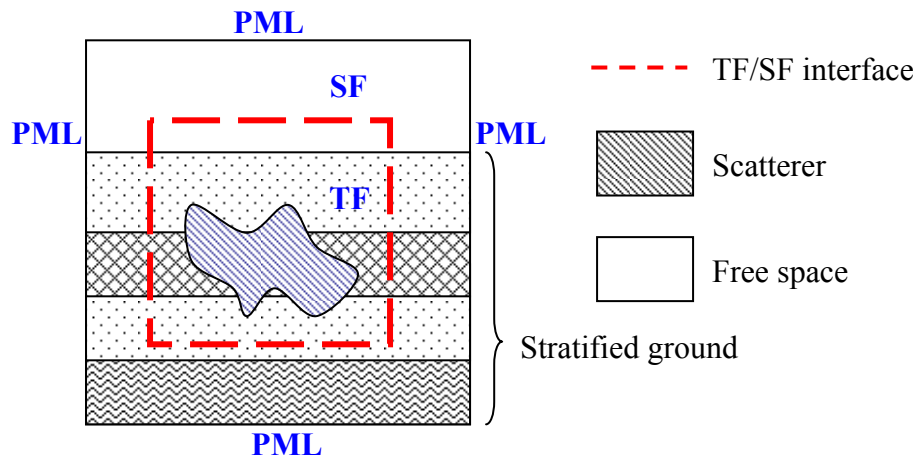


Fig. 4.2: Total-field/scattered field zoning of the FDTD space lattice in the modified TF/SF approach, which is extended to stratified media to solve the problem of scattering from a buried-object. Note that the PML region is not drawn in the figure.

Another promising approach is to allow the TF/SF boundary partially embedded within the PML [64,65]. As depicted in Fig. 4.3, the infinite scatterer is terminated halfway within the PML, such that it can be confined by the TF/SF boundary, which is partly embedded inside the PML region. It has been demonstrated in [64,65] that usually a larger number of PML layers, say up to 16, is required to accommodate both the scatterer and the TF/SF boundary. The “incident field” on the part of the TF/SF interface within the PML is different from that within the free

space, and it depends on a number of factors, including the incident angle and polarization; FDTD cell-size; and the type of PML and its parameters. In addition, compared to the fields propagating in free space, these “incident fields” become weaker within the PML-wave-terminating boundary, and stronger within the PML-wave-sourcing boundary. Therefore, a number of preliminary FDTD runs are required to calibrate the performance of each PML region and compute these “incident fields” on each TF/SF segments within the PML. In each preliminary run, a plane wave is launched near the desired PML region by using a long segment of TF/SF interface, and the fields inside the PML region are recorded and used to evaluate the level of the “incident fields” on the TF/SF segments within the PML region. Although it has been demonstrated that this approach can launch a nearly perfect plane wave propagating at oblique angles relative to the PML boundary, the calibration process is rather involved, since the setting of each preliminary run depends on the incident direction and the relative location of the TF/SF interface within the PML regions. In addition, when the incident direction is nearly parallel to any face of the TF/SF boundary located inside the PML region, the calibration of “incident fields” on this face becomes impossible because of the difficulty in launching a plane wave at the desired angle in a preliminary run.

All the modified TF/SF techniques, mentioned above, only apply to launching a uniform plane wave in the total field region. However, nothing forbids the use of the TF/SF technique in exciting other forms of incident field distributions. For instance, the Gaussian beam is also a commonly-used source when the scattering effect on a localized region of the structure is desired, for example in a rough-surface-scattering problem.

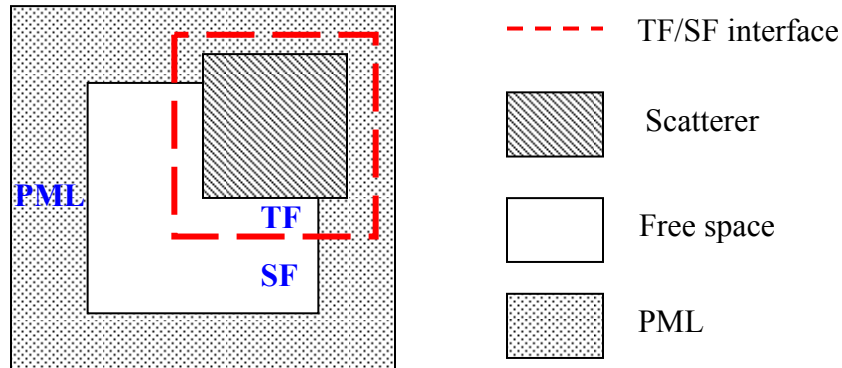


Fig. 4.3: Total-field/scattered field zoning of the FDTD space lattice in the generalized-TF/SF approach, where the TF/SF interface is allowed to be partially embedded with the PML region.

In this chapter, we propose a simple and efficient excitation scheme, which based on a modification of the conventional TF/SF approach, and is designed to launch the desired incident field distribution in scattering problems [66]. Instead of using a closed TF/SF box in the conventional TF/SF approach, we apply the TF/SF technique only on a single plane, which divides the domain into two half-spaces, namely the total-field and the scattered-field region. The scatterer can therefore be either one of finite size or of infinite extent, since it can now be terminated inside the PML, if necessary. On the other hand, we apply a window function to the “incident field” excited on the TF/SF interface in order to generate the desired incident field distribution, which can be something other than a uniform plane wave.

It should be noted that this excitation scheme is not perfect, because reflections may occur if the incident field distribution near the edge of the TF/SF interface is not negligible, as in the case of a plane wave illumination. However, we have found that the reflection can be considerably reduced by extending the TF/SF interface into the PML. This reflection is barely present at normal incidence, and is acceptably small for small angles of incidence.

In the following, we begin by presenting the implementation of the proposed excitation scheme based on the TF/SF technique. Next, we perform a parametric study to evaluate the performance of this scheme while launching a Gaussian beam type of wave, and follow this with some numerical examples. Following this, we evaluate the performance of this scheme in launching a plane wave source at different incident angles and polarizations, and set up a guideline for using this source to get accurate results. Numerical example for plane wave illumination will follow.

4.2 Implementation of the Proposed Excitation Scheme

The main idea of the TF/SF technique is to divide the computational domain into two regions, namely the total- and the scattered-field regions. In most situations, the inner region is the total-field region, which is required to enclose all the objects, while the outer region is free space, which is usually terminated by PML (see Fig. 4.1). The fields inside these two regions (except for those near the TF/SF interface) can be computed by using the conventional FDTD update equations, since the scattered and total fields can be dealt with separately to conform Maxwell's equations. On the other hand, the fields near the TF/SF interface require a special treatment, because some of the neighboring nodes of the update location may be located in different field region. Consequently, the incident field, computed before the start of the FDTD simulation, needs to be added to or subtracted from the neighbor cells accordingly, depending on whether the field at the neighboring node is being converted from the scattered field to the total field, or vice versa. The interested reader is referred to [21] for details of implementing this scheme.

In order to simulate the scattering by an infinite structure, we propose the application of the TF/SF technique on a single plane only (instead of a closed box), which divides the domain into two half-spaces. In the present scheme, the scatterer, which is located in the total-field half-space, is allowed to terminate inside the PML at the infinite end without truncating the TF/SF interface, as shown in Fig. 4.4. For a finite structure, there exists more than one choice for the orientation of the TF/SF interface (see Figs. 4.5(a) and (b)), but one should always choose the TF/SF interface with its normal oriented closest to the direction of incidence to obtain accurate results, especially for a plane wave illumination. How the accuracy of the excitation scheme described above depends on the incident angle will be examined thoroughly in Sec. 4.4.

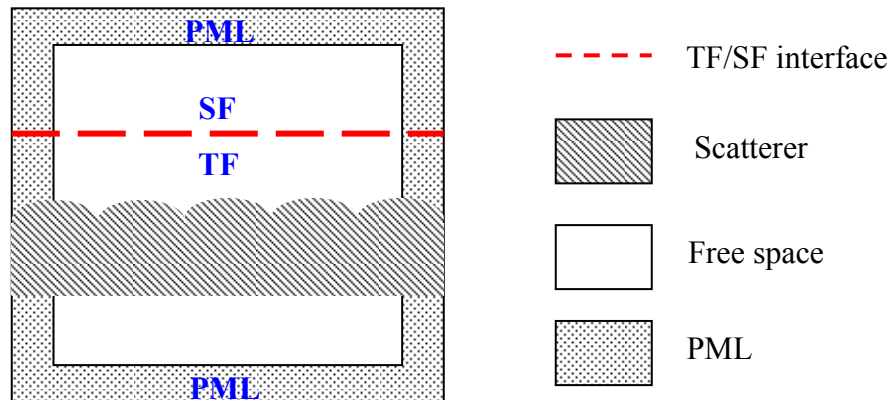


Fig. 4.4: Total-field/scattered field zoning of the FDTD space lattice in our proposed TF/SF approach, where the scatterer is allowed to be extended into the PML region without truncating the TF/SF interface.

Another modification brought about by the proposed scheme is the extension of the TF/SF interface into the PML region. In contrast to the approach described in [63,64], which performs multiple preliminary runs to calibrate the “incident fields” on the TF/SF interface within the PML, we assume that these incident fields are the same as those that would exist when

the PML is simply replaced by free space. Therefore, neither a calibration process, nor the implementation of other extra steps is needed in our approach. In addition, no modification to the PML updating equations is required when the convolutional PML (CPML) is utilized instead of the uniaxial PML (UPML).

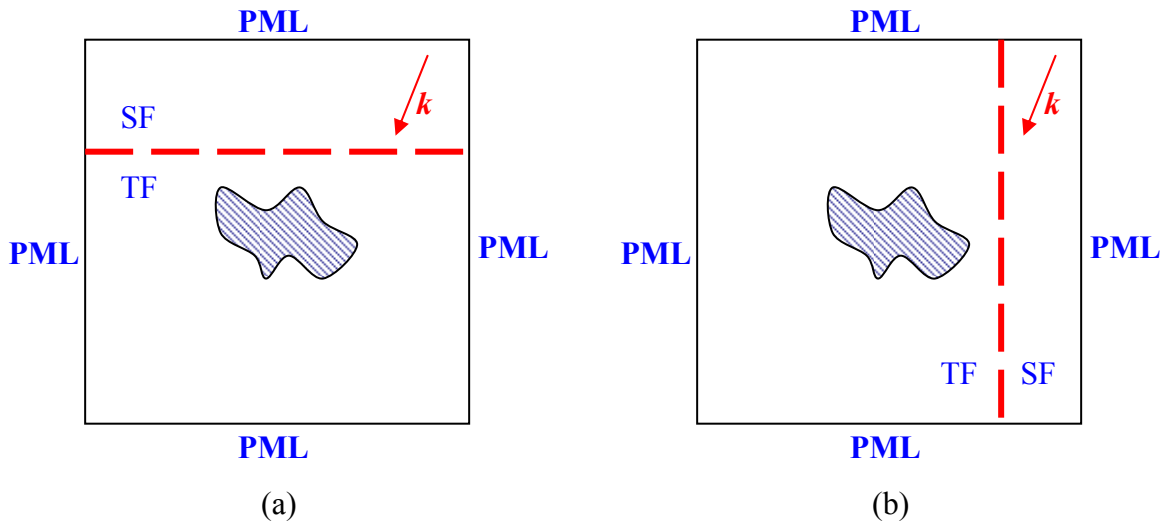


Fig. 4.5: Two possible total-field/scattered field zoning of the FDTD space lattice in the proposed TF/SF approach for a finite scatterer. The TF/SF setting in (a) is preferable to that in (b) since the incidence wave propagates along a direction closer to that of the normal of the TF/SF interface in (a).

Nevertheless, reflections due to numerical artifacts could still occur in our proposed scheme, because of the following reasons. First, the discrepancy between the “incident fields” within the PML region and the free space has not been accounted for. Second, this excitation scheme is inherently imperfect because of the use of a single TF/SF plane instead of a closed box; therefore, reflections may originate from the edge of the TF/SF interface. However, for a plane wave illumination, which will be discussed in Sec. 4.4, we have observed a significant reduction in the level of reflection, because of the second reason mentioned above, when the TF/SF interface is extended into the PML region. In addition, the total reflection is barely observed at

normal incidence, and remains acceptably low for small incident angles. On the other hand, for a localized Gaussian beam illumination, the incident field would decay to a low level in the PML regions, and, therefore, the reflection would also be very low.

This scheme can also be extended to excite a localized incident field distribution by applying the corresponding window function to a plane wave, which would normally be used in the conventional TF/SF formulation. The time delay of the incident fields on the TF/SF boundary remains the same as that in the case of a plane wave incident from the same angle. For the case of Gaussian beam, the amplitude of the “incident field” on a TF/SF interface lying on the x-y plane is as follows:

$$E_{inc}(x, y) = E_{inc0} * \exp(-r(x, y)^2 / w^2) \quad (4.1)$$

where E_{inc0} is the amplitude of the plane wave, w is spot size of the Gaussian beam, and r is the perpendicular distance from the beam axis. It is important to note that the incident beam should be well confined within the interior of the TF/SF boundary, in order to reduce the reflection from the edge of TF/SF interface.

4.3 The Performance of the Proposed Excitation Scheme for Launching a Gaussian Beam

In this section, we perform a parametric study of the proposed excitation scheme for launching a Gaussian beam at normal and oblique incidence for different polarizations. Two parameters, namely the size of the computational domain and the electrical length of the spot size, are varied independently. In all test cases, a Gaussian beam of the same spot size (w) of 90 mm is excited at the center of the TF/SF interface lying on the x-y plane and extended into the

surrounding PML region (6-layer PML). Three different incident settings are simulated as follows:

- (i) Normal incidence: Wave is incident from $\theta = 0^\circ$ with E_x polarization.
- (ii) Oblique TE_z incidence: Wave is incident from $(\theta = 30^\circ, \phi = 270^\circ)$ with E_ϕ polarization.
- (iii) Oblique TM_z incidence: Wave is incident from $(\theta = 30^\circ, \phi = 180^\circ)$ with E_θ polarization.

A uniform FDTD cell-size Δ of 1.0 mm, which is equal to $\lambda_0/30$ at the highest frequency of interest (10 GHz), is employed throughout the computational domain, which is free space. During the FDTD simulation, the field distribution on the TF/SF interface at the desired frequency is extracted by employing the DFT technique from the time-domain data. Finally, these field distributions are then compared with the incident field distribution.

4.3.1 Effect of the Size of the Computational Domain

When we increase the size of the computational domain, while keeping the spot size of the Gaussian beam unchanged, the incident field decays to a lower level at the inner PML boundary; therefore, the reflection from the PML or from the edge of the TF/SF interface is expected to be lower.

We perform some numerical tests by varying the size (L_x and L_y) of the computational domain in three ways: (i) $L_x = L_y = 2w$; (ii) $L_x = L_y = 3w$; and, (iii) $L_x = L_y = 4w$, where w is the spot size (= 90 mm), which is fixed in all tests. By using (4.1), the incident field is found to decay to -8.7 dB, -19.5 dB and -34.7 dB below its maximum value at the inner PML boundary

for the three cases, respectively. Figures 4.6 (a)–(f) show the E_x distribution measured on the TF/SF interface at 10 GHz ($w = 3 \lambda$) and the incident field distribution for the three different domain settings. No difference can be observed between the measured and incident field distributions. Figures 4.7 (a)–(f) compare the magnitude differences between the measured fields and the incident fields at 10 GHz for the above three settings of the computational domain mentioned earlier. The match between the measured and incident fields is excellent for almost all cases. We note that there is a very slight difference near the end on the plane of incidence (see Fig. 4.7 (e)) for the case of oblique TM_z incidence (30° off-normal), when the size of the computational domain is either $2w$ or $3w$. As expected, the performance of our proposed excitation scheme improves with the size of the computational domain for an illuminating Gaussian beam with a fixed spot size. Moreover, since the area of interest is usually larger than that covered by the spot size ($L_x, L_y > 2w$), this excitation scheme is suited for launching the Gaussian beams for practical simulations.

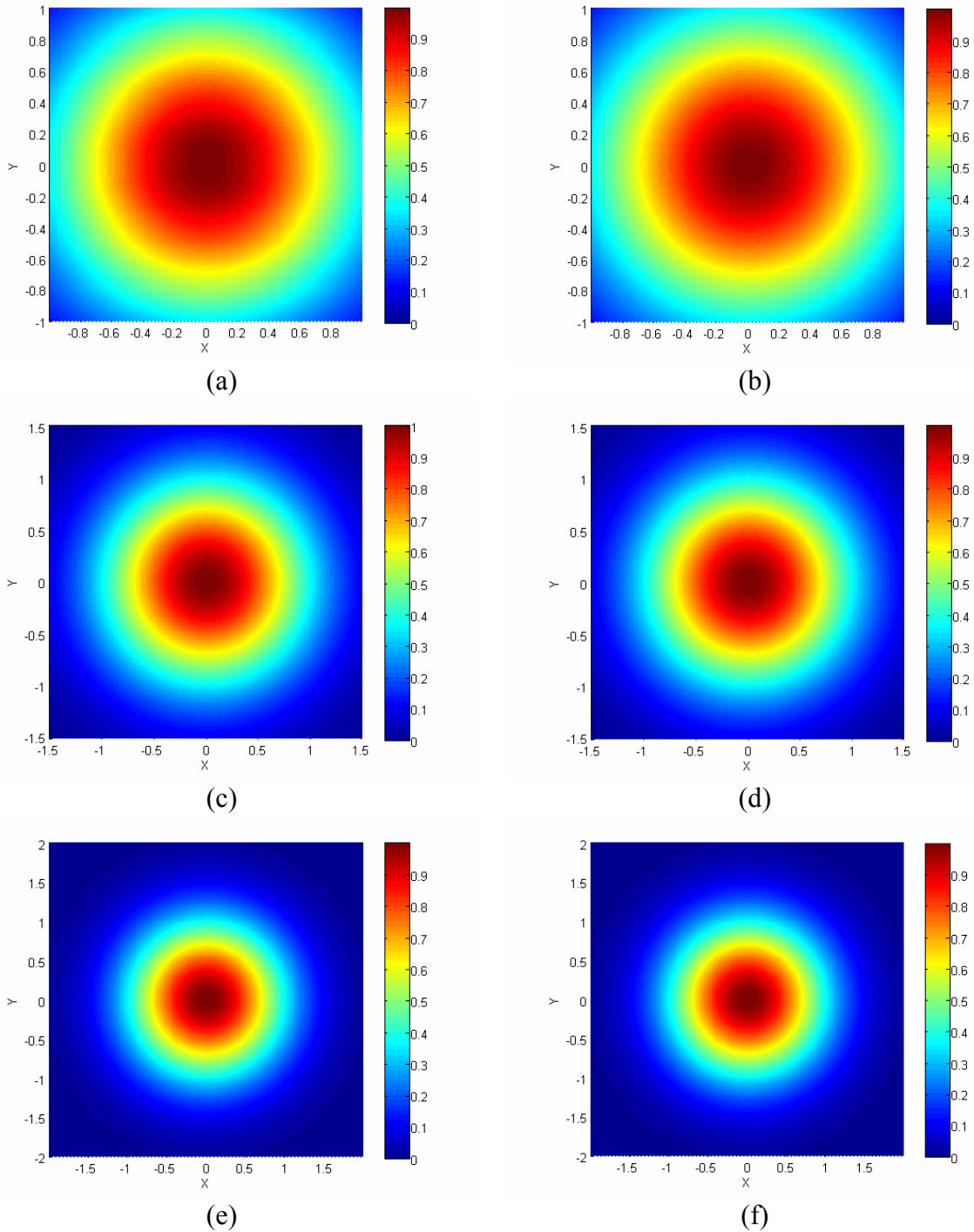


Fig. 4.6: The $|E_x|$ distribution for the measured field on the TF/SF interface (Left) and the incident field (Right) at 10 GHz, when a normally incident Gaussian beam of spot size (w) is excited inside a computational domain of three different sizes (L): (i) $L = 2w$; (ii) $L = 3w$; and (iii) $L = 4w$.

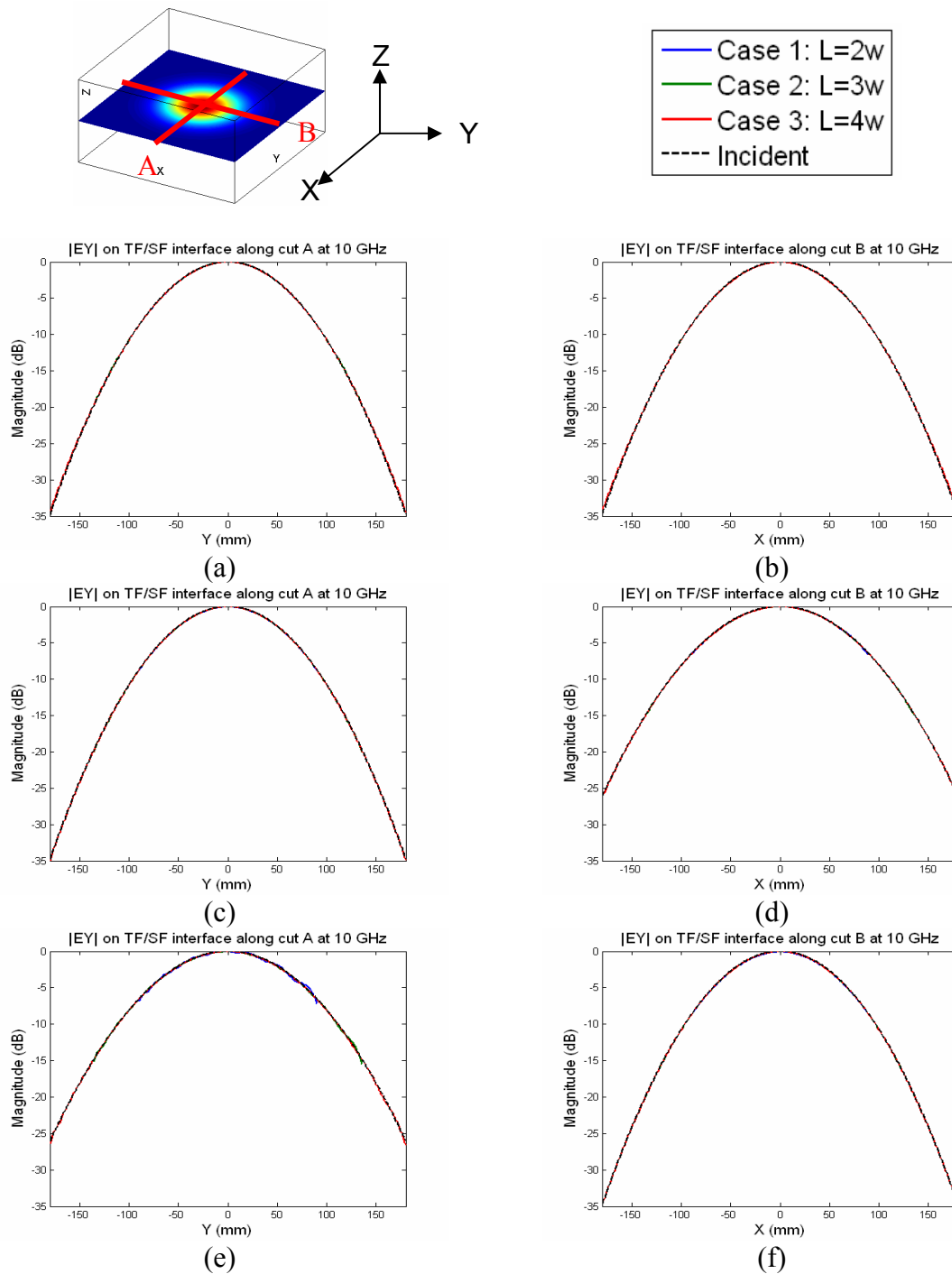


Fig. 4.7: Comparisons of the measured $|E_x|$ on the TF/SF interface for three different domain sizes and the incident $|E_x|$ at 10 GHz on the line of observation along the x- (Left) and y- (Right) directions, respectively. The Gaussian beam settings are as follows: (a) and (b) Normal incidence; (c) and (d) Oblique 30° TE_z incidence from $\phi=270^\circ$; and (e) and (f) Oblique 30° TM_z incidence from $\phi=180^\circ$.

4.3.2 Effect of the Electrical Length of the Spot Size

The windowing function in (4.1) is a simplified version of the Gaussian beam under the paraxial approximation [67]. For example, (4.1) does not consider the bending of the wavefront as the true Gaussian beam propagates away from the beam waist; therefore, the wavefront of the excited Gaussian beam on the TF/SF interface is always planar and perpendicular to the beam axis. This implies that the excited Gaussian beam will propagate with the minimum spot size (beam waist w_0) of w at the TF/SF interface.

In addition, (4.1) does not provide any information on the values of w for which the paraxial approximation is valid. Consequently, an arbitrary choice of the value of w in (4.1) may result in a non-physical incident field distribution. As a result, we perform the numerical tests for different electrical lengths of w (physical length fixed at 90mm) by varying the frequency. We observe the field distribution at 1.67 GHz, 3.33 GHz, 5.0 GHz, and 10 GHz, corresponding to the spot size at 0.5λ , 1.0λ , 1.5λ , and 3λ , respectively. The computational domain has a size of $3w$, such that the reflection from the PML would be negligible (see Sec. 4.3.1).

Figures 4.8 (a)–(d) show the measured $|E_x|$ on the TF/SF interface at different frequencies for the normal incidence case. The incident field distribution, which is frequency-dependent, is also shown in Fig. 4.8 (e) for comparison. As may be seen from the above figures, the measured field distribution at 1.67 GHz ($w = 0.5 \lambda$) obviously deviates from the incident field, while the measured field distributions at higher frequencies are similar to the incident field.

Figures 4.9 (a)–(f) compare $|E_x|$, the difference between the measured and incident fields at different frequencies, for three different incident settings mentioned earlier. Again, we see the measured field at 1.67 GHz differs noticeably from the incident field, while these fields match quite well at other frequencies. In fact, the paraxial approximation is only valid when the beam

waist w_0 is greater than $2\lambda/\pi \sim 0.64 \lambda$ [67]. As a result, the Gaussian distribution in (4.1) is non-physical at 1.67 GHz, where $w_0 = w = 0.5 \lambda$; thus the measured field on the TF/SF interface is distorted from the “assumed” incident field.

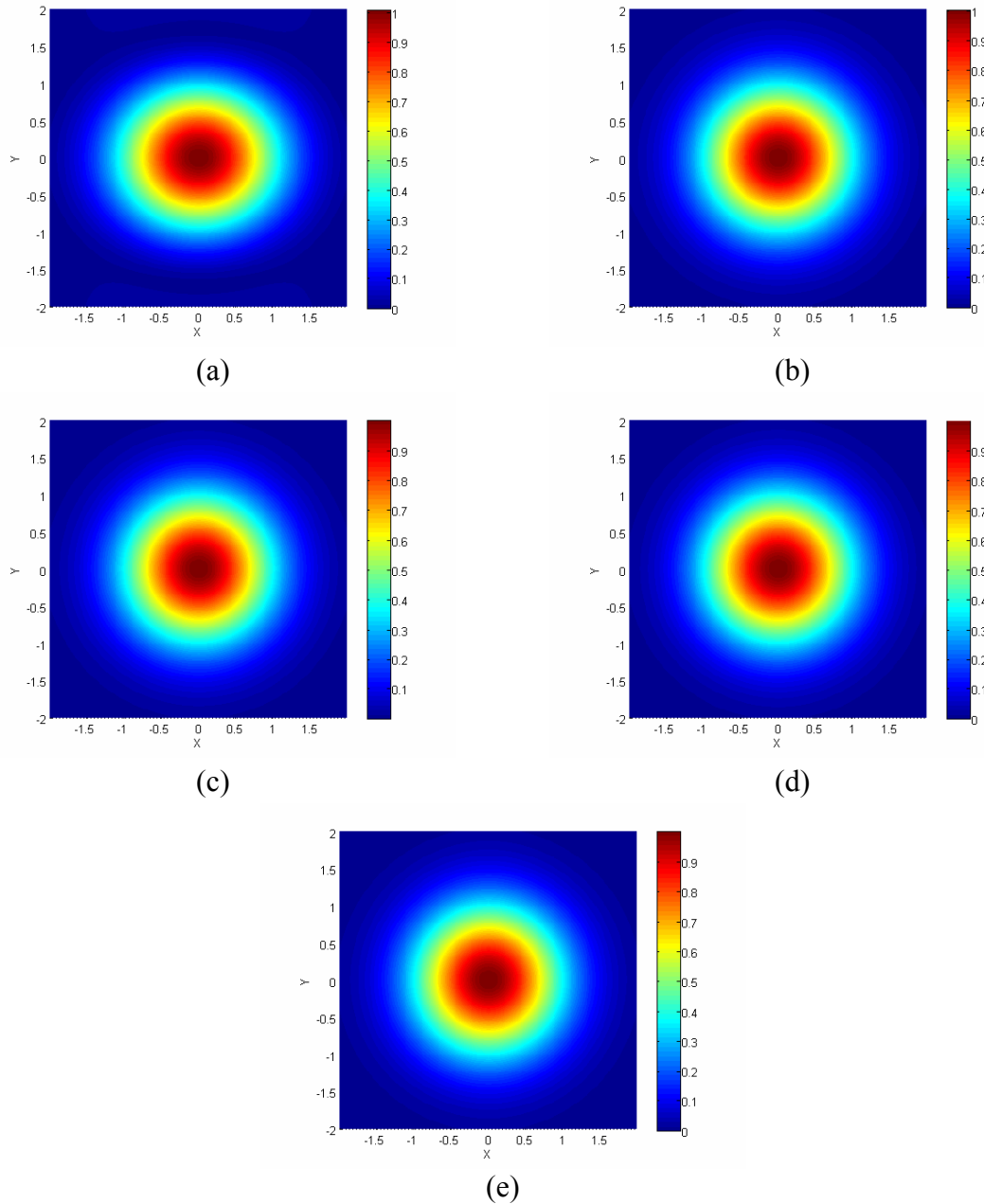


Fig. 4.8: The $|E_x|$ distribution for the measured field on the TF/SF interface at (a) 1.67 GHz, (b) 3.33 GHz, (c) 5.0 GHz, and (d) 10 GHz, when a normally incident Gaussian beam of spot size ($w = 90$ mm) is excited. The frequency-independent incident field distribution is also shown in (e).

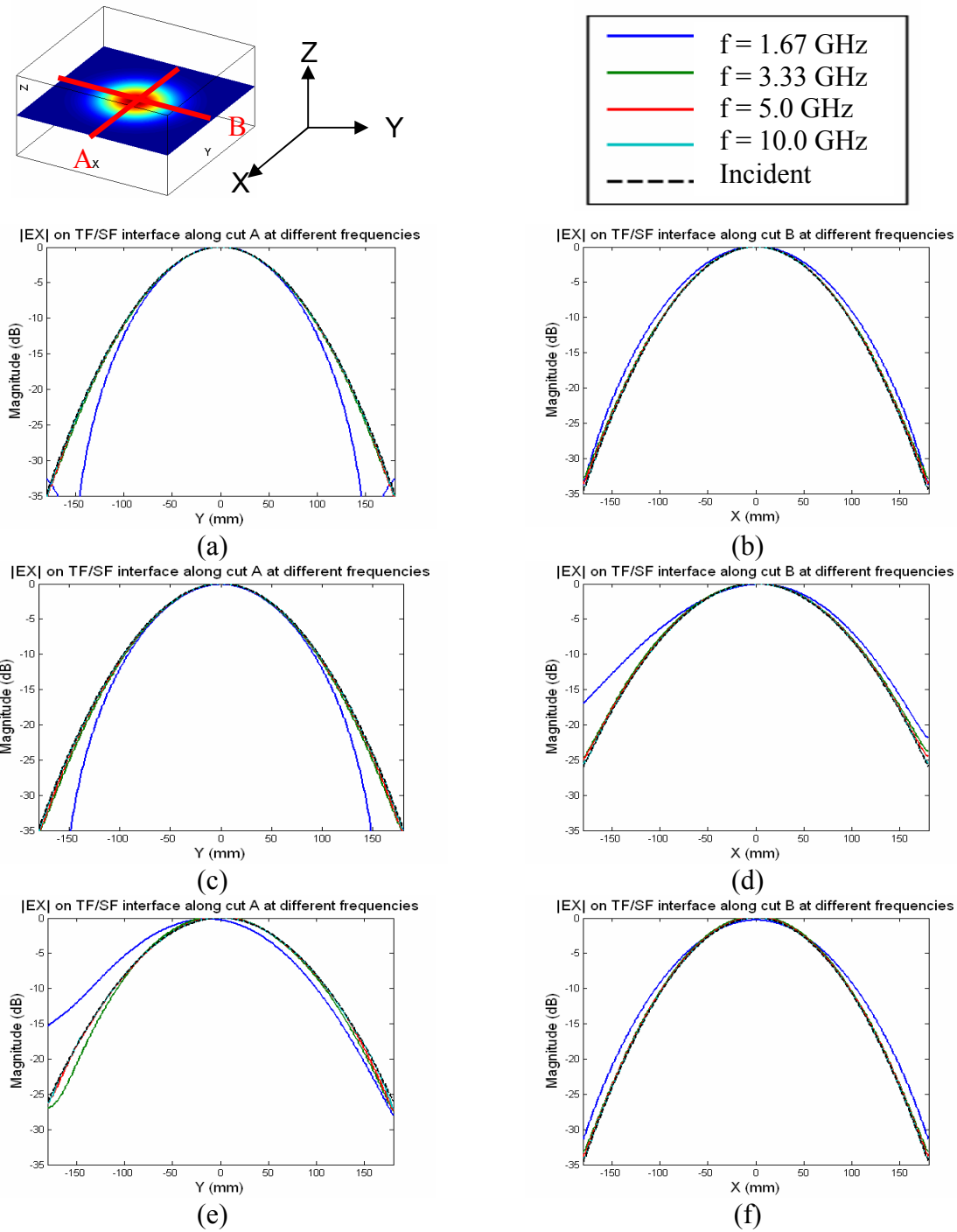


Fig. 4.9: Comparisons of the measured $|E_x|$ on the TF/SF interface at four different frequencies and the incident $|E_x|$ on the line of observation along the x- (Left) and y- (Right) directions, respectively. The Gaussian beam settings are as follows: (a) and (b) Normal incidence; (c) and (d) Oblique 30° TE_z incidence from $\phi = 270^\circ$; and (e) and (f) Oblique 30° TM_z incidence from $\phi = 180^\circ$.

4.4 Numerical Examples for Gaussian Beam Illumination

4.4.1 Study of the Extraordinary Transmission (ET) in Stacks of Doubly-Periodic Subwavelength Hole Arrays

It has been reported [68] that a left-handed metamaterial can be realized by stacking a number of screens with sub-wavelength-size array of holes, to form a photonic band-gap structure. By tuning the parameters of the array such as the periodicity of the holes, their diameter, and the separation distance between the plates, a left-handed propagation has been observed at the Extraordinary Optical Transmission (EOT) frequency, where modes inside the hole are evanescent but the transmission of these modes is still high through the multilayered medium.

Experimental investigation of the EOT [69] of this type of structure has been performed by exciting it with Gaussian beams in the Fresnel zone. The structure under investigation (see Fig. 4.10) is a single copper plate (diameter = 62.4 mm; thickness $t = 35 \mu\text{m}$), perforated with periodic ($d_x = 1.5 \text{ mm}$, $d_y = 4 \text{ mm}$) holes of diameter $a = 1.2 \text{ mm}$. The plate is sandwiched between two dielectric slabs ($\epsilon_r = 2.43$) of thickness 0.49 mm to reduce the EOT frequency. The frequency range of interest is 48 to 68 GHz. The experimental set up is shown in Fig. 4.11, in which an undistorted Gaussian beam of Ey-polarization is formed such that its beam waist ($w_0 = 13.95 \text{ mm}$) is right on the surface of the structure.

The above structure can be simulated by using an FDTD solver, which employs the excitation scheme proposed above to launch the desired Gaussian beam. The TF/SF interface is placed one FDTD cell ($\Delta z = 0.035 \text{ mm}$) away from the surface of the structure in order to excite a Gaussian beam with its beam waist on the surface. The transmission power is then computed

by applying the time-domain near-to-far transformation [70] to the fields on the Huygen's surface, which is located one FDTD cell away from the transmitting side of the plate.

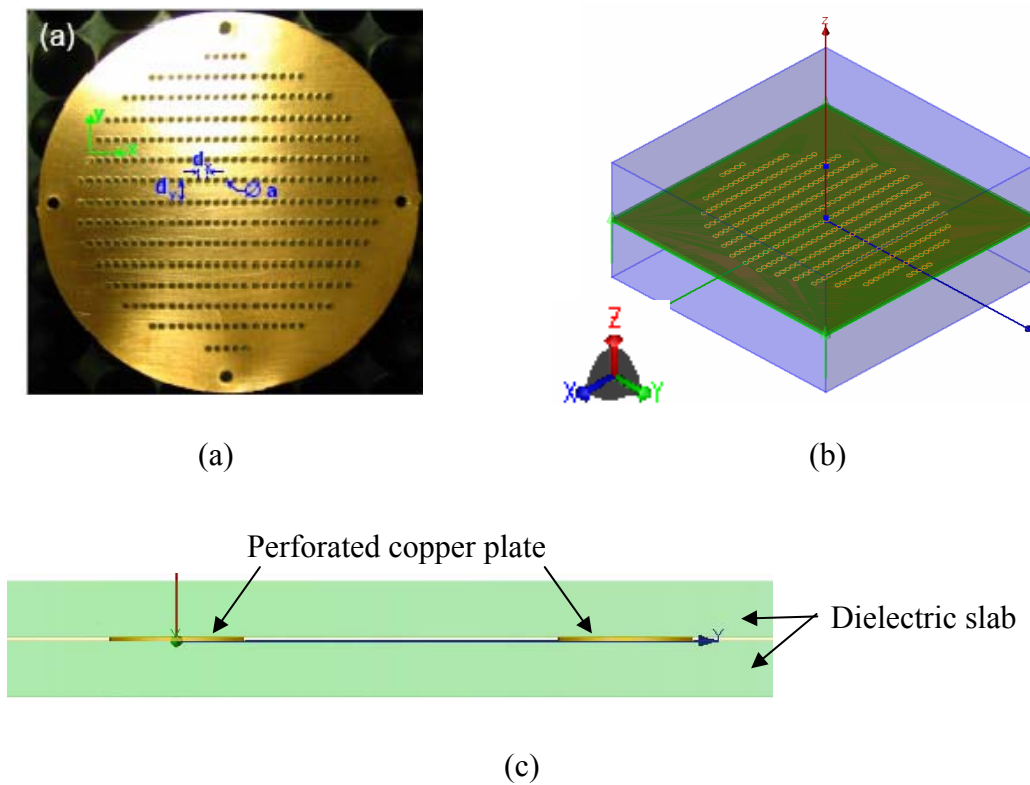


Fig. 4.10: (a) Photograph of the copper plate perforated with subwavelength hole arrays (Source: Fig. 1 (a) of Ref. [70]). (b) 3-D view, and (c) side view of the whole structure in FDTD model.

A non-uniform mesh is employed throughout the computational domain, with a finer cell-size ($\Delta x = \Delta y = 0.1$ mm, $\Delta z = 0.035$ mm) near the structure for an accurate modeling of the hole array. The total number of FDTD cells is $824 \Delta \times 824 \times \Delta 491$. The simulations have been run for a total of 10000 time-steps until the field reaches a steady state. The simulation takes about 2.5 hours when using 15 CPUs on GEMS Box. A comparison between the transmission coefficient,

obtained from the FDTD simulation, and the experimental data is shown in Fig. 4.12. We observe the presence of a transmission peak in both results, but at slightly different frequencies.

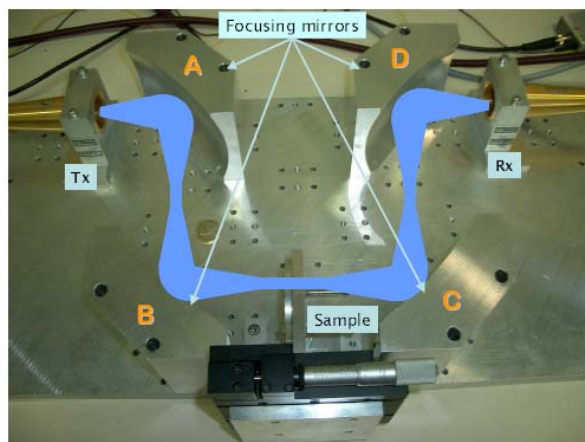
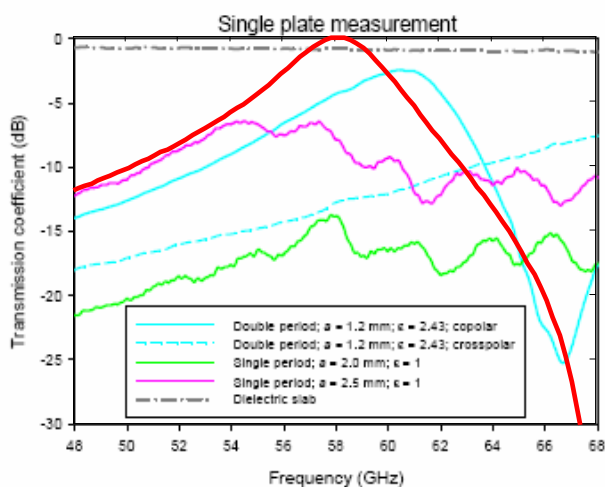


Fig. 4.11, Experimental quasi-optical bench set-up. The propagating path of the Gaussian beam is highlighted in blue. (Source: Fig. 3 of Ref. [70])



Red solid: FDTD result (Co-pol.)
 Cyan solid: Expt. Result (Co-pol.)
 Cyan dash: Expt. Result (Cross-pol.)
 Other curves: Expt. Result of other settings

Fig. 4.12: Comparison of the transmission coefficient between the FDTD result and the experimental data in Ref. [70]. The co-pol. FDTD result is shown in red and the cross-pol. level is below -80 dB (not shown). The experimental results from ref. [70] for the co-pol. and cross-pol. are shown in cyan solid and dashed line, respectively, for the same setting.

4.4.2 Double-Negative (DNG) Array

A localized beam can be used in scattering problems to simulate the EM response of metamaterial slabs in a manner that is closely analogous to that of a ray. The Gaussian beam approach offers a significant advantage over the plane wave illumination method. Chapter 5 will discuss the problem of a Gaussian beam used to study the EM response of a DNG structure, comprising of an infinite, doubly-periodic array comprising of split-ring resonators and thin wires. We will also investigate two interesting and unusual phenomena, namely the negative refraction and super-focusing effect of a DNG slab under the Gaussian beam illumination at normal and oblique incidences. The interested reader is referred to Chapter 5 for the results of this investigation.

4.5 The Performance of the Proposed Excitation Scheme in Launching a Uniform Plane Wave

As have been discussed in Sec. 4.3, reflections might occur at the edge in our proposed excitation scheme, when the incident field amplitude is still substantial near the edge of the TF/SF interface, because of two reasons: (i) only a single plane (instead of a closed box) is used for excitation; and (ii) the discrepancy between the “incident fields” within the PML region and the free space has been neglected. As a result, it is important to evaluate the performance of this scheme for launching a uniform plane wave, with a view to setting up some guidelines for when and how to use this scheme properly to obtain accurate results in practical simulations. These are the goals that we want to achieve in the following two sections.

All numerical tests in this section follow the same FDTD settings as given below:

- (i) The TF/SF interface lies on the x-y plane and divides the computational domain into two half spaces. The upper space belongs to the total-field (TF) region while the lower one belongs to the scattered-field (SF) region. Therefore, the plane wave comes from the lower hemisphere.
- (ii) The plane of incidence is always the x-z plane. The plane wave, either E_{θ} - or E_{ϕ} -polarized, is only allowed to be incident from $\phi = 180^\circ$, and $90^\circ < \theta \leq 180^\circ$ (normal incidence).
- (iii) The computational domain is free space.
- (iv) A six-layer CPML is employed to terminate the computational domain in all directions.
- (v) A modulated Gaussian pulse of both modulated and 3-dB frequencies at 8 GHz is used as the excitation. The highest frequency of interest is 15 GHz. The amplitude of the incident pulse is always unity.
- (vi) A uniform cell-size of 1 mm is employed throughout the computational domain. At the highest frequency of interest, the cell-size is equal to 1/15 of its free space wavelength.

4.5.1 Effect of Extending the TF/SF Interface into the PML Region

A TF/SF interface is placed at the plane at $z = 20 \Delta$, to launch a normally incident Ex-polarized plane wave into the computational domain of size $(100 \Delta)^3$. The TF/SF interface is either extended all the way through the PML, or truncated at the inner PML boundary. Snapshots of Ex on the x-z plane located in the center of the computational domain are shown in Figs. 4.13 (a) and (b) for the two different source implementations, namely the TF/SF interface with and

without extended into PML, respectively. As can be seen clearly from the above figures, a uniform plane wave is formed inside the TF region in (a) but not in (b). Similar results are also found for oblique incidence cases. Therefore, we conclude that artificial reflections from the edge of the TF/SF interface or PML region can be reduced considerably by extending the TF/SF interface into the surrounding PML region, and we will utilize this scheme for the rest of the simulations.

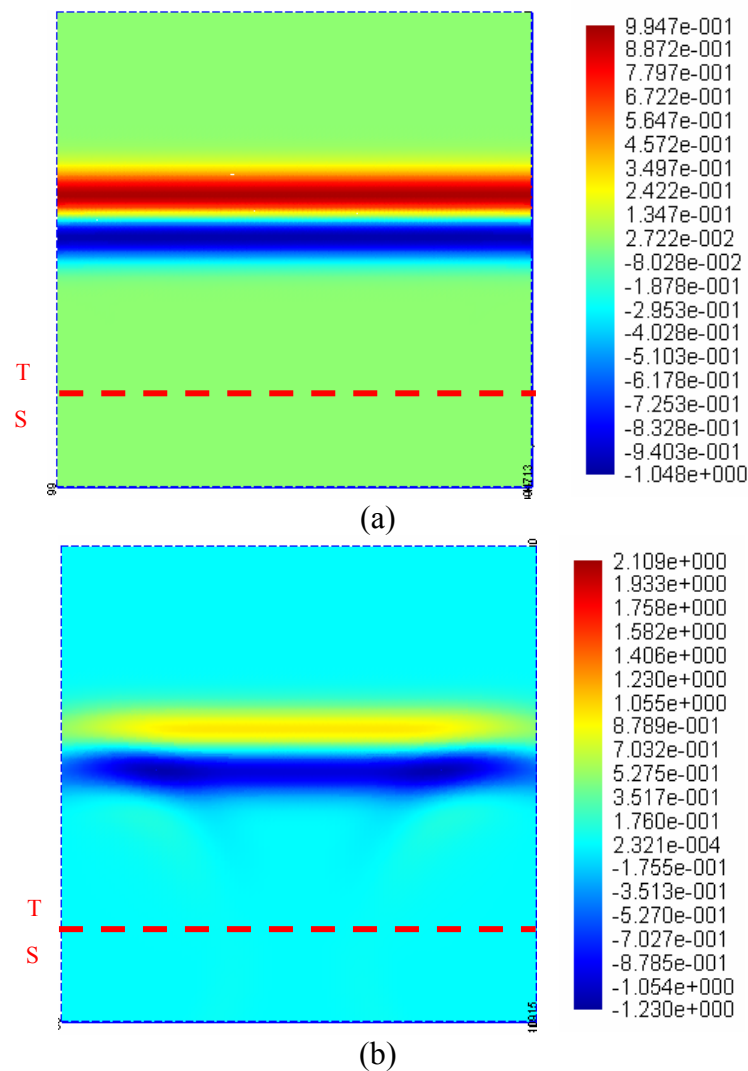


Fig. 4.13: Snapshots of E_x on the XZ plane for an E_x -polarized plane wave incident from $\theta=180^\circ$, computed by using the proposed TF/SF formulation (a) extending into the PML; and (b) truncated at the inner PML boundary.

Another finding from the above simulations is that the field is uniform along the y -direction for an Ex-polarized plane wave, when we extend the TF/SF interface into the PML region. Therefore, we can reduce our problem to a nearly 2-D one by using only a single FDTD cell in the y -direction, and terminating the two boundaries on the positive and negative y -ends with a perfectly magnetic conductor (PMC).

4.5.2 Effect of the Size of the TF/SF Interface in the Direction Normal to the Plane of Incidence

In this section, we consider the excitation of plane waves at different oblique angles (10° and 45° off-normal) and polarizations (E_θ and E_ϕ) into the same computational domain as was used in Sec. 4.5.1. The plane of incidence always coincides with the x - z plane. The field distributions are measured at the TF/SF interface at different frequencies.

We have observed that the fields are completely uniform along the y -direction for all E_θ -polarized cases. On the other hand, for the E_ϕ -polarized cases, the fields are only nearly uniform along the y -direction. The maximum relative deviations of the fields along the y -direction for all E_ϕ -polarized cases at each frequency are shown in Table 4-1.

Table 4-1: Maximum relative deviation of the E and H fields along the y -direction for E_ϕ -polarized plane waves.

Incident direction	Frequency (GHz)	Max. Deviation in E_y	Max. Deviation in H_x
$\theta = 170^\circ$ (10° off-normal)	5	5.2×10^{-4}	1.4×10^{-3}
	15	9.0×10^{-4}	8.2×10^{-4}
$\theta = 135^\circ$ (45° off-normal)	5	2.7×10^{-3}	3.5×10^{-3}
	15	8.0×10^{-3}	3.6×10^{-3}

The same numerical tests have been performed for the E_ϕ -polarized waves with an extension of the computational domain in the y -direction from 100Δ to 500Δ . The field deviation level along the y -direction has been found to be close to that shown in Table 4-1.

Consequently, we conclude that for our proposed excitation scheme, the dimension of the TF/SF interface along the y -direction, which is normal to the plane of incidence, has no effect on the performance of an E_θ -polarized plane wave, and has very little effect on the performance of an E_ϕ -polarized plane wave.

We can make use of this information to simplify all numerical tests that follow. The original 3-D problem can be reduced to a 2-D problem by using a single FDTD cell in the y -direction, and terminating the computational domain on the y ends either by perfect electric conductors (PEC) for a E_ϕ -polarized wave, or by perfect magnetic conductors (PMC) for a E_θ -polarized wave.

4.5.3 Effect of the Incident Direction, Polarization, and Frequency of the Excited Wave

We begin by studying the performance of a normally incident plane wave. The snapshot shown in Fig. 4.13 (a) depicts the excitation of a uniform plane wave in the TF region. The maximum errors of the excited fields measured on the TF/SF interface for different frequencies (different FDTD cell-size in wavelengths) and domain sizes are plotted in Fig. 4.14. We can see that the maximum error does not vary much, even when the domain size is changed by more than an order of magnitude, and the maximum error reduces with FDTD discretization. It should be noted that the maximum error has been kept to a very low value ($\leq 0.3\%$) for all domain sizes $\geq 0.3 \lambda$, and $\Delta < \lambda/20$.

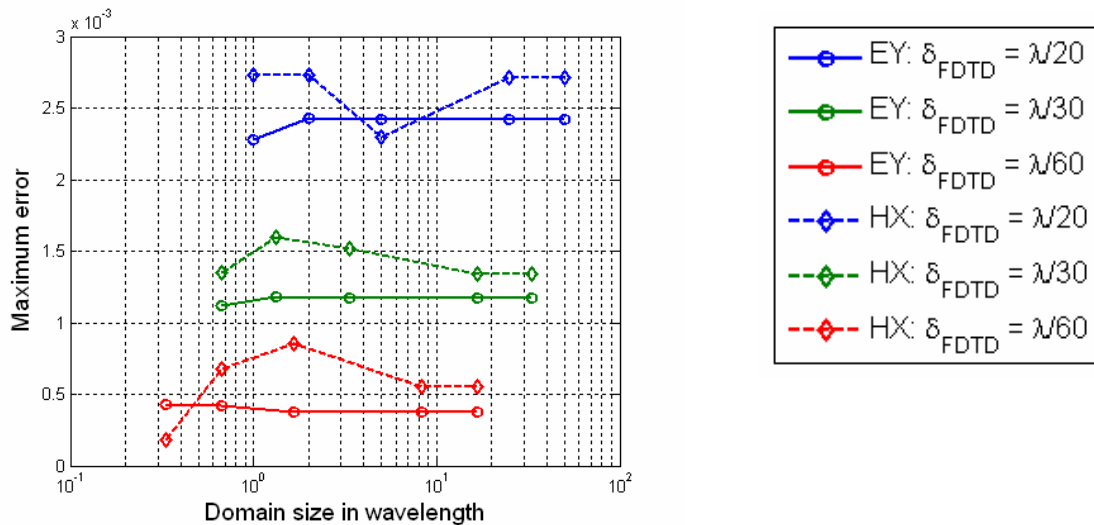


Fig. 4.14: Maximum error of E and H fields measured on the TF/SF interface for a normally incident plane wave as computed by using the proposed TF/SF formulation for different domain sizes and FDTD discretizations.

Figures 4.15 (a) and (b) show the magnitude of the measured E_x and H_x at 10 GHz ($\Delta = \lambda/30$) on the x - z plane, within the region 1λ away from the TF/SF interface at $Z = 0$. The domain is 1000 mm ($= 33.3 \lambda$) long along the x -direction. We can see that the excited field over this region is very uniform. The maximum deviations of the E and H fields from the incident field are found to be only 0.39 %. Therefore, this proposed excitation scheme is capable of exciting a uniform plane wave at normal incidence into the TF region, for all domain size and FDTD discretization $\Delta < \lambda/20$.

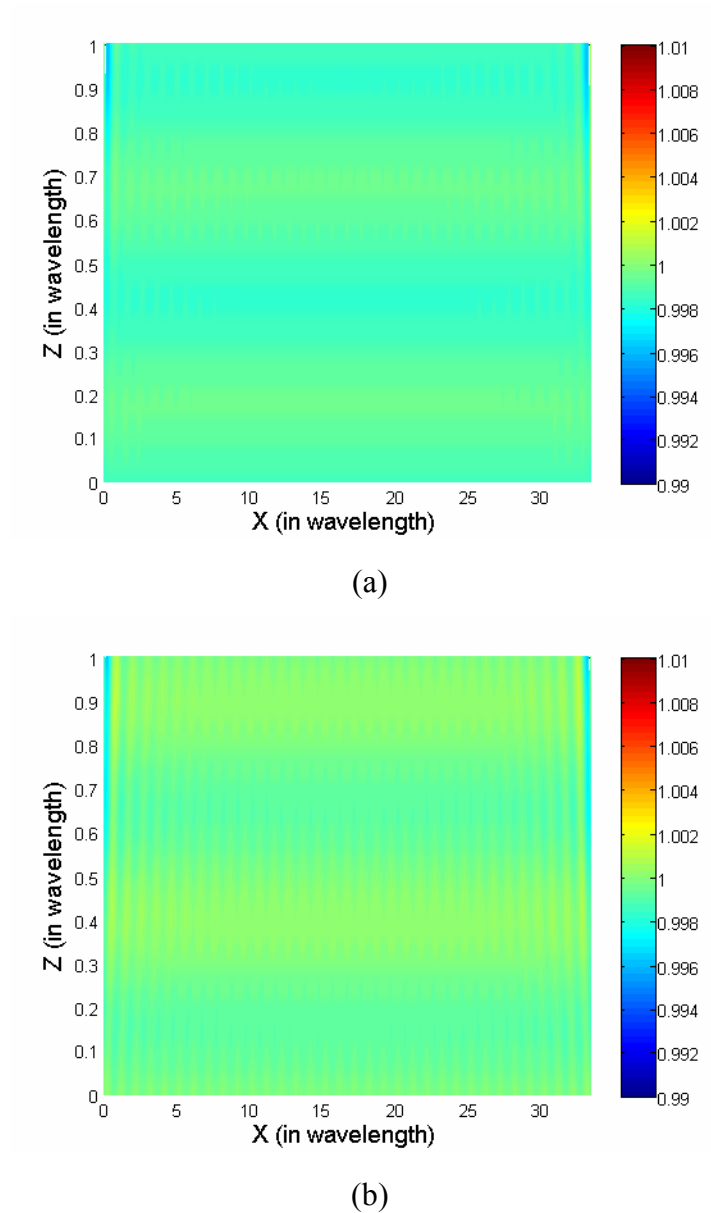


Fig. 4.15: Normalized magnitude of the measured (a) E_x and (b) H_y at 10 GHz, in the TF region up to 1λ away from the TF/SF interface. A normally incident E_x -polarized plane wave is excited by using the proposed TF/SF formulation at $Z=0$. The relative error of both E_x and H_y ranges from -0.39% to 0.12% within this region.

Next, we study the oblique incidence case. Snapshots of E_x on the x - z plane for E_0 -polarized plane waves incident from $\theta=170^\circ$ and 150° are shown in Figs. 4.16 and 4.17,

respectively. We can see that parts of the excited fields that are located away from the two side boundaries appear to be uniform and propagating at the desired direction. However, a slight distortion of the excited fields can be observed near the left boundary in Fig. 4.16 (b). For $\theta=150^\circ$, distortions can be seen near both the left and right boundaries, and the level of distortion is worse than that for $\theta=170^\circ$. These preliminary results have shown that the performance of our proposed scheme gets worse when the incident direction deviates further from the normal. In addition, from examining all the snapshots taken during the simulation, we have clearly observed that the incident field is distorted by the reflections coming from the parts of the TF/SF interface, which is embedded within the two PML regions at the positive and negative ends of x-axis.

Numerical tests have been carried out to quantitatively evaluate the performance of our excitation scheme at oblique incidence. In all of these tests, the computational domain has a size of $1000 \Delta \times 1 \Delta \times 135 \Delta$ ($\Delta=1\text{mm}$), with the boundaries on the x- and z-ends terminated by PML, and the boundaries on the y-end terminated by a PEC (PMC) for an E_ϕ (E_θ)-polarized plane wave. The TF/SF interface is placed at the plane $z = 60 \Delta$ to excite a plane wave incident from $\phi=180^\circ$ and $\theta=170^\circ$, 160° or 150° . In other words, the wave always propagates towards the positive x- and z-directions. The simulations have been run for a total of 2500 time-steps so that the field reaches its steady state. The results are presented in the following.

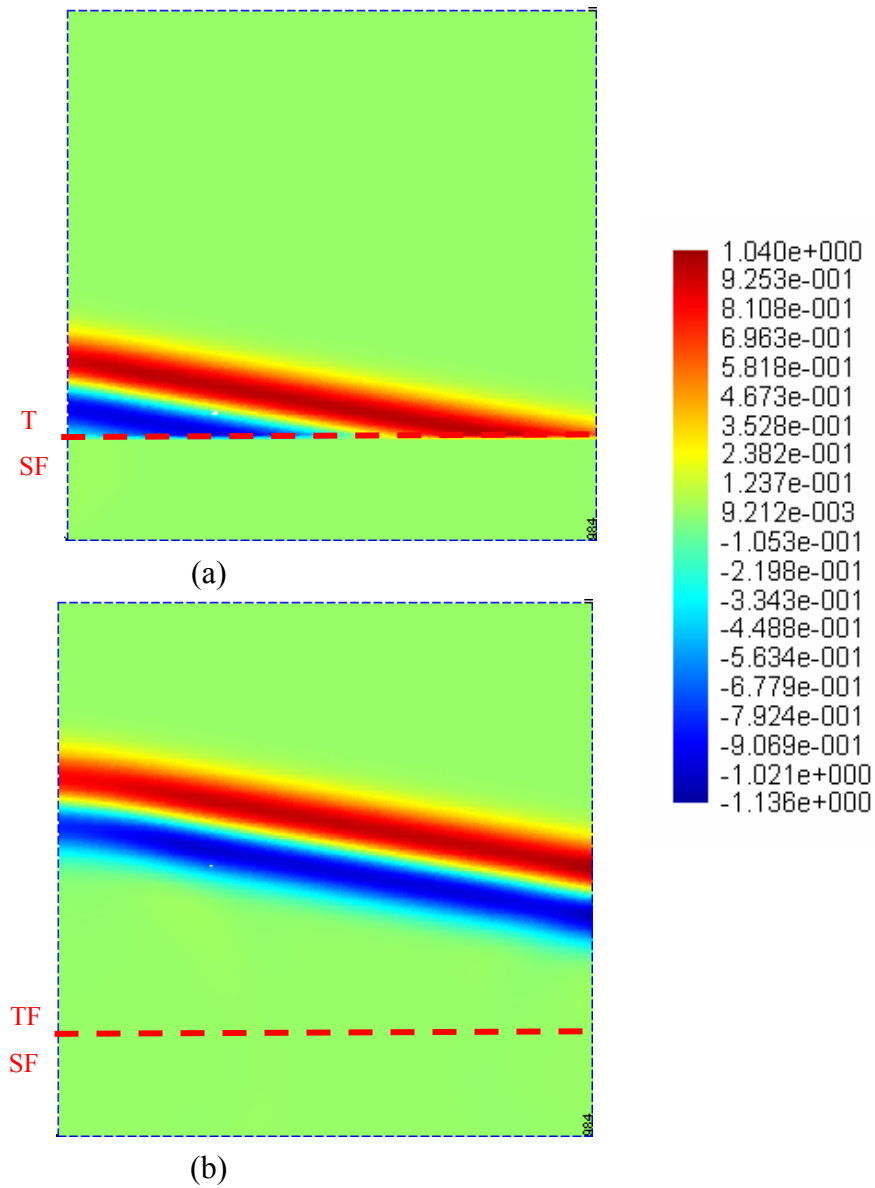


Fig. 4.16: Snapshots of E_x on the XZ plane for an E_0 -polarized plane wave incident from $(\theta=170^\circ, \phi=180^\circ)$, excited by using the proposed TF/SF formulation, at (a) $t = 0.11$ ns and (b) $t = 0.24$ ns.

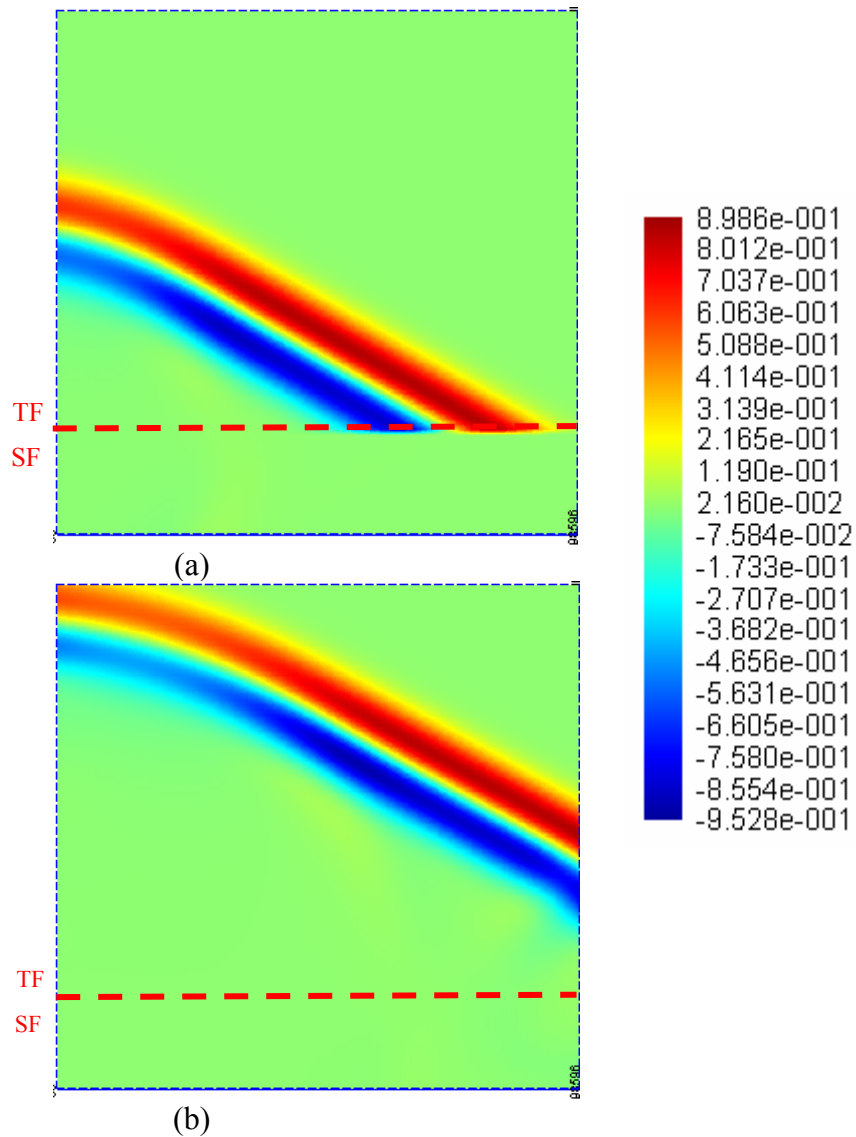
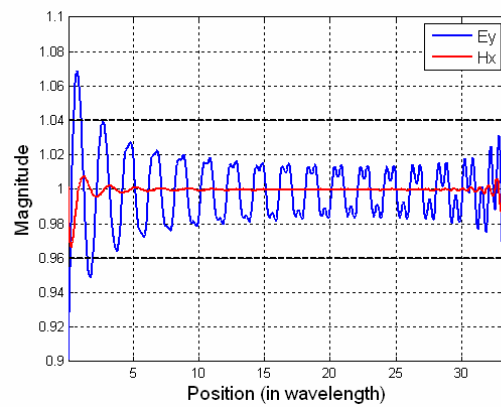


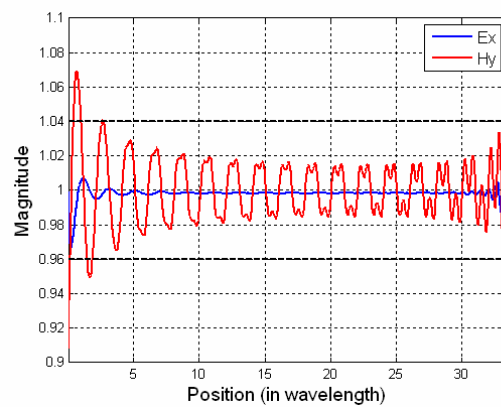
Fig. 4.17: Snapshots of E_x on the XZ plane for an E_0 -polarized plane wave incident from $(\theta=150^\circ, \phi=180^\circ)$, excited by using the proposed TF/SF formulation, at (a) $t = 0.21$ ns and (b) $t = 0.32$ ns.

Figures 4.18 (a) and (b) plot the normalized magnitude of the E and H fields measured on the TF/SF interface along the x-direction at 10 GHz, for the E_ϕ - and the E_θ -polarized plane waves incident from $\theta=150^\circ$. The field distributions for the two polarizations appear to be symmetric;

that is, the E_y (H_x) distribution for the E_ϕ -polarized wave is similar to the H_y (E_x) distribution for the E_θ -polarized wave. In addition, from Fig. 4.18 (b), the level of fluctuation in E_y is greater than that in H_x for E_ϕ -polarization. This property can also be observed at other locations inside the TF region, and for other incident angles except the normal incident case. In the following, we limit our study to the excited wave with E_θ -polarization, since the behavior of the E_ϕ -polarized wave can be deduced by invoking duality.



(a)



(b)

Fig. 4.18: Normalized magnitude of E and H fields measured on the TF/SF interface along the x-direction, for (a) an E_ϕ -polarized and (b) an E_θ -polarized plane wave incident from ($\theta=150^\circ$, $\phi=180^\circ$), computed by using the proposed TF/SF formulation.

Figure 4.19 plots the comparison of the H_y distributions at 10 and 15 GHz on the TF/SF interface for the E_0 -polarized waves that we studied previously. The position along x is listed in terms of wavelength. At these frequencies, the domain sizes are 33.3λ and 50λ , respectively. An interference pattern can be clearly seen in the above figure. Two waves begin to appear from the two inner PML boundaries in the x -direction, decay with propagation distance, and interfere with the incident field of unity level. It can be seen that the reflection at the leading end (negative x -end) is stronger than that at the trailing end (positive x -end), and the fields decay as they propagate to the interior of the TF region. In addition, the starting levels of these reflections at the two ends remain relatively unchanged with a change in the FDTD discretization in terms of wavelength ($\Delta \leq \lambda/20$).

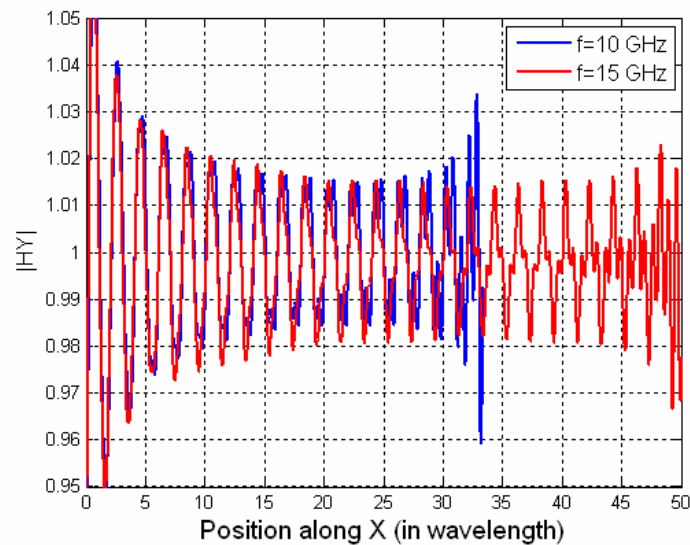
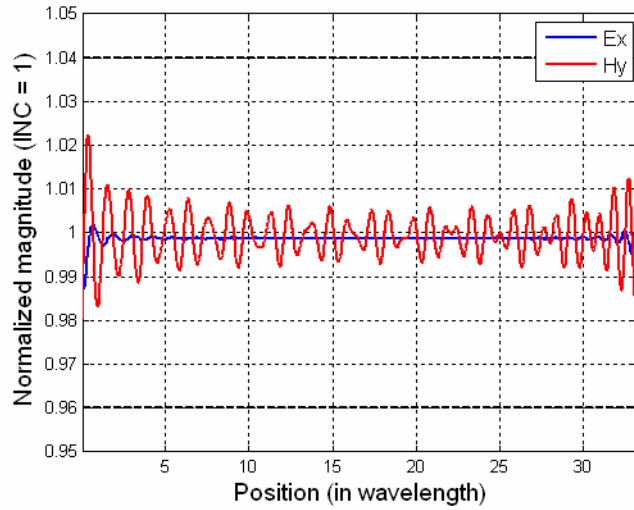


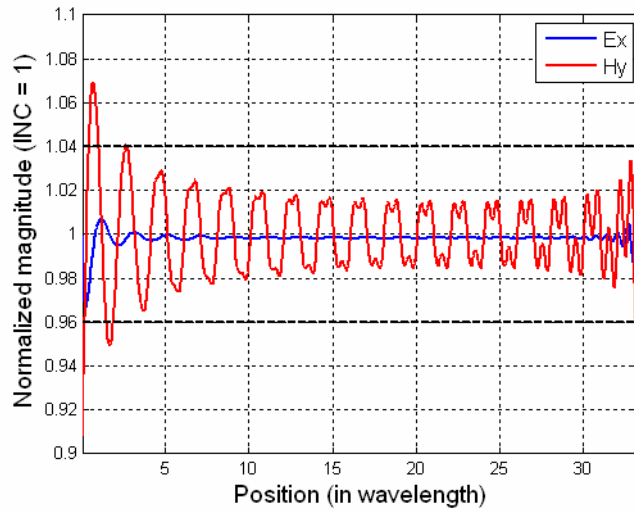
Fig. 4.19: Normalized magnitude of H_y (at 10 and 15 GHz) on the TF/SF interface along the x -direction expressed in terms of wavelength. An E_0 -polarized plane wave coming from ($\theta=150^\circ$, $\phi=180^\circ$) is excited by using the proposed TF/SF formulation in a domain of size 1000 mm.

Figures 4.20 (a) and (b) plot the magnitude of E_x and H_y at 10 GHz, measured at the TF/SF interface for $\theta=170^\circ$ and 150° , respectively. The deviation from the incident fields is seen to be greater for $\theta=150^\circ$. Figures 4.21 (a) and (b) plot these fields measured at the plane located 30 mm (1λ) above the TF/SF interface. We can see that the level of fluctuation becomes slightly stronger in the interior region, and the reflection at the two ends grows much faster. In addition, we can observe a shadow region—where the field level is significantly weaker than the incident level—at the leading side (negative x -end). This region is formed since the field that was excited inside the nearby PML region, decays before it reaches the shadow region. Figures 4.23 (a)-(d) show the distributions of $|E_x|$ and $|H_y|$ on the x - z plane, in the TF region up to 1λ away from the TF/SF interface for $\theta=170^\circ$ and $\theta=150^\circ$.

Figure 4.22 (a) and (b) show the comparison of the phase of H_y measured at the plane located 30 mm above the TF/SF interface and that of the incident field at the two incident angles. Excellent agreement can be observed for this case, even in the shadow region.

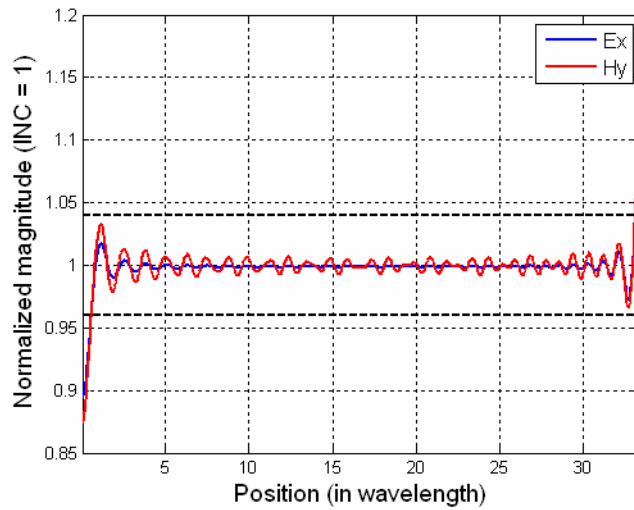


(a)

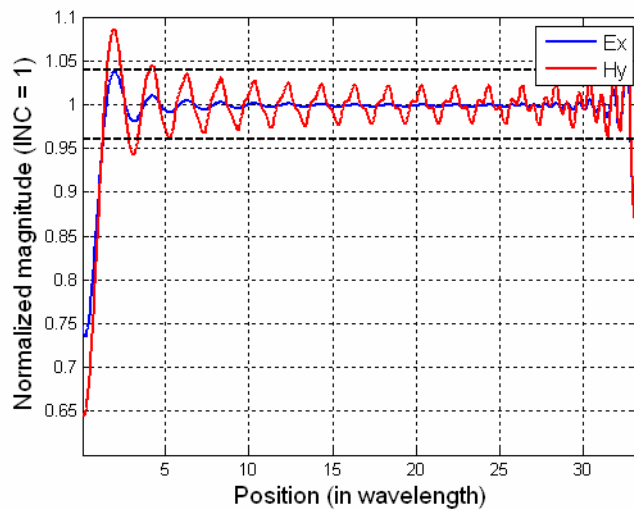


(b)

Fig. 4.20: Normalized magnitude of E_x (Blue) and H_y (Red) at 10 GHz, along the x -direction, measured on the TF/SF interface. The excited E_θ -polarized plane wave is incident from $\phi = 180^\circ$ and (a) $\theta = 170^\circ$; and (b) $\theta = 150^\circ$. Region between the two black dashed lines has a relative error of less than 4%.

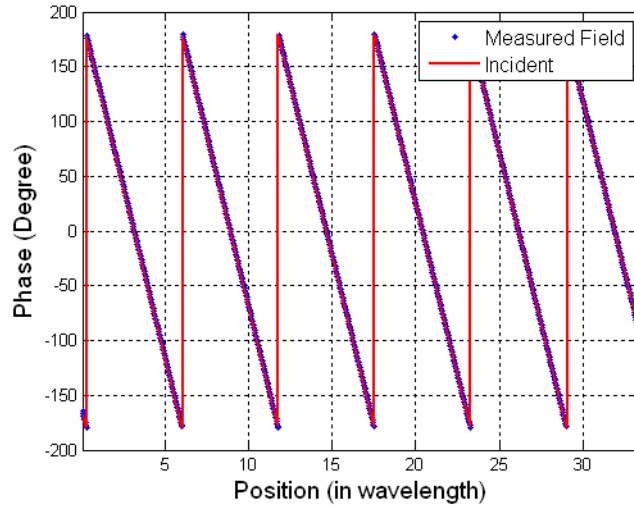


(a)

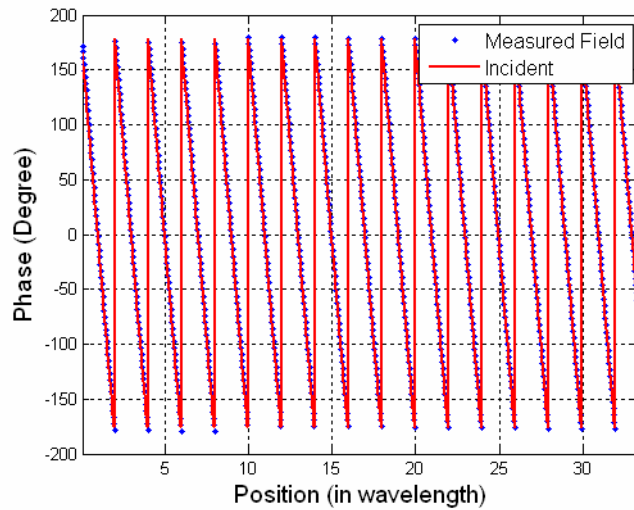


(b)

Fig. 4.21: Normalized magnitude of E_x (Blue) and H_y (Red) at 10 GHz, along the x -direction, measured at one wavelength above the TF/SF interface. The excited E_θ -polarized plane wave is incident from $\phi = 180^\circ$ and (a) $\theta = 170^\circ$; and (b) $\theta = 150^\circ$. Region between the two black dashed lines has a relative error of less than 4%.



(a)



(b)

Fig. 4.22: Comparison of the phase of H_y at 10 GHz along the x-direction, between the measured and the incident fields, located at one wavelength above the TF/SF interface. The excited E_0 -polarized plane wave is incident from $\phi = 180^\circ$ and (a) $\theta=170^\circ$; and (b) $\theta=150^\circ$.

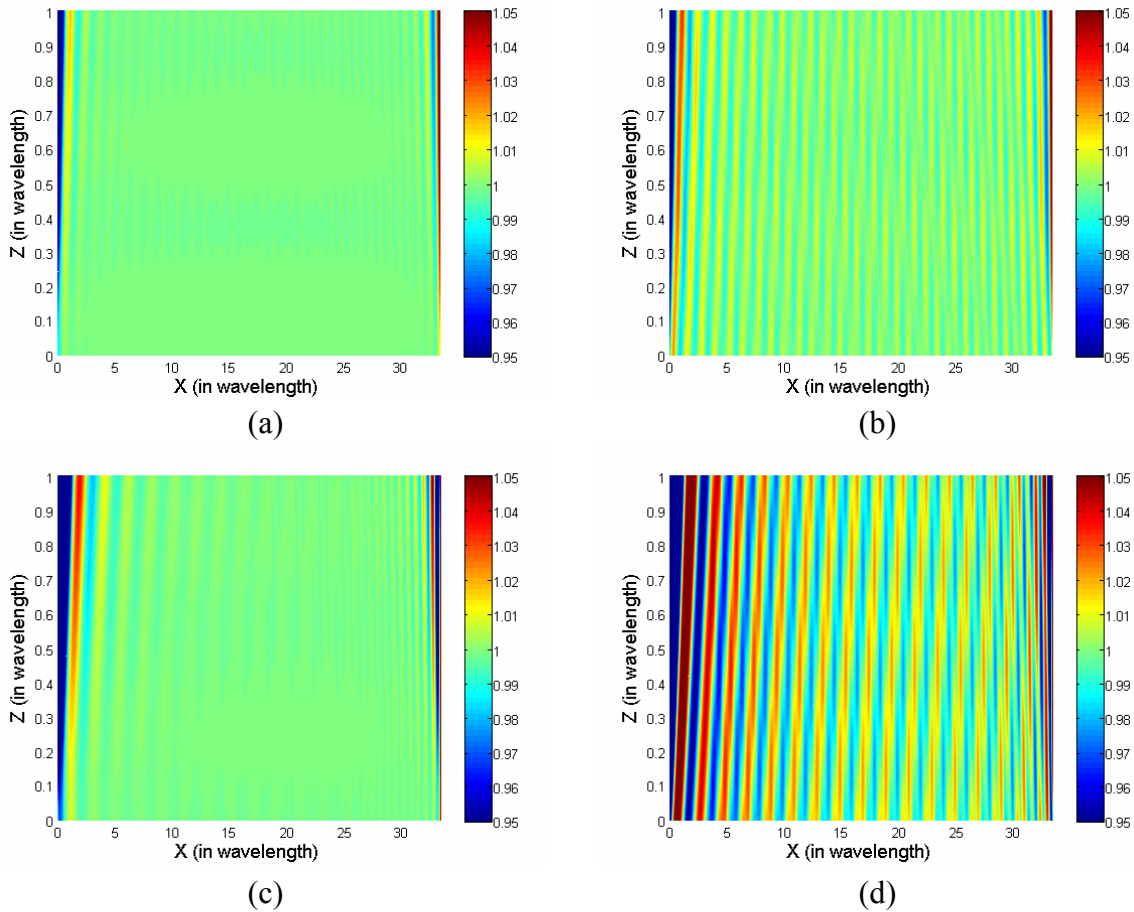


Fig. 4.23: Normalized magnitude of the measured E_x (Left) and H_y (Right) at 10 GHz, in the TF region up to 1λ away from the TF/SF interface (at $Z = 0$). The excited E_0 -polarized plane wave is incident from $\phi = 180^\circ$ and (a) and (b) $\theta = 170^\circ$; and (c) and (d) $\theta = 150^\circ$.

4.5.4 Accuracy Improvement by Applying Window to the Incident Field Used on the TF/SF Interface Within the PML Region

In the previous sections, it has been demonstrated that the reflections originate from the part of the TF/SF interface that is embedded inside the PML. As a result, we have attempted to reduce this reflection by applying a window to the fields excited on the TF/SF interface within the PML region.

First, we apply a half-Gaussian window in the PML region at the positive x-end. To ensure the continuity of the excited fields, the window (see Fig. 4.24) has a maximum value of 1 at the inner PML boundary, and it decays to $1/e^2$ at the outermost PML boundary. Figure 4.25 shows a snapshot of E_x on the x-z plane for E_θ -polarized plane waves incident from $\theta=150^\circ$ after applying a Gaussian window. The snapshot taken here is the same as that in Fig. 4.17 (b). Comparing these figures, the field distortion, which appeared on the right boundary in Fig. 4.17 (b), can no longer be seen in Fig. 4.25. Figures 4.26 (a)-(d) show the comparison of the field distribution measured at different distances from the TF/SF interface, with and without the Gaussian window inside the PML. It can be seen that most of the reflected waves on the positive x-end have been suppressed. Figure 4.27 shows the field distribution of $|E_x|$ and $|H_y|$ on the x-z plane, in the TF region up to 1λ away from the TF/SF interface when the window is applied. Only one set of reflected waves can be observed. In all of the figures above, the dominant reflected field, which comes from the PML region at the negative x-end, is not reduced, and the shadow region still remains.

The effect of applying a fixed Gaussian window varies with the direction of incidence. When the incident angle is less than 20° off-normal, applying a Gaussian window creates additional reflections. On the other hand, when the incident angle is greater than or equal to 20° off-normal, applying such a window always reduces the reflection from the PML region, but the level of reduction gets worse for large incident angles.

Two mechanisms help explain the effect of applying a Gaussian windowing, or any tapering window, in the PML region on the positive end. First, as the “incident field” applied near the edge of the TF/SF interface is reduced, the reflection from that edge is also reduced. Second, it is well known that the field decays when it enters the PML region. Therefore, a

tapering “incident-field” should be used at the TF/SF interface lying inside that region to accurately excite a uniform plane wave. Since the decay rate changes with the incident angles, the applying of a fixed Gaussian window cannot fully account for all the incident cases.

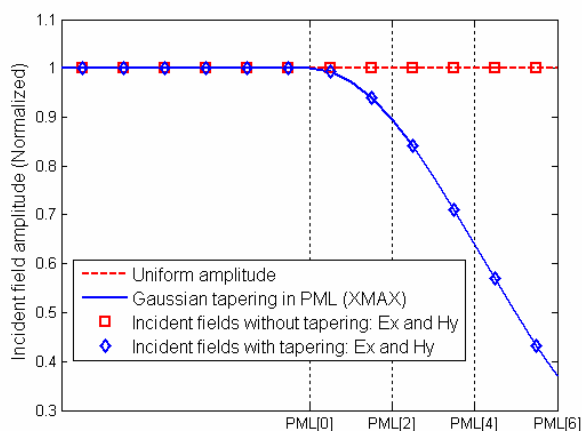


Fig. 4.24: Incident field amplitude (Red) applied on the TF/SF interface along the x-direction, with field tapering inside the PML region on the positive x-end. The amplitude falls to $1/e^2$ at the outermost PML layer.

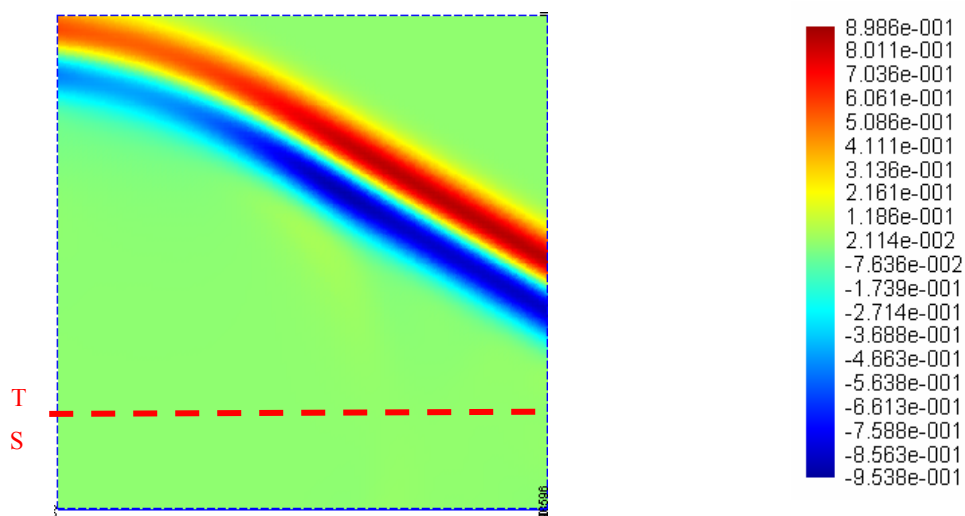


Fig. 4.25: Snapshot of E_x at $t = 0.32$ ns, on the XZ plane for an E_0 -polarized plane wave incident from $(\theta=150^\circ, \phi=180^\circ)$. The plane wave is excited by using the proposed TF/SF formulation and an addition of Gaussian window on the incident field amplitude as shown in Fig. 4.23.

Choosing an appropriate window in the PML regions at the negative x-end is much more difficult, since these two mechanisms work in opposite ways inside this region. On one hand, the excited field at the edge of the TF/SF interface should be reduced to suppress the reflection; on the other hand, an amplifying “incident field” should be used for excitation in order to compensate for the decay before it enters the computational domain from the PML region.

A compromise approach can be utilized to solve the problem for $\theta = 150^\circ$. Towards this end, we first compute the incident fields inside the two PML regions for $\theta = 150^\circ$, by using the calibration process described in [64]. The calibrated incident field is plotted in Fig. 4.28 in blue. However, the direct application of this incident field distribution on the TF/SF interface can create large reflections because of high levels of reflection at the left edge of the TF/SF interface. Therefore, we reduce the value of the incident field at the edge to that at the neighboring node (see red curve of Fig. 4.28).

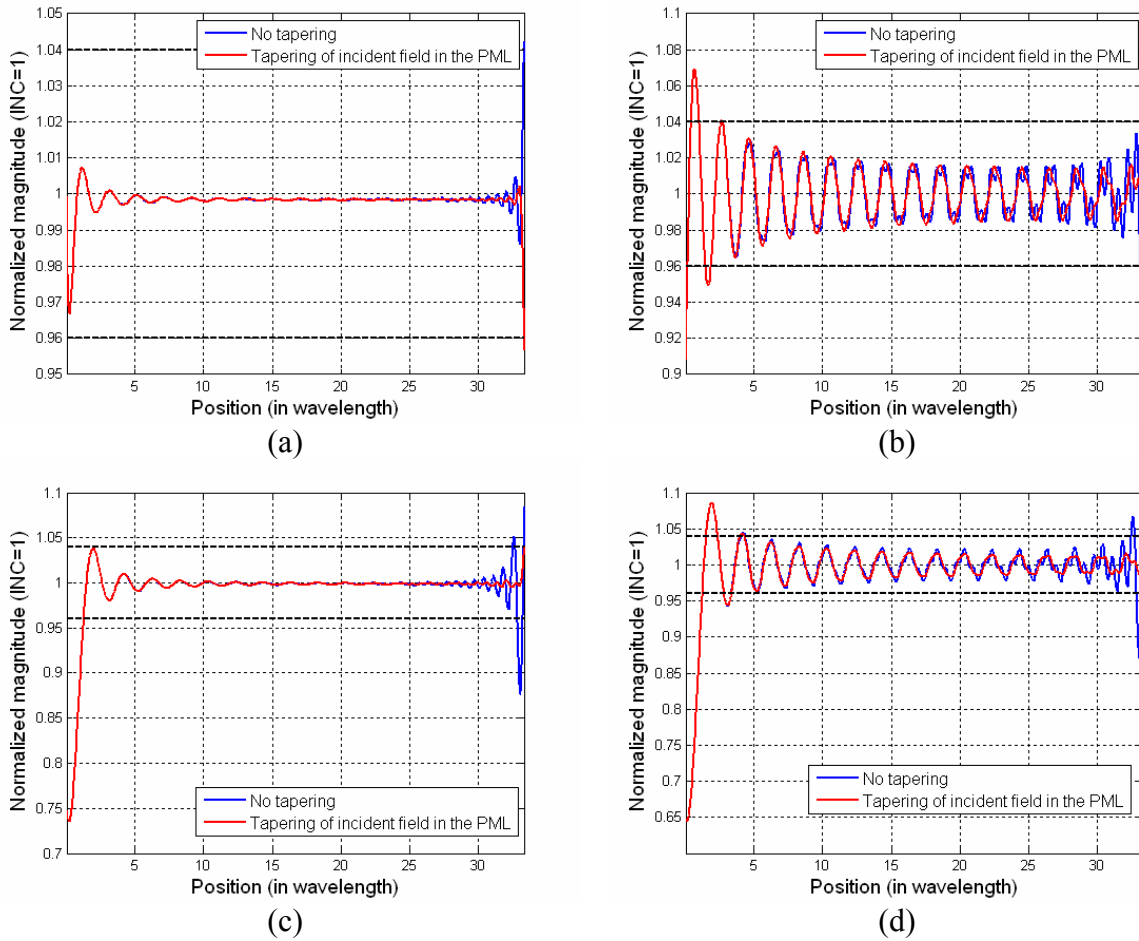


Fig. 4.26: Comparison of the normalized magnitude of E_x (Left) and H_y (Right) at 10 GHz excited with (Red) and without (Blue) applying a Gaussian tapering window on the “incident field” in the PML region on the positive x-end. The excited E_0 -polarized plane wave is incident from $\phi = 180^\circ$ and $\theta = 150^\circ$. The fields are measured on the TF/SF interface (a-b); and at one wavelength above the TF/SF interface (c-d), respectively.

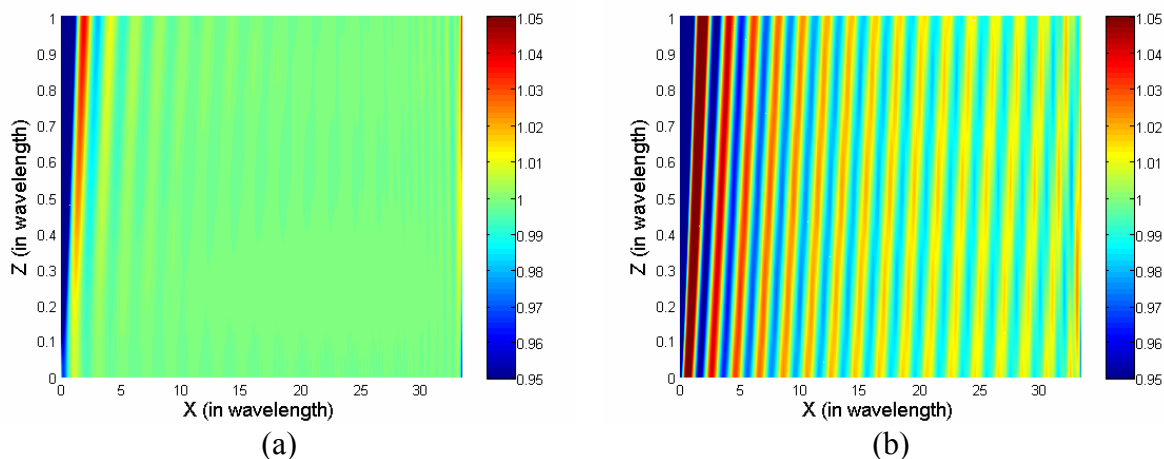


Fig. 4.27: Normalized magnitude of the measured E_x (Left) and H_y (Right) at 10 GHz, in the TF region up to 1λ away from the TF/SF interface (at $Z = 0$). A Gaussian tapering window is applied to the “incident field” in the PML region on the positive x end. The excited E_0 -polarized plane wave is incident from $\phi = 180^\circ$ and $\theta = 150^\circ$.

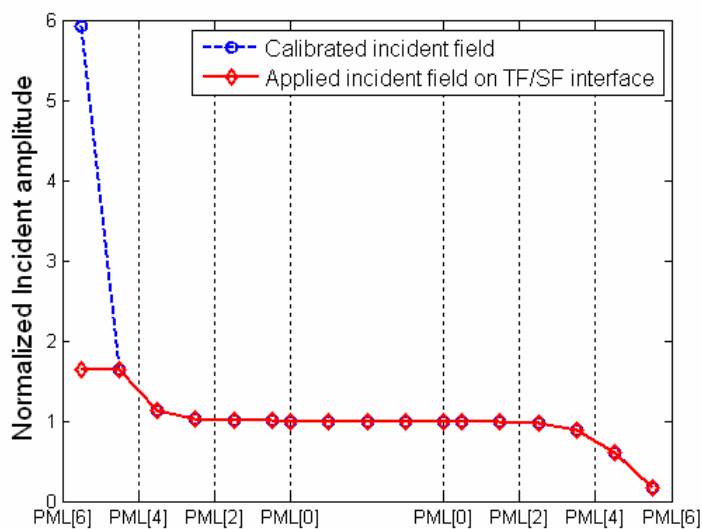


Fig. 4.28: Comparison of the incident field inside the PML region (Blue) which is computed by using the calibration process in [64], and the incident field that we actually apply (Red) on the TF/SF interface.

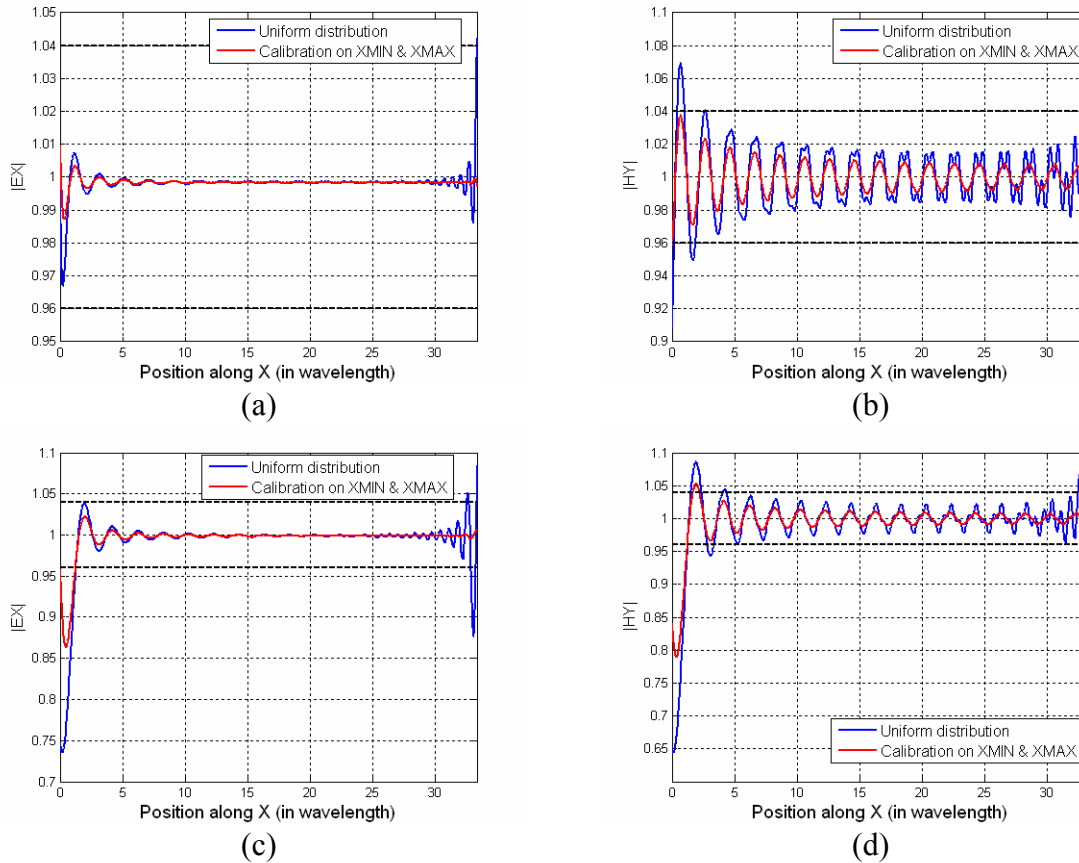


Fig. 4.29: Comparison of the normalized magnitude of E_x (Left) and H_y (Right) at 10 GHz excited with (Red) and without (Blue) using the calibrated incident field (shown in Fig. 4.28) inside the PML region. The excited E_0 -polarized plane wave is incident from $\phi = 180^\circ$ and $\theta = 150^\circ$. The fields are measured on the TF/SF interface (a-b), and at one wavelength above the TF/SF interface (c-d), respectively.

Figures 4.29 (a)-(d) show the comparison of the field distribution X measured on different distance from the TF/SF interface, with and without using the calibrated incident field inside the PML. It can be seen that the reflection originating from the positive x -end has been suppressed considerably, while the one from the negative x -end has been reduced. A shadow region still exists at the negative end, but the level of the field inside the shadow region is closer to the incident level. The remainder of the reflection originated from the edge of the TF/SF interface at

the negative x-end, since the “incident field” is still strong there. Figures 4.30 (a)-(b) show the $|E_x|$ and $|H_y|$ field distribution on the x-z plane, in the TF region up to 1λ away from the TF/SF interface, when the incident field inside the PML is calibrated. It can be seen that the field distribution in the interior of the TF region is much more uniform, as compared to that in the previous cases presented in Figs. 4.23 (c)-(d) and Figs. 4.27 (a)-(b).

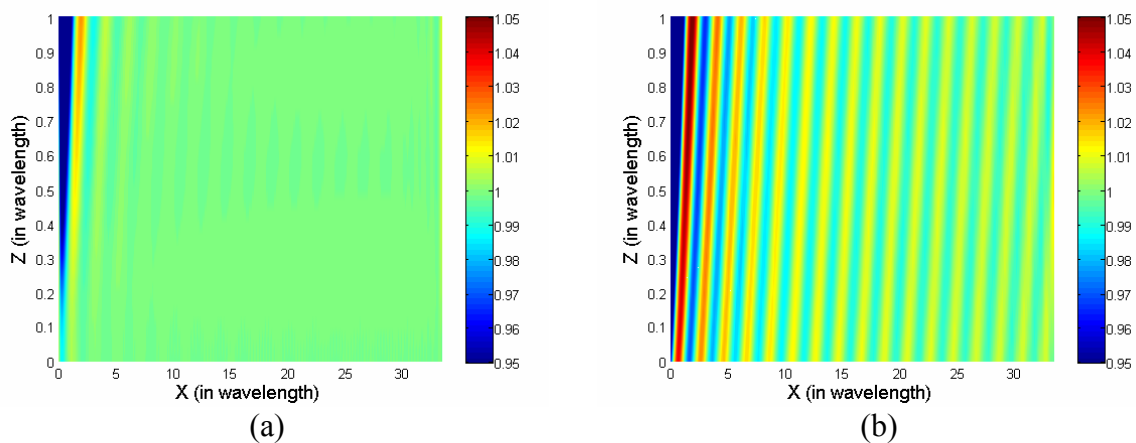


Fig. 4.30: Normalized magnitude of the measured (a) E_x and (b) H_y at 10 GHz, in the TF region up to 1λ away from the TF/SF interface (at $Z = 0$). The incident field inside the PML region is calibrated and applied on the TF/SF interface. The excited E_0 -polarized plane wave is incident from $\phi = 180^\circ$ and $\theta = 150^\circ$.

4.6 Guidelines for Using the Proposed Excitation Scheme in Plane Wave Excitation

For the normal incidence case, the proposed excitation scheme works well when launching a uniform plane wave in the TF region for all computational domain size and FDTD discretizations of $\Delta \leq \lambda/20$. However, it is always a good practice to put the TF/SF interface close to the scattering structure to reduce the error introduced by the dispersive nature of the FDTD grid.

For the oblique incidence case, the proposed excitation scheme works well for small incident angles, say less than 20° , and its performance deteriorates when this angle increases. Figure 4.31 (a) shows the typical field distribution in the plane of incidence for the oblique incidence case. Two non-uniform field regions are formed near the leading and trailing ends of the computational domain, with the region near the leading end dominating the one near the trailing end. The size of the non-uniform field regions expands steadily when moving away from the TF/SF interface. The field located between these two regions is much more uniform and propagates as a plane wave along the desired direction. A windowing technique can be applied in our excitation scheme to remove the non-uniform field region near the trailing end, and shrink the region of non-uniform field near the leading end. We note here that the fields are largely uniform along the direction normal to the plane of the incidence.

Even with the existence of non-uniform field regions for moderate incident angles, we can still apply the proposed excitation scheme to accurately simulate the scattering problems. The idea is to keep the interested region of the scattering structure completely inside the uniform field region and away from the non-uniform field region (see Fig. 4.31 (a)), and this can be achieved in two different ways. First, the TF/SF interface should be placed close to the scattering structure, since the uniform field region shrinks when we move away from the TF/SF interface. Second, if the interested region is not within the uniform field region (see Fig. 4.31 (b)), we can extend both the structure and the computational domain in a way such that the interested region is completely encased within the uniform field region. It should be noted that the proposed excitation scheme is inefficient for large incident angles, since the computational domain must be extended to a size several times that of the original problem to obtain accurate results.

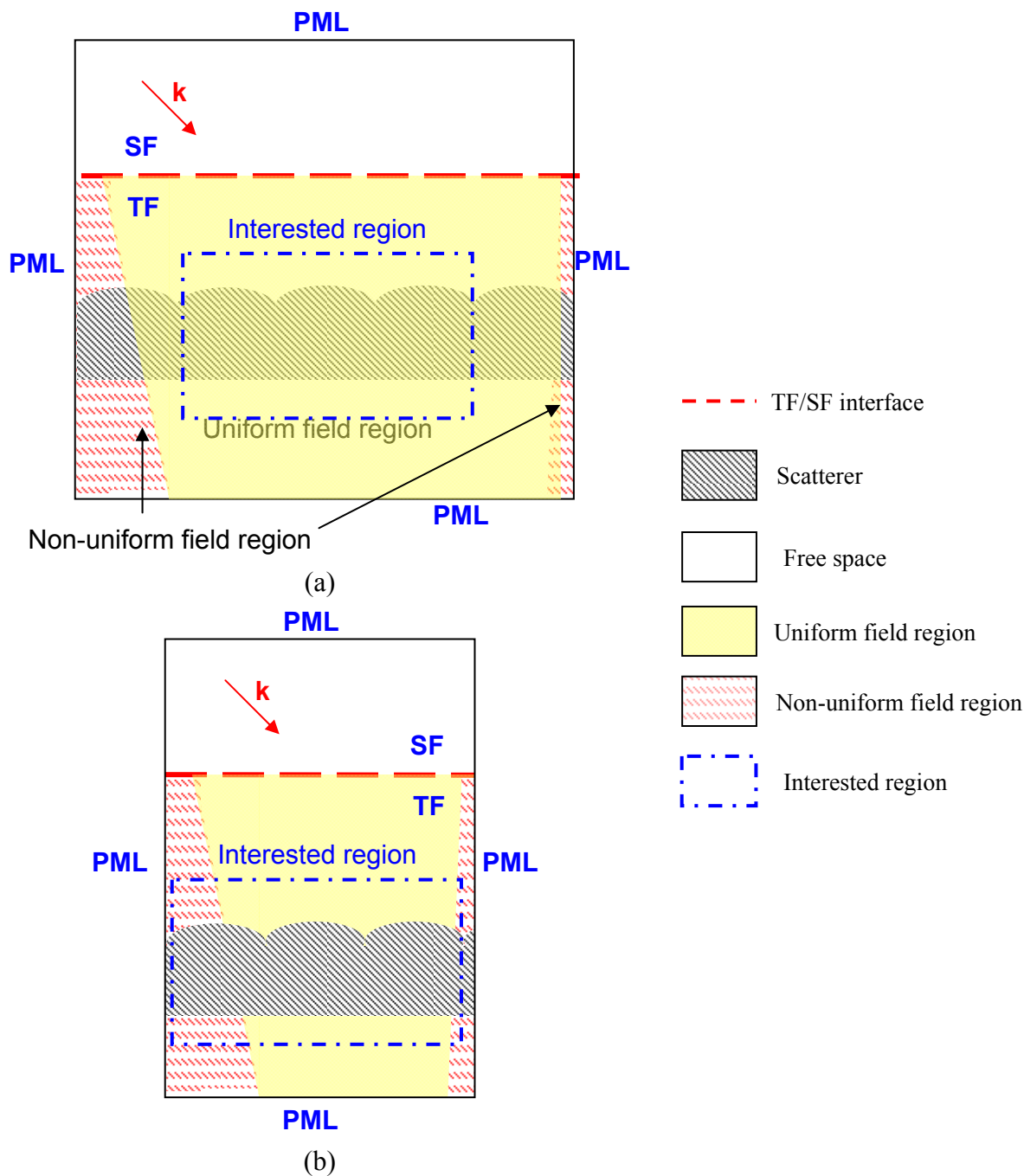


Fig. 4.31: The typical field distribution in the plane of incidence, when a plane wave of moderate incident angle is excited by using our proposed scheme. (a) The interested region is completely embedded inside the uniform field region, and (b) The interested region is partly embedded inside the non-uniform field region. An extension of computational domain is necessary to obtain accurate results.

4.7 Numerical Example for Plane Wave Illumination

In this example, a dielectric cube is buried in an infinite half-space, which is illuminated by a normally incident plane wave, and we desire the backscattered field from the cube in the far-zone. Figure 4.32 shows the geometry of this problem. The cube, whose material properties are $\epsilon_r = 2.9$ and $\sigma = 0.00167$ S/m, has the dimensions of $0.1 \text{ m} \times 0.1 \text{ m} \times 0.1 \text{ m}$; thus its sides are 0.2λ at the frequency of interest (600 MHz). The center of the cube lies 0.1 m beneath the surface of a homogeneous, lossy dielectric ground ($\epsilon_r = 3.0$ and $\sigma = 0.00334$ S/m).

A TF/SF interface is introduced at three FDTD cells ($\Delta = 0.01 \text{ m}$) above the ground in order to excite a plane wave by using the proposed scheme described above. The scattered far-field in the backward direction is measured by applying the near-to-far transformation to the aperture field, located one FDTD cell above the TF/SF interface. In order to obtain the scattered far-field contributed by the dielectric cube, we run two simulations, one with the ground only, and the other with both the ground and the dielectric cube, and then subtract the results from these two simulations to get the scattered far-field pattern by the dielectric cube only.

The computational domain has the dimensions of $5 \text{ m} \times 5 \text{ m} \times 0.45 \text{ m}$, much larger than that used in [71] along the transverse direction ($0.455 \text{ m} \times 0.455 \text{ m} \times 0.455 \text{ m}$). It has been demonstrated that our proposed scheme works well for all domain sizes when employed to launch a plane wave at normal incidence; therefore, there is no need to extend the ground to obtain a uniform field distribution. However, in our far-field calculation, the Huygen's surface, which resides above the ground, needs to be sufficiently large, so as to capture all of the fields scattered backward from the dielectric cube for accurate results. On the other hand, both the plane wave excitation and the near-to-far transformation steps have been significantly modified

in [71], such that both the TF/SF interface and the Huygen's surface are allowed to be partially embedded in the homogeneous ground. However, these approaches only work in special cases, where a closed-form solution of the "incident field" in the presence of the ground, and the Green's function for the ground can be derived.

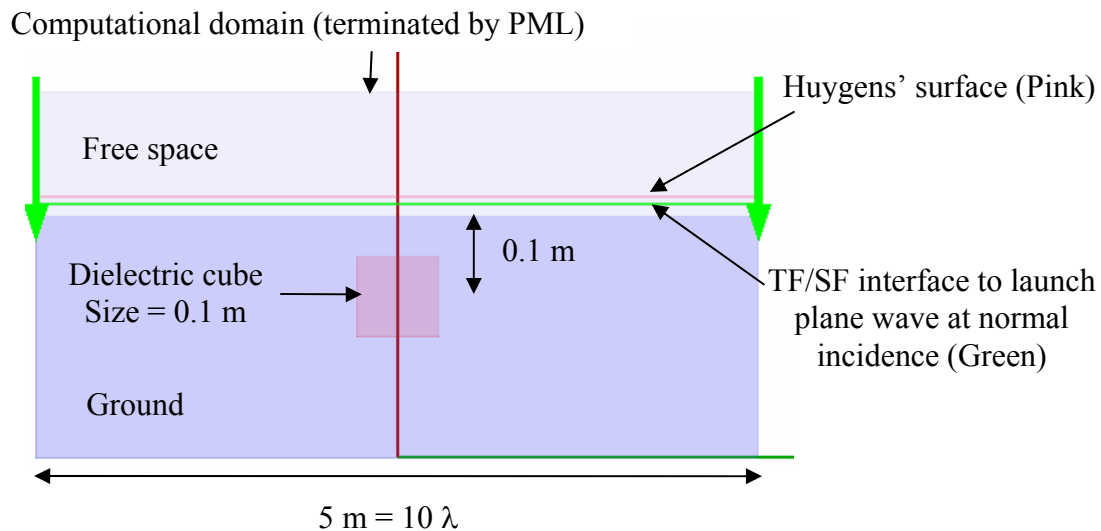
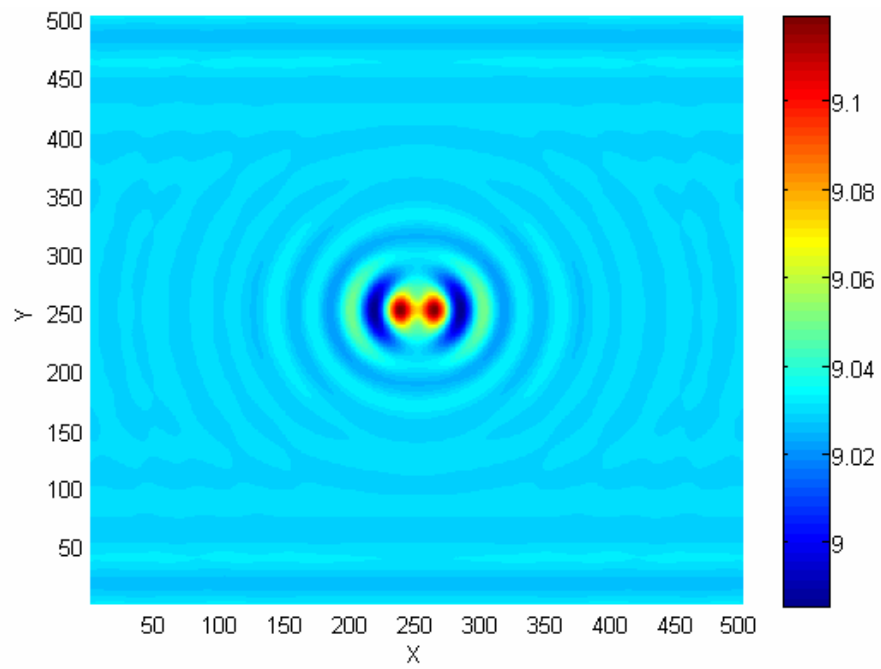
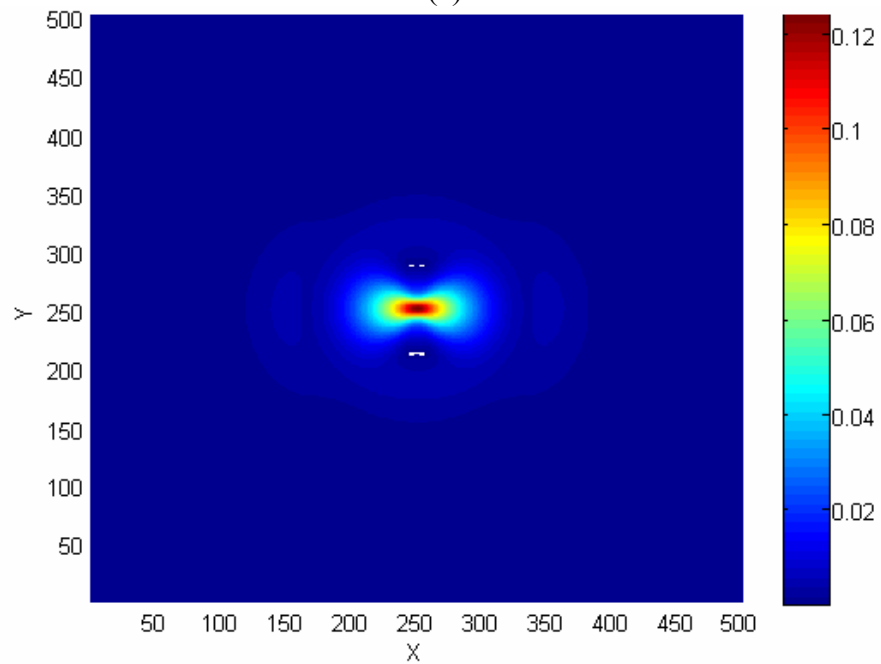


Fig. 4.32: Geometry of the scattering problem of a buried object.

Figure 4.33 (a) shows the scattered field distribution in the presence of both the ground and the dielectric cube at 600 MHz. By subtracting the scattered field measured in the two simulations as described above, we obtain the scattered field distribution (see Fig. 4.33 (b)), contributed by the dielectric cube alone. Figure 4.34 compares the far-zone scattered electric fields from the dielectric cube, with the FDTD results displayed in red and those reported in [64] in black. The agreement between the two results is seen to be excellent.



(a)



(b)

Fig. 4.33: (a) The scattered field in the presence of the ground and the dielectric cube (b) The scattered field contributed by the dielectric cube only.

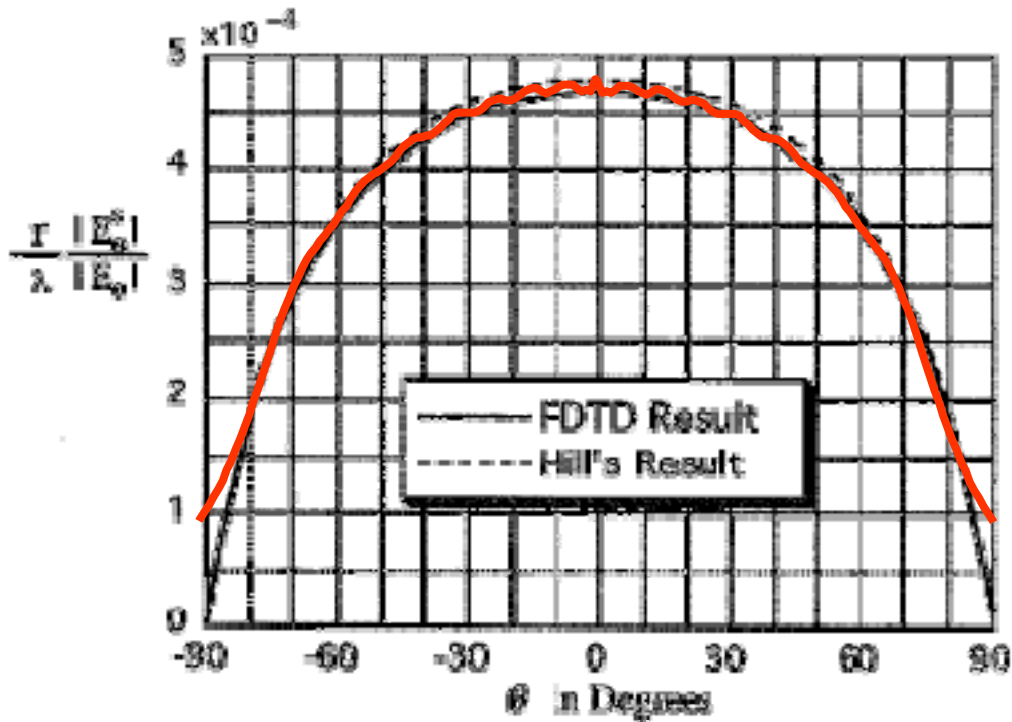


Fig. 4.34: The far-zone scattered electric field from a dielectric cube for our FDTD result (Red) and those obtained in [71] (Black solid and dashed lines).

4.8 Conclusions

In this chapter, we have proposed an excitation scheme, based on modifying the conventional TF/SF approach, to launch the desired incident field distribution in scattering problems involving infinite structures. Instead of using a closed TF/SF box in the conventional TF/SF approach, we have applied the TF/SF technique only on a single plane. A windowing function can also be applied to the “incident field” excited on the TF/SF interface to generate the desired incident field distribution, which can be something other than a uniform plane wave.

For a Gaussian beam illumination, we have demonstrated that the proposed scheme works excellently for practical situations, provided the beam waist of the Gaussian beam is greater than one wavelength, and the interested region is larger than the spot size.

For a plane wave illumination, we have shown that the reflection from the edge of the TF/SF interface has been reduced significantly by extending the TF/SF interface into the PML region. This reflection is barely observed at normal incidence, and remains acceptably low for small incident angles. We have also demonstrated the reduction of the reflection level by applying a window function to the incident fields used on the TF/SF interface within the PML region. In addition, guidelines have been set up for “when and how to” use this scheme in order to obtain accurate results in practical simulations.

The main limitation of this scheme stems from the reflection arising from the edge of the TF/SF interface, which precludes its usage for plane waves incident at highly oblique angles. Further efforts are needed to overcome this shortcoming of the proposed excitation scheme.

Chapter 5

INVESTIGATION OF DOUBLE-NEGATIVE METAMATERIAL SLABS BY USING THE FDTD TECHNIQUE

5.1 Introduction

Metamaterials are man-made composite structures that are tailored to exhibit certain unusual properties not readily found in nature. In particular, double-negative (DNG) metamaterials, whose electric permittivity and magnetic permeability both have negative real parts, have attracted much attention recently because of their interesting properties, as well as potential applications. This type of metamaterials is also known as “left-handed” material (LHM), negative refractive index material (NRIM), backward wave medium (BWM), negative phase velocity medium (NPVM), and so on. All of these names suggest that they have unusual properties that differentiate them from the majority of the conventional materials.

Veselago was perhaps one of the first to propose the concept of negative electric permittivity (ϵ) and magnetic permeability (μ) in a paper [47] published in 1968. He pointed out that since the square of the refractive index equals the product of ϵ and μ , wave propagation is possible inside a lossless medium whose ϵ and μ are either simultaneously positive or negative. He also classified all known materials into 4 quadrants in the ϵ - μ space, as depicted in Fig. 5.1. Most known materials fall in the first quadrant with positive ϵ and μ , and the plasma medium belongs to the second quadrant with negative ϵ and positive μ , when it is excited below the plasma resonant frequency. He left the third and fourth quadrants empty because there was no single substance found with negative μ at that time. He suggested that the DNG materials in the

third quadrant would exhibit properties very different from those of the conventional ones. Some of these properties, depicted in Figs. 5.2 and 5.3, are: (i) E and H fields, and the wave vector (k) form a left-handed system of vectors; (ii) the wave vector is anti-parallel to the Poynting vector; and, (iii) the refractive index is negative. He further postulated a superlensing effect (see Fig. 5.4), which is attributed to the fact that rays emanating from a point source outside a flat DNG slab, whose refractive index is -1 , would be refocused at a point on the other side of the slab, and the total phase shift between the source and image would be zero. Later, Pendry [72] claimed that the DNG slab can also recover the evanescent waves at the image location, and, hence, he argued that this focusing effect would not be limited by the diffraction limit that is associated with conventional lenses. However, because of the lack of material that exhibits negative values of the permeability, Veselago's work laid dormant for nearly 30 years.

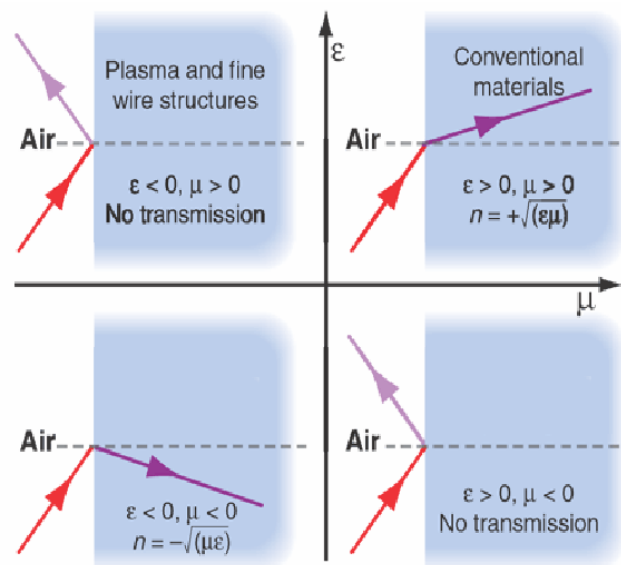


Fig. 5.1: ϵ - μ space.

It was not until 1999, Pendry [58,59] argued on the basis of the effective medium theory, that the array of thin wires would have a negative effective permittivity and low loss, while the array of split-ring resonators (SRRs) would exhibit negative permeability at microwave frequencies. Based on these ideas, Smith et al. [48] have experimentally demonstrated the realization of the first DNG metamaterials by combining these two array structures, and the first prototype they produced is shown in Fig. 5.5 (a). The group suggested that the DNG behavior could be confirmed by the appearance of a passband for the combined structure over those frequencies at which neither the constituent structures, namely the SRR or the wire media, are transmitting, as may be seen from Fig. 5.5 (b). Later, these experiments were repeated by several groups and negative refractions were demonstrated experimentally using a DNG wedge [73]. The emerging beam in such a wedge was found to be directed at an angle which is different from that in a double-positive (DPS) wedge, as shown in Fig. 5.6, albeit at a much lower level. Since then, research on DNG metamaterials has become a topic of considerable interest to many research groups around the world. The interested reader is referred to the existing review literature for more details [74-76].

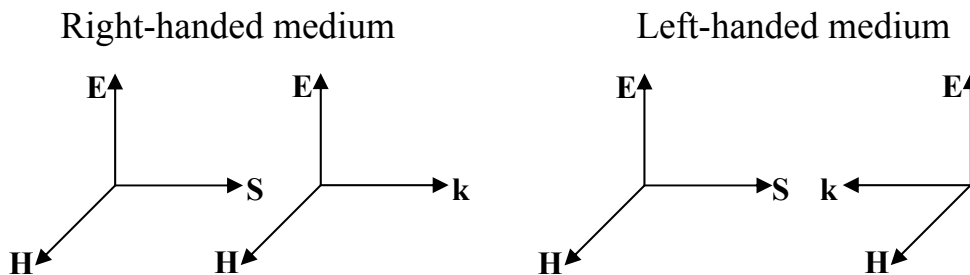


Fig. 5.2: Left-handed and right-handed medium.

It is very common to make use of the effective medium representation to characterize the metamaterials. This representation is often based on the premise that the inclusions in the medium have sizes and periodicities that are sufficiently small in comparison to the wavelength of the impinging radiation. Under this condition, the fine structures of the charge and current distributions are considered to be indiscernible; therefore, the metamaterials structure is simply represented by a homogeneous one that can be represented by its effective material parameters, namely ϵ_{eff} and μ_{eff} , that are determined from the macroscopic EM response of the metamaterials structure.

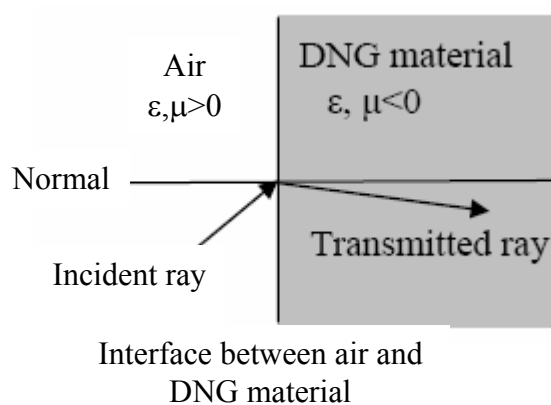


Fig. 5.3: Refraction at the interface between air and DNG material.

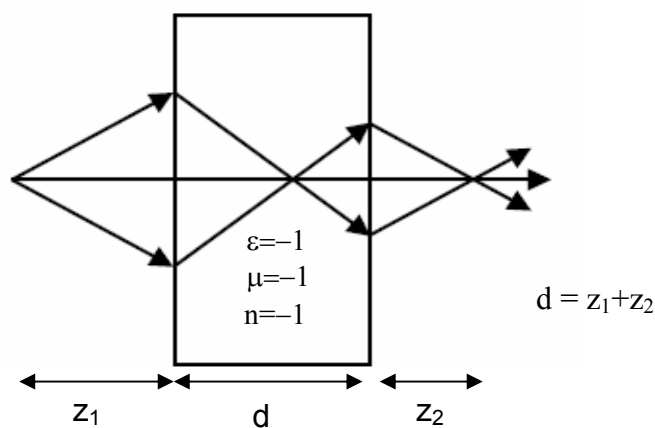
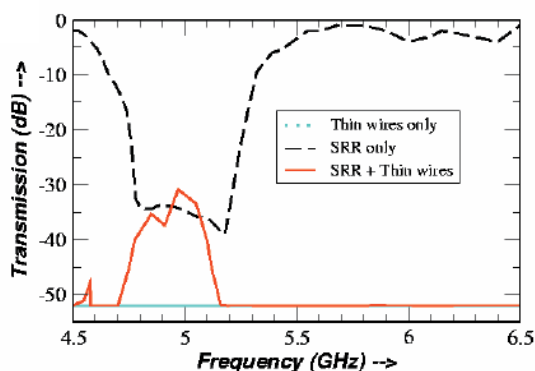


Fig. 5.4: Superlensing effect by a DNG slab.

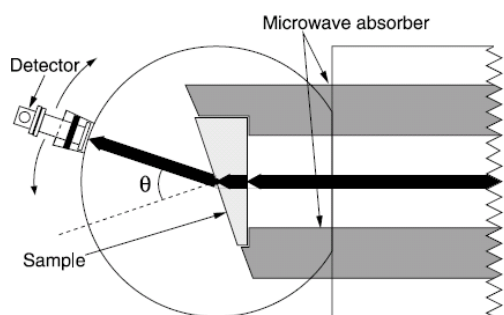


(a)

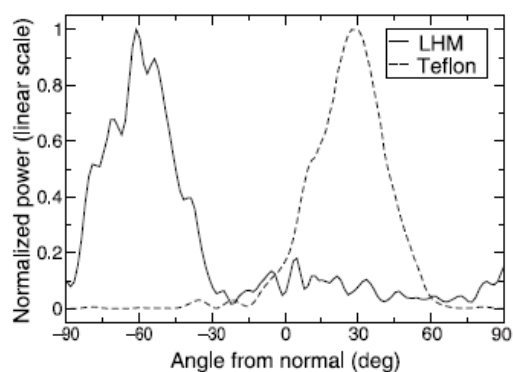


(b)

Fig. 5.5: (a) First prototype of DNG structure made of split-ring resonator (SSR) and wires; (b) Measured transmission magnitude.



(a)



(b)

Fig. 5.6: (a) Diagram of experimental set up; (b) Measured power at different direction.

While the concept of effective material parameters of a slab of material is quite straightforward, and while it is relatively simple to use to characterize complex structures, there is a danger that the use of these parameters may oversimplify the EM properties of the metamaterials, so much so that the above parameters may fail to accurately predict the true performance of the antenna/metamaterials composite in real-world applications. For example, the retrieval of these effective material parameters is usually based on the data obtained by illuminating an infinite, doubly-periodic metamaterials slab of finite thickness with a normally incident plane wave, which is typically linearly polarized. As a consequence, these parameters

often fail to predict the true response of the structure when the incident angle or the polarization of the impinging wave is varied, since the EM response at oblique incident angles, and/or for different polarizations, can be very different from that of the normal incidence case, because of the anisotropic nature of the inclusions. Since a practical antenna/metamaterials composite is typically excited by a localized source, whose spectrum comprises a set of plane waves, with different incident angles and polarizations, it is important to carry out a rigorous simulation of the original physical structure—instead of using one that is based on the effective medium representation—for an accurate analysis of the performance of the composite system.

To date, negative refraction has been demonstrated experimentally only for wedges and not slabs with planar interfaces. Moreover, a true perfect-lens type of focusing effect obtained by using negative index materials has yet to be demonstrated. We should add the remark that while the negative refraction phenomenon in a slab and the perfect lens have been confirmed by many researchers using numerical simulations, this has been the case only when the physical DNG medium has been replaced by a homogenous one with desired effective medium characteristics, such as one satisfying the Drude model. To-date, none of these works have demonstrated the existence of the above two phenomena through rigorous simulations that deal with a physical medium containing real inclusions, whose effective medium properties are DNG in nature, and in which the mutual coupling effects between various elements have been accounted for rigorously. Furthermore, the periodicity in the longitudinal direction, which plays a rather important role, has been ignored in the homogenized version of the configuration, which summarily ignores the effects of higher-order Floquet modes (longitudinal) that invariably exist in the medium.

Perhaps one of the main reasons that dissuades many researchers from performing a rigorous numerical analysis of the entire system, and drives them toward the use of the simplified models based on effective material parameters—despite the shortcomings of the latter that we pointed out previously—is that the task of numerically simulating these complex, multi-scale structures can be formidable, to say the least. This is because the periodicities of the inclusions are often required to be smaller than the wavelength at the desired frequency to justify the effective medium approach, and because these inclusions often have irregular shapes with fine structures in order to generate the electric and magnetic resonance responses that we desire. Therefore, the number of Degrees of Freedom (DoFs) associated in the modeling problem can be so large as to be prohibitive for any EM full-wave solver running on a single processor, because of the heavy burden placed on the computational resources, even by a moderate-size problem. However, the parallel FDTD solver, which we have employed extensively in this work, is well capable of accurately modeling inhomogeneous materials with complex configurations, requiring the solution of very large problems, which are accomplished by exploiting its highly efficient nature of the parallel implementation of the FDTD algorithm. For instance, we can routinely solve problems involving upward of $10E9$ unknowns, by running the parallel FDTD solver on parallel platforms.

In this chapter, we first analyze the EM response of an infinite, doubly-periodic DNG slab comprising of arrays of a combination of split-rings and wires, by using the PBC/FDTD technique, which was described in Chapter 3. Next, we examine the concept of effective material parameters, by going through the retrieval process of these parameters using one of the most widely used techniques, namely, the inversion approach. We will also summarize the difficulties encountered in the retrieval process, and identify some issues and problem areas that may be

encountered when using effective material parameters in real-world applications. Finally, we will simulate a finite, moderate-size DNG slab excited by Gaussian beams, as well as a small dipole, to search for the existence of two interesting phenomena, namely the negative refraction inside the slab and the superlensing effect, that has yet to be demonstrated by using rigorous numerical simulations of slabs containing real inclusions.

5.2 EM Response of the Infinite, Doubly-Periodic DNG Slab with Plane Wave Illumination

5.2.1 Model Description of the Array Comprising of Split-Ring Resonators and Wires

The metamaterial slab considered in this investigation is an infinite, doubly-periodic array comprising of a combination of split-ring resonators (SSRs) and thin wires, beginning with one and going up to six layers in the longitudinal direction, that stand alone in free space. The configuration of this unit cell, which is identical to the one used in Sec. 3.6.2 (see Figs. 3.21 and 3.22), is also similar to the one used in the first DNG structure realized by Smith et al.[48], shown in Fig. 5.5, except that a somewhat simpler configuration of a “single” split-ring is employed in the present study, as opposed to a double ring. It should be pointed out that the configuration of the unit cell and the separation distance between the layers are kept the same throughout all the work in this chapter, since we do not intend to perform a parametric study of the microscopic configuration of metamaterial structures.

An explanation of the DNG behavior, exhibited by a composite comprising of SRRs and thin wires, is as follows. First, it is shown that a 2-D array of thin, continuous wires exhibits a resonant frequency response similar to that of plasma medium. Below the resonant frequency, which is determined by the spacing and cross-sectional area of the wires, the permittivity is negative and hence, no transmission is possible. Second, it is demonstrated that a negative

permeability could be achieved by using an array of SRRs. The SRRs act like magnetic dipoles, with a resonant response resulting from internal inductance and capacitance, that are contributed by the loop area and the split in the ring (also the gap between the inner and outer rings in the double-ring configuration), respectively. Close to resonance, the SRRs generate strong magnetic fields whose directions are opposite to that of the incident magnetic field, which, in turn, results in a negative effective permeability. Finally, we obtain a DNG structure by combining these two elements whose frequency bands of negative permittivity (for wires) and negativity permeability (for SRRs) have an overlapping region, provided the mutual coupling effects between these two types of elements is small*. In the overlapping band, the composite exhibits a DNG behavior, and transmits the incident signal through, because its wave number, given by $k = (\omega/c)(\epsilon\mu)^{1/2}$, is real. Since the SRRs and the wires in the slab both lie in the same plane (y-z), the slab is anisotropic; thus it only couples to E_y and H_x when exhibiting the DNG behavior.

For details of the geometry of the structure and the FDTD settings, the reader is referred to Sec. 3.6.2. The array has periodicities of 2.25 mm and 5 mm along the x- and y-directions, respectively, and a separation distance of 4 mm between layers for multi-layer configuration. A uniform FDTD cell-size Δ of 0.125 mm is employed throughout the computational domain, which requires a total of $18 \Delta \times 40 \Delta \times 84 \Delta$ and $18 \Delta \times 40 \Delta \times 225 \Delta$ to represent the 1- and 6-layer cases, respectively.

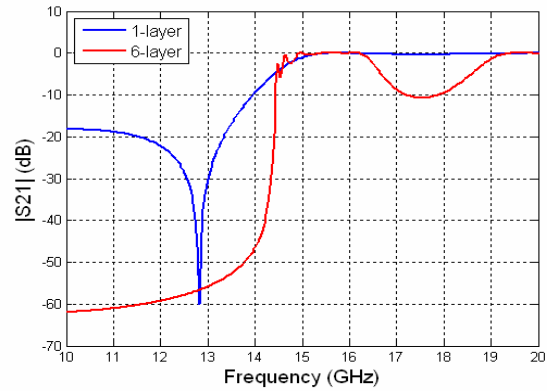
5.2.2 Scattering Parameters Measurements Obtained from the PBC/FDTD Code

The S-parameters for the slab of three different types of inclusions, specifically a combination of SRRs and wires, wires only, or SRRs only, are obtained by using the parallel

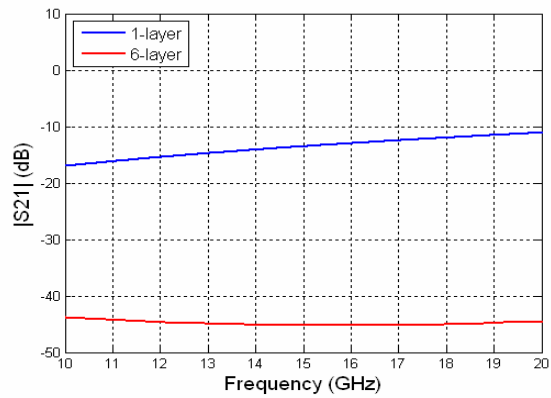
* Note, the numerical simulation we carry out takes full account of the mutual coupling and is rigorous.

PBC/FDTD technique (see Chapter 3), for both the 1- and 6-layer configurations, that are illuminated by a normally incident plane wave. Figures 5.7 and 5.8 plot the transmission magnitude and phase, while Figs. 5.9 and 5.10 display the reflection magnitude and phase for all configurations, respectively.

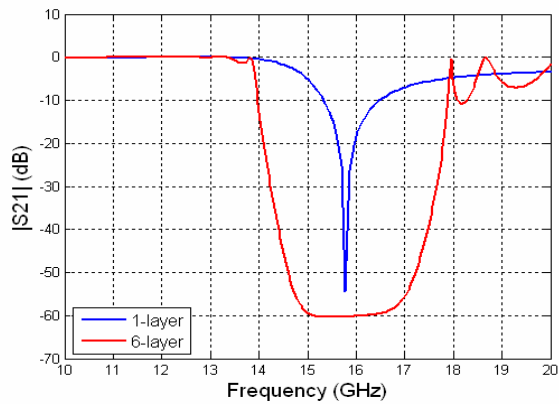
As discussed in the previous section, one clear piece of evidence of the DNG behavior is the existence of a passband for the combined structure, over those frequency bands in which no transmission occurs for the individual structures, though this evidence alone is not conclusive. We can see from Fig. 5.9 (b) that the array of wires is nearly totally reflecting over the entire observed frequency band ranging from 10 to 20 GHz for both the 1- and 6-layer cases. This is expected, since the resonant frequency has been found to be around 30 GHz (not shown in the figure). For the SRR arrays, Fig. 5.9 (c) shows that the 3-dB stopbands are located between 14.8 to 20.0 GHz for the 1-layer case, and between 13.8 to 19.9 GHz for the 6-layer case, except for the two narrow gaps near 18.0 and 18.6 GHz for the 6-layer case. For the combined structure, a 3-dB passband is observed, starting at 14.8 and going up to 20 GHz for the 1-layer case, while two passbands are observed for the 6-layer case, one ranging from 14.7 to 16.4 GHz and the other from 18.8 to 20 GHz. Since all of the passbands of the combined structure fall within the stopbands of the individual structures, it is possible to realize a DNG behavior of the combined structure in these passbands. However, as mentioned before, the transmission characteristic alone is not sufficient to conclude that the material is exhibiting a DNG behavior, since the interaction between the SRRs and wires may lead to a positive effective permittivity and permeability of the medium, which would then be transmitting type in this frequency regime.



(a)

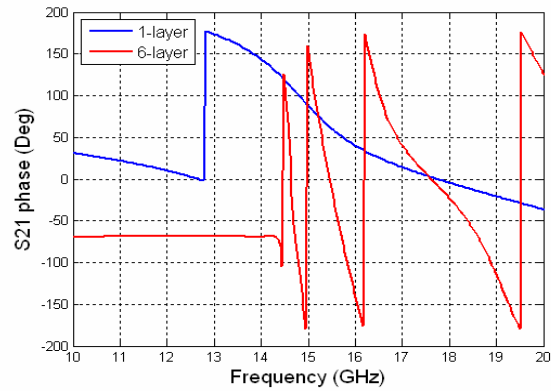


(b)

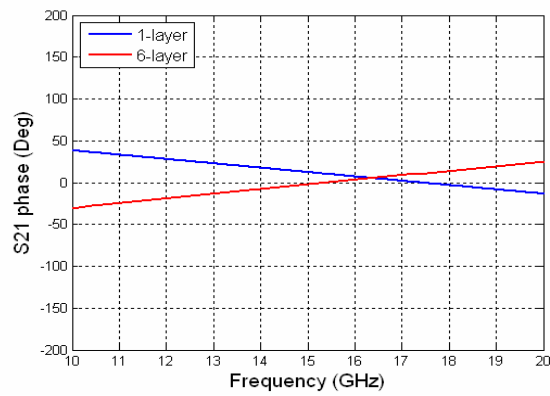


(c)

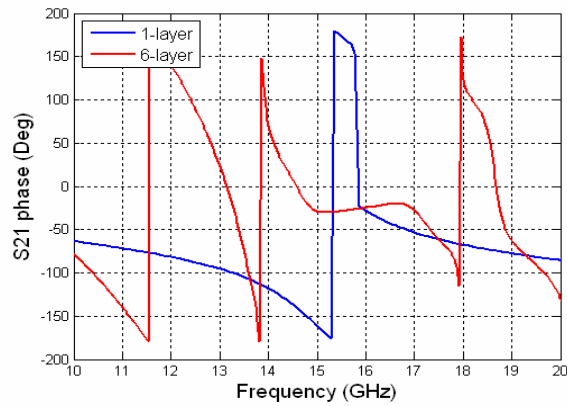
Fig. 5.7: Magnitude of the transmission coefficient for the 1-layer (Blue) and 6-layer (Red) slabs with different types of inclusions: (a) split-ring and wires; (b) wires alone; and (c) split-ring alone.



(a)

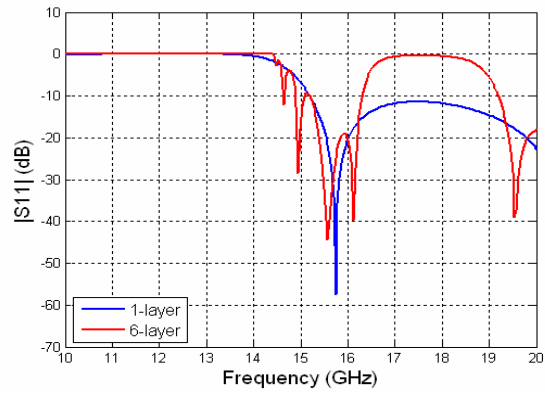


(b)

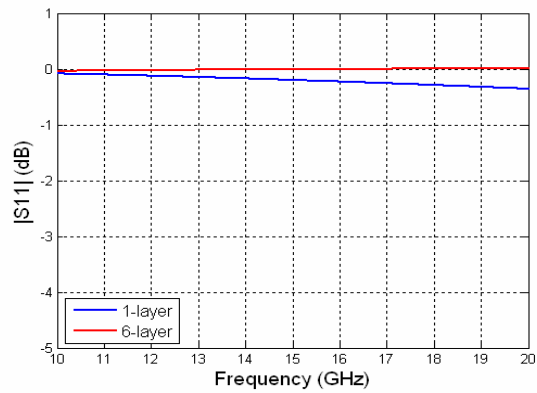


(c)

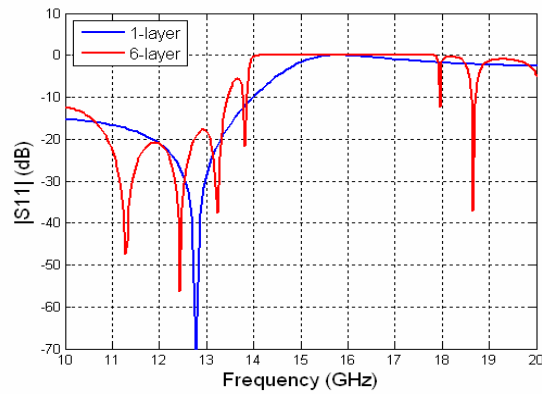
Fig. 5.8: Phase of the transmission coefficient for the 1-layer (Blue) and 6-layer (Red) slabs with different types of inclusions: (a) split-ring and wires; (b) wires alone; and (c) split-ring alone.



(a)

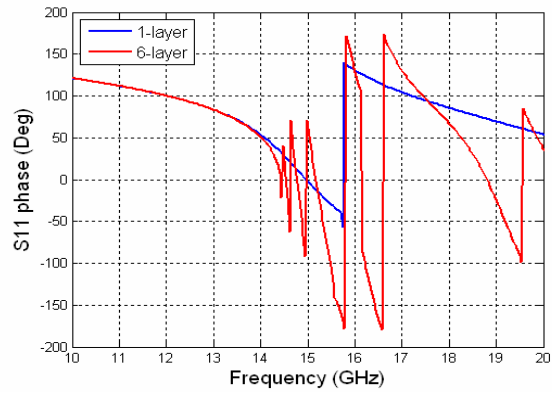


(b)

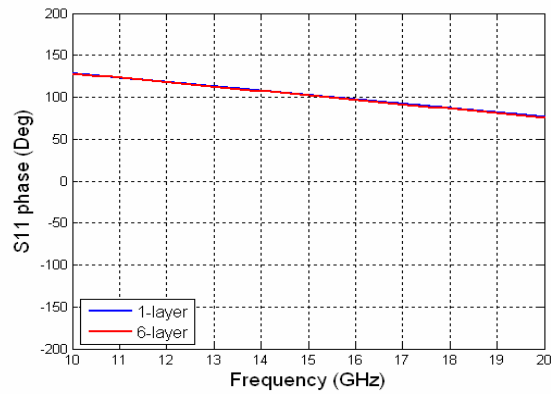


(c)

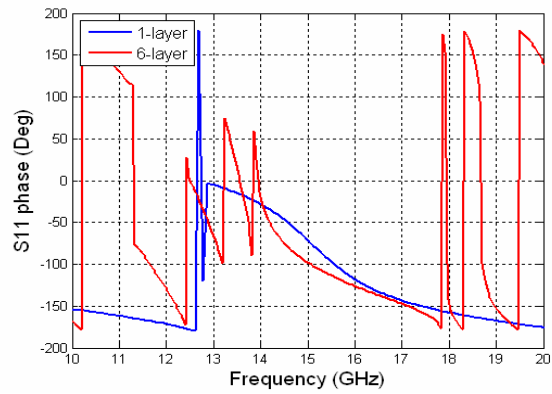
Fig. 5.9: Magnitude of the reflection coefficient for the 1-layer (Blue) and 6-layer (Red) slabs with different types of inclusions: (a) split-ring and wires; (b) wires alone; and (c) split-ring alone.



(a)



(b)



(c)

Fig. 5.10: Phase of the reflection coefficient for the 1-layer (Blue) and 6-layer (Red) slabs with different types of inclusions: (a) split-ring and wires; (b) wires alone; and (c) split-ring alone.

5.2.3 Phase Data Inside the DNG Slab

A more rigorous test to demonstrate the DNG nature of the slab is to directly measure the phase of a propagating wave inside the slab—which can be readily obtained from the FDTD simulations—and for the predicted negative phase velocity of a negative index medium.

In the FDTD simulation of a 6-layer array, comprising of a combination of SRRs and wires, the time-domain fields are recorded along two lines along the z-direction (propagation direction) inside the slab, at different positions on the transverse plane. The DFT technique is then employed to extract the magnitude and phase at the desired frequency from the time-domain data, and phase unwrapping is used to recover the correct phase progression along each line. The normalized magnitude and phase of E_y (note: incident field is E_y -polarized) on these two lines along the direction of propagation are plotted in Figs. 5.11 (a) and (b) at 15.2 and 19.6 GHz, respectively, where the circles are used to denote the boundaries between the adjacent layers. From the slope of the above phase plots, it is evident that the phase propagates backward at 15.2 GHz, while it is forward-propagating at 19.6 GHz. Therefore, the DNG behavior is only observed at 15.2 GHz, within the first passband, but not at 19.6 GHz, which falls within the second passband.

Next, we compute the real part of the refractive index from the phase shift data for frequencies within the two passbands. The slope of the phase is computed as a function of the propagation distance by fitting a straight line to the phase data at the boundaries between the adjacent layers (denoted by circles in Fig. 5.11), and the results are plotted in Fig. 5.12 (a). Since we know that the phase change is equal to a product of n' (real part of refractive index), the free-space wave number (k_0) and the propagation distance (d), the computed values of n' are plotted in Fig. 5.12 (b). It can be seen from this figure that, for the 6-layer case, a negative refraction is

observed in the first transmission band, while the refraction is positive in the second. In other words, for the case of the 6-layer slab, the phase data inside the slab confirms the DNG behavior in the first passband, which ranges from 14.7 to 16.4 GHz, while the permittivity and permeability are positive in the second passband that goes from 18.8 to 20 GHz.

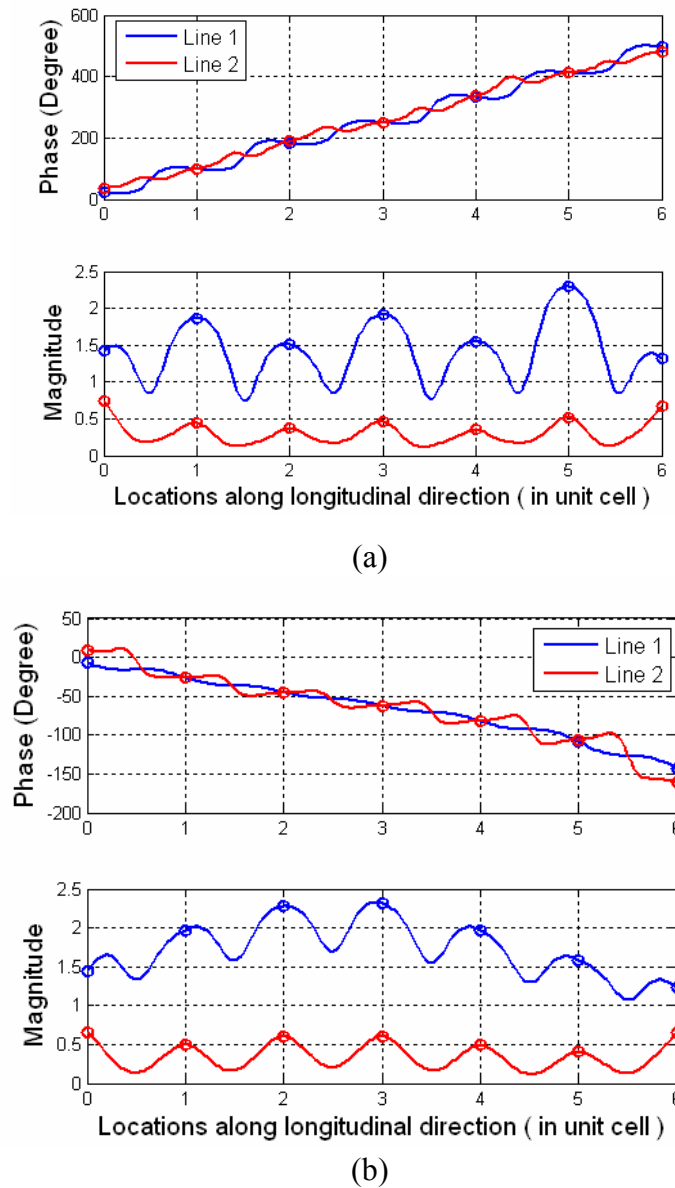
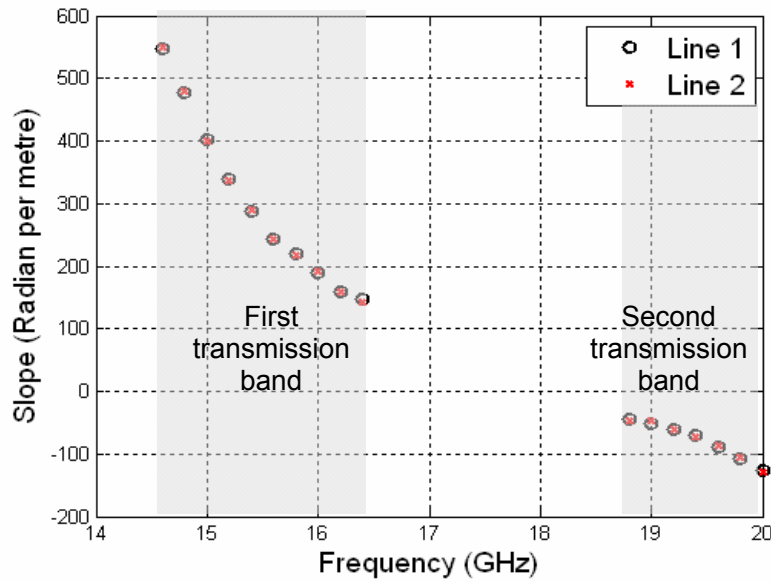
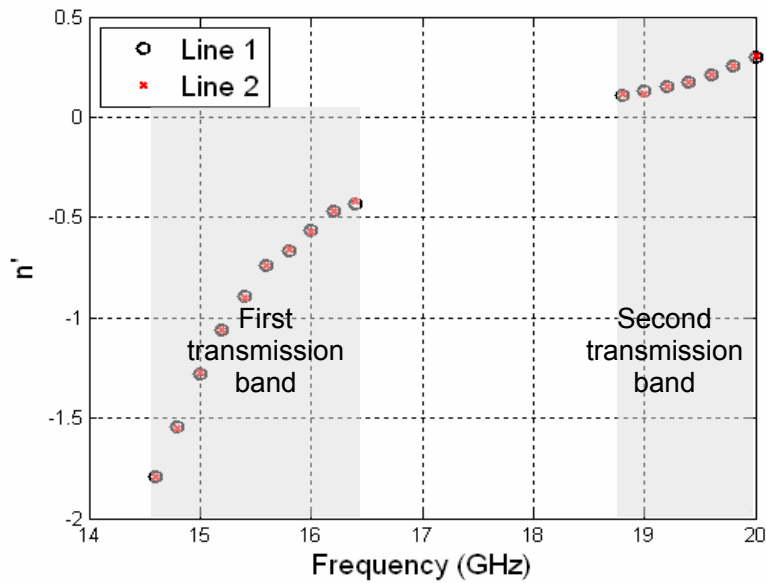


Fig. 5.11: Magnitude and Phase measured inside the 6-layer DNG slab, along two different lines in the propagation direction at (a) 15.2 GHz; and (b) 19.6 GHz. The circles represent the boundaries between the adjacent layers.



(a)



(b)

Fig. 5.12: (a) The slope of the phase against propagation distance computed using the phase data obtained from FDTD simulations. (b) The real part of refractive index extracted from the slope in (a). The slope and the refractive index are only computed within the two 3-dB passbands (in grey) of the 6-layer slab.

5.3 Retrieval of Effective Material Constitutive Parameters Using the Inversion Approach

Availability of a robust method for characterizing an antenna system or its components is essential in engineering applications, since we always seek to achieve a design that meets the specifications for the applications we have in mind, in terms of the operating frequency, bandwidth, loss, and so on. The design process invariably relies upon characterization methods that must be both robust as well as reliable. Following the first experimental realization of DNG metamaterials, researchers began to search for ways to characterize their properties in a systematic way. A great deal of ongoing research has been directed towards determining the effective permittivity and permeability values of a composite that are both self-consistent and unambiguous. Some approaches reported in the literature to obtain the effective parameters from numerical data include: inversion techniques [33,77,78]; averaging methods [58,79,80] based on effective medium theory; or and the use of results of phase velocity calculation [81] obtained from time-domain simulations. The inversion approach is one of the popular methodologies employed for this purpose. Unlike some of the other approaches, which make use of the knowledge of the field distribution inside the composite, the inversion method relies entirely upon the knowledge of the S-parameters of the slab illuminated by a normally incident wave. Note that the above parameters can be obtained either from experimental measurements, or from numerical simulations.

In the following sections, we will first discuss the basic premises upon which effective material parameters concepts are based. Next, we will review the inversion procedure for the retrieval of these parameters, and propose a modified one that helps us to choose the correct branch of the solution when certain approximations are found to be valid. Following this, we

apply the modified approach to process the scattering parameters generated from the FDTD simulations, obtained by using the PBC/FDTD technique discussed previously in Chapter 3. The simulations are carried out for a number of different array settings, namely arrays of wires alone, SSR alone, and combinations thereof, beginning with one and going up to six layers. Finally, we will summarize the difficulties encountered in applying the inversion approach, and follow this up with a discussion on the use of effective material parameters for real-world applications.

5.3.1 Basic Assumption of Effective Material Constitutive Parameters

It is well known that metamaterials are frequently represented by using their effective medium representation. This representation is based on the premise that the inclusions in the metamaterial medium have sizes and periodicities that are sufficiently small in comparison to the wavelength of the impinging radiation. As a consequence, the radiation effectively encounters a spatial average of the polarizabilities of the inclusions filling the medium. In other words, the fine structures of the charge and current distributions are not discernible when the medium is represented in terms of its effective parameters, but only a few average field quantities, such as $\langle D \rangle$, $\langle E \rangle$, $\langle B \rangle$, and $\langle H \rangle$ can be used to describe the medium. The effective electric permittivity and the magnetic permeability of the bulk metamaterials can be defined by relating to these average fields in a simple way.

It is important to note that only certain metamaterials have been found to exhibit the DNG behavior, and that too over a limited frequency range. Furthermore, no single substance has been discovered yet that exhibits the DNG behavior over a wide band. These facts will be evident from the example shown below.

5.3.2 Review of the Inversion Approach

The inversion approach [33] is the most widely used method for retrieving the effective material parameters. It has been investigated by several groups of researchers [77,78], who have developed robust techniques for extracting the effective parameters of the metamaterials. A significant contribution in this area is credited to Chen et al. [78], who proposed significant improvements over the methods previously available. In particular in this work they investigated several important aspects of the inversion procedure in detail, including the determination of the boundary of the homogenized slab; selection of the sign of the roots when solving for the impedance Z ; determination of the branch of the real part of refractive index n . They also explained the origin of the spikes appearing in the impedance Z retrieved, by following the procedure they proposed.

An important attribute of this approach is that it requires no additional assumption except, of course, that the effective medium concept be valid. However, this method does suffer from an inherent multiple-branch ambiguity problem arising from multi-valued nature of the logarithmic and square root functions appearing in the expressions for the refractive index n and the impedance Z . To sort out this situation, the strategy is to eliminate the non-physical solutions by following a set of rules, and assuming that the only solution that survives is the correct one. The procedure for extracting the effective medium parameter from the S-parameters, as well as the selection rules for choosing the correct branches will be discussed in detail in the following paragraphs.

We assume that the electromagnetic fields have the $e^{j\omega t}$ time dependence*. The scattering parameters of a homogeneous slab of thickness d in free space at normal incidence are given by:

$$S_{11} = \frac{\Gamma(1 - e^{-j2nk_0d})}{1 - \Gamma^2 e^{-j2nk_0d}} \quad (5.1)$$

$$S_{21} = \frac{(1 - \Gamma^2)e^{-jnk_0d}}{1 - \Gamma^2 e^{-j2nk_0d}} \quad (5.2)$$

where $\Gamma = \frac{Z-1}{Z+1}$ is the reflection coefficient at the boundary between the two media under study, as shown in Fig. 5.13; Z ($Z = Z' + jZ''$ is assumed) is the wave impedance; n ($n = n' + jn''$ is assumed) is the refractive index of the slab; and k_0 is the free space wave number. Once the reflection and transmission coefficients have been obtained, the refractive index as well as the wave impedance can be calculated by inverting (5.1) and (5.2) to get:

$$Z = \pm \sqrt{\frac{(1 + S_{11})^2 - S_{21}^2}{(1 - S_{11})^2 - S_{21}^2}} \quad (5.3)$$

$$Y = e^{-jnk_0d} = X \pm j\sqrt{1 - X^2} \quad (5.4)$$

$$X = \frac{1}{S_{21}}(1 - S_{11}^2 + S_{21}^2) \quad (5.5)$$

The refractive index n can be calculated from (5.4) and (5.5) by using the expression:

$$n = \frac{1}{k_0d} \{ [\ln(e^{-jnk_0d})]'' + 2m\pi + j[\ln(e^{-jnk_0d})]' \} = \frac{1}{k_0d} \{ [\ln(Y)]'' + 2m\pi + j[\ln(Y)]' \} \quad (5.6)$$

* It should be noted that in most of the references on this topic, a time dependence of $e^{-j\omega t}$ is assumed though this is not being explicitly stated. However, we adopt a time dependence of $e^{j\omega t}$ in this dissertation, which is followed in the convention used in the FDTD as well as in most engineering disciplines.

where m is an integer related to the branch index of n' (real part) and is related to the thickness of the slab, expressed in terms of the wavelength. Once the refractive index and the wave impedance have been found, the permittivity and permeability can be obtained from:

$$\epsilon_{eff} = n / Z \quad (5.7)$$

$$\mu_{eff} = nZ \quad (5.8)$$

The expressions appearing in (5.3), (5.4) and (5.6) contain complex and multi-valued functions. We must, therefore, impose additional constraints to obtain consistent and unambiguous results for the permittivity and permeability. The impedance is a square root function, whose sign ambiguity can be resolved by imposing the condition Z' (*real part*) > 0 , that must be satisfied by all passive materials. However, when the values of Z' are close to zero, even a slight perturbation in the values of the S-parameters can cause the signs of Z' to switch, and this in turn, causes the retrieval procedure to fail. To overcome this difficulty, it has been recommended that the expression that relates n and Z be employed to determine the sign of the impedance [78]. This relationship is given by:

$$e^{-jnk_0d} = \frac{S_{21}}{1 - S_{11} \frac{Z-1}{Z+1}} \quad (5.9)$$

The sign of Z is chosen by using (5.9) such that the corresponding refractive index has a non-negative imaginary part, or equivalently $\left| e^{-jnk_0d} \right| \leq 1$. The impedance Z can be determined explicitly by following these two rules.

The imaginary part of the effective refractive index, i.e., n'' , should be zero or negative, to satisfy the passivity condition. Here we point out that the two roots in (5.4) result in two values of $\ln(e^{-jnk_0d})$, and that only their signs are different. Thus, when n'' is not close to zero, only one root in (5.4) yields a non-positive value for n'' , and the other should be discarded. However, when n'' is close to zero, both the roots should be examined as possible choices when determining the real part of n . Nevertheless, n'' can be determined explicitly and unambiguously in both of these cases.

Up to this point, the impedance Z and the imaginary part of the refractive index n have been determined in an explicit manner. However, when n'' is close to zero, the real part of the refractive index still suffers from ambiguities introduced by the branches of the logarithmic function given in (5.6), and there exists the possibility of two acceptable roots in (5.4). The first ambiguity becomes even more problematic when the retrieval method is used for a thicker slab. This is because d , the thickness of the slab, appears in the denominator of the r.h.s. of (5.6), and the term $\frac{2\pi m}{d}$ becomes small for a large d , making it difficult to choose the correct solution as all the branches now become very closely-spaced. To circumvent this problem, it has been suggested that we use a slab whose thickness is relatively small, and require that the $\varepsilon(f)$ and $\mu(f)$ be continuous functions of frequency [77]. An iterative approach has been suggested in [78] to implement this continuity condition. Assuming that we have obtained the value of the refractive index $n(f_0)$ at a frequency f_0 , we still need to choose m , the branch index, from all the correct roots in (5.4) (note: more than one correct root exist only when n'' is close to zero) such that $n(f_1)$ for the chosen m is closest to $n(f_0)$, where f_1 is the next frequency adjacent to f_0 .

Additionally, the requirements $\mu'' \leq 0$ and $\varepsilon'' \leq 0$ must be imposed since the material is passive, and this helps to discard the non-physical solutions of n' .

The initial solution of n' still needs to be determined at the starting frequency for this iterative approach to work. We can simplify this task by starting at a low frequency, as we will now explain. First, at low frequencies where $k_0 d$ is very small, the branch index m and the root in (5.4) should be chosen such that $[\ln(e^{-jnk_0 d})]'' + 2m\pi$ is close to zero, since this term represents the total phase change across the slab at this frequency. Second, at frequencies well below the first resonance, we would not expect to see DNG-type behavior, which implies that the correct solution should be one for which $n' \geq 0$. The real part of n , i.e., n' , can then be determined at the frequency of interest by imposing these two conditions.

As discussed above, the process for choosing the correct solution in the inversion approach is complex. In Ziolkowski's work [82], this difficult process was avoided by making the approximation of $e^{-jnk_0 d} \sim 1 - jnk_0 d$, which simplifies the expression for the refractive index to yield:

$$n = \frac{k}{k_0} = \frac{1}{jk_0 d} \frac{(1 - V_1)(1 + \Gamma)}{(1 - \Gamma V_1)} \quad (5.10)$$

where $V_1 = S_{11} + S_{21}$, and $\Gamma = \frac{Z - 1}{Z + 1}$ are the reflection coefficients at the two media interfaces,

and Z is the wave impedance that can be computed by using the inversion approach in an unambiguous manner. However, we note that, according to [82], the above approximation is valid when

$$|n' k_0 d| \leq 1 \quad (5.11)$$

while others have pointed out that the correct condition for this approximation to hold is:

$$|nk_0d| \ll 1 \quad (5.12)$$

For the sake of the discussion below, we will refer the solution in (5.10) to be the Small-Phase-Small-Loss (SPSL) solution.

Even though (5.12) holds for a very limited range, we will employ the SPSL solution to assist the selection of the correct root in the inversion method, when all the solutions remaining after the elimination of the non-physical ones satisfy (5.12).

We will now summarize the steps in our modified inversion procedure in the following.

They are:

- (I) Compute Z using (5.3). The sign can be determined by using the following rules:
 - a. If Z' is not close to zero, choose the root with the positive real part.
 - b. If Z' is close to zero, choose the root, by using (5.9), such that $\left|e^{-jnk_0d}\right| \leq 1$.
- (II) Compute all possible solutions of n by using (5.4) to (5.6) for the two roots in (5.4) and a set of chosen branch indices $\{m\}$. Compute the effective ε and μ for all solutions of n and the Z extracted by using (5.7) and (5.8).
- (III) At this point, we have multiple sets of solutions, but only one of these sets is physical. Choose the correct solution by eliminating the non-physical ones. These physical rules are:
 - a. At frequency well below the first resonance, choose the solution that yields $n'' \leq 0$ and n' is closest to 0 from the positive side.
 - b. When n'' is not close to zero, discard the solutions computed from the root that yields a positive n'' .

- c. Examine ϵ'' and μ'' associated with the remaining solutions. Discard the solutions that give rise to positive ϵ'' or μ'' .
 - d. Enforce the continuity of n' .
- (IV) If more than one solution still satisfies the requirements set forth above in this stage, we check the values of $|nk_0d|$ for all of the remaining solutions. If $|nk_0d| \ll 1$ still holds for all of the remaining solutions, apply the SPSL criterion, given in (5.10), to choose the correct branch.

5.3.3 Retrieval of the Effective Material Parameters from the Numerical S-Parameters Obtained from FDTD Simulations of Metamaterials

The first step taken in the inversion approach is to define the location of the two effective boundaries of a metamaterial slab, which does not have a well-defined surface as does a homogeneous slab. Since we know that the impedance of a homogeneous slab does not depend on thickness of the slab, we can define the surfaces of the slab such that the results for the impedances extracted for the slabs show a consistent behavior as the number of layers is progressively increased. The S-parameters measurement uses these effective surfaces as the input and output ports, and the effective thickness (d) of slab is defined to be the separation distance between these surfaces.

We will now study the DNG array, described in Sec. 5.2, starting with one layer and going up to three, by using the PBC/FDTD code as described in Chapter 3. Three pairs of measurement planes, positioned at one, two and three FDTD cells, respectively, beyond the outermost edge of the metallic inclusions on each side of the slab, are tested for the optimal effective surfaces, as shown in Fig. 5.13. For each pair of test planes (at the transmission and

reflection sides, respectively), the S-parameters were derived by using the technique described in Sec. 3.5.2, and the wave impedance was computed by using the inversion approach, with the effective slab thickness defined as the separation distance between these planes. The optimal locations of the interfaces are found by minimizing the mismatch of the impedance for different number of layers. Figures 5.14 (a) – (f) show the real and imaginary parts of the wave impedance for one to three-layer cases, that are retrieved from the S-parameters computed for the three pairs of test planes described above, respectively. It can be seen that the mismatch of the wave impedance for different layers is the smallest when the test planes are located at three FDTD cells beyond the outermost edge of metallic inclusions (see Figs. 5.14 (c) and (d)). For this reason, we define these planes to be the effective surfaces for the slab.

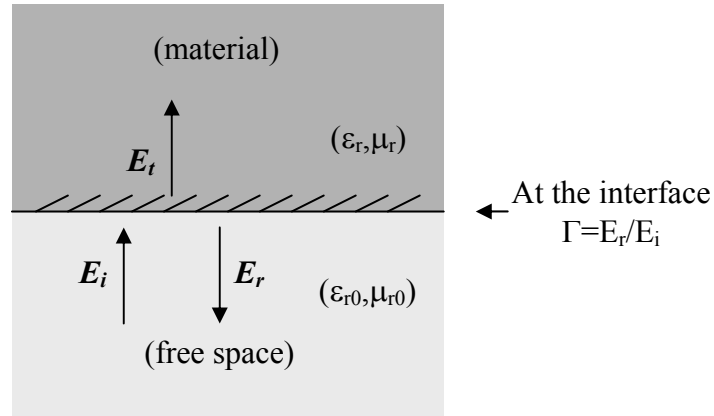


Fig. 5.13: Wave reflection and transmission at normal incidence by a planar interface.

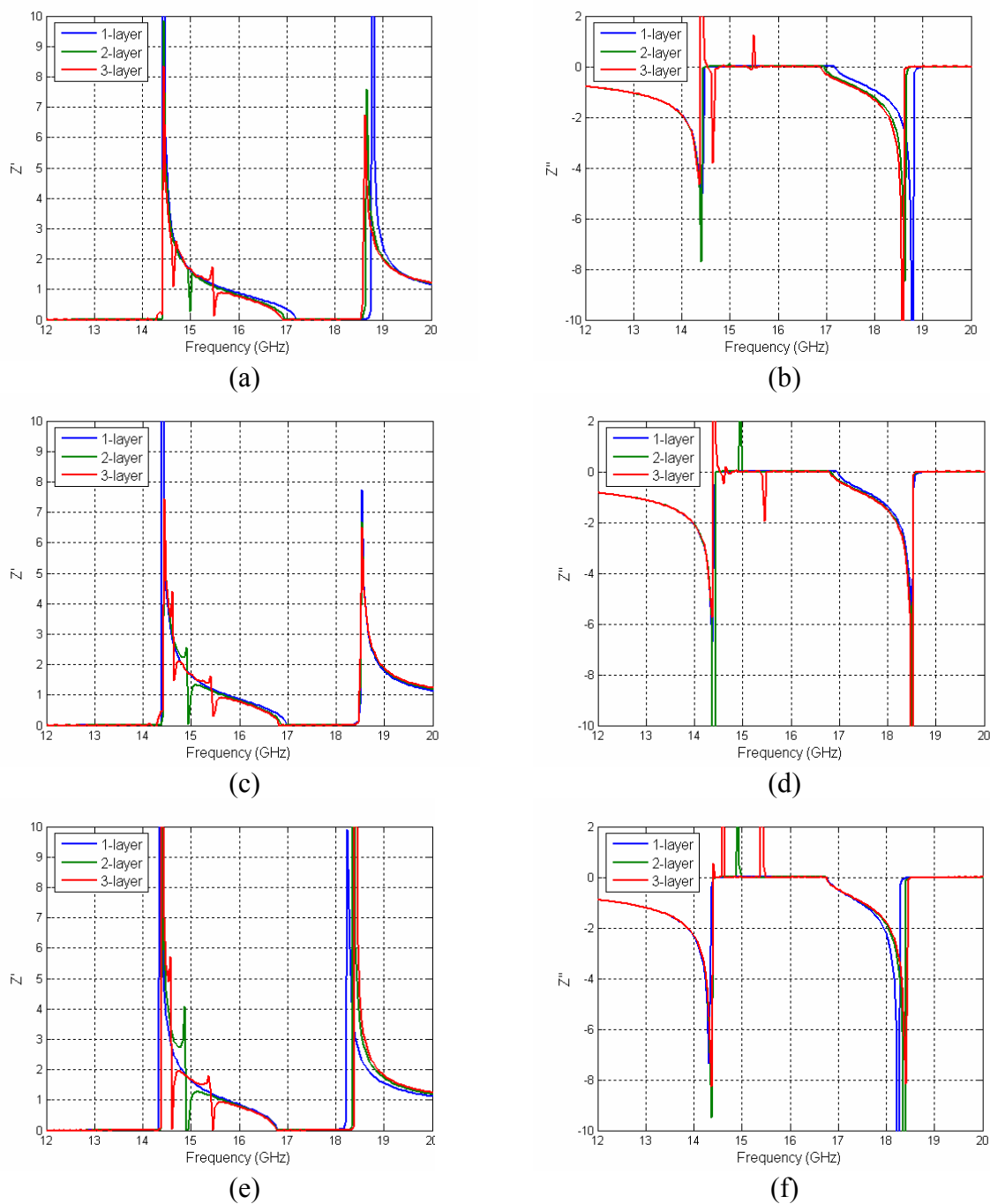


Fig. 5.14: Comparison of the extracted impedance Z (LEFT: real part, RIGHT: imaginary part) for slabs of 1-, 2-, and 3-layers with inports and outputs placed at different locations: (a) and (b) 1 FDTD cell; (c) and (d) 2 FDTD cells; and (e) and (f) 3 FDTD cells beyond the outermost edge of the metallic inclusions on each side of the slab.

We now begin to demonstrate the retrieval process for the single-layer DNG array case. Figure 5.15 shows the wave impedance which has been determined by using (5.3) and (5.9), without ambiguity. Figure 5.16 shows the solution of n'' derived from the two roots in (5.4), by using (5.6). As can be seen from the above figure, it is convenient to divide the span of the frequency spectrum, ranging from 10 to 20 GHz, into 5 regions, and then determine the correct solution in these regions separately. These regions are: (i) below 12.80 GHz; (ii) 12.8 – 14.4 GHz; (iii) 14.4 – 17.0 GHz; (iv) 17.0 – 18.5 GHz; and, (v) above 18.5 GHz. Since $n'' \leq 0$, the solutions with the negative roots in the frequency regions (i) and (ii), as well as the solutions with positive roots in the frequency region (iv) should be discarded.

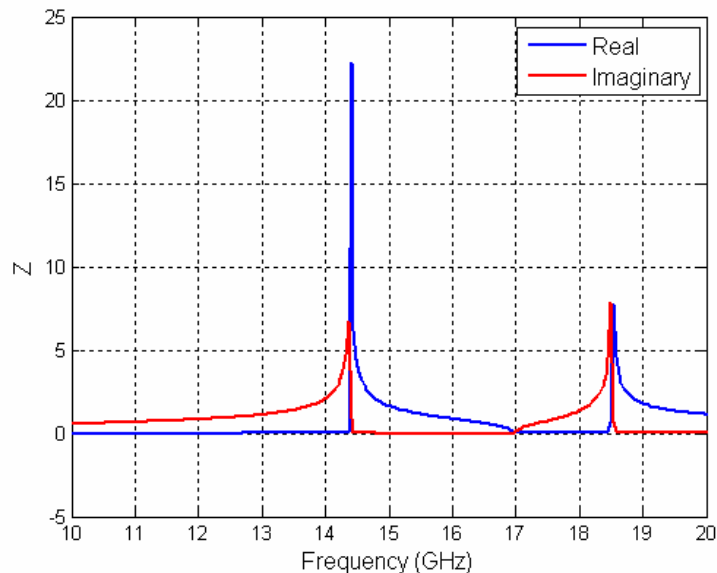


Fig. 5.15: The wave impedance retrieved from the 1-layer slab.

Figures 5.17 (a) – (c) show the solutions for n' , ϵ'' , μ'' , computed by using the positive root for the branch indices $m = 0$, -1 , and $+1$, respectively. Figures 5.18 (a) – (c) show the corresponding solutions computed by using the negative root. In region (i), only three possible

solutions of different branch indices with positive root survive. As can be seen from Figs. 5.17 (b) and (c), the solution with branch index +1 and -1 should be discarded, because either ϵ'' or μ'' are found to be positive. Thus, the only solution that survives is the one with positive root and $m = 0$; which is assumed to be the correct one. Similarly, in region (iv), only one solution—the negative root with $m = 0$ —survives, when we examine the sign of ϵ'' or μ'' in Figs. 5.18 (b) and (c).

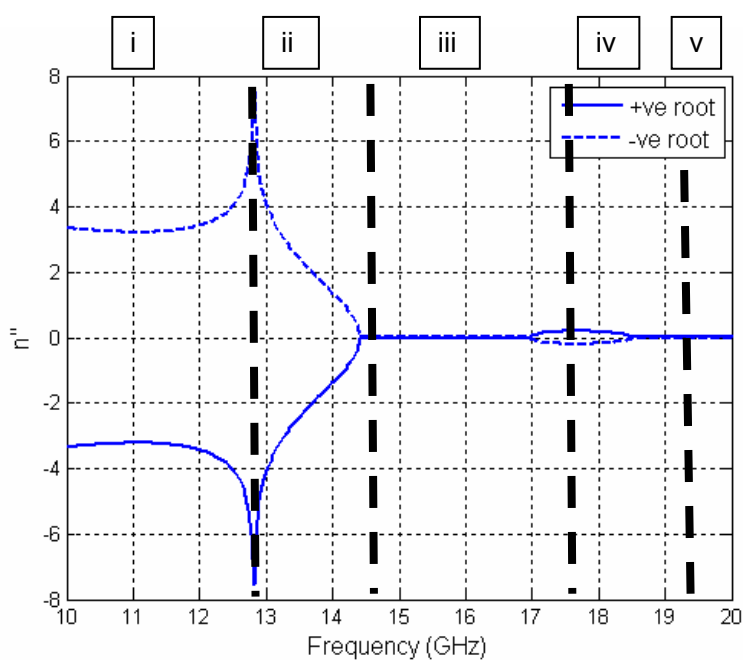


Fig. 5.16: The solutions for n'' derived from the two roots in (7.4) for the 1-layer slab.

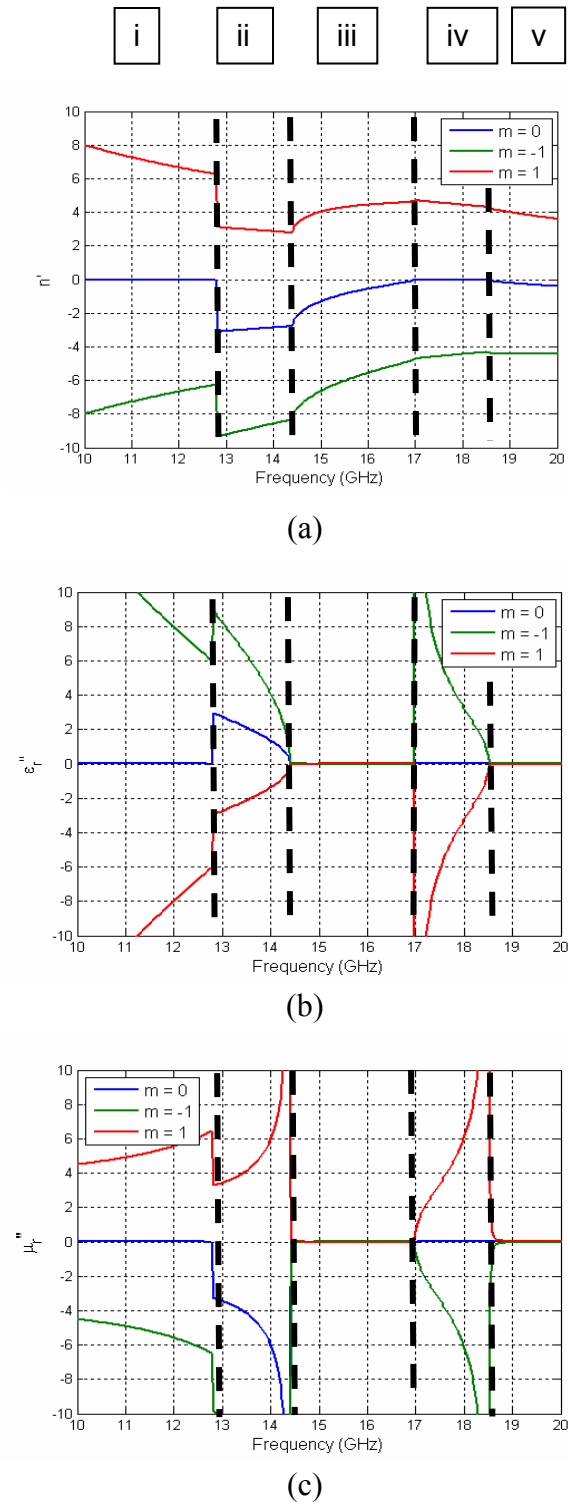


Fig. 5.17: The solutions for (a) n' , (b) ϵ'' , and (c) μ'' , computed by using the positive root in (7.4) with a branch index of $m = 0, -1$, and $+1$, respectively.

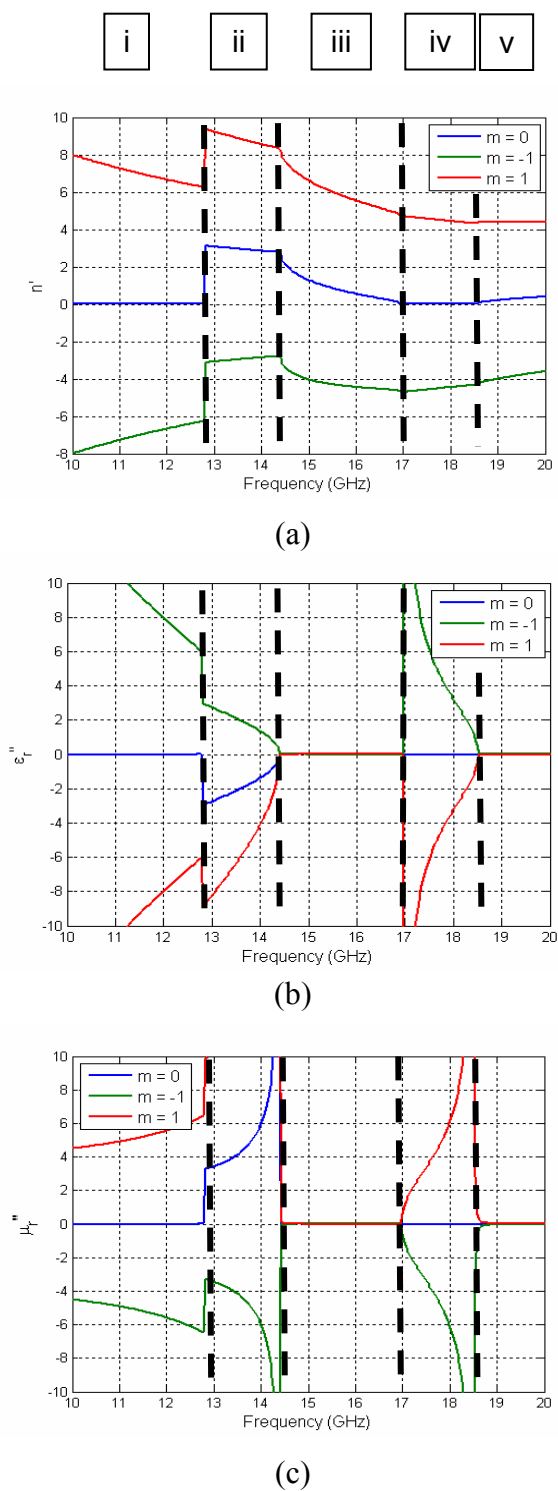
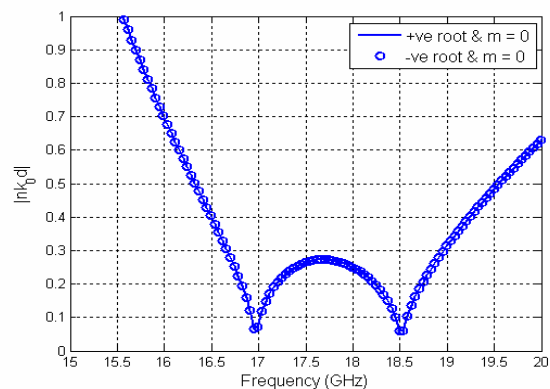


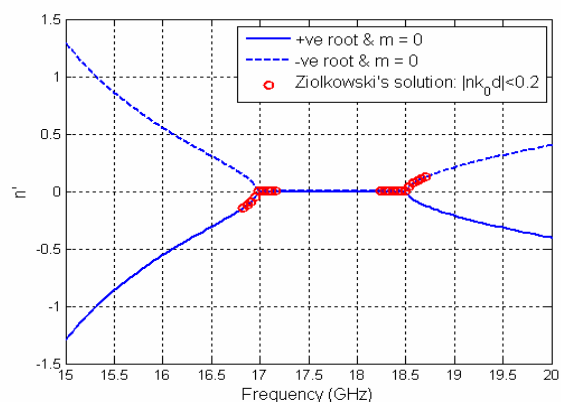
Fig. 5.18: The solutions for (a) n'' , (b) ϵ'' , and (c) μ'' , computed by using the negative root in (7.4) with a branch index of $m = 0, -1$, and $+1$, respectively.

In regions (iii) and (v), all six solutions are still acceptable, insofar as the physical constraints are satisfied by n'' , ϵ'' , μ'' . However, we can make use of the known solution in region (iii), together with the requirement on the continuity of n' , to eliminate the four solutions that have a nonzero m . Then, only two solutions survive, both with $m = 0$, one from the positive root and the other from the negative one.

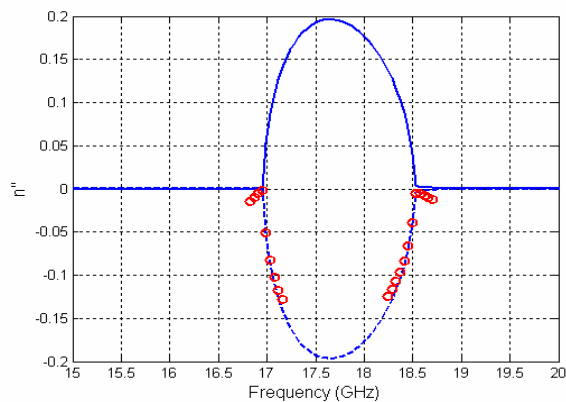
Next, we compute the value of $|nk_0d|$ for all possible solutions surviving in the frequency band (iii) through (v), and plot them in Fig. 5.19 (a). Let us use the condition $|nk_0d| < 0.2$ to define the frequencies at which the SPSL approximation is valid. Two narrow frequencies bands, one ranging from 16.8 to 17.2 GHz and the other from 18.2 to 18.6 GHz, can be found to satisfy the above condition. Figures 5.19 (b) and (c) plot the real and imaginary parts of n for all the acceptable solutions computed by using the inversion approach, along with the valid SPSL solution in these frequency bands. We can see that the two valid frequency bands happen to cover the upper end of region (iii) and the lower end of region (v), respectively; therefore, the branches can be correctly chosen in these regions by matching the above two solutions. In region (iii), the positive root with $m = 0$ is selected, whereas in region (v), the negative root with $m = 0$ is chosen. The SPSL solutions are also plotted in Fig. 5.20 over the entire observed frequency band.



(a)

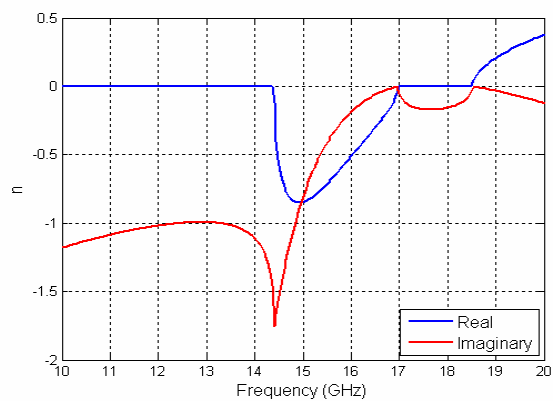


(b)

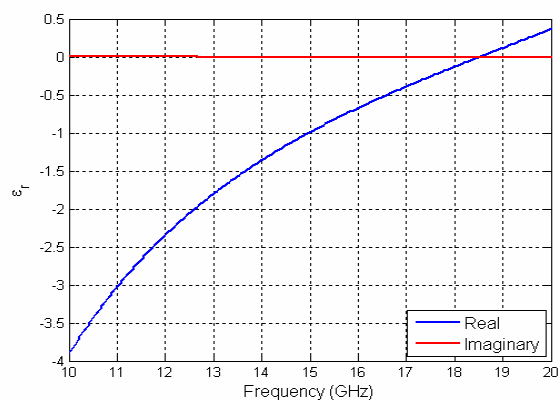


(c)

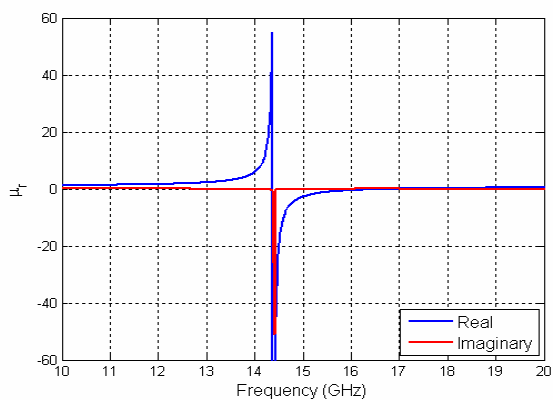
Fig. 5.19: (a) The value of $|nk_0 d|$ for all remaining solutions obtained from the inversion approach; Comparison of the (b) real and (c) imaginary parts of n for all remaining solutions obtained from the inversion approach (lines) and from the SPSL approximation (circles), in the frequency band (iii) through (v) as shown in Fig. 5.16 (b).



(a)



(b)

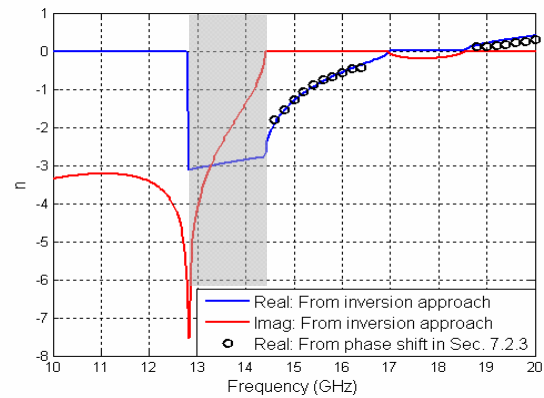


(c)

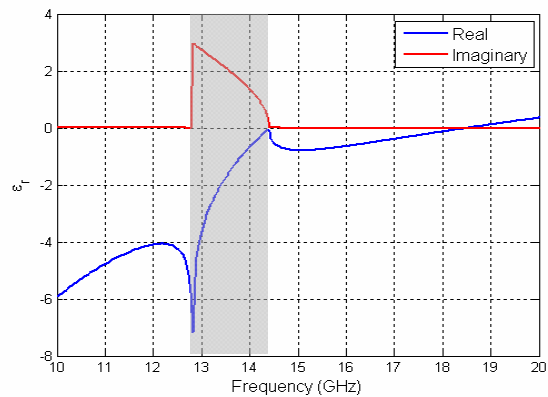
Fig. 5.20: The SPSL solutions over the entire observation frequency band: effective (a) n ; (b) ϵ_r ; and (c) μ_r . Note that the SPSL condition is not satisfied over the entire band.

It should be pointed out that none of the solutions in region (ii) appear to be physical since the condition that both ε'' , $\mu'' \leq 0$ is violated by all solutions. It has been argued [77,83] that such solutions are still physical, even when one of the ε'' , μ'' is positive while the other is negative, as long as the electromagnetic losses, expressed in terms of the integral, $Q = \frac{1}{2\pi} \int d\omega \omega [-\varepsilon'' |E|^2 - \mu'' |H|^2]$, is still positive. Some have also suggested [84] that there are higher-order modes inside this resonance band, whose levels may be comparable to that of the first order one. The effective medium theory fails under these circumstances and, hence, the effective material constitutive parameters can no longer be defined. This issue is still controversial, and we will not dwell on it much longer. We just add the remark here that we still choose the positive root with $m = 0$ as our solution in this region, so as to render n' continuous at the interface between region (ii) and (iii), while keeping $n'' \leq 0$.

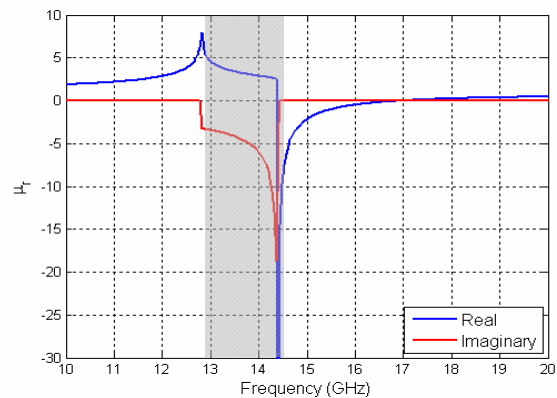
The refractive index n , and the effective material parameters ε and μ of the medium all are extracted by using the inversion approach described above, and are plotted in Figs. 5.21 (a) – (c), with the grey area representing the non-physical region, in which the criterion ε'' , $\mu'' \leq 0$ is violated. The medium exhibits a DNG behavior in the frequency range of 14.4 to 17.0 GHz, which is consistent with the result presented earlier in Sec. 5.2.



(a)



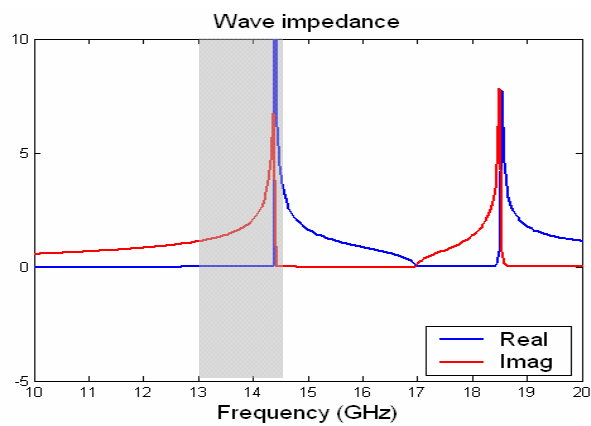
(b)



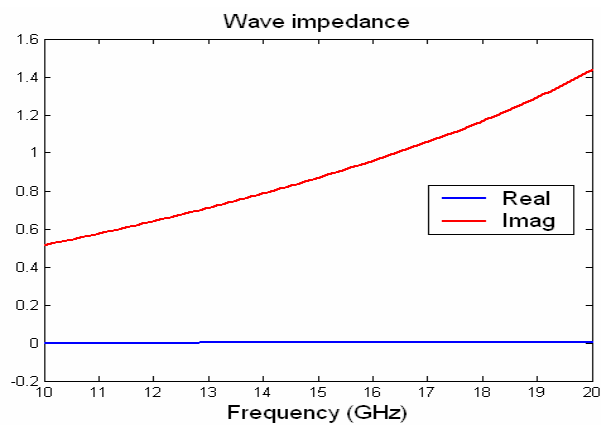
(c)

Fig. 5.21: The extracted material parameters for the 1-layer case: (a) n ; (b) ϵ ; and (c) μ . Grey area represents the non-physical region where no solutions can be found to satisfy both ϵ'' and $\mu'' \leq 0$. The black circles in (a) represent the refractive index computed by using the phase data computed in Sec. 5.2.3.

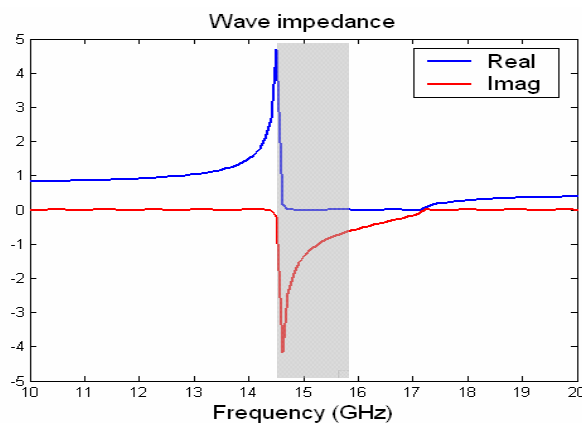
We have also studied the S-parameters for the arrays of slabs comprising of either wires or SSR, by using the inversion approach for the single-layer case. Their wave impedance, refractive index, and effective ϵ and μ are plotted in Figs. 5.22 through 5.25, respectively. Again, the frequency bands marked in grey represents the non-physical regions, because of the signs of ϵ'' and/or μ'' are positive in these regions. Not unexpectedly, the array of wires, or the SSRs, do not independently exhibit a DNG behavior, as shown Fig. 5.23 (b) and (c). A negative μ' region is found in the frequency band ranging from 15.8 to 17.0 GHz for the SSR array, while ϵ' is negative over the entire observed frequency band investigated, which ranges from 10.0 to 20.0 GHz for the array of wires. We also notice that the medium parameters of the SRR array exhibits a non-physical behavior in the frequency band ranging from 14.4 to 15.8 GHz (see Figs. 5.24 (c) and 5.25 (c)), but such regions are not present in the effective medium characteristics of the array of wires.



(a)

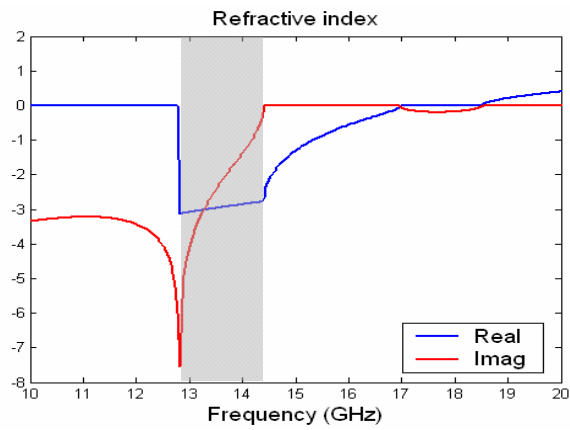


(b)

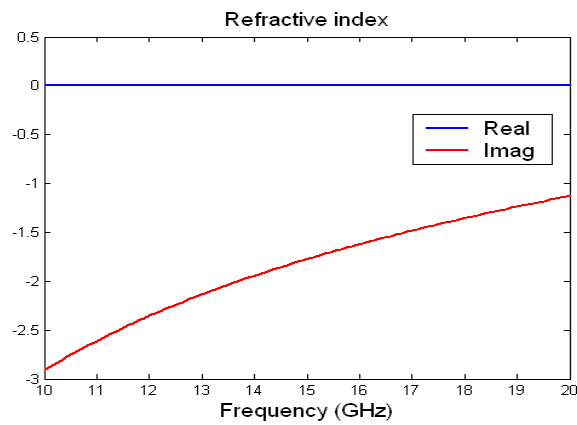


(c)

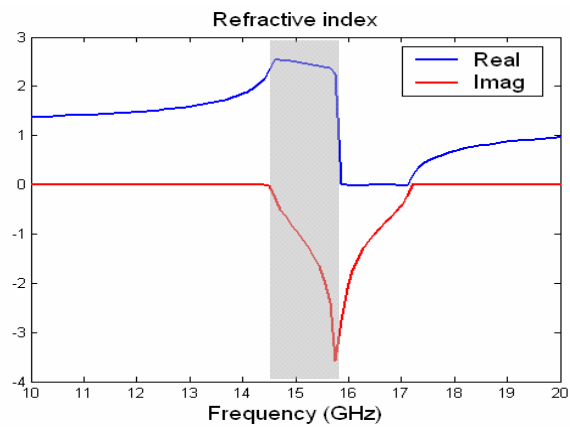
Fig. 5.22: The wave impedance retrieved for the 1-layer slab comprising of different types of inclusions: (a) SSRs and wires; (b) wires alone; and (c) SSRs alone. Grey area represents the non-physical region where no solutions can be found to satisfy both $\epsilon'' \leq 0$ and $\mu'' \leq 0$.



(a)

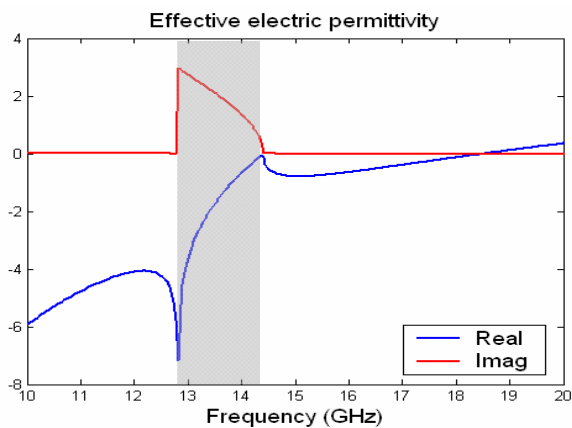


(b)

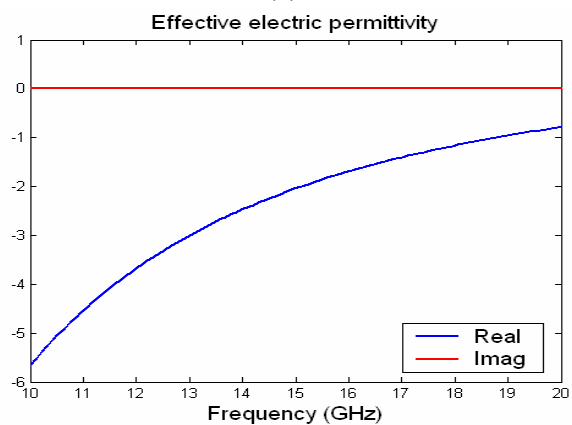


(c)

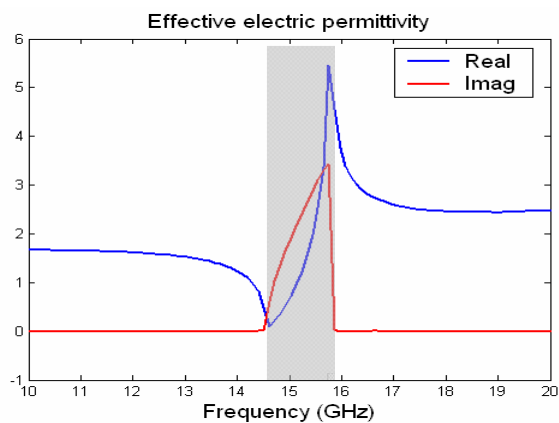
Fig. 5.23: Refractive index retrieved for the 1-layer slab, comprising of different types of inclusions: (a) SSRs and wires; (b) wires alone; and (c) SSRs alone. Grey area represents the non-physical region where no solutions can be found to satisfy both ϵ'' and $\mu'' \leq 0$.



(a)

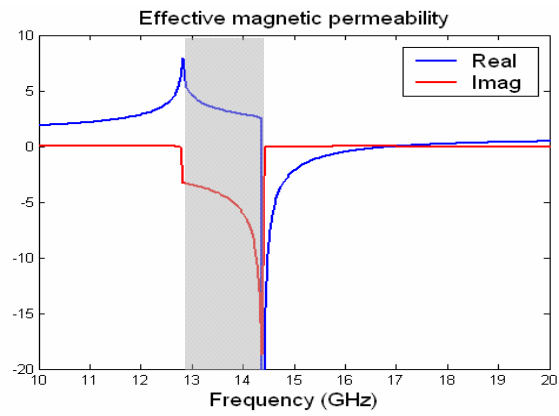


(b)

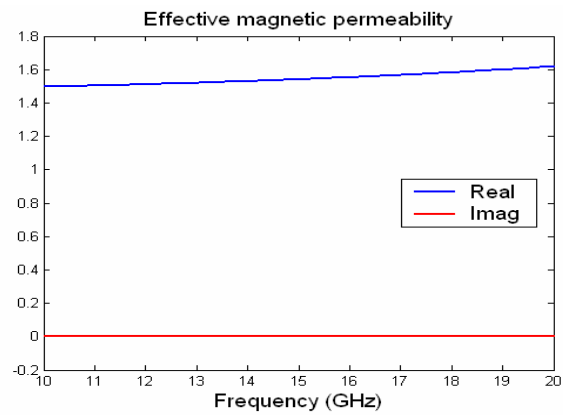


(c)

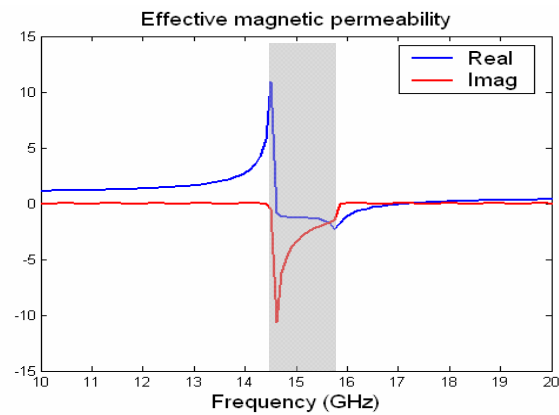
Fig. 5.24: Effective electric permittivity retrieved for the 1-layer slab, comprising of different types of inclusions: (a) SSRs and wires; (b) wires alone; and (c) SSRs alone. Grey area represents the non-physical region where no solutions can be found to satisfy both ϵ'' and $\mu'' \leq 0$.



(a)



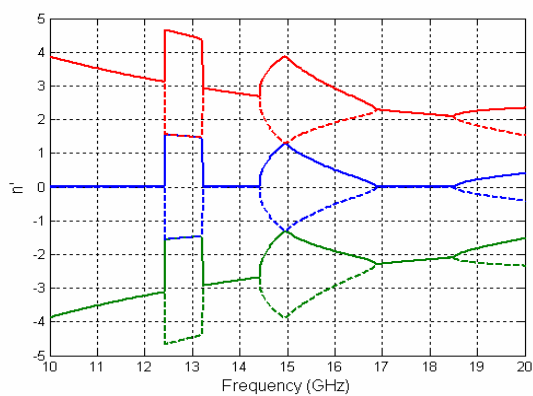
(b)



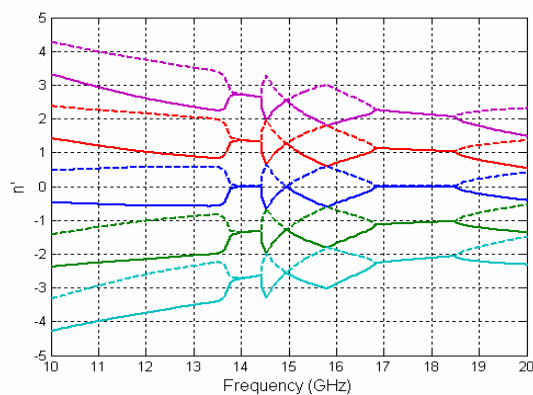
(c)

Fig. 5.25: Effective magnetic permeability retrieved for the 1-layer slab comprising of different types of inclusions: (a) SSRs and wires; (b) wires alone; and (c) SSRs alone. Grey area represents the non-physical region where no solutions can be found to satisfy both ϵ'' and $\mu'' \leq 0$.

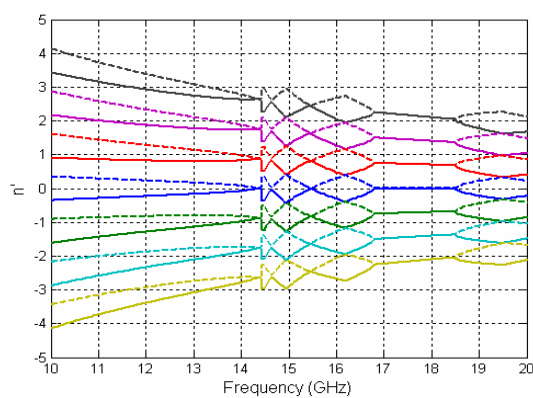
Next, we investigate the effective material parameters for a multi-layer array comprising of a combination of SRRs and wires, by using the modified inversion approach discussed above. The effective surfaces are defined in the same way as before, and the effective thickness of the array is allowed to vary from two to six layers as follows: 7.75 mm, 11.75 mm, 13.75 mm, 17.75 mm, 21.75 mm. Figures 5.26 (a) - (c) and 5.29 (a) - (c) show all the possible solutions of the refractive indices for the two-layer, four-layer and six-layer cases. We see from Figs. 5.26 (a) - (c) that when we increase the number of layers, the entire frequency band of interest must be divided into increasing number of sub-regions, since the spacing between the n' plots for different branch indices, that is proportional to $1/(k_0d)$, becomes increasingly smaller. For the same reason, a larger range of branch index needs to be applied such that the set of all solutions can cover the correct solution. As a result, the selection process for the correct solution become very complex for structures with multiple layers as the number of layers is increased. Besides, as mentioned earlier, the higher-order Floquet harmonics are totally ignored when the slab thickness is increased by stacking multiple layers, and this can have serious consequences when we attempt to predict the performance of a thick metamaterial slab.



(a)



(b)



(c)

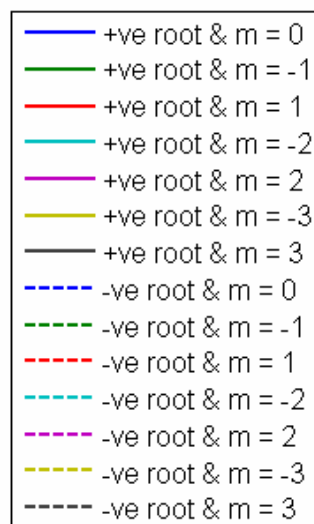
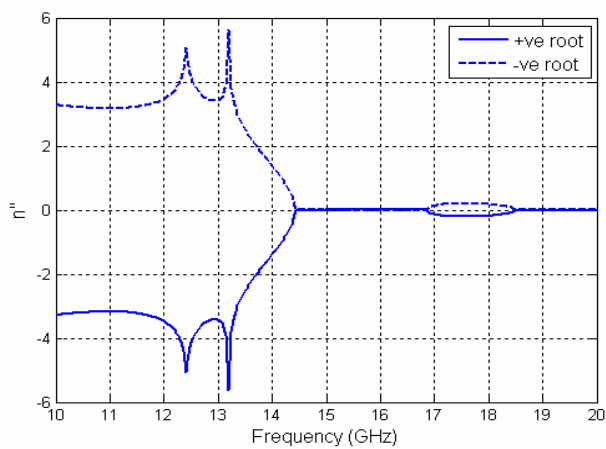
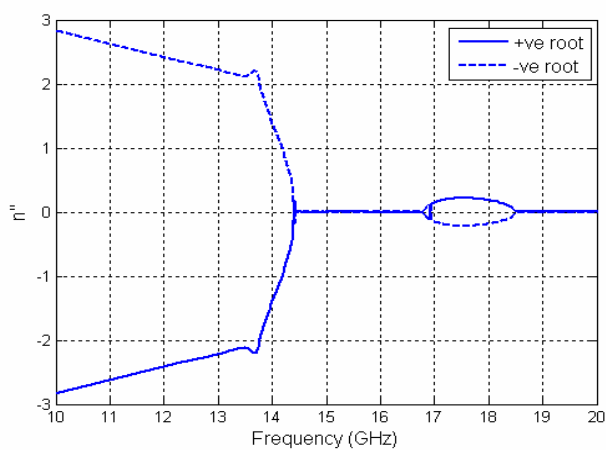


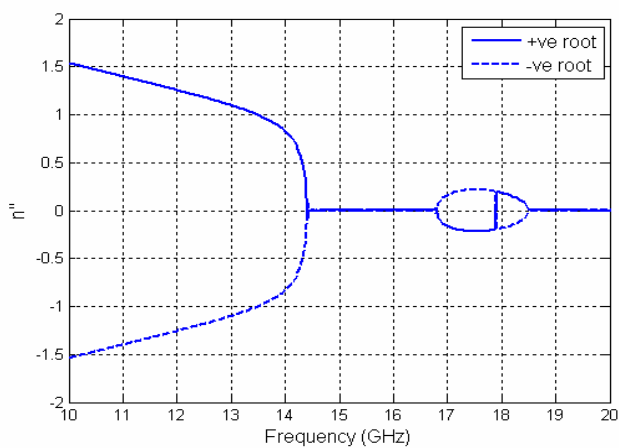
Fig. 5.26: The set of all possible solutions of n' for the DNG slabs with multi-layer inclusion: (a) 2-layer; (b) 3-layer; and (c) 6-layer.



(a)

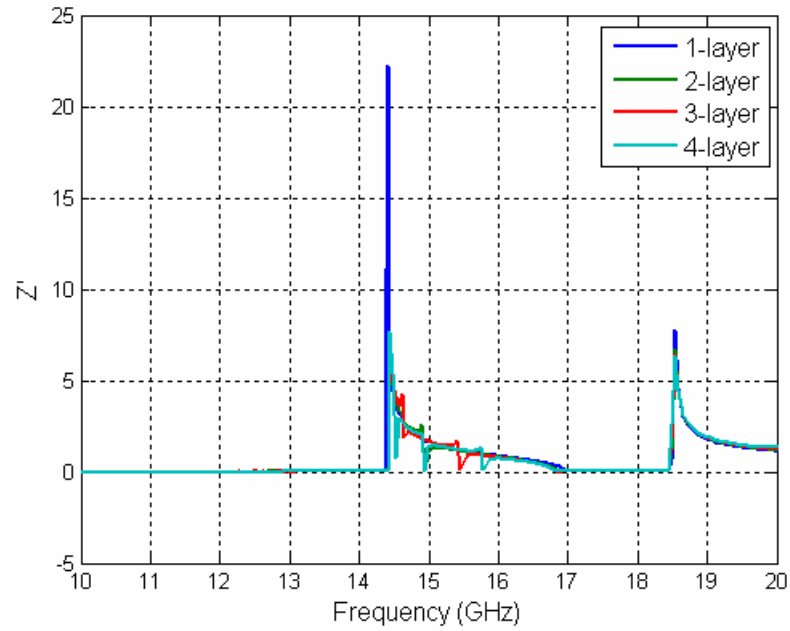


(b)

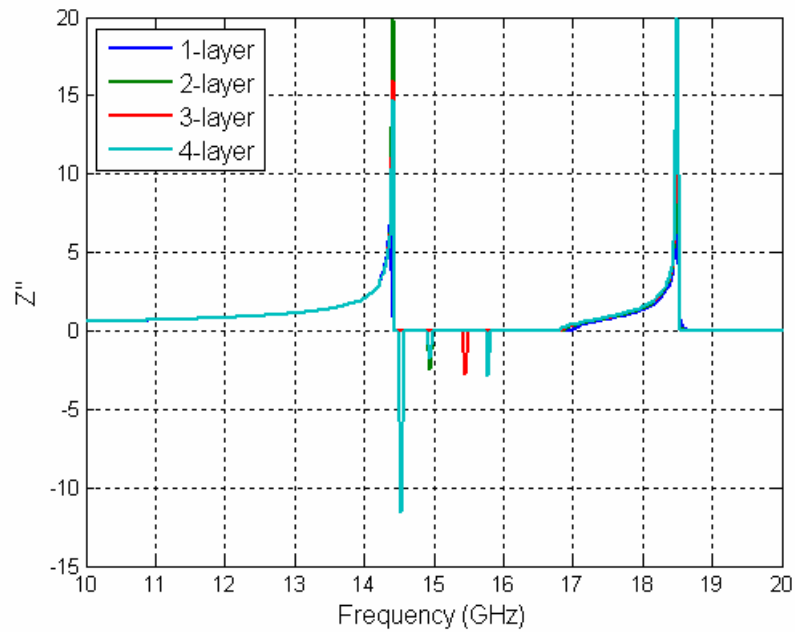


(c)

Fig. 5.27: The set of all possible solutions of n'' for the DNG slabs with multi-layer inclusion: (a) 2-layer; (b) 3-layer; and (c) 6-layer.

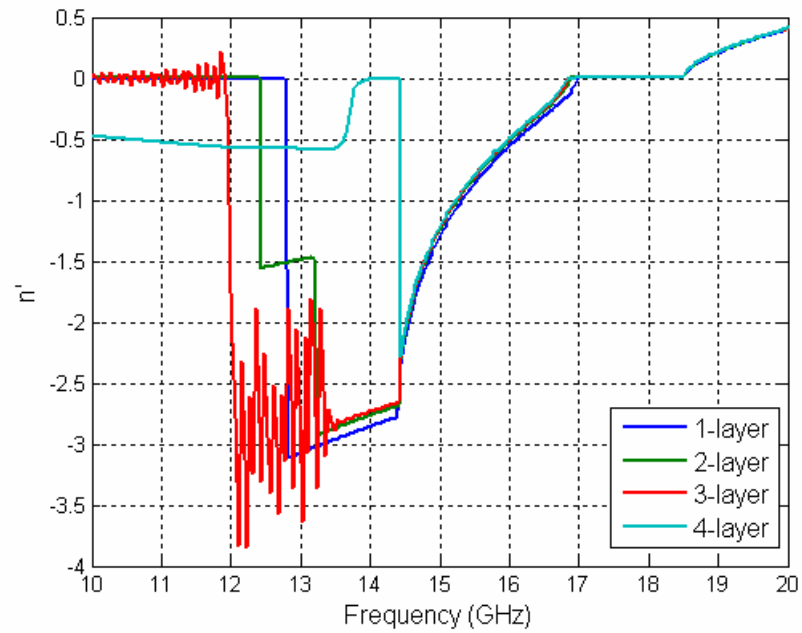


(a)

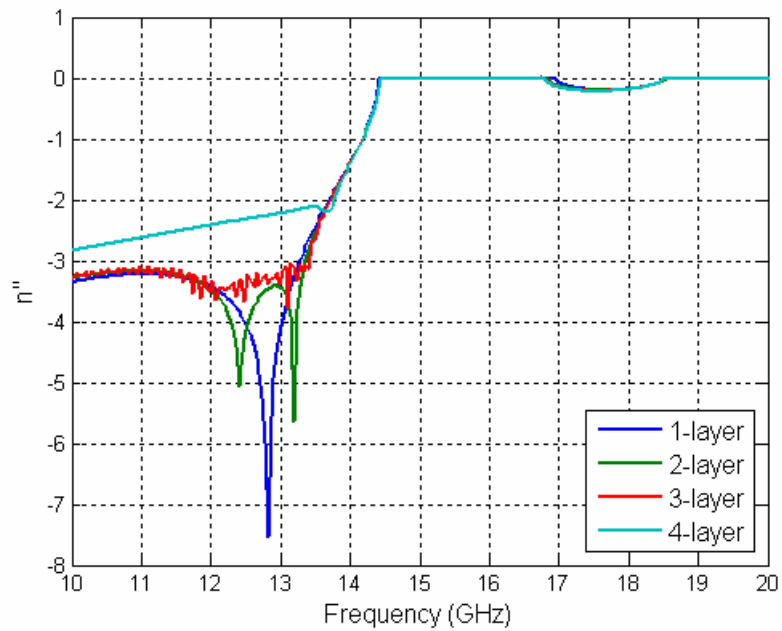


(b)

Fig. 5.28: Comparison of the wave impedance extracted for the DNG slab, starting from one and up to four layers: (a) real; and (b) imaginary part.



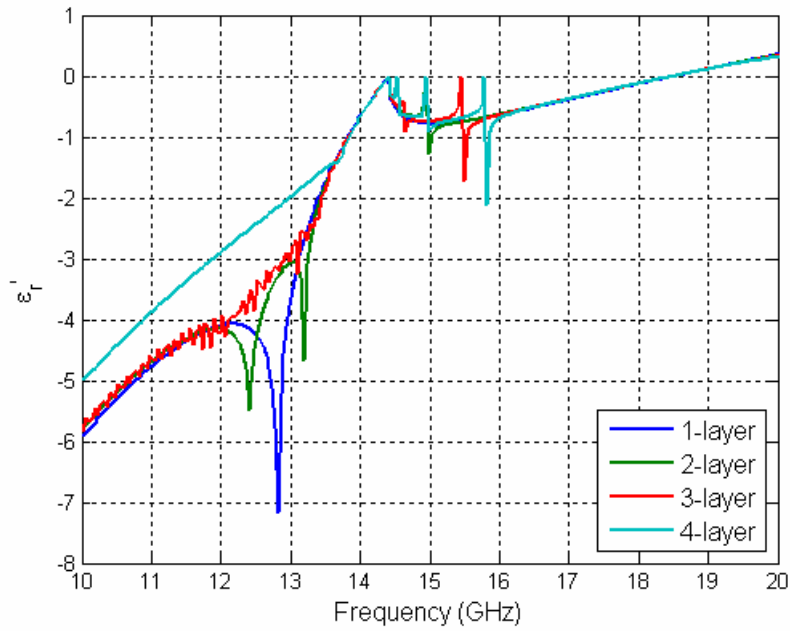
(a)



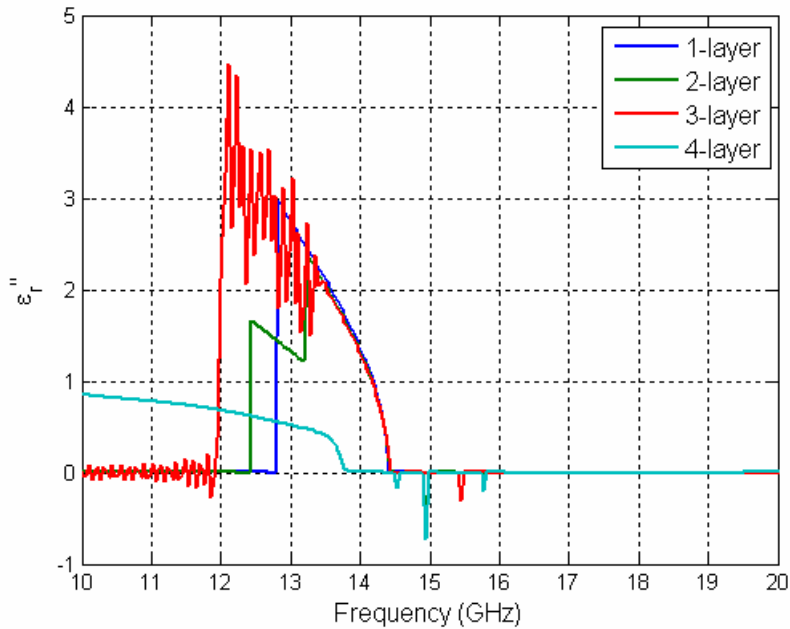
(b)

Fig. 5.29: Comparison of the refractive index extracted for the DNG slab, starting from one and up to four layers: (a) real; and (b) imaginary part.

In view of the complexity of the selection process, we have attempted to apply the inversion approach only up to four-layer cases. Figures 3.30 through 3.33 plot the extracted wave impedance Z , effective refractive index n , ε and μ , respectively, starting from a single-layer and going up to four-layer cases in the frequency band ranging from 10 to 14.0 GHz. For the wave impedance, plotted in Figs. 5.28 (a) and (b), we observe more spikes in the frequency range between 14.4 to 17.0 GHz as the number of layers is increased. One might think that the occurrence of spikes is caused by the mutual coupling between the elements in different layers. However, we also note that the locations of these spikes coincide with the dips of S_{11} ; therefore, they might simply be caused by the numerical noise present in the computed S-parameters, since the wave impedance is inherently very sensitive to the variations in the S-parameters, whenever S_{11} is small. Even though the refractive index is more or less continuous in this frequency range, spikes in the wave impedance would, in turn, generate spikes in the effective ε and μ . No conclusion can be drawn at this point, as to whether the mutual coupling between the layers has a significant effect. Apart from the spikes, the effective material parameters match quite well as the number of layers is changed. For the refractive index n , the matching is good above 14.4 GHz for different number of layers (see Figs. 5.29 (a) and (b)). It should be noticed that the DNG property, which is exhibited between 14.4 and 17.0 GHz, is consistent in all cases. However, some discrepancies of refractive index do occur between 12.8 to 14.4 GHz, which belongs to the non-physical region.

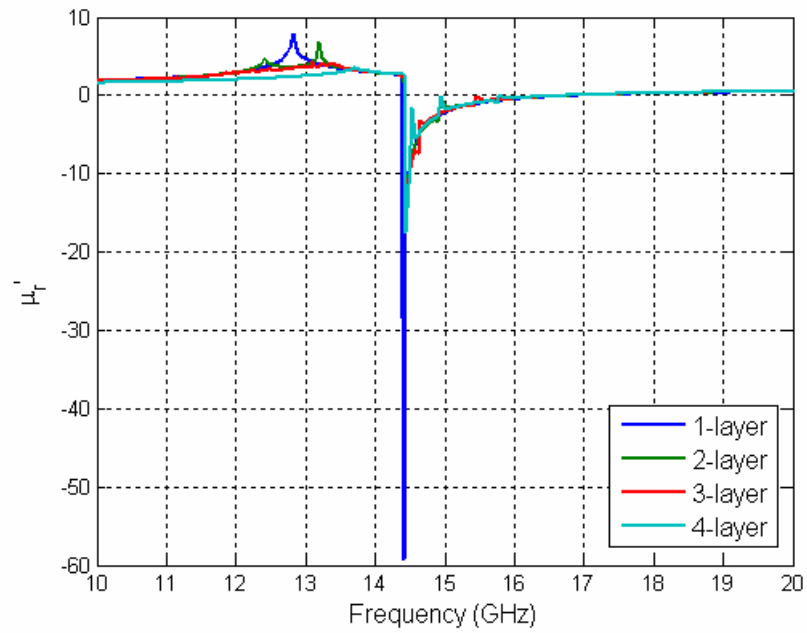


(a)

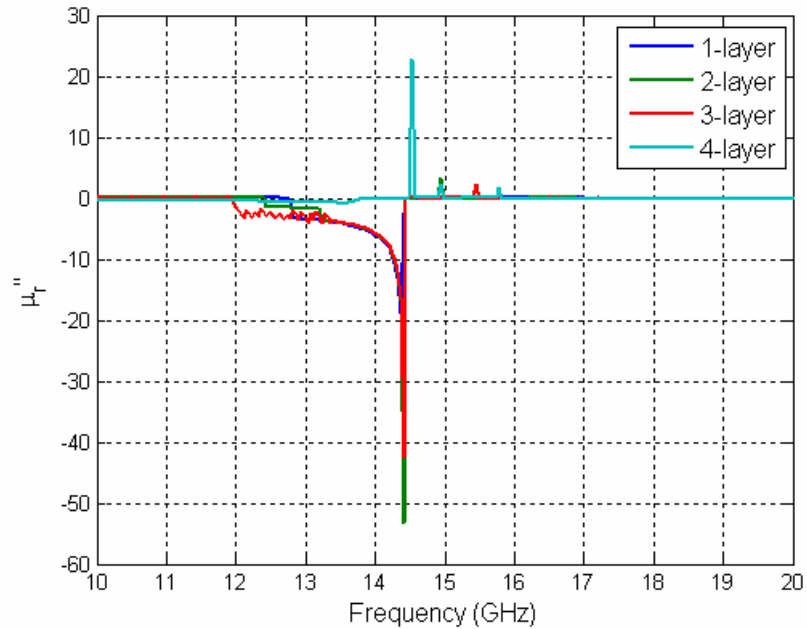


(b)

Fig. 5.30: Comparison of the effective electric permittivity extracted for the DNG slab, starting from one and up to four layers: (a) real; and (b) imaginary part.

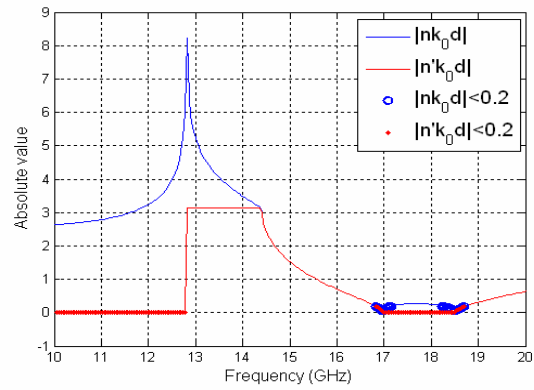


(a)

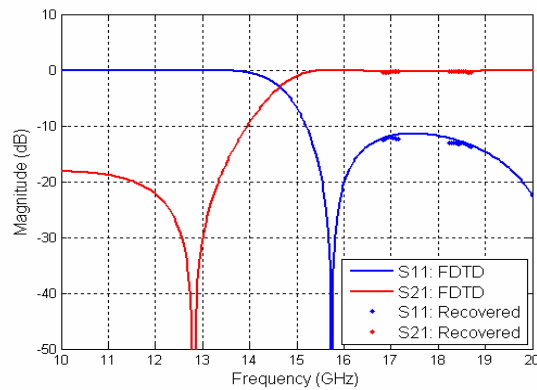


(b)

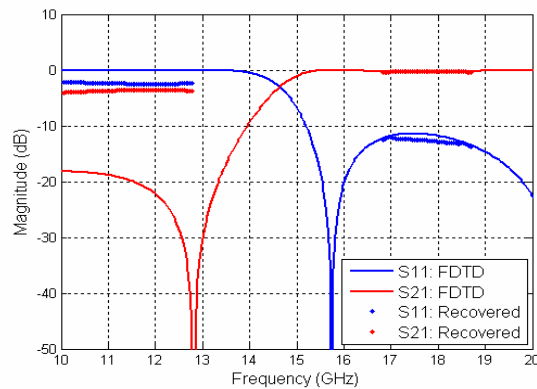
Fig. 5.31: Comparison of the effective magnetic permeability extracted for the DNG slab, starting from one and up to four layers: (a) real; and (b) imaginary part.



(a)



(b)



(c)

Fig. 5.32: (a) The values of $|nk_0d|$ (blue) and $|n'k_0d|$ (red), where n is computed by using the inversion approach; and the comparison of the S-parameters obtained by using FDTD (lines) and those recovered by using the SPSL solutions (dots) in the region where (b) $|nk_0d| < 0.2$; and (c) $|n'k_0d| < 0.2$.

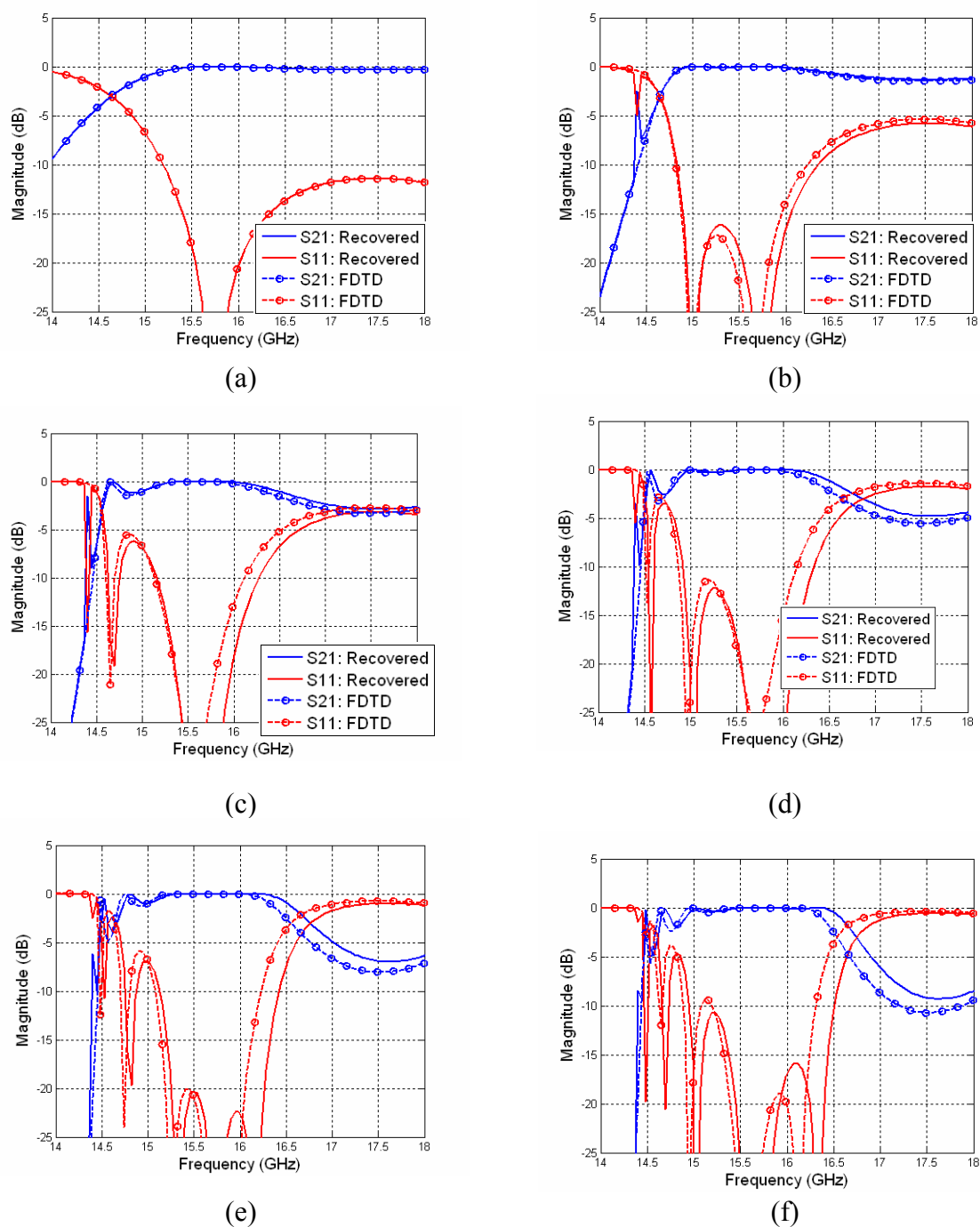


Fig. 5.33: Comparison of the magnitude of the S-parameters, recovered from the retrieved n and Z of the 1-layer slab (solid) and obtained from the direct FDTD simulations (circle dash) for 1-layer up to 6-layer slabs in (a) through (f).

Finally, let us justify the condition $|n'k_0d| \leq 1$ proposed by Ziolkowski in [82], to approximate $e^{-jnk_0d} \sim 1 - jnk_0d$. We argue on the basis of the results presented below, that the condition should really be $|nk_0d| \ll 1$, by testing Ziolkowski's condition on the results for the single-layer DNG array. We first evaluate the values $|nk_0d|$ and $|n'k_0d|$, where n is the effective refractive index extracted by using the modified inversion approach, as plotted in Fig. 5.32 (a). From these values, we locate the frequencies at which $|nk_0d|$ or $|n'k_0d|$ is small compared to 1, say less than 0.2, which is denoted by the blue circles and red dots in Fig. 5.32 (a), respectively. Next, we compute the SPSL solutions for the refractive indices, that are subsequently used to recover the S-parameters by using (5.1) and (5.2). Figure 5.32 (b) and (c) plot the comparison of the recovered and original S-parameters for small values of $|nk_0d|$ and $|n'k_0d|$, respectively. It is clearly seen that the matching is excellent for small $|nk_0d|$, but not necessarily good for small $|n'k_0d|$. Therefore, we conclude that the correct condition for this solution to be valid should be $|nk_0d| \ll 1$. It should also be pointed out that the valid frequency range can be very limited, and even non-existent sometime, for the metamaterials slab we have investigated. Also, it is very important to guarantee that the condition $|nk_0d| \ll 1$ be satisfied when using this solution, in the alternative approach, for example, for the inversion method as stated before.

5.3.4 Summary of the Difficulties Encountered Using the Inversion Approach for Effective Medium Characterization

In summary, the main difficulty encountered in the retrieval procedure arises during the process of selecting the correct branch from the multiple set of possible solutions. Although

some guidelines are available for eliminating the non-physical solutions, the unavoidable numerical artifacts present in the S-parameters, obtained either from experiments or from numerical simulations, often make it very difficult to apply these selection rules.

For example, enforcing the passivity condition on the extracted parameters, namely that n'' , ϵ'' and $\mu'' \leq 0$, for all the admissible solutions, is not as easy as one would think. When values of n'' , ϵ'' or μ'' are near zero, attempting to strictly enforce the condition that n'' , ϵ'' and $\mu'' \leq 0$, simply leads to a rejection of all the solutions, because the parameters we desire may be so corrupted by the presence of numerical artifacts in the near-zero region, as to render them non-physical. Consequently, from a practical point of view it may be better to work with a tolerance level and discard the solutions only when $n'' > \delta_1$, $\epsilon'' > \delta_2$ or $\mu'' > \delta_3$, where δ_1 , δ_2 and δ_3 are small positive numbers. We point out, however, that the choice of the values of these small parameters must be made with some care. For instance, if these parameters are chosen to be too large, an enforcement of the rules given above will not help eliminate the non-physical solutions; on the other hand, if these parameters are too small, all solutions, including the correct ones, would be discarded. What is even worse, the optimal values for these parameters are problem-dependent, and they are strongly affected by the level of the noise present in the S-parameters, be they computed or measured.

Additionally, a frequency band can be found such that no solutions can satisfy the condition that either both ϵ'' and $\mu'' \leq 0$, or are smaller than some small positive numbers, in order to accommodate the numerical errors that are inevitably present in the S-parameters. This seemingly non-physical region often appears adjacent to the DNG region, or near the frequency at which spikes and notches appear in the retrieved impedance, when S_{11} is small. Since none of

the branches can be chosen to yield a physical solution in this region, the iterative process [78] that makes use of the continuity of the refractive index as a function of frequency fails as we move from one region to the next.

In addition, we have encountered some metamaterials structures for which multiple solutions still survive, even after applying all the selection rules alluded to above. In this situation, we cannot determine the correct solution by using the inversion approach we have described above.

A sensitivity analysis has been performed in [78], and they have shown that the effective material parameters extracted for a given problem are very sensitive to the noise in the S-parameters, whenever either $|S_{11}|$ or $|S_{21}|$ is small. When $|S_{21}|$ is small, the extracted values of refractive index turn out to be very sensitive to small perturbations of S_{21} . On the other hand, a small S_{11} generates spikes in the extracted impedance values, as may be clearly seen by referring to Fig. 5.28 for the multi-layer cases. As a result, the retrieved effective parameters turn out to be unreliable when either of the S-parameters is small.

5.3.5 Re-examination of the Concept of the Effective Material Parameters

After the first realization of DNG metamaterial structure many researchers have invested much effort forward developing and improving the techniques for extracting the effective material parameters for metamaterials, since they offer a simple representation of the EM properties of complex structures by replacing them with a homogeneous medium. It is evident that, once the effective material parameters have been retrieved, the analysis and design process for various applications would become relatively easy when the metamaterial structure is simply replaced with a homogenous block assigned with the extracted effective parameters, rather than

modeling the fine inclusions located inside the metamaterial slab. At this point, an inquisitive scientist or engineer might ask these questions: Can the EM response of the metamaterials be fully represented by these effective material parameters, as we can for homogeneous materials? Can we rely entirely on these parameters to predict the true EM response in a real-world application, say, one involving a metamaterial slab placed near an antenna in order to enhance the antenna performance? In the following, we will attempt to provide some insightful answers to the above questions.

We begin the discussion by re-examining the scattering properties of the DNG metamaterial slabs illuminated by a normally incident plane wave. It is well known that the material parameters of a homogeneous slab are independent of its thickness. Thus, we would prefer that the effective parameters of a metamaterial slab do not vary as we change its thickness by varying the number of layers. We find that this is not the case, however, because these parameters are affected by the mutual coupling effects between various layers that comprise the thick slab.

To see this, we first use the retrieved values of n and Z of the 1-layer slab to recover the S-parameters of the slabs up to 6-layers, by using (5.1) and (5.2), under the assumption that these retrieved parameters remain the same even when the number of layers changes. Figures 5.33 (a)-(b) plot the S-parameters recovered from the retrieved effective parameters along with those obtained from the FDTD simulations, starting with one and going up to six layers, respectively. Figure 5.33 (a) shows an exact match between the recovered data and the FDTD data for the 1-layer case, which is expected, since the effective parameters used are computed from the S-parameters for the 1-layer case. For other slab configurations, we can see that the difference between these two sets of S-parameters becomes larger as we increase the number of layer, and a

small spike appears in the recovered S-parameters at 14.4 GHz, which is the upper end of the non-physical region for the 1-layer case. The discrepancy between the two results for the S-parameters can be explained by the fact that the effective parameters retrieved from the 1-layer slab do not account for the mutual coupling effects between different layers when we are dealing with a multi-layer slab.

Next, we repeat the above test, but this time we use the retrieved n and Z values of the 3-layer slab to recover the S-parameters by the procedure described above. Figures 5.34 (a)-(b) compare the recovered S-parameters with those obtained directly from the FDTD simulations. Again, the expected perfect match between these S-parameters is observed in Fig. 5.34 (c) for the 3-layer case. For all other configurations, the matching shows improvement as compared to those of the previous test using the retrieved parameters of the 1-layer case, except at the frequencies in which three unexpected and non-physical type of spikes appear in the S-parameters. The locations of these spikes remain the same for all configurations, with peaks appearing at 14.4, 14.6 and 15.5 GHz, respectively, and coinciding with the locations where the spikes appear in the retrieved Z of the 3-layer slab (see Fig. 5.29). Therefore, the large discrepancy between the recovered S-parameters from that obtained from direct simulation can be attributed in part to the inaccuracy of the impedance Z , resulting from the numerical noise in the measured S-parameters. However, we do notice the small difference between these two S-parameters above 16 GHz, which is outside the frequency region of the spikes. This indicates that the mutual coupling effects between different layers are different when the number of layers is varied, so that no single set of effective parameters can accurately represent the properties of the metamaterial slabs of different “thickness”. In this respect, the effective material parameters of a metamaterial slab are different from the conventional material parameters of a homogeneous medium.

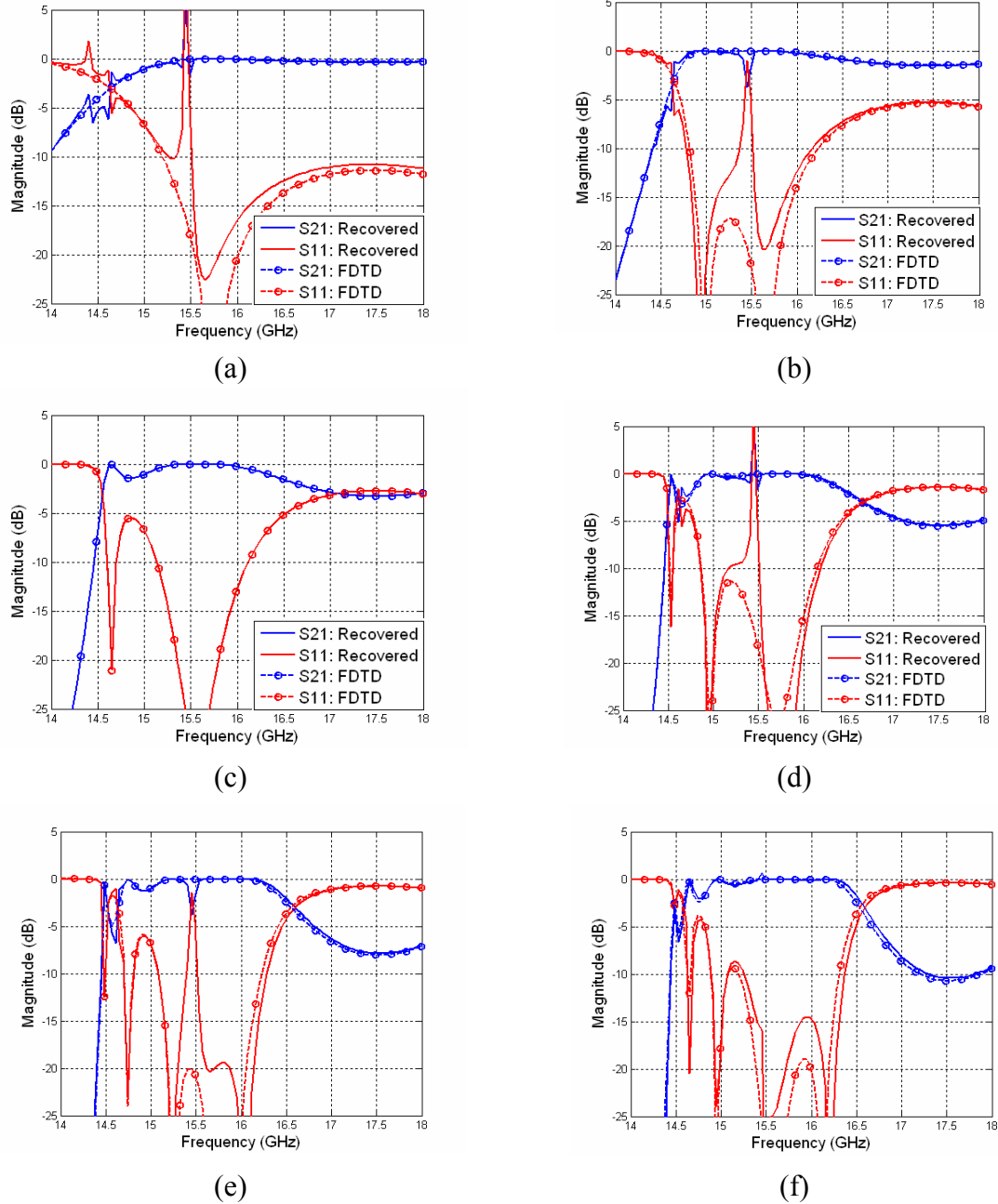


Fig. 5.34: Comparison of the magnitude of the S-parameters, recovered from the retrieved n and Z of the 3-layer slab (solid) and obtained from the direct FDTD simulations (circle dash) for 1-layer up to 6-layer slabs in (a) through (f).

In addition, it should be pointed out that the effective material parameters retrieved by using most of the existing techniques are usually based on the data obtained by illuminating an infinite, doubly-periodic metamaterials slab of finite thickness with a normally incident plane wave for certain polarization; therefore, these parameters often fail to predict the true response when the incident angle or the polarization of the impinging wave is changed, since the EM response at oblique incident angle or other polarization can be considerably different from that at normal incidence due to the anisotropic nature of the inclusions. It is worthwhile to point out here that, in a practical antenna-metamaterial structure, the excitation is usually a localized source, which is comprised of a spectrum of plane waves with different incident angles and polarizations. Also, the interaction between the antenna and the inclusions inside the metamaterials should not be neglected when they are placed in close proximity of each other. Hence, the use of these effective material parameters can be somewhat questionable for some real-world applications.

Having said that, we point out that we do not wish to downplay the importance and usefulness of the effective material parameter representation and that of the techniques used to extract these parameters, in the process of characterizing the design of metamaterials. However, we should keep in mind that the concept of effective material parameter is based only a simplified model; after all, they are not true physical quantities. Last, but not least, it is both important and necessary, in real-world applications, to perform a rigorous simulation of the practical system, where the inclusions inside the metamaterial structures are also modeled accurately, in order to evaluate, reliably, the performance of a system that contains such materials.

5.4 EM Response of a Finite Artificial-DNG* Slab with Localized Beam Illumination

In this section, we study the EM response of a moderate-size, finite DNG array comprising of inclusions that are identical to those we studied previously, when the array is illuminated by a localized Gaussian beam incident either normally or from an oblique angle. We wish to investigate two interesting and unusual phenomena, namely the negative refraction and super-focusing effect of an artificial-DNG slab, by employing a localized beam instead of a plane wave excitation, to simulate the EM response that can be made closely analogous to that illustrated by the ray picture (see Fig. 5.35). For the purpose of comparison, in terms of both the homogeneity of material and the sign of electric permittivity and magnetic permeability, we also study the EM response of a homogeneous dielectric slab ($\epsilon_r = 4$), with the same dimensions as that of the artificial-DNG array, when it is illuminated by the same Gaussian beam.

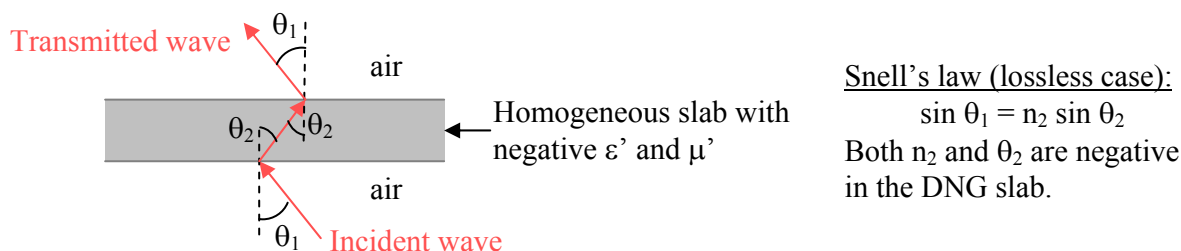


Fig. 5.35: Ray picture illustrating the propagation of a uniform plane wave through a homogeneous DNG slab in free space.

* In the following, we use the term “artificial-DNG” instead of simply “DNG” to describe the array we used in the simulations with localized beam or dipole illumination, in order to distinguish ours from the ideal DNG materials. In general, many physicists and engineers associate the usage of the latter term with a hypothetical material that has negative permittivity and permeability in nature. However, for most engineered structures, or metamaterials, such as the one studied in this work, their DNG nature is usually characterized by a set of effective material parameters, which are extracted from either the experimental data or simulation results for the normal incidence case. Therefore, these structures may not possess the DNG properties for oblique incidence angles and/or other polarizations, and the effective medium representation, derived for normal incidence, may not be valid in the general case.

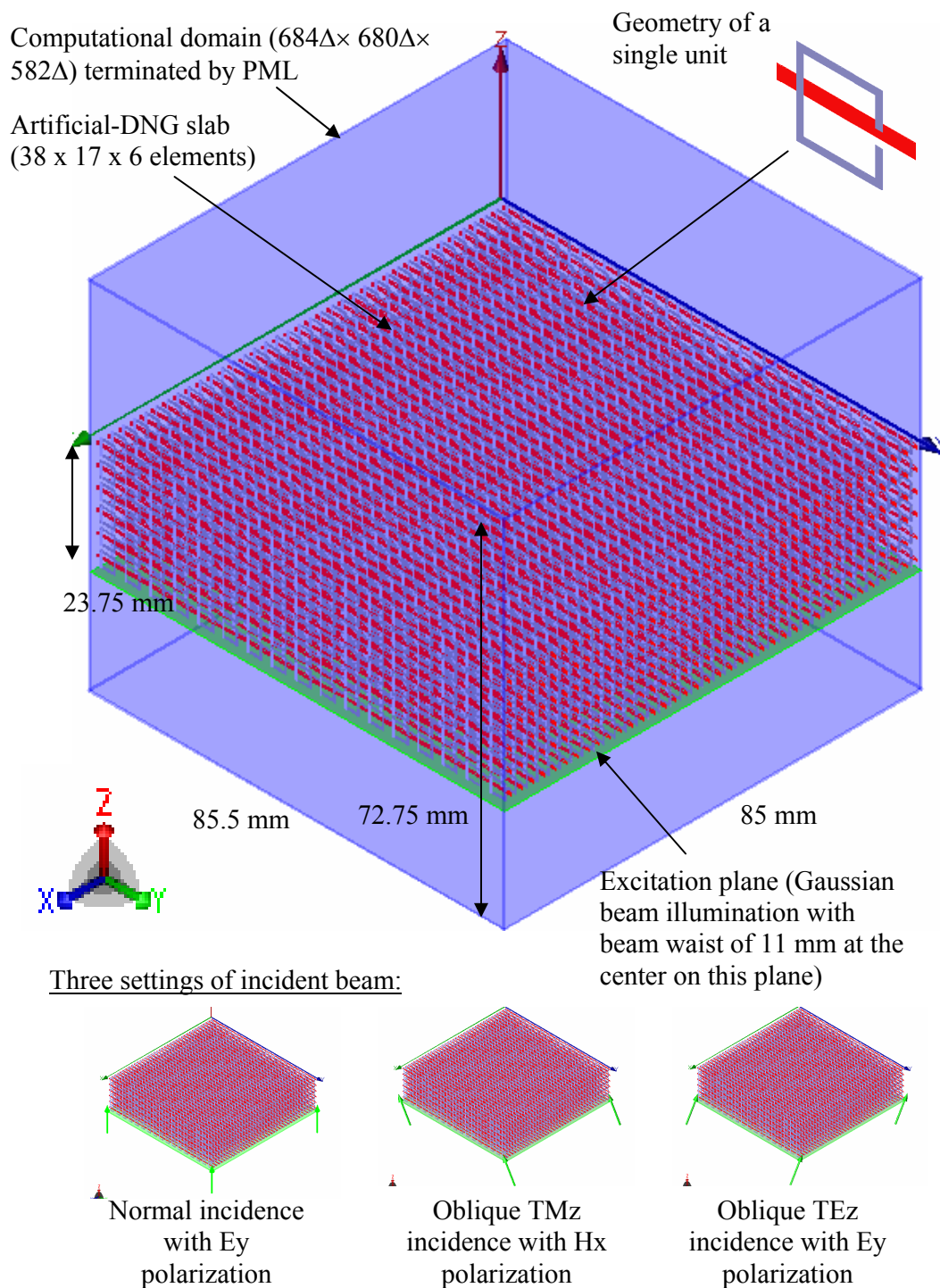


Fig. 5.36: Geometry of a six-layer artificial DNG slab and three incident settings.

5.4.1 FDTD Model

The artificial-DNG slab in our study is comprised of six layers, as shown in Fig. 5.36, and consists of identical inclusions with the same periodicities as that studied previously. It contains a total of $38 \times 17 \times 6 = 3876$ pairs of SSR and wire, and has the dimensions of $85.5 \text{ mm} \times 85 \text{ mm} \times 23.75 \text{ mm}$, corresponding to $4.3 \lambda \times 4.3 \lambda \times 1.2 \lambda$ at the center frequency of interest (15 GHz). The slab, residing on the x-y plane, is illuminated by a Gaussian beam excitation located at one FDTD cell ($\Delta = 0.125 \text{ mm}$) away from the bottom surface of the slab. The incident beam, whose beam maximum points toward the center of the slab, has a beam waist of 11 mm at the excitation plane, and covers a total of 34 pairs of inclusions (up to 10 and 5 inclusions along the x- and y-directions, respectively) in the first layer, within its spot size. By setting a time delay in the excitation pulse across the x-y plane, as was done in Chapter 6, we can simulate the Gaussian beam excitation at oblique incident angles. Considering the anisotropic nature of the inclusions, we simulate the beam with three different settings of incident angles and polarizations, so as to trigger the DNG behavior of the slab at normal and oblique incidences. These three settings are:

- (i) Normal incidence: Wave is incident from $\theta = 180^\circ$, with E_y polarization.
- (ii) Oblique TM_z incidence: Wave is incident from $(\theta = 150^\circ, \phi = 90^\circ)$ with H_x polarization.
- (iii) Oblique TE_z incidence: Wave is incident from $(\theta = 150^\circ, \phi = 0^\circ)$ with E_y polarization.

The computational domain has the dimensions of $85.5 \text{ mm} \times 85 \text{ mm} \times 72.75 \text{ mm}$, and it contains a total of $684 \Delta \times 680 \Delta \times 582 \Delta$ with a uniform discretization of 0.125 mm. At 15 GHz,

the cell-size is small, only $\lambda/160$, and this is necessary to accurately model the fine features of the inclusions. The computational domain is terminated by PMLs in all directions to absorb the outgoing waves. In this problem, the total number of FDTD cells, excluding the PMLs, is around 270 millions, and the total number of unknown fields to be solved exceeds 1.6 billion. This, obviously, places a heavy burden on the computational resources that is not available in a single processor. Therefore, it is necessary to carry out the simulation by using a parallel FDTD code, running on multiple processors.

We have simulated this problem on two different computing platforms: GEMS Box and LOFAR Bluegene/L. The simulations have been run for a total of 21000 time-steps, until the field reaches its steady state. The simulation takes about 17 hours, using 15 CPUs in GEMS Box, while it takes about 14 hours when using 504 CPUs on LOFAR Bluegene/L. The difference in the simulation times arises from the fact that the configurations of the platforms are different, in that they have different c.p.u. speeds and memory, as well as different I/O speeds of the nodes and communication networks.

5.4.2 Total Transmission and Reflection Power Under Gaussian Beam Illumination

Before examining the detailed EM response of the artificial-DNG array, it is necessary to first determine if the chosen spot size of the incident beam is suitable for the study of the macroscopic response of the metamaterial slab. For instance, if the spot size is too small, say smaller than or comparable to the periodicities of the inclusions, we can only observe the scattering characteristics contributed by a few inclusions or perhaps just by a single one. Various concepts commonly used to study the metamaterials, such as the effective medium theory, cannot be applied under these circumstances.

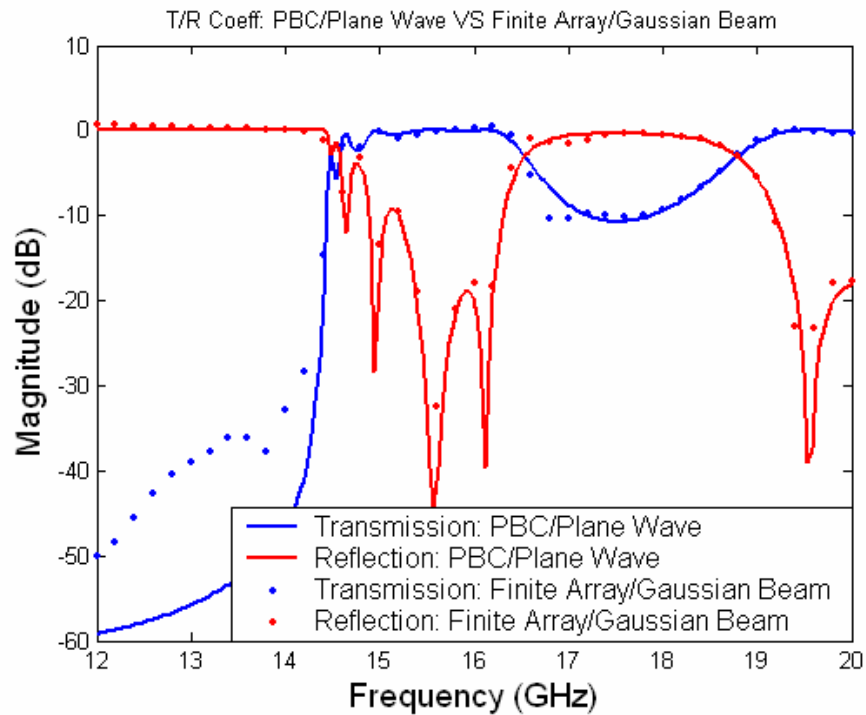
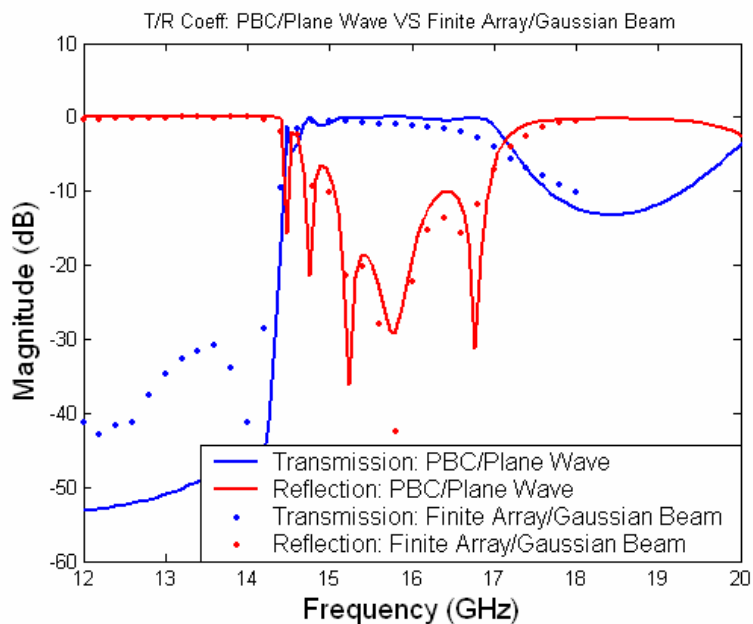


Fig. 5.37: Comparison of the magnitude of transmission and coefficient coefficients for the infinite array under plane wave illumination (solid lines) and finite array under Gaussian beam illumination (dots) at normal incidence for E_y polarization.

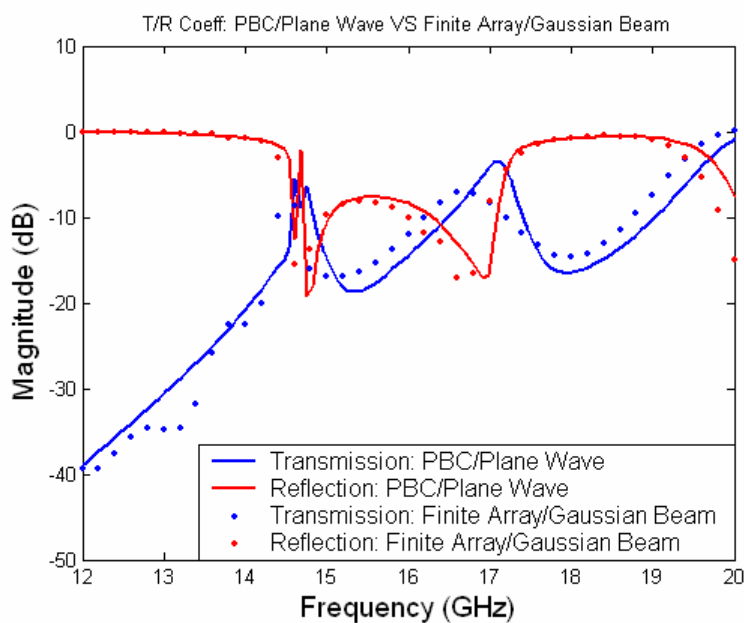
A convenient indicator of the macroscopic response of the array under certain illumination is the total transmitted or reflected power along different directions. The total transmitted and reflected powers along the specular angles can be computed by applying the near-to-far-transformation to the aperture fields on surfaces located at the transmission side of the slab and the scattered-field region behind the excitation plane, respectively. Similarly, the incident power along the propagation direction can be computed by using the aperture fields on the excitation plane when the array is removed. The ratios of the total transmission or reflection power and the incident power for the finite array case are then compared to the magnitude of transmission and reflection coefficients for the infinite array case, illuminated by a plane wave

incident from the same angle. Figure 5.37 shows an excellent agreement between the transmission/reflection coefficients for the finite and infinite arrays for the normal incidence case. Figures 5.38 (a)-(b) compare the results for the oblique incidence case of 30° off-normal, for TM_z and TE_z polarizations, respectively. As may be seen from the above figures, the match between these results is still good for an oblique incidence, though not as close as it was for the normal incidence case. It should also be noted that the scattering characteristics at oblique incidence with TE_z polarization is quite different from that of the normal incidence case; therefore, the DNG behavior might not be observed in the former case, for angles that are not close to normal.

Since a good agreement is observed between the magnitude of the transmission and reflection coefficients for the finite array case with a Gaussian beam illumination, and for the infinite array case with plane wave illumination for both the normal and oblique incidence cases, we conclude that the Gaussian beam with the chosen spot size is suitable for the study of the macroscopic response of the artificial-DNG array



(a)



(b)

Fig. 5.38: Comparison of the magnitude of transmission and coefficient coefficients for the infinite array under plane wave illumination (solid lines) and the finite array under Gaussian beam illumination (dots) at oblique incidence (30° off-normal), for (a) TMz polarization and (b) TEz polarization.

5.4.3 EM Response of the Artificial-DNG Slab at Normal Incidence with Ey Polarization

We begin by examining the field distribution at 15.3 GHz, where the array is totally transmitting, and has the refractive index closest to -1 ($n = -1.01 - 0.0004j$, $Z = 1.30 - 0.0004j$, $\epsilon_{r_{\text{eff}}} = -0.776 - 0.0006j$ and $\mu_{r_{\text{eff}}} = -1.32 - 0.0001j$). The effective material parameters are computed by applying the inversion approach—described earlier in Sec. 5.3—to the S-parameters of the infinite, periodic array of single layer at normal incidence.

The magnitudes and phases of E_y at 15.3 GHz on the y-z (E-plane) and x-z planes (H-plane) are shown in Figs. 5.39 and 5.40, respectively, for three different configurations: (a) and (b) with artificial-DNG slab; (c) and (d) for the artificial-DNG slab replaced by a dielectric slab of $\epsilon_r = 4$ of the same size; and, (e) with all structures removed, i.e., only for free space. The observation planes, with the axis of the Gaussian beam lying within, are located at the center of the computational domain, and their z-coordinates range from -24 mm to 22 mm, with the slab occupying the region between $z = -23.75$ mm to 0 mm. The region above $z = 0$ mm is free space, at the transmission side of the slab. From the plots for the magnitudes in both of these figures, it is evident that the magnitude decays smoothly in the free space region. Inside the dielectric slab, we clearly see an interference pattern, formed by the standing waves that are caused by the reflection at the two dielectric/air interfaces. On the other hand, the distribution inside the artificial-DNG array is dominated by strong fields arising from the discontinuities presented by the inclusions, and no clear interference patterns could be seen in these field plots.

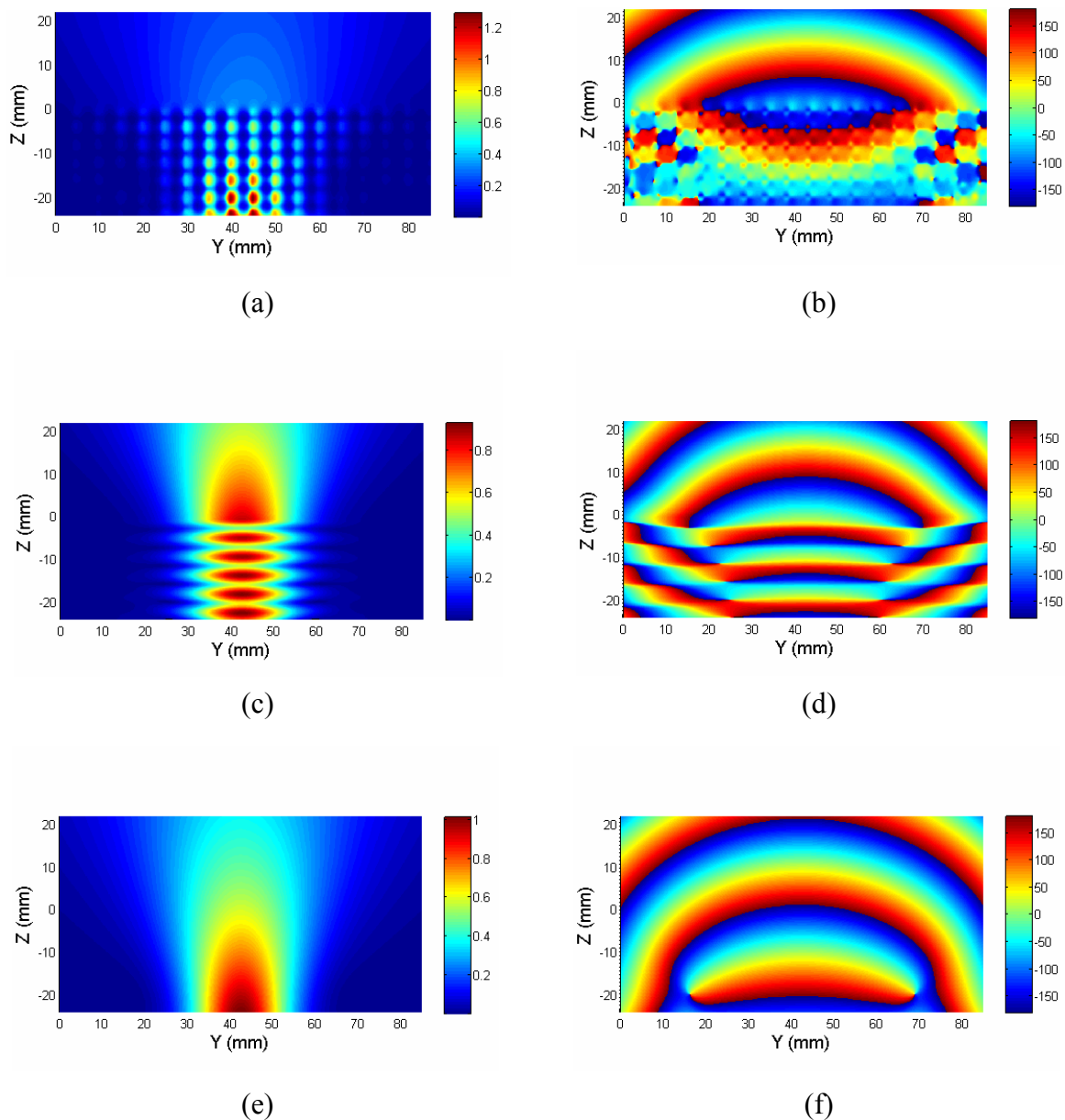


Fig. 5.39: The magnitude (Left) and phase (Right) of E_y at 15.3 GHz on the YZ plane (E-plane), for three different configurations at normal incidence: (a) and (b) With DNG slab; (c) and (d) for the DNG slab replaced by a dielectric slab of $\epsilon_r = 4$ of the same size; and (e) only for free space. The DNG or dielectric slab occupies the region between $z = -23.75$ and 0 mm, the excitation plane is on $z = 0$ mm, and the region above 0 mm is free space.

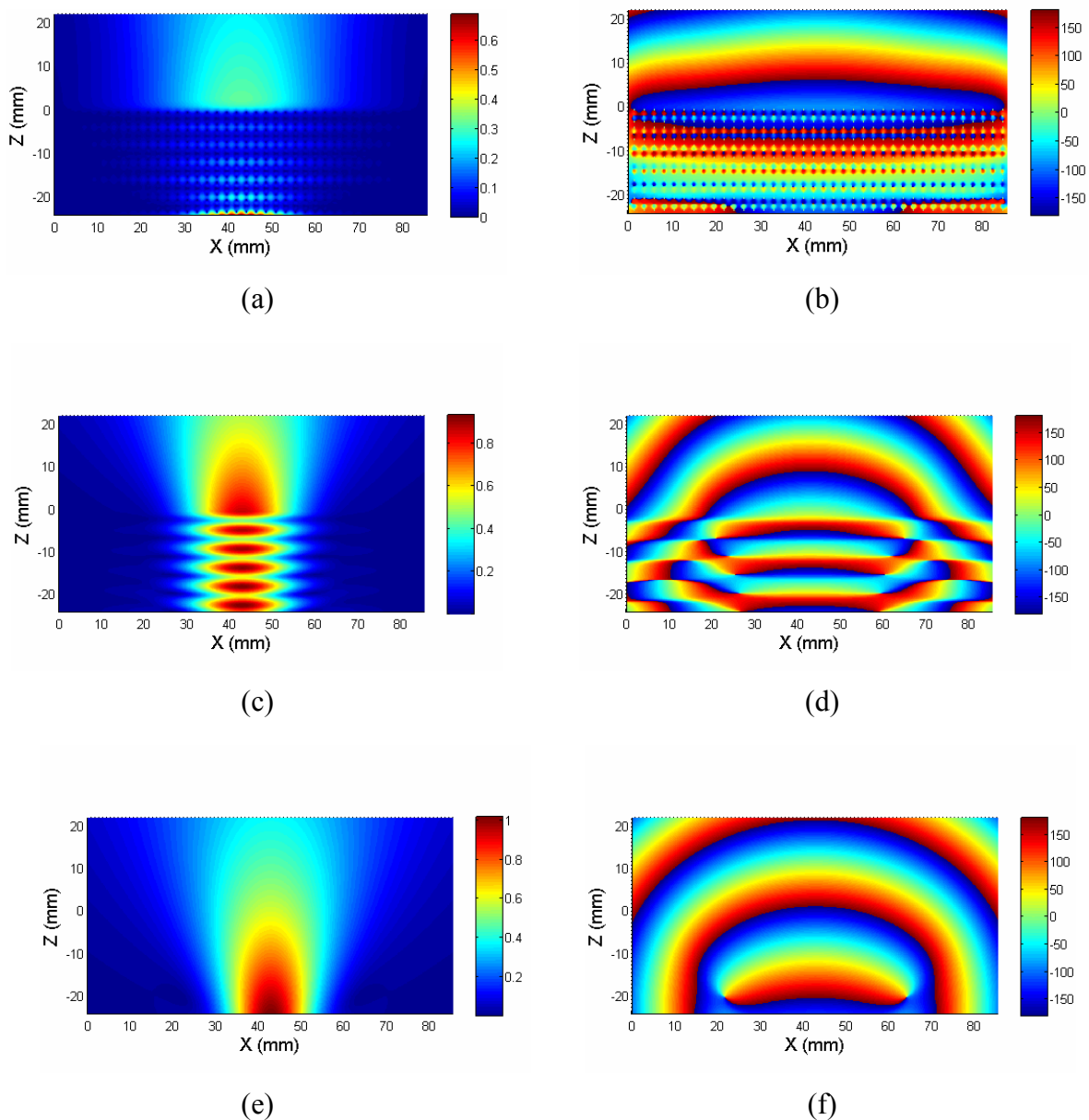


Fig. 5.40: The magnitude (Left) and phase (Right) of E_y at 15.3 GHz on the XZ plane (H-plane), for three different configurations at normal incidence: (a) and (b) With DNG slab; (c) and (d) for the DNG slab replaced by a dielectric slab of $\epsilon_r = 4$ of the same size; and (e) only for free space. The DNG or dielectric slab occupies the region between $z = -23.75$ and 0 mm, the excitation plane is on $z = 0$ mm, and the region above 0 mm is free space.

However, the phase distribution clearly demonstrates the backward wave nature of the phase velocity, which is one of the unusual characteristics of the DNG materials as well as of backward leaky wave structures. A positive phase velocity is indicated by the decreasing trend of phase along the propagating direction, i.e., the positive z -direction, and vice versa for the negative phase velocity. From the phase plots of the above figures, a positive phase velocity can be clearly observed in the free space region. Inside the dielectric slab, the phase velocity is found to be smaller than that in the free space, which is indicated by the smaller spacing between the phase fronts, though it is still positive. Inside the artificial-DNG slab, we can clearly see that the phase velocity is negative. Also, the shape of the phase front inside the artificial-DNG slab curves inward towards the source, which is located at $z = -24$ mm (indicated by the planar wavefront near the bottom center of Figs. 5.39 (f) and 5.40 (f) for incident field), while the shapes of the phase front inside the free space and the dielectric slab always curve away from the source.

The magnitudes of E_y at 15.3 GHz in the transverse plane at 2 mm and 19.5 mm away from the top surface of the slab are also plotted in Figures 5.41 (a)–(f) for three different configurations. We see from Fig. 5.41 (a) that when the observation plane is only 0.1λ away from the slab, we can still observe the granularity of the field due to the inclusions inside the array, though these variations appear to die out as we move the observation plane to about 1λ away (see Fig. 5.41 (b)). For the other two configurations, no similar field variations can be observed because of the truly homogeneous nature of the materials themselves. It should be noted that the transverse field distribution for the artificial-DNG array case is highly astigmatic, and the distribution is always found to suffer an elongation in the y -direction for this structure.

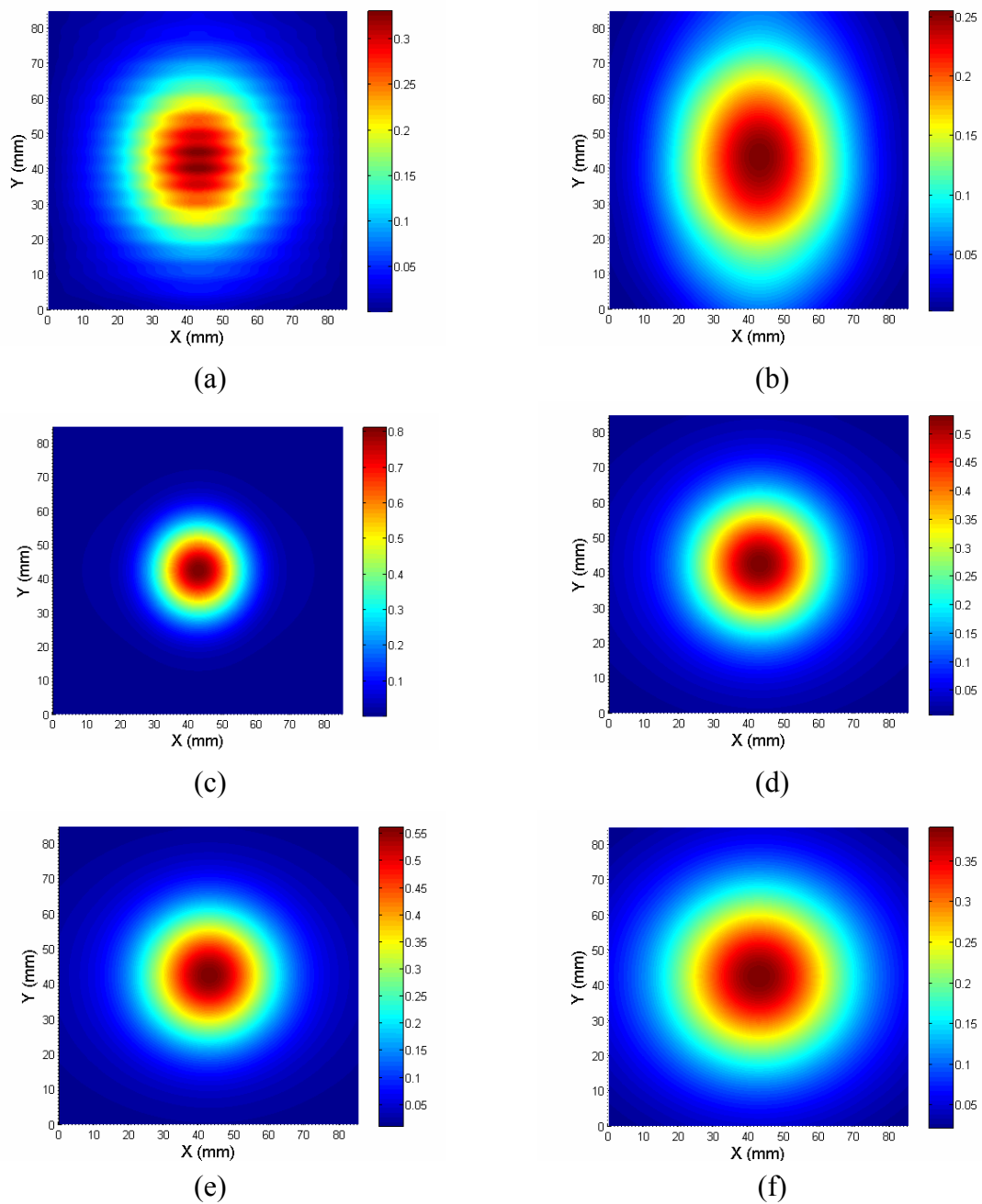


Fig. 5.41: Magnitude of E_y at 15.3 GHz on the XY plane at 2 mm (Left) and 19 mm (Right) from the top surface of the slab, for three different configurations at normal incidence: (a) and (b) With DNG slab; (c) and (d) for the DNG slab replaced by a dielectric slab of $\epsilon_r = 4$ of the same size; and (e) only for free space.

Next, we investigate the focusing effect by the artificial-DNG slab under the illumination of Gaussian beam at normal incidence. It is known that when the refractive index of an isotropic, homogeneous slab is equal to -1 for a matched medium ($\epsilon_r = \mu_r = -1$), an image can be formed at a distance h_2 from the slab (see Fig. 5.4), where $h_2 = d - h_1$, and h_1 is the distance of the source from the slab of thickness d . Its image properties would be quite different from those of the image formed by a conventional lens. For instance, it has been predicted that the phase at the image would be restored to its value at the source; and the image size can be smaller than a wavelength, because the evanescent waves are amplified by a real DNG slab to form the image. These two properties have encouraged many research groups throughout the world to attempt to realize this type of super-lens that could possibly breach the diffraction limit associated with a conventional lens. Nevertheless, we point out that the slab we study is not a matched medium ($\epsilon_{r_{\text{eff}}} = -0.776 - 0.0006j$ and $\mu_{r_{\text{eff}}} = -1.32 - 0.0001j$) at 15.3 GHz where the refractive index equals -1 ; however, we still expect that the slab would form an image, though the amplitude may be weaker.

Figure 5.42 shows the phase of E_y at 15.3 GHz along the beam axis, starting from the source, which is at 0.25 mm ($z = -24$ mm) below the artificial-DNG slab. As can be seen from the above figure, the phase propagates backward within the slab spanning the space between $z = -23.75$ and 0 mm, and then it becomes forward in free space, and restores to the same value as that of the source at $z = 23.5$ mm, which is the expected location of the image for this source location, if the slab had a refractive index of -1 .

Next, we examine the change of the magnitude of E_y near the image position along both the longitudinal and transverse directions, by inspecting the magnitude of E_y along the beam axis

(see Fig. 5.43 (a)), and the 3-dB beamwidths in the E- and H-planes (see Fig. 5.43 (b)), respectively, for the emerging beam. Neither of these plots indicates any localization of fields near the expected image position, at which all rays emanating from the source should pass. In addition, we observe a larger 3-dB beamwidth in the E-plane as compared to that on the H-plane, which is consistent with the field distribution on the transverse plane, shown previously in Fig. 5.41.

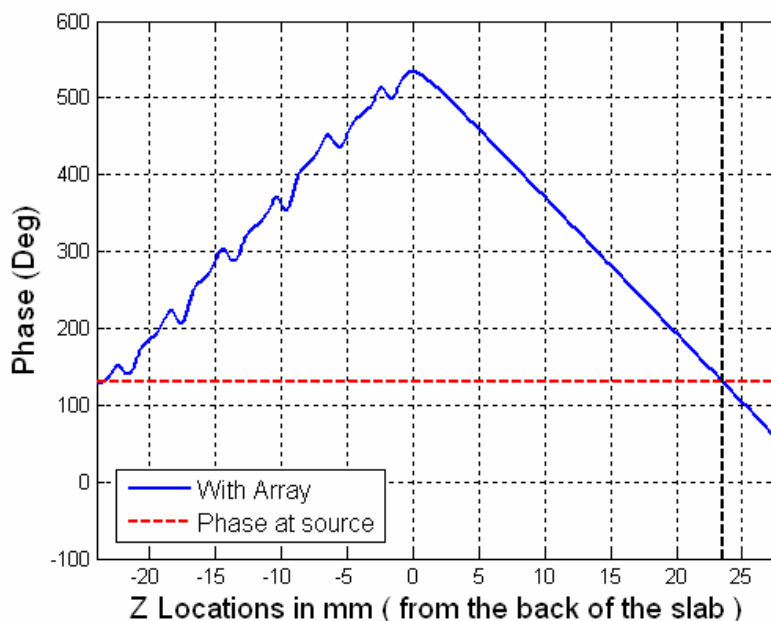
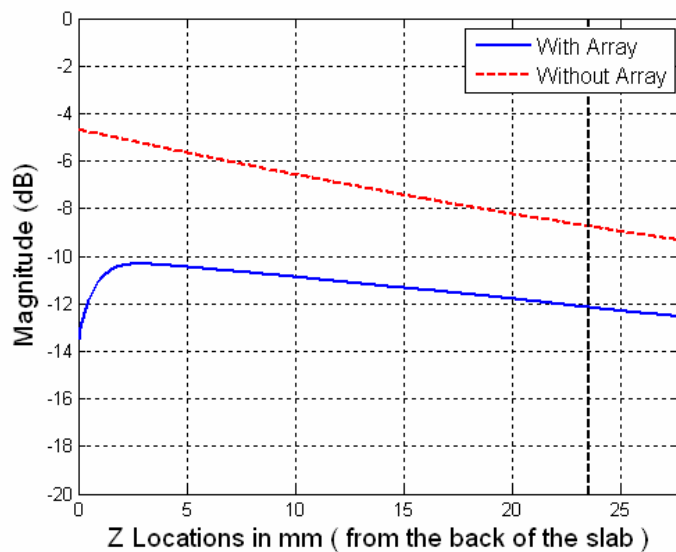
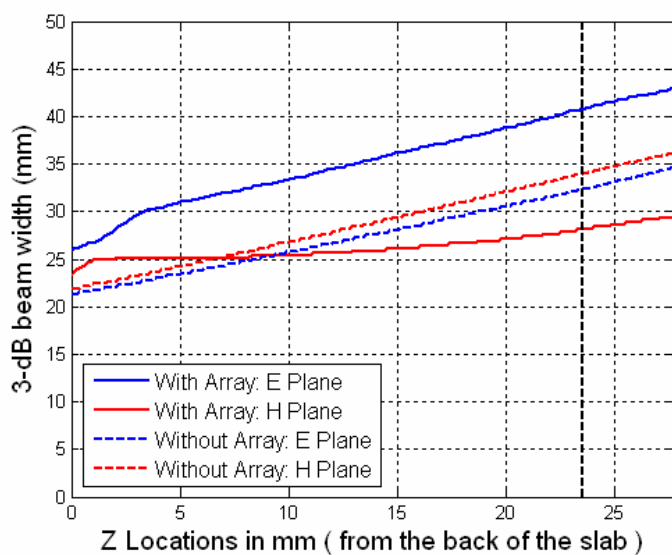


Fig. 5.42: Phase of E_y at 15.3 GHz along the beam axis from $z = -24$ to 27.75 mm, with the DNG slab occupying the region between $z = -23.75$ and 0 mm. The red dashed line indicates the value of phase at the source. Notice that the measured phase restores to its value at the source at $z = 23.5$ mm, indicated by the vertical black dashed lines, which is the expected image location when the refractive index of the slab is equal to -1 .



(a)



(b)

Fig. 5.43: (a) Magnitude of E_y at the beam axis and (b) the 3-dB beam width on the E- and H-planes along the longitudinal direction at 15.3 GHz, inside the transmission region of the DNG slab. The corresponding magnitude and beam width with all structures removed are also plotted in dotted lines. The vertical dash line at $z = 23.5$ mm indicates the expected image location when the refractive index of the slab is equal to -1 .

To summarize the results of our investigation on the focusing effect, we do observe a restoration of phase at the expected image position; however, we do not find any localization of field in its neighborhood. Therefore, we conclude that the focusing effect is not fully exhibited for this artificial-DNG slab at the frequency where the effective refractive index has been found to be -1 , under the illumination of Gaussian beam at normal incidence.

5.4.4 EM Response of the Artificial-DNG Slab at Oblique TM_z Incidence Coming from ($\theta=150^\circ$, $\phi=90^\circ$) with H_x Polarization

Another unusual phenomenon associated with the negative refraction is the bending of rays towards the same side of the normal at the interface, when the rays enter a DNG slab from free space, or vice versa, at oblique incidence, as shown in Fig. 5.35. The Snell's law can still be applied by having negative values of refractive index, found inside a DNG medium. Since the transmission and reflection characteristics of the artificial-DNG array at 30° off-normal incidence for the TM_z polarization are similar to those of the same array at normal incidence, the DNG behavior is expected to be retained for the oblique incidence case for TM_z polarization.

Figures 5.44 (a)-(f) plot the magnitudes and phases of E_y at 15.3 GHz on the y - z plane (E-plane), which is also the plane of incidence, for three different configurations that are identical to those appearing in Fig. 5.39. As shown in Figs. 5.44 (e) and (f), the incident beam, excited at $z = -24$ mm with its maximum at $y = 42.5$ mm (centre of the computational domain), propagates along the positive z -direction, with decreasing y . A rough estimate of the beam direction can be made by tracking the beam maxima. For the dielectric slab, the beam first bends slightly towards the normal when it enters the slab, and then bends away from the normal when it exits the slab, which is an indication of positive refraction of the medium. For the artificial-DNG

slab (see Fig. 5.44 (a)), it is unable to define a continuous beam path inside the slab because of the strong irregularity of fields in the inhomogeneously-filled slab. Nonetheless we can still assert the fact that the beam does not bend towards the same side of the normal when it enters the slab, as we would expect when we have negative refraction, since the beam lies on the left half of the figure, all through the slab and, of course, when it exits the slab in the free space region.

The magnitudes of E_y on the x-y plane at 19.5 mm above the slab are shown in Figs. 5.45 (a)-(c) for the same three configurations. From fig 5.45 (a), we observe the presence of more than one beam along the y-direction, which is different from those observed for the cases of homogeneous dielectric slab and with free space, or even for the artificial-DNG slab illuminated by a normally incident beam. Since we do not observe any significant shift of the beam in the positive y-direction as compared to the incident beam in Fig. 5.45 (c), once again negative refraction is not seen to be present in this test example.

The distribution of the z-component of the Poynting vector, which is a more accurate representation of the energy flow, is also shown in Figs. 5.46 (a) and (b) for the dielectric and artificial-DNG slabs, respectively. The bending of the beam at the entrance and exit the dielectric slab is seen much clearly because of the absence of interference pattern; however the path of the energy flow is still not defined precisely inside the artificial-DNG slab. Figure 5.46 (c) shows the z-component of the Poynting vector in the free space region above the artificial-DNG slab. We observe that there are more than one beams emerging from different positions at the surface of the slab and traveling in different directions. Nevertheless, all emerging beams appear to exit from the left side of the slab, and negates, once again, the presence of negative refraction of the beam at the interface between the DNG medium and free space.

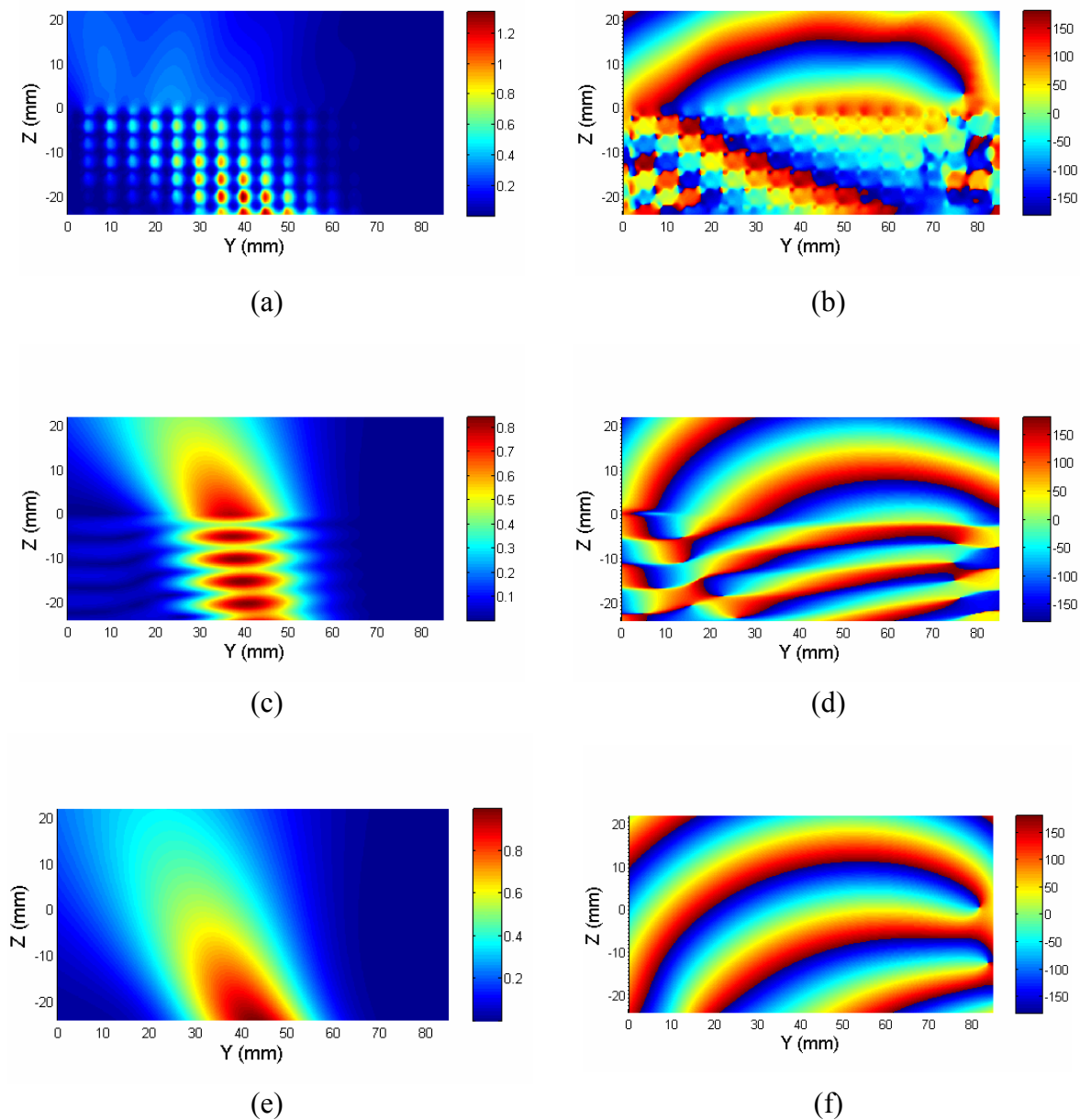


Fig. 5.44: The magnitude (Left) and phase (Right) of E_y at 15.3 GHz on the YZ plane (E-plane), for three different configurations at oblique TMz incidence (30° off-normal): (a) and (b) With DNG slab; (c) and (d) for the DNG slab replaced by a dielectric slab of $\epsilon_r = 4$ of the same size; and (e) only for free space. The DNG or dielectric slab occupies the region between $z = -23.75$ and 0 mm, the excitation plane is on $z = 0$ mm, and the region above 0 mm is free space.

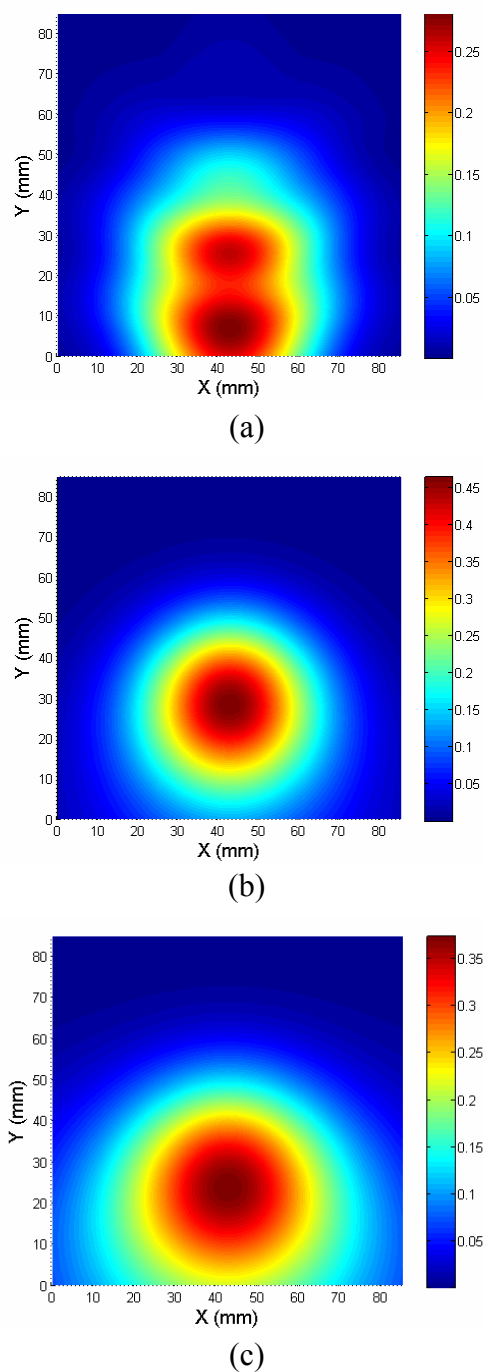
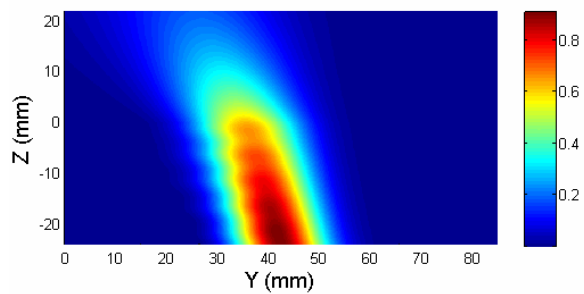
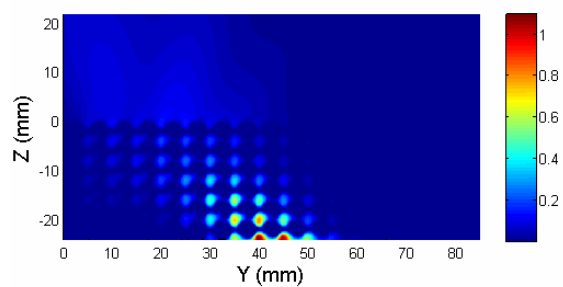


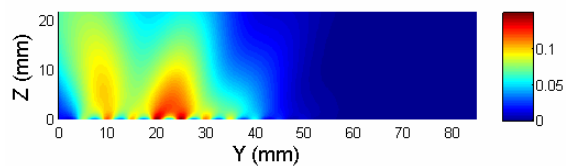
Fig. 5.45: Magnitude of E_y at 15.3 GHz on the XY plane at 19 mm above the slab at oblique TMz incidence (30° off-normal) for three different configurations: (a) With DNG slab; (b) for the DNG slab replaced by a dielectric slab of $\epsilon_r = 4$ of the same size; and (c) only for free space.



(a)



(b)



(c)

Fig. 5.46: The normalized magnitude of S_z at 15.3 GHz on the YZ plane (E-plane) between $z = -24$ mm and 0 mm at oblique TMz incidence (30° off-normal) for two different configurations: (a) dielectric slab; (b) DNG slab. (c) is the figure extracted from (b) over the free space region above the DNG slab.

We further determine the exit locations of the transmitting beam at the artificial-DNG slab by tracing the path at which the Poynting vector is at its maximum along the transverse direction, and then projecting the path backward to the top surface at the slab by using a linearly curve-fitting. Figure 5.47 plots the y-coordinates of the beam maximum (in blue line) along the longitudinal direction on the y-z plane at 15.3 GHz. Large jumps in the locations of the maxima occur near $z = 13$ mm, which can be explained by the existence of two emerging beams, as shown in Fig. 5.46 (c). Each beam decays at a different rate, causing one beam to dominate in the region near the slab and the other be strong in the region further away from the slab. By employing the above steps on the fields in these two regions separately, we find that the two beams exit at $y = 11.5$ mm and 22.5 mm, respectively, which are both on the opposite side of the normal where the incident beam first enters the slab at $y = 42.5$ mm.

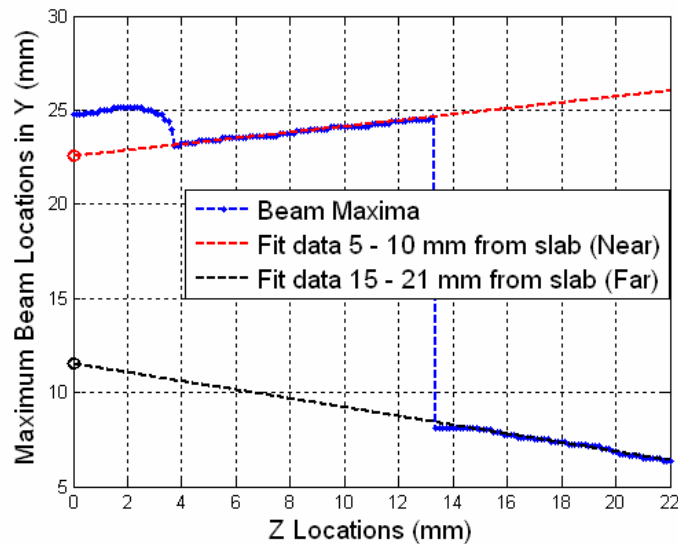


Fig. 5.47: The transmitted beam maxima locations versus the longitudinal direction (Blue) at 15.4 GHz for TMz incidence of DNG slab. These data are separated into two groups according to the distances from the slab, and utilized to track the exit location of the beam at the slab surface at $z = 0$ mm. See the red and black lines for the trace path using the fields near to (5 – 10 mm) and far away from (15-21 mm) the slab.

The exit locations of the beams for the artificial-DNG slab, along with those for the dielectric slab as well as free space at $z = 0$ mm, are plotted in Fig 5.48 at frequencies within the first transmission band of the artificial-DNG slab, ranging from 14.6 to 16.2 GHz. The refractive indices increase monotonically from -1.89 to -0.45 within this frequency band. We see that only a single beam is present for the dielectric slab as well as for the free space case, and a single exit location can be determined by following the same steps as described earlier. From the above figure, we deduce that the refracted beam always bends towards the normal at the dielectric/free-space interface, which is expected for a positive-index medium. Except at 14.6 GHz, the refracted beam for the artificial-DNG slab always bends away from the normal at the interface between the DNG medium and free space, which is contradictory to what is expected for a negative index medium.

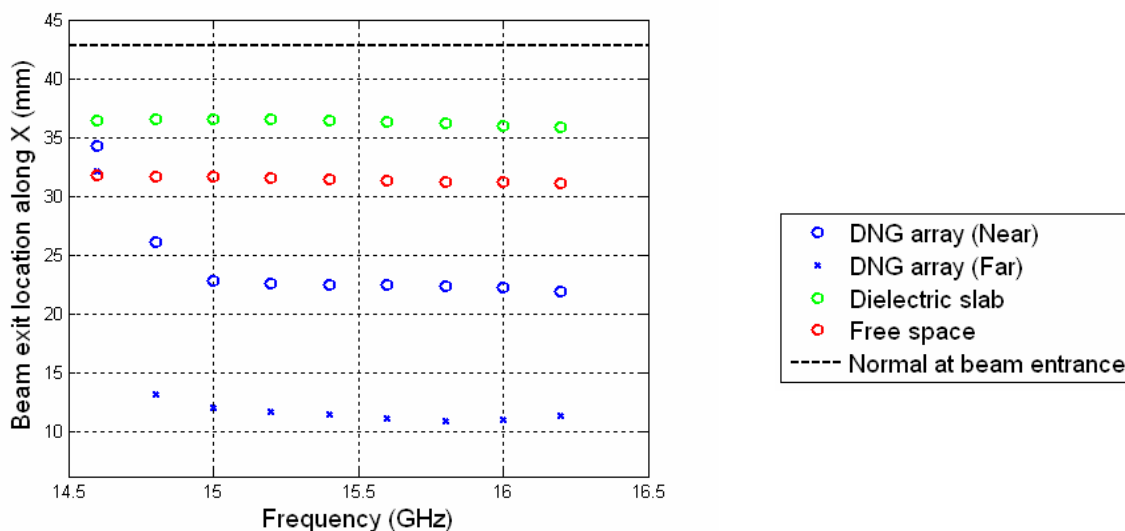


Fig. 5.48: The exit location of the beam at the top surface of the slab on $z = 0$ at TMz incidence, for three different configurations: (i) the beam that dominate in the region near to (Blue circles) and far away (Blue crosses) from the DNG slab ;(ii) With dielectric slab (Green circles); and (iii) only for free space. (Red circles). The incident beam enters the slab at $x = 42.75$ mm (black line).

In contrast to the magnitude distribution of the field, or the energy flow, the phase distribution inside the artificial-DNG slab clearly exhibits negative refraction. As can be seen in Fig. 5.44 (b), the normal of the phase front bends towards the same side of the normal of the slab at both interfaces between DNG medium and free space. In addition, we observe the backward wave propagates within the artificial-DNG slab, which was also true for the normal incidence case.

5.4.5 EM Response of the Artificial-DNG Slab at Oblique TE_z Incidence Coming from ($\theta=150^\circ$, $\phi=0^\circ$) with E_y Polarization

Since the transmission and reflection characteristics for the incident angle of $\theta=150^\circ$ and $\phi=0^\circ$ and TE_z polarization are quite different from those for the normal incidence case, the DNG behavior may not be observed in this case.

We begin by examining the field distribution at 15.3 GHz, where the array is partially transmitting and partially reflecting for the present illumination. Figures 5.49 (a)-(f) show the magnitudes and phases of E_y at 15.3 GHz on the x - z plane (H-plane), which is the plane of incidence, for the same configurations as studied previously. From the plots of Figs. 5.49 (a) and (b), we can see that the beam energy propagates in the direction close to the normal within the artificial-DNG slab, while the phase propagates backward within the slab, and the normal to the phase bends towards the same side of the normal of the slab at the interface between the DNG medium and free space. In contrast to the oblique incidence case when the polarization was H_x , only a single beam emerges from the artificial-DNG slab. It is further confirmed by the E_y distribution on the transverse plane which is at 19.5 mm above the slab (see Fig. 5.50 (a)). In

addition, we can deduce from Fig. 5.50 (a) and (c) that the beam bends towards the normal when it enters the slab.

Figure 5.51 plots the exit locations of the transmitting beam at the artificial-DNG slab, along with those for the dielectric slab, as well as free space, at $z = 0$ mm, at frequencies ranging from 14.6 to 16.2 GHz. From the results, we deduce that the refracted beam bends towards the normal at the DNG medium/free-space interface, indicating a positive refraction where the slab has a refractive index of greater than unity. Below 15.4 GHz, the beam travels close to the normal within the artificial-DNG slab. So far, none of the above results has demonstrated the bending of beam towards the same side of the normal at the interface between the DNG medium and free space.

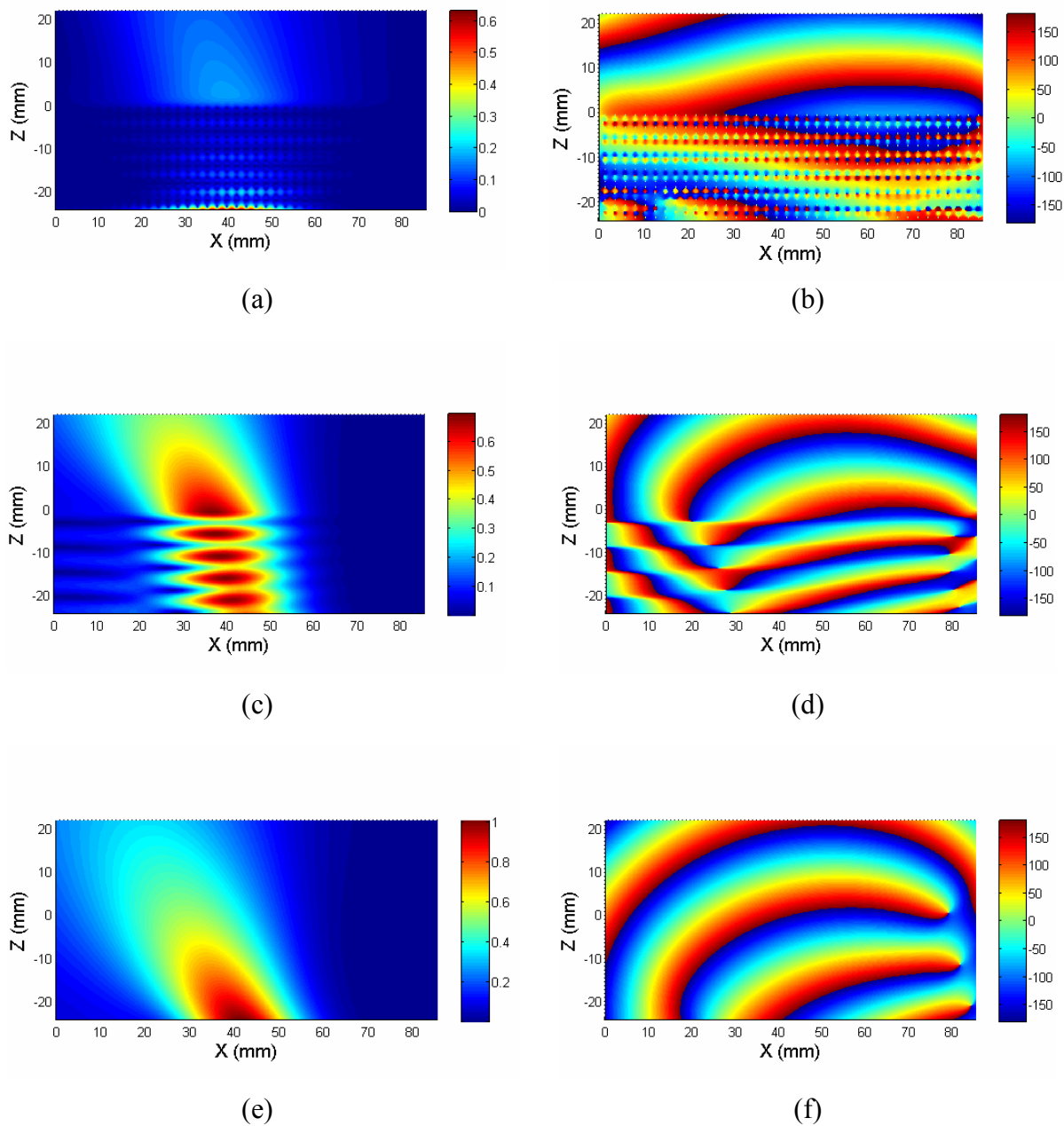
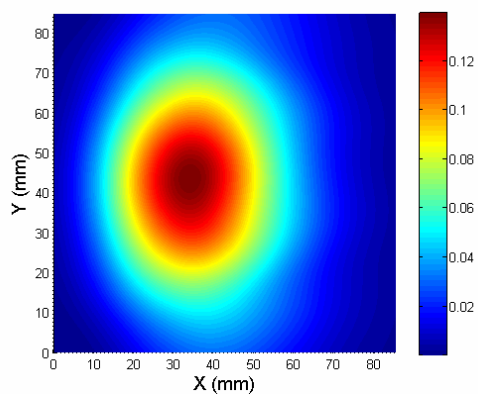
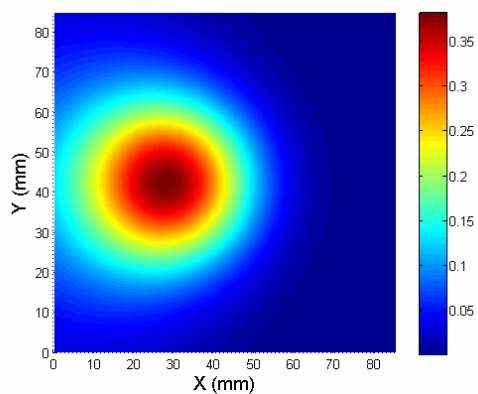


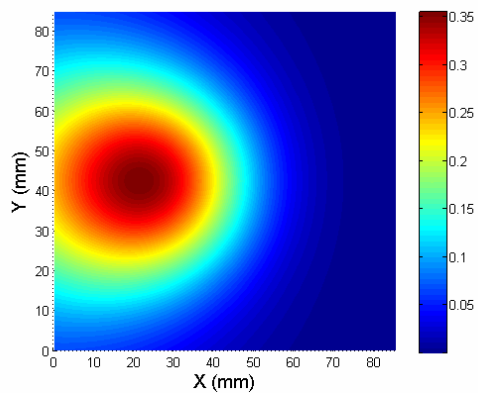
Fig. 5.49: The magnitude (Left) and phase (Right) of E_y at 15.3 GHz on the XZ plane (H-plane) at oblique TE $_z$ incidence (30° off-normal) for three different configurations: (a) and (b) With DNG slab; (c) and (d) for the DNG slab replaced by a dielectric slab of $\epsilon_r = 4$ of the same size; and (e) only for free space. The DNG or dielectric slab occupies the region between $z = -23.75$ and 0 mm, the excitation plane is on $z = 0$ mm, and the region above 0 mm is free space.



(a)



(b)



(c)

Fig. 5.50: The exit location of the beam at the top surface of the slab on $z = 0$ for three different configurations: (i) the beam that dominates in the region near to (Blue circles) and far away (Blue crosses) from the DNG slab ;(ii) With dielectric slab (Green circles); and (iii) only for free space. (Red circles). The incident beam enters the slab at $x = 42.75$ mm (black line).

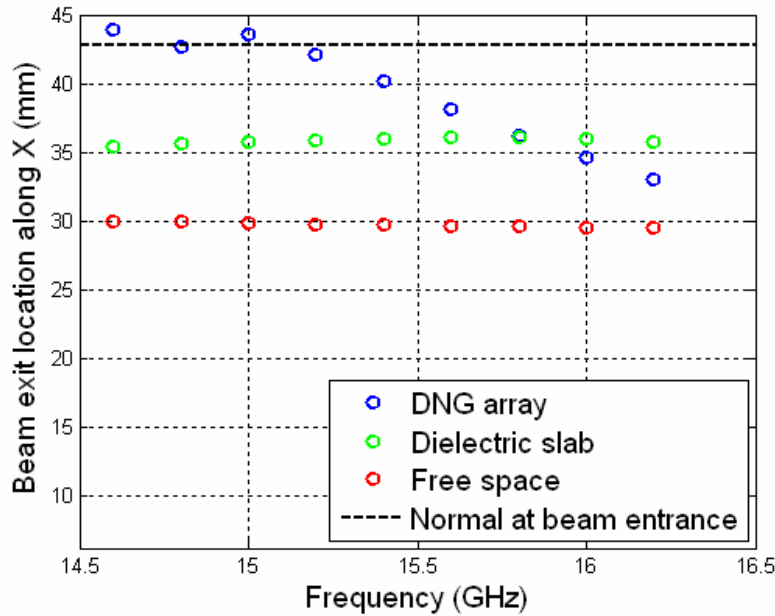


Fig. 5.51: The exit location of the beam at the top surface of the slab on $z = 0$ at TE_z incidence, for three different configurations: (i) With DNG slab (Blue); (ii) With dielectric slab (Green); and (iii) only for free space. (Red). The incident beam enters the slab at $y = 42.5$ mm (black line).

5.5 EM Response of a Finite Artificial-DNG Slab Excited by Small Dipole

In the previous sections, we have extensively studied the EM response of the artificial-DNG array illuminated by a Gaussian beam, with a spot size on the order of the wavelength. It is also worthwhile to study the focusing effect of the artificial-DNG slab when a small source is used for excitation.

The artificial-DNG array and all the FDTD settings remain the same as those employed previously in Sec. 5.4, except that the Gaussian beam excitation is now replaced with a y -oriented dipole. The excitation is applied at the edge of the FDTD cell at the centre of the x - y plane, and located at 11.5 mm below the slab ($z = -32.25$ mm). At this source location, an image is expected to form at 12.25 mm above the slab with a refractive index of -1 .

Figures 5.52 (a)-(b) and 5.53 (a)-(b) show the magnitudes and phases of E_y at 15.3 GHz on the y - z (E-plane) and x - z (H-plane) planes, respectively. The field distributions, with the artificial-DNG array removed, are also shown in the same figures, viz., (c) and (d), for comparison. Note that the magnitude is only shown for the transmission region 1.5 mm above the slab, in order to have a clear view of the transmitted field. From the above figures, we notice a highly astigmatic amplitude distribution in the transmission region of the artificial-DNG slab. In the H-plane, the field distribution is much narrower than that when the artificial-DNG slab is removed, while on the E-plane, the field distribution is much boarder than that without the artificial-DNG array. In addition, we note that there are multiple nodes on this plane. This broadening and narrowing of the field distribution along different directions are also observed when the array is illuminated by a Gaussian beam at normal and oblique incidence, while the existence of multiple nodes along the y -direction is only observed at oblique TM_z incidence of Gaussian beam. On the other hand, in common with the case of a Gaussian beam illumination, the phase distribution inside the artificial-DNG slab clearly demonstrates the presence of negative refraction accompanied by a backward phase velocity.

Figures 5.54 (a)–(c) show the magnitude of E_y on the x - y plane at 12.25 mm above the slab at 14.8, 15.3 and 16.0 GHz, respectively. The corresponding refractive indices of the slab at these frequencies are -1.54 , -1.01 , and -0.554 ; therefore, an image is expected to form on the observation plane only at the second frequency. From the magnitude plots, we notice multiple nodes, with a difference in the relative strength, are formed at nearly the same locations for all three frequencies, despite of the large differences in the refractive indices. No clear image can be observed at 15.3 GHz. We also plot the magnitude of E_y at the centre axis, and the 3-dB

beamwidth on the H-plane at 15.3 GHz in Figs. 5.55 (a) and (b), respectively. We find that none of these plots show any localization of field near the expected image location.

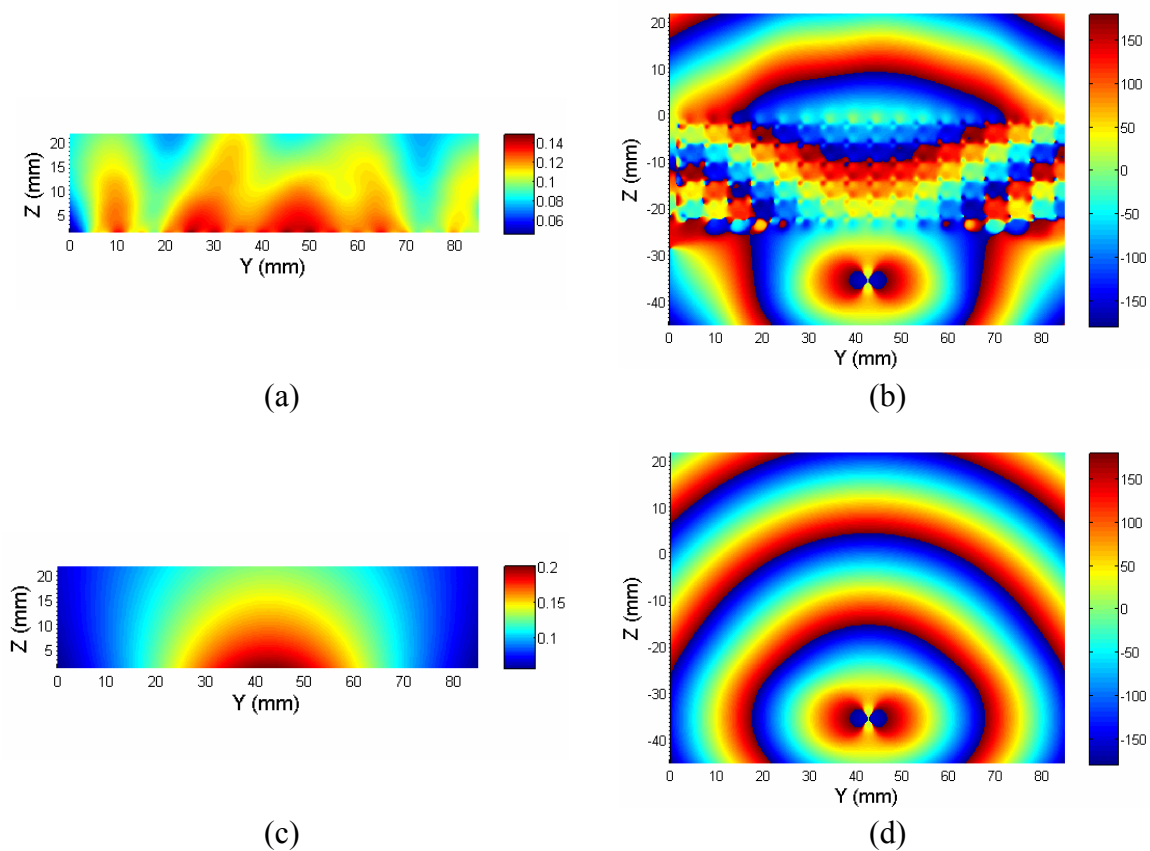


Fig. 5.52: The magnitude (Left) and phase (Right) of E_y at 15.3 GHz on the YZ plane (E-plane), for two different configurations with dipole excitation at $z = -32.35$ mm: (a) and (b) With DNG slab; (c) and (d) only for free space. The DNG slab occupies the region between $z = -23.75$ and 0 mm, and the region above 0 mm is free space.

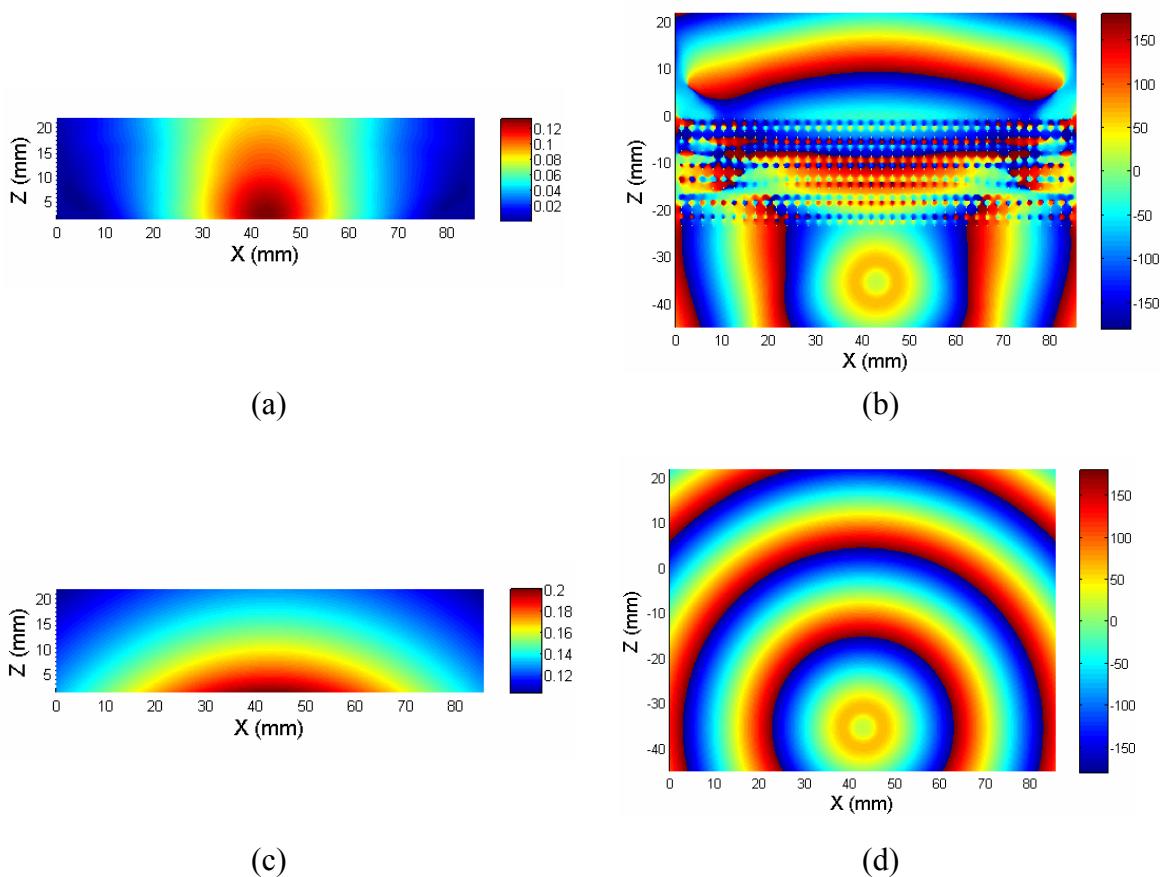
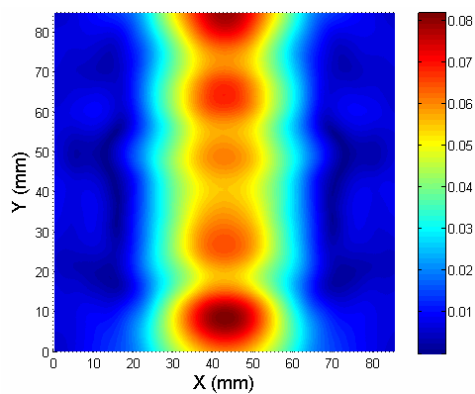
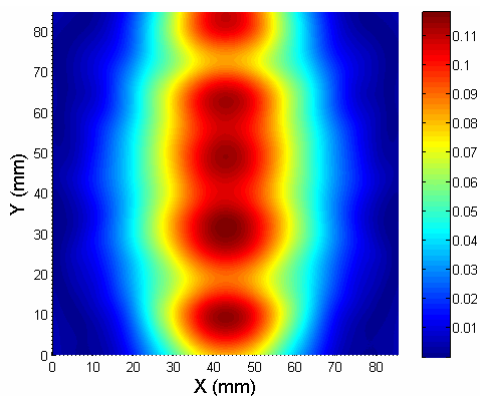


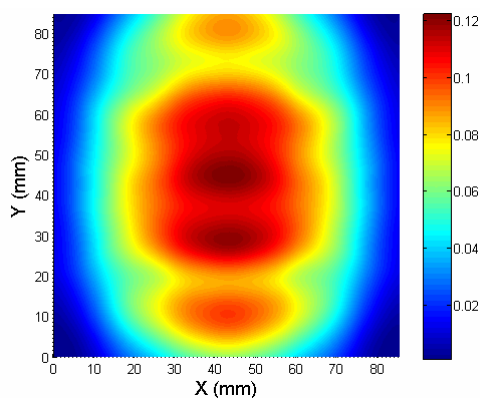
Fig. 5.53: The magnitude (Left) and phase (Right) of E_y at 15.3 GHz on the XZ plane (H-plane), for two different configurations with dipole excitation at $z = -32.35$ mm: (a) and (b) With DNG slab; (c) and (d) only for free space. The DNG slab occupies the region between $z = -23.75$ and 0 mm, and the region above 0 mm is free space.



(a)

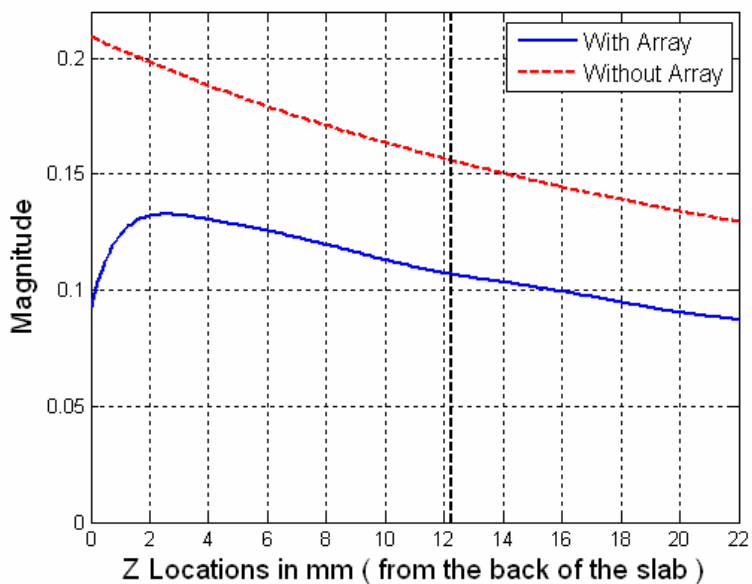


(b)

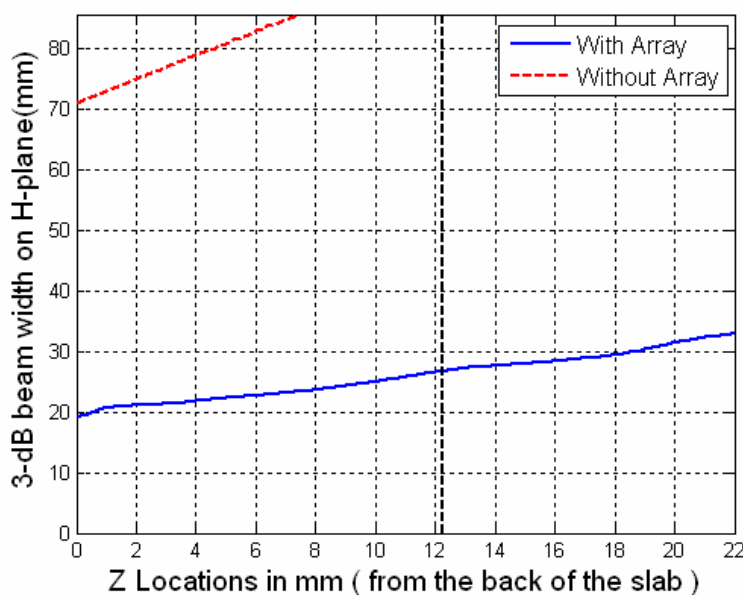


(c)

Fig. 5.54: Magnitude of E_y on the XY plane at 12.25 mm above the DNG slab at frequencies of (a) 14.8 GHz, (b) 15.4 GHz, and (c) 16.0 GHz with dipole excitation at 11.5 mm below the bottom surface of the slab.



(a)



(b)

Fig. 5.55: (a) Magnitude of E_y at the centre axis and (b) the 3-dB beam width on the E- and H-planes along the longitudinal direction at 15.3 GHz, inside the transmission region of the DNG slab excited by small dipole. The corresponding magnitude and beam width with all structures removed are also plotted in dotted lines. The vertical dash line at $z = 12.25$ mm indicates the expected image location when the refractive index of the slab is equal to -1 .

5.6 Conclusions

In this chapter, we have carried out an extensively study of the EM response of an artificial-DNG slab, comprising of a combination of split-rings and wires, by using the parallel FDTD technique. A preliminary analysis of the scattering characteristics of the infinite array, illuminated by a plane wave, has been performed by using the PBC/FDTD code, which was described in Chapter 3. The effective material parameters for the DNG slab have been extracted by using the modified inversion approach. We have also discussed the difficulties encountered in the retrieval process, identified some problem areas that may be encountered when using the effective material parameters in real-world applications, and pointed out the importance of performing rigorous simulation of the physical structure, in which the inclusions inside the metamaterial structure are also modeled accurately, in order to evaluate the performance of such system in a reliable manner.

In addition, we have demonstrated the power of a highly efficient, parallel FDTD code when rigorously simulating the EM response of the finite artificial-DNG array when illuminated by a Gaussian beam, or a small dipole, where the total number of unknown fields to be solved exceeds 1.6 billions. Two unique phenomena of DNG medium, namely the negative refraction and the focusing effect, have been investigated. At the frequency where the slab has a refractive index of -1 , the phase clearly demonstrates a backward phase velocity inside the slab, and restores the value of the source at the expected image position. However, none of the results has demonstrated the bending of beam towards the same side of normal when the beam enters the artificial-DNG slab from free space, or any localization of fields near the image location. Also, the emerging beam has been found to be highly astigmatic in nature. Even multiple beams have been observed in the transmission region when the array is illuminated by a TM_z Gaussian beam

at an oblique angle, or excited by a small dipole. None of these behaviors can be explained by using the effective medium concept, or deduced from the result of the simulation for the infinite, periodic array illuminated by plane wave.

It is possible that the main reason for the failure of our artificial-DNG array to fully demonstrate the negative refraction and focusing effect is the anisotropic nature of the unit cell element we have chosen. Though, according to the published literature, the SRR and wire combination is the distinct frontrunner among the candidates for the metamaterial elements that exhibit a DNG behavior, as we have also conformed by evaluating its effective medium properties of the chosen element.

Chapter 6

CONCLUSIONS AND FUTURE WORK

The primary objectives of research reported in this thesis have been twofold: (i) the development of numerically efficient schemes for a 3-D parallel FDTD solver that fills the gap in the present FDTD technique; and, (ii) the application of this technique to the study of metamaterial structures.

In Chapter 2 we have presented the algorithm of the parallel FDTD technique, followed by a discussion on some design rules for the parallel setting, that helps extract the best parallel performance from the FDTD solver. The efficiencies of the parallel FDTD solver, running on different computer clusters, have been measured. Finally, three practical examples have been presented to demonstrate the power of the 3-D parallel FDTD solver in solving electrically large and complex problems in a time-efficient manner.

In Chapter 3 we have proposed an efficient, parallel implementation of the split-field based PBC/FDTD solver, which can significantly reduce the total simulation time when multiple processors are used. The parallel technique utilizes the domain decomposition approach, as discussed in Chapter 2. It has been demonstrated that the efficiency of the parallel PBC/FDTD code is nearly as high as that of the parallelized 3-D FDTD code. In addition, we have identified an instability issue occurring when we attempt to combine the most recently developed CPML with the split-field PBC/FDTD method, which has been successfully implemented in the past in the conventional FDTD method. This instability originated from the employment of the forward-

differencing form of the update equations. A stable, and yet simple implementation of CPML in the PBC/FDTD algorithm has been proposed, and discussed in detail.

In Chapter 4, we have proposed an excitation scheme, based on modifying the conventional TF/SF approach, to launch the desired incident field distribution in scattering problems involving infinite structures. Instead of using a closed TF/SF box in the conventional TF/SF approach, we have applied the TF/SF technique only on a single plane. We have shown that a windowing function can also be applied to the “incident field” excited on the TF/SF interface to generate the desired incident field distribution, which can be something other than a uniform plane wave. The performance of the proposed scheme in launching two different incident field distributions has been studied. For a Gaussian beam illumination, we have demonstrated that the proposed scheme works excellently for practical scenarios, provided that the beam waist of the Gaussian beam is greater than one wavelength, and the interested region is larger than the spot size. For a plane wave illumination, we have shown that the reflection from the edge of the TF/SF interface is significantly reduced by extending the TF/SF interface into the PML region. This reflection is barely noticeable at normal incidence, and remains acceptably low for small incident angles. We have also demonstrated that a reduction of the reflection level is achieved by applying a window function to the incident fields, at the TF/SF interface, located within the PML region. In addition, guidelines have been set up for “when and how to” use this scheme in order to obtain accurate results in practical simulations.

In Chapter 5, we have extensively studied the EM response of an artificial-DNG slab comprising of a combination of split-rings and wires by using the parallel FDTD technique. A preliminary analysis on the scattering characteristics of the infinite array, illuminated by a plane wave, has been performed by using the parallel PBC/FDTD solver. The effective material

parameters for the DNG slab are then extracted by using the modified inversion approach. We have also discussed the difficulties encountered in the retrieval process, identified some problem areas that may be encountered when using effective material parameters in real-world applications, and pointed out the importance of performing rigorous simulation of the physical structures, where the inclusions inside the metamaterial structures are also modeled accurately, in order to evaluate the performance of such systems in a reliable manner.

In addition, we have demonstrated the power of the highly efficient, parallel FDTD code to rigorously simulate the EM response of the finite artificial-DNG array under the illumination of a Gaussian beam, as well as a small dipole, where the total number of unknown fields to be solved exceeds 1.6 billion. Two unique phenomena associated with a DNG medium, namely the negative refraction and the focusing effect, have been investigated. At the frequency where the slab has a refractive index of -1 , the phase behavior clearly exhibits a backward phase velocity inside the slab, and restores the value of the source at the expected image position. However, neither of these results have demonstrated the bending of beam towards the same side of normal when the beam enters the artificial-DNG slab from free space, nor have they shown any indication of localization of the fields near the image position. Also, the emerging beam has been found to be highly astigmatic in nature. Even multiple beams have been observed in the transmission region when the array is illuminated by a TM_z Gaussian beam at an oblique angle, or excited by a small dipole.

In the aspect of the development of numerical schemes in FDTD, we see room for further improvement and development of the schemes proposed in this thesis. First, the present PBC/FDTD solver works only for a non-dispersive medium, and can be generalized to work for dispersive medium for wider applications. In Chapter 3, we have identified an instability issue

that arises when we combine the CPML and PBC/FDTD algorithm, and have proposed a stable scheme to address this problem. Since both schemes for the dispersive material analysis and the CPML implementation utilize the recursive convolution technique, the stability and accuracy problems may surface again if the scheme for dispersive material is not implemented properly in the PBC/FDTD solver. From our experience discussed in Chapter 3, we may apply a similar scheme—by using twofold auxiliary variables and update them in alternate cycles—to ensure the stability and accuracy of a dispersive PBC/FDTD scheme.

In addition, we have found that the proposed excitation scheme discussed in Chapter 3 has major limitations for plane wave excitation for moderate-to-large incident angles, because of edge reflections at the TF/SF interface. Further efforts are needed to overcome this shortcoming of the excitation scheme.

In the aspect of the study of metamaterials, our chosen artificial-DNG array found little evidence of the negative refraction and focusing effects predicted by simple and approximate theories. One of the possible reasons is the anisotropic nature of the unit cell element chosen. It would be interesting to design another unit cell element that provides a nearly-isotropic scattering response, and then repeat the same steps described in Chapter 5 to see if the results indeed agree with those predicted by the effective medium approach.

Bibliography

1. R.F. Harrington, *Field Computation by Moment Methods*, New York: Macmillan, 1968.
2. K. R., Umashankar, "Numerical analysis of electromagnetic wave scattering and interaction based on frequency-domain integral equation and method of moments techniques," *Wave Motion*, Vol. 10, pp. 493-525, 1988.
3. K. S. Yee, "Numerical solution of initial boundary value problems involving Maxwell's equations in isotropic media," *IEEE Trans. Antennas Propagat.*, vol. 14, pp. 302-307, 1966.
4. R. Luebbers and F. Hunsberger, K. Kunz, R. Standler, and M. Schneider, "A frequency-dependent finite-difference time-domain formulation for dispersive materials," *IEEE Trans. Electromagnetic Compatibility*, vol. 32, pp. 222 - 229, 1990.
5. T. Kashiwa and I. Fukai, "A treatment by FDTD method of dispersive characteristics associated with electronic polarization," *Microwave Opt. Technol. Lett.*, vol. 3, pp. 203-205, 1990.
6. P. M. Goorjian and A. Taflove, "Direct time integration of Maxwell's equations in nonlinear dispersive media for propagation and scattering of femtosecond electromagnetic solitons," *Optics Letters*, vol. 17, pp. 180-182, 1992.
7. S. D. Gedney, "An anisotropic perfectly matched layer absorbing media for the truncation of FDTD lattices," *IEEE Trans. Antennas Propagat.*, vol. 44, no. 12, pp. 1630 - 1639, 1996.
8. J. A. Roden and S. D. Gedney, "Convolutional PML (CPML): An efficient FDTD implementation of the CFS-PML for arbitrary media," *Microwave Opt. Technol. Lett.*, vol. 27, pp. 334-339, 2000.
9. J. P. Berenger, "A perfectly matched layer for the absorption of electromagnetic waves," *J. Computational Physics*, vol. 114, pp. 185-200, 1994.
10. T. G. Jurgens, A. Taflove, K. R. Umashankar, and T. G. Moore, "Finite-difference time-domain modeling of curved surfaces," *IEEE Trans. Antennas Propagat.*, vol. 40, pp. 357 - 366, 1992.
11. S. Dey and R. Mittra, "A locally conformal finite-difference time-domain algorithm for modeling three-dimensional perfectly conducting objects," *IEEE Microwave Guided Wave Lett.*, vol. 7, pp. 273-275, 1997.

12. A. C. Cangellaris, C.-C. Lin, and K. K. Mei, "Point-matched time-domain finite element methods for electromagnetic radiation and scattering," *IEEE Trans. Antennas Propagat.*, vol. 35, pp. 1160-1173, 1987.
13. V. Shankar, A. H. Mohammadian and W. F. Hall, "A time-domain finite-volume treatment for the Maxwell's equations," *Electromagnetics.*, vol. 10, pp. 127-145, 1990.
14. N. K. Madsen and R. W. Ziolkowski, "A three-dimensional modified finite volume technique for Maxwell's equations," *Electromagnetics.*, vol. 10, pp. 147-161, 1990.
15. P. Monk and E. Suli, "A convergence analysis of Yee's scheme on non-uniform grids," *SIAM J. Numerical Analysis*, vol. 31, pp. 393-412, 1994.
16. A. Taflove and M. E. Brodwin, "Numerical solution of steady-state electromagnetic scattering problems using the time-dependent Maxwell's equations," *IEEE Trans. Antennas Propagat.*, vol. 23, no. 6, pp. 623 - 630, 1975.
17. K. R. Umashankar, A. Taflove, B. Beker, "Calculation and experimental validation of induced currents on coupled wires in an arbitrary shaped cavity," *IEEE Trans. Antennas Propagat.*, vol. 35, pp. 1248 – 1257, 1987.
18. A. Taflove, K. R. Umashankar, B. Beker, F. A. Harfoush, and K. S. Yee, "Detailed FDTD analysis of electromagnetic fields penetrating narrow slots and lapped joints in thick conducting screens," *IEEE Trans. Antennas Propagat.*, vol. 36, pp. 247 – 257, 1988.
19. S. Zivanovic, K. S. Yee and K. Mei, "A subgridding method for the time-domain finite-difference method to solve Maxwell's equations," *IEEE Trans. Microwave Theory and Techn.*, vol. 39, No. 3, pp. 471 -479, 1991.
20. M. Marrone and R. Mittra, "A new stable hybrid three-dimensional generalized finite difference time domain algorithm for analyzing complex structures," *IEEE Trans. Antennas Propagat.*, vol. 53, no. 5, pp. 1729 - 1737, 2005.
21. A. Taflove and S. C. Hagness, *Computational Electrodynamics: The Finite-Difference Time-Domain Method*, Artech House, Boston, London, 2005.
22. V. Varadarajan and R. Mittra, "Finite-Difference Time-Domain (FDTD), Analysis Using Distributed Computing," *IEEE Microwave and Guided Wave Letters*, Vol. 4, No. 5, May 1994, pp. 144-145.
23. S. Gedney, "Finite Difference Time Domain Analysis of Microwave Circuit Devices in High Performance Vector/Parallel Computers," *IEEE Transactions on Microwave Theory and Techn.*, Vol. 43, No. 10, October 1995, pp. 2510-2514.

24. W. Yu, R. Mittra, T. Su, Y. Liu, and X. Yang, *Parallel Finite Difference Time Domain Method*, Artech House, MA, 2006.
25. W. Yu, X. Yang, Y. Liu, L.-C. Ma, T. Su, N.-T. Huang, R. Mittra, R. Maaskant, Y. Lu, Q. Che, R. Lu, and Z. Su, "New direction in computational electromagnetics—solving large problems using the parallel FDTD on the BlueGene/L supercomputer providing teraflop-level performance", to be submitted to the *IEEE Antennas Propag. Magazine*.
26. M. R. Hashemi, R. Mittra, D. N. de Araujo, M. Cases, N. Pham, E. Matoglu, P. Patel, and B. Herrman, "Delay analysis using FDTD for source synchronous interfaces," IEEE 14th Topical Meeting on Electrical Performance of Electronic Packaging, pp. 217-220, Oct. 2005.
27. D. R. Smith, W. J. Padilla, D. C. Vier, S. C. Nemat-Nasser, and S. Schultz, "Composite Medium with Simultaneously Negative Permeability and Permittivity," *Phys. Rev. Lett.*, vol. 84, No. 18, pp. 4184-4187, 2000.
28. General Electromagnetic Simulator (GEMS), Computer and Communication Unlimited, State College, PA 16801, website: <http://www.2comu.com>.
29. W. Yu, Y. Liu, T. Su, N.-T. Huang, and R. Mittra, "A robust parallel conformal finite-difference time-domain processing package using the MPI library," *IEEE Antennas & Propag. Mag.*, vol 47, no. 3, pp. 39- 59, 2005.
30. T. Su, Y. Liu, W. Yu, and R. Mittra, "A conformal mesh-generating technique for the conformal finite-difference time-domain (CFDTD) method," *IEEE Antennas & Propag. Mag.*, vol 46, no. 1, pp. 37- 49, 2004.
31. J. A. Roden, S. D. Gedney, M. P. Kesler, J. G. Maloney, and P. H. Harms, "Time-domain analysis of periodic structures at oblique incidence: orthogonal and nonorthogonal FDTD implementations," *IEEE Trans. Microwave Theory and Techn.*, vol. 46, No. 4, pp. 420 - 427, 1998.
32. K. R. Umashankar and A. Taflove, "A novel method to analyze electromagnetic scattering of complex objects," *IEEE Trans. Electromagnetic Compatibility*, Vol. 24, pp. 397-405, 1982.
33. D. R. Smith, S. Schultz, P. Markos, and C. M. Soukoulis "Determination of effective permittivity and permeability of metamaterials from reflection and transmission Coefficients," *Phys. Rev. B*, vol. 65, 195104, 2002.
34. K. S. Kunz, R. J. Ruebbers, *The Finite Difference Time Domain Method for Electromagnetics*, CRC Press, 1993.

35. K. L. Shlager and J. B. Schneider, "A selective survey of the finite-difference time-domain literature," *IEEE Antennas Propagat. Magazine*, vol. 37, no. 4, pp. 39-57, 1995.
36. A. Taflove, "A perspective on the 40-year history of FDTD computational electrodynamics" *ACES Journal*, vol. 22, No. 1, pp. 1-21, 2007.
37. K. Chew and V. Fusco, "A Parallel Implementation of the Finite Difference Time Domain Algorithm," *International journal of Numerical Modeling Electronic Networks, Devices and Fields*, Vol. 8, pp. 293-299, 1995.
38. C. Guiffaut and K. Mahdjoubi, "A Parallel FDTD Algorithm Using the MPI Library," *IEEE Antennas Propagat. Magazine*, vol. 43, no. 2, pp. 94-103, 2001.
39. MPI Forum, MPI: A Message Passing Interface Standard, Version 1.1, June 1995, <http://www.mpi-forum.org>.
40. MPI Forum, MPI-2: Extension to the Message Passing Interface, July 1997, <http://www.mpi-forum.org>.
41. W. Gropp, E. Lusk, and A. Skjellum, Using MPI. Portable Parallel Programming with the Message Passing Interface, Cambridge, Massachusetts, MIT Press, 1994.
42. X. Yang, W. Yu, and R. Mittra, "Conformal FDTD package development based on ACIS and HOOPS," *APMC 2005 Proceedings*.
43. LOFAR Website, <http://www.lofar.org/BlueGene/>.
44. N. T. Huang, R. Mittra, R. Maaskant, W. Yu, "Investigation of the Vivaldi Array for Square Kilometer Array (SKA) Application Using the Parallelized FDTD Code GEMS on the LOFAR BlueGene/L Supercomputer", *The 2007 IEEE International Symposium on Antennas and Propagat.*, held in Honolulu, Hawaii, June 10-14, 2007.
45. M. Ivashina, J. Simons, and J. G. bij de Vaatte, "Efficiency analysis of focal plane arrays in deep dishes", *Experimental Astronomy, The Square Kilometre Array: An engineering perspective*, ISBN 1-4020-3797-X, Vol. 17, No. 1-3, pp. 149-162, 2004.
46. R. Mittra,; N. T. Huang; R. Hashemi, W. Yu; D. N. Araujo, B. Mutnury, M. Cases, "Modeling Multilayered Packages Using the Parallel Finite Difference Time Domain (PFDTD) Approach," *IEEE 15th Topical Meeting On Electrical Performance of Electronic Packaging*, Oct. 2006 pp. 295 – 298.
47. V. G. Vesalago, "The electrodynamics of substances with simultaneously negative values of ϵ and μ ," *Sov.Phys.Uspekhi*, vol. 10, No. 4, pp. 509-514, 1968.

48. D. R. Smith, W. J. Padilla, D. C. Vier, S. C. Nemat-Nasser, and S. Schultz, "Composite Medium with Simultaneously Negative Permeability and Permittivity," *Phys. Rev. Lett.*, vol. 84, No. 18, pp. 4184-4187, 2000.
49. T. K. Wu (Ed.), *Frequency Selective Surface and Grid Array*, Wiley Inter-Science, New York, 1995.
50. B. A. Munk, *Frequency Selective Surfaces: Theory and Design*. New York: Wiley, 2000.
51. M. E. Veysoglu, R. T. Shin, and J. A. Kong, "A finite-difference time-domain analysis of wave scattering from periodic surfaces: Oblique incidence case," *J. Electromagn. Waves Apps.*, Vol. 7, pp. 1595-1607, 1993.
52. P. Harms, R. Mittra and W. Ko, "Implementation of the periodic boundary condition in the finite-difference time-domain algorithm for FSS structures," *IEEE Trans. Antennas Propagat.*, vol. 42, no. 9, pp. 1317 - 1324, 1994.
53. Y.C. Kao, and R. G. Atkins, "A finite-difference time-domain approach for frequency selective surfaces at oblique incidence," in *IEEE Antennas and Propagat. Society Int. Symp.*, AP-S. Digest, Vol. 2, pp. 1432-1435, 1996.
54. A. Aminian and Y. Rahmat-Samii, "Spectral FDTD: A novel technique for the analysis of oblique incident plane wave on periodic structures," *IEEE Trans. Antennas Propagat.*, vol. 54, no. 6, pp. 1818 - 1825, 2006.
55. M. Kuzuoglu and R. Mittra, "Frequency dependence of the constitutive parameters of casual perfectly matched anisotropic absorbers," *IEEE Microwave Guided Wave Lett.*, vol. 6, pp. 447-449, 1996.
56. W. C. Chew and W. H. Weedon, "A 3D perfectly matched medium from modified Maxwell's equations with stretched coordinates," *Microwave Opt. Technol. Lett.*, vol. 7, pp. 599-604, 1994.
57. J. A. Roden, P. Skinner, S. Johns, "Shielding Effectiveness of 3D Gratings using the Periodic Technique and CPML", *IEEE/ACES International Conf. On Wireless Communications and Applied Electromagnetics*, 2005.
58. J. B. Pendry, A. J. Holden, W. J. Stewart, and I. Youngs, "Extremely low frequency plasmons in metallic mesostructures," *Phys. Rev. Lett.*, vol. 76, No. 25, pp. 4773-4776, 1996.
59. J. B. Pendry, A. J. Holden, D. J. Robbins, and W. J. Stewart, "Magnetism from Conductors and Enhanced Non-linear Phenomenon," *IEEE Trans. Microwave Theory and Techn.*, vol. 47, No. 11, pp. 2075-2084, 1999.

60. B. Ferguson and X.-C. Zhang, "Materials for Terahertz Science and Technology," *Nature Materials*, vol. 1, pp. 26-33, 2002.
61. K. Z. Rajab, R. Mittra, M. Naftaly, E. H. Linfield, M. T. Lanagan, "Terahertz Transmission Through Periodic Arrays of Dielectric and Conducting Spheres", in *IEEE Antennas and Propagat. Society Int. Symp.*, June 10-14, 2007.
62. G. Mur, "Absorbing boundary conditions for the finite-difference approximation of the time-domain electromagnetic field equations," *IEEE Trans. Electromagnetic Compatibility*, Vol. 23, pp. 377-382, 1981.
63. K. Demarest, R. Plumb, and Z. Huang, "FDTD modeling of scatterers in stratified media," *IEEE Trans. Antennas Propagat.*, vol. 43, no. 10, pp. 1164-1168, 1995.
64. V. Anantha and A. Taflove, "Efficient modeling of infinite scatterers using a generalized total-field/scattered-field FDTD boundary partially embedded within PML," *IEEE Trans. Antennas Propagat.*, vol. 50, no. 10, pp. 1337-1349, 2002.
65. J. H. Chang and A. Taflove, "Three-dimensional diffraction by infinite conducting and dielectric wedges using a generalized total-field/scattered-field FDTD formulation," *IEEE Trans. Antennas Propagat.*, vol. 53, no. 14, pp. 1444-1454, 2005.
66. L.-C. Ma and R. Mittra, "Implementation of Gaussian beam sources in FDTD for scattering problems," in *IEEE Antennas and Propagat. Society Int. Symp.*, June 10-14, 2007.
67. Saleh, Bahaa E. A. and Teich, Malvin Carl, *Fundamentals of Photonics*, New York: John Wiley & Sons. Chapter 3, "Beam Optics," pp. 80-107, 1991.
68. M. Beruet, M. Sorolla, and I. Campillo, "Left-handed extraordinary optical transmission through a photonic crystal of subwavelength hole arrays," *Opt. Express*, Vol. 15, 1107-1114, 2007.
69. M. Beruet, M. Sorolla, M. Navarro, and F. Falcone, "Extraordinary transmission and left-handed propagation in miniaturized stacks of doubly periodic subwavelength hole arrays," *Opt. Express*, Vol. 15, 1107-1114, 2007.
70. R. J. Luebbers, K. S. Kunz, M. Schneider, and F. Hunsberger, "A finite-difference time-domain near zone to far zone transformation," *IEEE Trans. Antenna Propagat.*, vol. 39, pp. 429-433, 1991.
71. K. Demarest, Z. Huang and R. Plumb, "An FDTD near- to far-zone transformation for scatterers buried in stratified grounds," *IEEE Trans. Antenna Propagat.*, vol. 44, no. 8, pp. 1150-1157, 1996.

72. J. B. Pendry, "Negative Refraction makes a Perfect Lens," *Phys. Rev. Lett.*, vol. 85, No. 18, pp. 3966-3969, 2000.
73. R. A. Shelby, D. R. Smith, and S. Schultz, "Experimental Verification of a Negative Index of Refraction," *Science*, vol. 292, pp. 77-79, 2001.
74. M. McCall, A. Lakhtakia, and W. S. Weiglhofer, "The negative index of refraction demystified," *Eur. J. Phys.*, vol. 23, pp. 353-359, 2002.
75. P. Markos and C. M. Soukoulis, "Left-handed materials," *Preprint cond-mat/0212136*, 2002.
76. S. A. Ramakrishna, "Physics of negative refractive index materials," *Rep. Prog. Phys.*, vol. 68, pp. 449-521, 2005.
77. P. Markos and C. M. Soukoulis, "Transmission Properties and Effective Electromagnetic Parameters of Double Negative Metamaterials," *Opt. Express*, vol. 11, No. 7, pp. 649-651, 2003.
78. X. Chen, T. M. Grzegorzczuk, B. Wu, J. Pacheco, and J. A. Kong, "Robust Method to Retrieve the Constitutive Effective Parameters of Metamaterials," *Phys. Rev. E*, vol. 70, No. 1, 016608: 1-7, 2004.
79. O. Archer, A. L. Adenot, and F. Duverger, "Fresnel Coefficients at an Interface with a Lamellar Composite Material," *Phys. Rev. B*, vol. 62, No. 20, pp. 13748-13756, 2000.
80. T. Weiland, R. Schuhmann, R. B. Greigor, C. G. Parazoli, A. M. Vetter, D. R. Smith, D. C. Vier, and S. Schultz "Ab initio Numerical Simulation of Left-Handed Metamaterials: Comparison of Calculations and Experiments," *J. Appl. Phys.*, vol. 90, No. 10, pp. 5419-5424, 2001.
81. C. D. Moss, T. M. Grzegorzczuk, Y. Zhang, and J. A. Kong, "Numerical Studies of Left Handed Metamaterials," *Prog. Electromagn. Res.*, Vol. 35, pp. 315-334, 2002.
82. R. W. Ziolkowski, "Design, Fabrication, and Testing of Double Negative Metamaterials," *IEEE Trans. Antennas and Propag.*, vol. 51, No. 7, pp. 1516-1528, 2003.
83. T. Koschny, P. Markos, D. R. Smith, and C. M. Soukoulis, "Resonant and antiresonant frequency dependence of the effective parameters of metamaterials," *Phys. Rev. E*, vol. 68, 065602: 1-4, 2003.
84. D. Seetharamdoo, R. Sauleau, K. Mahdjoubi and A. Tarot, "Effective Parameters of Negative Refractive Index Metamaterials: Interpretation and Validity," *J. Appl. Phys.*, vol. 98, No. 6, 063505: 1-4, 2005.

VITA

Lai-Ching (Kit) Ma

Lai-Ching Ma received her B. S. and M. Phil. degrees in Physics (minor in Mathematics) from the Chinese University of Hong Kong, Hong Kong in 1996 and 2001, respectively. From 1996 to 1999, she worked as a high school physics/science teacher. She began her doctoral studies in Electrical Engineering at the Pennsylvania State University in fall of 2001 and has held a research assistantship at the Electromagnetic Communication Laboratory, Pennsylvania State University since summer of 2002. Her research interests are in the area of antennas and computational electromagnetics with emphasis on the parallel finite difference time domain (FDTD) technique and its application to model and design the metamaterial/antenna or EBG/antenna composites for enhancing the antenna performance.

Selected Publications:

1. W. Yu, X. Yang, Y. Liu, L.-C. Ma, T. Su, N.-T. Huang and R. Mittra, R. Maaskant, "New Direction in Computational Electromagnetics —Solving Large Problem Using the Parallel FDTD on the BlueGene/L Supercomputer Yielding TeraHop-Level Performance," to be accepted by the *IEEE Antennas & Propagation Magazine*.
2. L.-C. Ma and R. Mittra, "Parallel Implementation of the Periodic Boundary Condition (PBC) in the FDTD for the Investigation of Spatial Filters", to be submitted to *IEEE Antennas & Propagation Society(AP-S) International Symposium/URSI*, San Diego, California, July 2008.
3. L.-C. Ma, J. Qu, R. Mittra and N. Farahat, "Understanding the Physical Mechanism of Performance Enhancement of Antennas via the Use of EBG Superstrate", to be submitted to *IEEE AP-S International Symposium/URSI*, San Diego, California, July 2008.
4. R. Mittra, L.-C. Ma and N. Farahat, "A Case for Rigorous Numerical Simulation to Model Antenna Metamaterial Composites", *Metamaterials 2007*, Rome, Italy, October 2007.
5. L.-C. Ma, R. Mittra, "Implementation of Gaussian Beam Sources in FDTD for Scattering Problems", *the IEEE AP-S International Symposium*, held in Honolulu, Hawaii, June 2007.
6. L.-C. Ma, R. Mittra, "Electromagnetic Scattering from Large bodies using an Extrapolation Technique," 2005 *IEEE AP-S International Symposium and USNC/URSI National Radio Science Meeting*, Washington DC, July 2005.
7. T. Su, L.-C. Ma, N. Farahat and R. Mittra, "Modeling of a Large Slotted Waveguide Phased Array Using the FDTD and Characteristic Basis Function (CBF) Approaches," *IEEE AP-S International Symposium/URSI*, Columbus, Ohio, June 2003.
8. L.-C. Ma, W. Yu, H. E. Abd El-Raouf, "Electromagnetic Modeling of Objects with Curved Edges and Surfaces using the Conformal FDTD," *IEEE AP-S International Symposium/URSI*, Columbus, Ohio, June 2003.
9. H. E. Abd El-Raouf, L.-C. Ma, W. Yu and R. Mittra, "Analysis of microstrip patch arrays using the FDTD method," *Microwave & Optical Technology Letters*, Vol. 36, No. 4, pp. 250-254, Feb. 2003.